

REPORT DOCUMENTATION PAGE

Form Approved OMB NO. 0704-0188

The public reporting burden for this collection of information is estimated to average 1 hour per response, including the time for reviewing instructions, searching existing data sources, gathering and maintaining the data needed, and completing and reviewing the collection of information. Send comments regarding this burden estimate or any other aspect of this collection of information, including suggestions for reducing this burden, to Washington Headquarters Services, Directorate for Information Operations and Reports, 1215 Jefferson Davis Highway, Suite 1204, Arlington VA, 22202-4302. Respondents should be aware that notwithstanding any other provision of law, no person shall be subject to any penalty for failing to comply with a collection of information if it does not display a currently valid OMB control number.

PLEASE DO NOT RETURN YOUR FORM TO THE ABOVE ADDRESS.

1. REPORT DATE (DD-MM-YYYY) 07-05-2010	2. REPORT TYPE Final Report	3. DATES COVERED (From - To) 19-Jul-2006 - 31-Aug-2009		
4. TITLE AND SUBTITLE Final Report on Magnetic Field-Induced Phase Transformation in Magnetic Shape Memory Alloys with High Actuation Stress and Work Output		5a. CONTRACT NUMBER W911NF-06-1-0319		
		5b. GRANT NUMBER		
		5c. PROGRAM ELEMENT NUMBER 611102		
6. AUTHORS Ibrahim Karaman, Dimitris C. Lagoudas		5d. PROJECT NUMBER		
		5e. TASK NUMBER		
		5f. WORK UNIT NUMBER		
7. PERFORMING ORGANIZATION NAMES AND ADDRESSES Texas Engineering Experiment Station Research Services Texas Engineering Experiment Station (TEES) College Station, TX 77845 -4645		8. PERFORMING ORGANIZATION REPORT NUMBER		
9. SPONSORING/MONITORING AGENCY NAME(S) AND ADDRESS(ES) U.S. Army Research Office P.O. Box 12211 Research Triangle Park, NC 27709-2211		10. SPONSOR/MONITOR'S ACRONYM(S) ARO		
		11. SPONSOR/MONITOR'S REPORT NUMBER(S) 50718-MS.1		
12. DISTRIBUTION AVAILABILITY STATEMENT Approved for Public Release; Distribution Unlimited				
13. SUPPLEMENTARY NOTES The views, opinions and/or findings contained in this report are those of the author(s) and should not be construed as an official Department of the Army position, policy or decision, unless so designated by other documentation.				
14. ABSTRACT The main goal of the project centers on the idea of identifying, fabricating, characterizing and modeling new magnetic shape memory alloys (MSMAs) and compositions to utilize field-induced phase transformation (FIPT) with the objective of obtaining large actuation stresses, large reversible actuation strains, work outputs, and operating temperature ranges. The novelty of the project arises from the utilization of a new magneto-mechanical mechanism in achieving high work output actuator materials (with the possibility of superior sensing and passive				
15. SUBJECT TERMS magnetic shape memory alloys, phase transformation, constitutive modeling, martensite, shape memory alloys, magnetic-field induced phase transformation, actuation, actuator				
16. SECURITY CLASSIFICATION OF: a. REPORT UU		17. LIMITATION OF ABSTRACT UU	15. NUMBER OF PAGES	19a. NAME OF RESPONSIBLE PERSON Ibrahim Karaman
				19b. TELEPHONE NUMBER 979-862-3923

Report Title

Final Report on Magnetic Field-Induced Phase Transformation in Magnetic Shape Memory Alloys with High Actuation Stress and Work Output

ABSTRACT

The main goal of the project centers on the idea of identifying, fabricating, characterizing and modeling new magnetic shape memory alloys (MSMAs) and compositions to utilize field-induced phase transformation (FIPT) with the objective of obtaining large actuation stresses, large reversible actuation strains, work outputs, and operating temperature ranges. The novelty of the project arises from the utilization of a new magneto-mechanical mechanism in achieving high work output actuator materials (with the possibility of superior sensing and passive power generation capabilities) from the new MSMAs. The major accomplishments of the project include: 1) the design of a NiMnCoIn composition that resulted in reversible FIPT under magnetic field magnitudes much less than what has been reported in iron based alloys; 2) growth of large single crystals from this composition, 3) the demonstration of magnetostress levels larger than 20 MPa/Tesla in the designed composition utilizing FIPT whereas all previously reported magnetostress levels have been always less than 10MPa/Tesla regardless of the alloy system, composition, and magneto-microstructural mechanism; 4) the investigation of complex magneto-mechanical loading paths; and 5) the analysis of nonlinear magnetostatic boundary value problems for MSMAs using finite element method and taking into account FIPT.

List of papers submitted or published that acknowledge ARO support during this reporting period. List the papers, including journal references, in the following categories:

(a) Papers published in peer-reviewed journals (N/A for none)

1. Dadda, J., Maier, H.J., Karaman, I., and Chumlyakov, Y.I., "High Temperature In-Situ Microscopy during Stress-Induced Phase Transformations in Co49Ni21Ga30 Shape Memory Alloy Single Crystals," International Journal of Materials Research, in press, 2010.
2. Monroe, J.A., Karaman, I., Karaca, H.E., Chumlyakov, Y.I., and Maier, H.J., "High Temperature Superelasticity and Competing Microstructural Mechanisms in Co49Ni21Ga30 Shape Memory Alloy Single Crystals Under Tension," Scripta Materialia, Vol.62, pp. 368-371, 2010.
3. Ito, W., Basaran, B., Umetsu, R.Y., Karaman, I., Kainuma, R., and Ishida, K., "Shape Memory Response in the Ni40Co10Mn33Al17 Polycrystalline Alloy," Materials Transactions JIM, Vol. 51, pp. 525-528, 2010.
4. Dadda, J., Maier, H.J., Karaman, I., and Chumlyakov, Y.I., "Cyclic Deformation and Austenite Stabilization in Co35Ni35Al30 Single Crystalline High-temperature Shape Memory Alloys," Acta Materialia, Vol. 57, pp. 6123-6134, 2009.
5. Karaca, H.E., Karaman, I., Basaran, B., Chumlyakov, Y.I., and Maier, H.J., "Magnetic Field-Induced Martensitic Phase Transformation in NiMnCoIn Ferromagnetic Shape Memory Alloys," Advanced Functional Materials, Vol. 19, pp. 983-998, 2009.
6. Kiefer B., and Lagoudas D. C., "Modeling the Coupled Strain and Magnetization Response of Magnetic Shape Memory Alloys under Magneto-mechanical Loading Paths," Journal of Intelligent Material Systems and Structures, Vol. 20, pp. 143-170, 2009.
7. Chumlyakov, Y.I., Panchenko, E.Y., Ovsyannikov, A.V., Chusov, S.V., Kirillov, V.A., Karaman, I., and Maier, H.J., "High-Temperature Superelasticity and the Shape-Memory Effect in [001] Co–Ni–Al Single Crystals," Physics of Metals and Metallography, Vol. 107, pp. 194-205, 2009.
8. Kireeva, I.V., Pobedennaya, Z.V., Chumlyakov, Y.I., Pons, J., Cesari, E., and Karaman, I., "Effect of Orientation on the High-Temperature Superelasticity in Co49Ni21Ga30 Single Crystals," Technical Physical Letters, Vol. 35, pp. 186-189, 2009.
9. Niklasch D., Dadda J., Maier H.J., and Karaman I., "Magneto-Microstructural Coupling During Stress-Induced Phase Transformation in Co49Ni21Ga30 Ferromagnetic Shape Memory Alloy Single Crystals," Journal of Materials Science, Vol. 43, pp. 6890-6901, 2008.
10. Karaca H.E., Karaman I., Brewer A., Basaran B., Chumlyakov Y.I., Maier H.J., "Shape Memory and Pseudoelasticity Response of NiMnCoIn Magnetic Shape Memory Alloy Single Crystals", Scripta Materialia, Vol. 58, Issue 10 pp. 815-818, 2008.
11. Kiefer B., and Lagoudas D.C., "Modeling of the Variant Reorientation in Magnetic Shape-Memory Alloys under Complex Magneto-mechanical Loading," Materials Science and Engineering A, Vol. 481-482, pp.339-342, 2008.
12. Kart S.O., Uludogan M., Karaman I., and Cagin T., "DFT Studies on Structure, Mechanics and Phase Behavior of Magnetic Shape Memory Alloys: Ni₂MnGa," Physica Status Solidi A, Vol. 205, pp. 1026-1035, 2008.
13. Niklasch D., Maier H.J., and Karaman I., "Design and Application of a Mechanical Load Frame for In-situ Investigation of Ferromagnetic Shape Memory Alloys by Magnetic Force Microscopy," Review of Scientific Instruments, Vol. 79, p. 113701, 2008.
14. Dadda J., Maier H.J., Niklasch D., Karaman I., Karaca H.E., and Chumlyakov Y.I., "Pseudoelasticity and Cyclic Stability in Co49Ni21Ga30 Shape Memory Alloy Single Crystals at Ambient Temperature," Metallurgical and Materials Transactions A, Vol. 39, pp. 2026-2039, 2008.
15. Chumlyakov Y.I., Panchenko E., Kireeva I.V., Karaman I., Sehitoglu H., Maier H.J., Tverdokhlebova A., and Ovsyannikov A., "Orientation dependence and tension/compression asymmetry of shape memory effect and superelasticity in ferromagnetic γ -o40Ni33Al27, Co49Ni21Ga30 and Ni54Fe19Ga27 single crystals," Materials Science and Engineering A, Vol. 481-482, pp. 95-100, 2008.
16. Chumlyakov, Y.I., Kireeva, I.V., Panchenko, E.Y., Timofeeva, E.E., Pobedennaya, Z.V., Chusov, S.V., Karaman, I., Maier, H.J., Cesari, E., and Kirillov, V.A., "High Temperature Superelasticity in CoNiGa, CoNiAl, NiFeGa, and TiNi Monocrystals," Russian Physics Journal, Vol. 51, pp. 1016-1036, 2008.
17. Karaca HE, Karaman I, Basaran B, Lagoudas DC, Chumlyakov YI, and Maier HJ, "On the Stress-Assisted Magnetic Field-Induced Phase Transformation in Ni2MnGa Ferromagnetic Shape Memory Alloys," Acta Materialia, Vol. 55, pp. 4253-4269, 2007.

18. Kiefer B, Karaca HE, Lagoudas DC, and Karaman I, "Characterization and Modeling of the Magnetic Field-Induced Strain and Work Output in Ni₂MnGa Magnetic Shape Memory Alloys," *Journal of Magnetism and Magnetic Materials*, Vol. 312, pp. 164-175, 2007.
19. Karaman I, Basaran B, Karaca HE, Karsilayan AI, and Chumlyakov YI, "Energy Harvesting Using Martensite Variant Reorientation Mechanism in a NiMnGa Magnetic Shape Memory Alloy," *Applied Physics Letters*, Vol. 90, 172505, 2007.
20. Dadda J, Canadinc D, Maier HJ, Karaman I, Karaca HE, and Chumlyakov YI, "Stress-Strain-Temperature Behavior of [001] Single Crystals of Co₄₉Ni₂₁Ga₃₀ Ferromagnetic Shape Memory Alloy under Compression," *Philosophical Magazine*, Vol. 87, No.16, pp. 2313-2322, 2007.
21. Canadinc D, Dadda J, Maier HJ, Karaman I, Karaca HE, and Chumlyakov YI, "On the Role of Cooling Rate and Crystallographic Orientation on the Shape Memory Properties of CoNiAl Single Crystals Under Compression," *Smart Materials and Structures*, Vol. 16, pp. 1006-1015, 2007.
22. Karaman I, Karaca HE, Basaran B, Lagoudas DC, Chumlyakov YI, and Maier HJ, "Stress-Assisted Reversible Magnetic Field-Induced Phase Transformation in Ni₂MnGa Magnetic Shape Memory Alloys," *Scripta Materialia*, Vol. 55, pp. 403-406, 2006.
23. Karaca HE, Karaman I, Basaran B, Lagoudas DC, Chumlyakov YI, and Maier HJ, "One-way Shape Memory Effect due to Stress Assisted Field-Induced Phase Transformation in Ni₂MnGa Magnetic Shape Memory Alloys," *Scripta Materialia*, Vol. 55, pp. 803-806, 2006.
24. Meyer D, Maier HJ, Dadda J, Karaman I, and Karaca HE, "Thermally and Stress-Induced Martensitic Transformation in CoNiAl Ferromagnetic Shape Memory Alloy Single Crystals," *Materials Science and Engineering A*, Vol. 438-440, pp. 875-878, 2006.
25. Dadda J, Maier HJ, Karaman I, Karaca HE, and Chumlyakov YI, "Pseudoelasticity at Elevated Temperatures in [001] Oriented Co₄₉Ni₂₁Ga₃₀ Single Crystals under Compression," *Scripta Materialia*, Vol. 55, pp. 663-666, 2006.

Number of Papers published in peer-reviewed journals: 25.00

(b) Papers published in non-peer-reviewed journals or in conference proceedings (N/A for none)

Number of Papers published in non peer-reviewed journals: 0.00

(c) Presentations

1. Haldar K., Lagoudas D.C., Basaran, B., and Karaman, I., "Modeling of Magnetic Field Induced Phase Transformation in NiMnCoIn Magnetic Shape Memory Alloys," The 2009 joint ASCE-ASME-SES conference on Mechanics and Materials, June 24-27, 2009, Blakburg, VT, 2009.
2. Lagoudas D.C., Kiefer B., and Haldar K., "Magnetic Field-Induced Reversible Phase Transformations in Magnetic Shape Memory Alloys," Conference on Behavior and Mechanics of Multifunctional and Composite Materials III, The International Society for Optical Engineering (SPIE) 16th Annual International Symposium on Smart Structures and Materials & Nondestructive Evaluation and Health Monitoring, March 9-12, 2009, San Diego, CA, 2009.
3. Karaman, I., Basaran, B., Zhu, R., Karaca, H.E., and Chumlyakov, Y.I., "Crystallographic Orientation and Heat Treatment Effect on Magnetic Field-Induced Phase Transformations of NiMnCoIn Metamagnetic Shape Memory Alloys," Symposium on Magnetic Shape Memory Alloys, MRS Fall Meeting, November 30 - December 4, 2009, Boston, MA, 2009.
4. Karaca, H.E., Karaman, I., Basaran, B., and Chumlyakov, Y.I., "Magnetic Field-Induced Phase Transformations in NiMn-based Shape Memory Alloys," Symposium on Active Materials, Mechanics and Behavior, ASME 2009 Conference on Smart Materials, Adaptive Structures and Intelligent Systems, September 21-23, 2009, Oxnard, CA, 2009.
5. Basaran, B., Karaman, I., Zhu, R., Karaca, H.E., and Chumlyakov, Y.I., "The Effect of Simultaneous Stress and Magnetic Field on the Actuator Type Response of NiMnCoIn and NiMnCoSn Metamagnetic Shape Memory Alloys," Symposium on Active Materials, Mechanics and Behavior, ASME 2009 Conference on Smart Materials, Adaptive Structures and Intelligent Systems, September 21-23, 2009, Oxnard, CA, 2009.
6. Lagoudas, D.C., Haldar, K., Basaran, B., and Karaman, I., "Constitutive Modeling of Magnetic Field-Induced Phase Transformations in NiMnCoIn Magnetic Shape Memory Alloys," Symposium on Active Materials, Mechanics and Behavior, ASME 2009 Conference on Smart Materials, Adaptive Structures and Intelligent Systems, September 21-23, 2009, Oxnard, CA, 2009.
7. Karaca, H.E., Karaman, I., Basaran, B., Chumlyakov, Y.I., and Maier, H.J., "Characterization of Ferromagnetic CoNiAl and NiFeGa Alloys for High Temperature Shape Memory Applications," Symposium on Active Materials, Mechanics and Behavior, ASME 2009 Conference on Smart Materials, Adaptive Structures and Intelligent Systems, September 21-23, 2009, Oxnard, CA, 2009.
8. Karaca, H.E., Basaran, B., Karaman, I., and Chumlyakov, Y.I., "Characterization of Magnetic Field-Induced Phase Transformations in NiMnCoIn Meta-magnetic Shape Memory Alloys," Symposium on Domain Microstructures and Mechanisms for Advanced Properties in Phase Transforming Materials, Materials Science & Technology 2009 Conference, October 25-29, 2009, Pittsburgh, PA, 2009.
9. Kireeva, I.V., Pobedennaya, Z.V., Chumlyakov, Y.I., Kretinina, I.V., Cesari, E., Pons, J., and Karaman, I., "Characteristics of Superelasticity in Ferromagnetic <001> Single Crystals of a CoNiGa Alloy during Compressive Deformation," The 8th European Symposium on Martensitic Transformations, September 7-11, 2009, Prague, Czech Republic, 2009.
10. Ren, Y., Wang, Y.D., Nie, Z.H., Karaman, I., Karaca, H.E., Gama, S., and Brown, D.E., "High-Energy Synchrotron X-Ray Diffraction for In-Situ Study of Structural Phase Transformations," Symposium on Domain Microstructures and Mechanisms for Advanced Properties in Phase Transforming Materials, Materials Science & Technology 2009 Conference, October 25-29, 2009, Pittsburgh, PA, 2009.
11. Chumlyakov, Y.I., Kireeva, I.V., Panchenko, E.Y., Maier, H.J., Karaman, I., Timofeeva, E.E., Pobedennaya, Z.V., and Kirillov, V.A., "High Temperature Superelasticity in Ferromagnetic Single Crystals with Thermoelastic Martensitic Transformation," The 8th European Symposium on Martensitic Transformations, September 7-11, 2009, Prague, Czech Republic, 2009.
12. Karaman I., Karaca H.E., Basaran B., and Chumlyakov Y.I., "Magnetic Field-Induced Phase Transformation in NiMnCoIn Metamagnetic Shape Memory Alloys," The Symposium on Shape Memory Alloys - Mechanisms, Multifunctionalities, and Applications, The 45th Annual Technical Meeting of Society of Engineering Science (SES), Urbana, IL, October 12 – 15, 2008.
13. Basaran B., Karaman I., Karaca H.E., and Karsilayan, A.I., "Utilization of Magnetic Shape Memory Alloys in Energy Harvesting," The International Conference on Martensitic Transformations (ICOMAT 08), June 29 – July 4, 2008, Santa Fe, NM, 2008.
14. Karaman I., Karaca H.E., Basaran B., Chumlyakov Y.I., and Maier, H.J., "Magnetic Field-Induced Phase Transformation in NiMnCoIn Shape Memory Alloys," The International Conference on Martensitic Transformations (ICOMAT 08), June 29 – July 4, 2008, Santa Fe, NM, 2008.

15. Karaca, H.E., Karaman, I., Badakhshan, S., Basaran, B., Chumlyakov Y.I., Niklasch D., and Maier H.J., "Shape Memory Behavior of NiFeGa(Co) Ferromagnetic Shape Memory Single Crystals," The International Conference on Martensitic Transformations (ICOMAT 08), June 29 – July 4, 2008, Santa Fe, NM, 2008.
16. Niklasch, D., Maier, H.J., Karaman, I., and Chumlyakov, Y.I., "In-Situ Characterization of Stress-Induced Martensite and Related Magnetic Domain Structure in Ni-Fe-Ga Ferromagnetic Shape Memory Alloy Single Crystals," International Conference on Martensitic Transformation (ICOMAT) 2008, June 29 – July 5, 2008, Santa Fe, NM, 2008.
17. Dadda, J., Maier, H.J., Karaman, I., and Karaca, H.E.*, "Functional Degradation of CoNiAl and CoNiGa High-Temperature Shape Memory Alloy Single Crystals at Elevated Temperatures upon Cyclic Deformation," International Conference on Martensitic Transformation (ICOMAT) 2008, June 29 – July 5, 2008, Santa Fe, NM, 2008.
18. Maier H.J., Niklasch D., and Karaman I., "Magneto-Microstructural Characterization of Magnetic Shape Memory Alloys," The 3rd International Conference on Smart Materials, Structures and Systems (CIMTEC 2008), Symposium A: Smart Materials and Micro/Nanosystems, June 8-13, 2008, Acireale, Sicily, Italy, 2008.
19. Karaman I., Karaca H.E., Basaran B., Chumlyakov Y.I., and Maier H.J., "Magnetic Field-Induced Phase Transformation in NiMnGa and NiMnCoIn Shape Memory Alloys," Conference on Behavior and Mechanics of Multifunctional and Composite Materials II, The International Society for Optical Engineering (SPIE) 15th Annual International Symposium on Smart Structures and Materials & Nondestructive Evaluation and Health Monitoring, March 9-13, 2008, San Diego, CA, 2008.
20. Karaca, H.E., Karaman, I., Chumlyakov, Y.I., and Maier, H.J., "Shape Memory Behavior of NiFeGa(Co) Ferromagnetic Shape Memory Single Crystals," Conference on Behavior and Mechanics of Multifunctional and Composite Materials, The International Society for Optical Engineering (SPIE) 15th Annual International Symposium on Smart Structures and Materials & Nondestructive Evaluation and Health Monitoring, March 9-13, 2008, San Diego, CA, 2008.
21. Karaman I., Karaca H.E., Basaran B., Chumlyakov Y.I., and Maier H.J., "Crystallographic Orientation Dependence of Magnetic Field-Induced Phase Transformation in NiMnCoIn Single Crystals," The Symposium on "Magnetic Shape Memory Alloys," 2007 Materials Research Society (MRS) Fall Meeting, November 26-30, 2007, Boston, MA, 2007.
22. Karaca H.E., Basaran B., Karaman I., Chumlyakov Y.I., Niklasch D., and Maier H.J., "Compressive response of NiFeGa Ferromagnetic Shape Memory Single Crystals," The Symposium on Shape Memory Alloys - Mechanisms, Multifunctionalities, and Applications, The 44th Annual Technical Meeting of Society of Engineering Science (SES), College Station, TX, October 21 – 24, 2007.
23. Basaran, B., Karaca H.E., Karaman I., and Chumlyakov Y.I., "Enhancing Actuator Properties of NiMnCoIn Magnetic Shape Memory Alloys by Field-Induced Phase Transformation," The Symposium on Shape Memory Alloys - Mechanisms, Multifunctionalities, and Applications, The 44th Annual Technical Meeting of Society of Engineering Science (SES), College Station, TX, October 21 – 24, 2007.
24. Karaca HE, Karaman I, Basaran B, and Chumlyakov YI, "Magnetic Field-Induced Phase Transformation in NiMnGa and NiMnCoIn Shape Memory Alloys," ASME Applied Mechanics and Materials Conference, Phase Transformations and Mechanochemistry Symposium, June 3-7, 2007, Austin, TX, 2007.
25. Karaman I, Karaca HE, and Basaran B, "Reversible field-induced phase transformation in Ni₂MnGa with large actuation stress and work output," Conference on Behavior and Mechanics of Multifunctional and Composite Materials, The International Society for Optical Engineering (SPIE) 14th Annual International Symposium on Smart Structures and Materials, March 18-22, 2007, San Diego, CA, 2007.
26. Lagoudas, D.C. and Kiefer, B., "Modeling of Magnetic Shape Memory Alloys", , The International Society for Optical Engineering (SPIE) 14th Annual International Symposium on Smart Structures and Materials, March 18-22, 2007, San Diego, CA, 2007
27. Basaran B, Karaca HE, Karaman I, Chumlyakov YI, and Maier HJ, "Effect of Magnetic Field on the Multi-Stage Martensitic Phase Transformation in NiMnGa Magnetic Shape Memory Alloys," Symposium on Fundamentals of Shape Memory and Related Transitions, TMS 2007 Annual Meeting, February 25 – March 1, 2007, Orlando, FL, 2007.
28. Lagoudas, D., Kiefer, B. and Broedersdorf, A., "Constitutive Modeling of Magnetic Shape Memory Alloys with Magneto-Mechanical Coupling," Comp-07 (International Symposium on Advanced Composite Technology), May 16-18, 2007, Corfu, Greece, 2007.

29. Lagoudas, D.C., Kiefer, B., and Broederdorff, A.J., "Accurate Interpretation of Magnetic Shape Memory Alloy Experiments Utilizing Coupled Magnetostatic Analysis", ASME International Mechanical Engineering Congress and Exposition 2006, November 5-10, 2006, Chicago, IL, 2006.
30. Kart SO, Uludogan M, Karaman I, and Cagin T, "DFT Studies on Magnetic Shape Memory Alloys," 62nd Southwest Regional Meeting of the American Chemical Society, October 19-22, 2006, Houston, Texas, 2006.
31. Karaman I, Karaca HE, Basaran B, Lagoudas DC, Chumlyakov YI, and Maier HJ, "Reversible Field-Induced Phase Transformation in Ni₂MnGa with Large Actuation Stress and Work Output," The 7th European Symposium on Martensitic Transformations and Shape Memory Alloys, September 10-15, 2006, Bochum, Germany, 2006.
32. Karaca HE, Karaman I, Basaran B, Chumlyakov YI, and Maier HJ, "Remarkable Pseudoelastic Response of Co₄₈Ni₃₃Al₉ and Ni₅₄Ga₂₇Fe₁₉ Ferromagnetic Shape Memory Alloys under Tension and Compression," The 7th European Symposium on Martensitic Transformations and Shape Memory Alloys, September 10-15, 2006, Bochum, Germany, 2006.
33. Basaran B, Karaca HE, Karaman I, Chumlyakov YI, and Maier HJ, "Guidelines to Increase Actuation Stress in NiMnGa Magnetic Shape Memory Alloys," The 7th European Symposium on Martensitic Transformations and Shape Memory Alloys, September 10-15, 2006, Bochum, Germany, 2006.
34. Dadda J, Maier HJ, Karaman I, Karaca HE, and Chumlyakov YI, "Pseudoelasticity in Co₄₉Ni₂₁Ga₃₀ Ferromagnetic Shape Memory Single Crystals Under Compression," The 7th European Symposium on Martensitic Transformations and Shape Memory Alloys, September 10-15, 2006, Bochum, Germany, 2006.
35. Chumlyakov YI, Panchenko E, Kireeva IV, Karaman I, Sehitoglu H, Maier H, Ovsyannikov A, and Tverdokhlebova A, "Orientation dependence of shape memory effect and superelasticity in ferromagnetic Co-Ni-Al, Co-Ni-Ga, Ni-Fe-Ga single crystals," The 7th European Symposium on Martensitic Transformations and Shape Memory Alloys, September 10-15, 2006, Bochum, Germany, 2006.

Number of Presentations: 35.00

Non Peer-Reviewed Conference Proceeding publications (other than abstracts):

Number of Non Peer-Reviewed Conference Proceeding publications (other than abstracts): 0

Peer-Reviewed Conference Proceeding publications (other than abstracts):

1. Haldar K., Lagoudas D. C., Basaran, B., and Karaman, I., "Constitutive Modeling of Magneto-Thermo-Mechanical Response of Field Induced Phase Transformation in NiMnCoIn Magnetic Shape Memory Alloy," Proceedings of ASME, International Mechanical Engineering Congress and Exposition 2010, Accepted, September 28-Octobar 01, 2010, Philadelphia, PA, 2010.
2. Haldar K., Lagoudas D. C., Basaran, B., and Karaman, I., "Constitutive Modeling of Magneto-Mechanical Coupling Response of Magnetic Field Induced Phase Transformations in NiMnCoIn Magnetic Shape Memory Alloys," Proc. Of SPIE 2010, Vol.7644, March 07-11, 2010, San Diego, CA, 2010.
3. Chatzigeorgiou G., Haldar K., and Lagoudas D. C., "Stability of Magnetomechanical Problem in Magnetic Shape Memory Alloys," Proc. Of SPIE 2010, Vol.7644, March 07-11, 2010, San Diego, CA, 2010.
4. Lagoudas D. C., Haldar K., Basaran, B., and Karaman, I., "Constitutive Modeling of Magnetic Field Induced Phase Transformation in NiMnCoIn Shape Memory Alloys," Proceedings of ASME, International Mechanical Engineering Congress and Exposition 2009, Paper SMASIS09-1469, September 21-23, 2009, Oxnard, CA, 2009.
5. Lagoudas D. C., Kiefer B., and Haldar K., "Magneto-mechanical Finite Element Analysis of Magnetic Shape Memory Alloys with Body Force and Body Couple," Proceedings of ASME, International Mechanical Engineering Congress and Exposition 2008, Paper SMASIS08-533.
6. Dadda, J., Maier, H.J., and Karaman, I., "Pseudoelasticity of Co49Ni21Ga30 High-Temperature Shape Memory Alloy Single Crystals under Compression," SMST-2007: Proceedings of the International Conference on Shape Memory and Superelastic Technologies, December 2-5, 2007, Tsukuba, Japan, Edited by S. Miyazaki, ASM International, Materials Park, OH 44073, p. 659, 2008.
7. Lagoudas, D.C., Kiefer, B., and Broederdorff, A.J., "Accurate Interpretation of Magnetic Shape Memory Alloy Experiments Utilizing Coupled Magnetostatic Analysis", ASME International Mechanical Engineering Congress and Exposition 2006, November 5-10, 2006, Chicago, IL, 2006.
8. Lagoudas, D., Kiefer, B. and Broederdorff, A., "Constitutive Modeling of Magnetic Shape Memory Alloys with Magneto-Mechanical Coupling," Comp-07 (International Symposium on Advanced Composite Technology), May 16-18, 2007, Corfu, Greece, 2007.

Number of Peer-Reviewed Conference Proceeding publications (other than abstracts):

8

(d) Manuscripts

1. Karaca H.E., Karaman I., Basaran B., Chumlyakov Y.I., Maier H.J., "Compressive Response of NiFeGa Magnetic Shape Memory Alloys," submitted to Acta Materialia, 2010.
2. Haldar K., Chatzigeorgiou G., and Lagoudas D. C., "Stability Analysis of Magnetostatic Boundary Value Problems for Magnetic SMAs," Journal of Intelligent Material Systems and Structures, submitted, 2010.

Number of Manuscripts: 2.00

Patents Submitted

Patents Awarded

Awards

Ibrahim Karaman

2008 Gary Anderson Early Achievement Award, Joint Award between The American Society of Mechanical Engineers (ASME) Adaptive Structures and Material System Technical Committee and the American Institute of Aeronautics and Astronautics (AIAA) Adaptive Structures Technical Committee.

The award is given for notable contribution(s) to the field of Adaptive Structures and Material Systems. The prize is awarded to a young researcher in his or her ascendancy whose work has already had an impact in the field.

Ibrahim Karaman

2007 Honorable Mention for the 2007 Early Career Faculty Fellow Award, The Minerals, Metals & Materials Society (TMS).

Early Career Faculty Fellow Award is a world-wide award from TMS. This award recognizes an assistant professor for his or her accomplishments that have advanced the academic institution where employed, and for abilities to broaden the technological profile of TMS.

Graduate Students

<u>NAME</u>	<u>PERCENT SUPPORTED</u>
Bjoern Kiefer	1.00
Haluk Ersin Karaca	1.00
Burak Basaran	1.00
Krishnendu Haldar	1.00
Ruixian Zhu	0.00
Cengiz Yegin	0.00
Sadegh Badakhshan Raz	1.00
Andrew L. Brewer	1.00
FTE Equivalent:	6.00
Total Number:	8

Names of Post Doctorates

<u>NAME</u>	<u>PERCENT SUPPORTED</u>
FTE Equivalent:	
Total Number:	

Names of Faculty Supported

<u>NAME</u>	<u>PERCENT SUPPORTED</u>	National Academy Member
Ibrahim Karaman	0.08	No
Dimitris C. Lagoudas	0.08	No
FTE Equivalent:	0.16	
Total Number:	2	

Names of Under Graduate students supported

<u>NAME</u>	<u>PERCENT SUPPORTED</u>
Alicia Broederdorf	1.00
James A. Monroe	1.00
FTE Equivalent:	2.00
Total Number:	2

Student Metrics

This section only applies to graduating undergraduates supported by this agreement in this reporting period

The number of undergraduates funded by this agreement who graduated during this period: 2.00
The number of undergraduates funded by this agreement who graduated during this period with a degree in science, mathematics, engineering, or technology fields:..... 2.00
The number of undergraduates funded by your agreement who graduated during this period and will continue to pursue a graduate or Ph.D. degree in science, mathematics, engineering, or technology fields:..... 1.00
Number of graduating undergraduates who achieved a 3.5 GPA to 4.0 (4.0 max scale):..... 1.00
Number of graduating undergraduates funded by a DoD funded Center of Excellence grant for Education, Research and Engineering:..... 0.00
The number of undergraduates funded by your agreement who graduated during this period and intend to work for the Department of Defense 1.00
The number of undergraduates funded by your agreement who graduated during this period and will receive scholarships or fellowships for further studies in science, mathematics, engineering or technology fields: 1.00

Names of Personnel receiving masters degrees

<u>NAME</u>
Ruixian Zhu
Andrew L. Brewer
Total Number:
2

<u>NAME</u>
Bjoern Kiefer
Haluk Ersin Karaca
Burak Basaran
Total Number:
3

Names of personnel receiving PHDs

<u>NAME</u>
Robert Barber
FTE Equivalent:
Total Number:
1

Names of other research staff

<u>NAME</u>
Robert Barber
FTE Equivalent:
Total Number:
1

Sub Contractors (DD882)

Inventions (DD882)

Scientific Progress

Technology Transfer

**Texas A&M University/Texas Engineering Experiment Station
Final Progress Report to ARO
on the W911NF-06-1-0319 Contract**

“Magnetic Field-Induced Phase Transformation in Magnetic Shape Memory Alloys with High Actuation Stress and Work Output”

For the Period of July 19, 2006 – August 31, 2009

By

Ibrahim Karaman and Dimitris C. Lagoudas

3 May 2010

SUMMARY

This is the final progress report of activities at Texas Engineering Experiment Station (TEES)/Texas A&M University (TAMU) on work related to the ARO Project titled, “Magnetic Field-Induced Phase Transformation in Magnetic Shape Memory Alloys with High Actuation Stress and Work Output.” The effective beginning date of Contract No. W911NF-06-1-0319 (ARO Proposal No. 50718-MS) was July 19, 2006.

ABSTRACT

The main goal of the project centers on the idea of identifying, fabricating, characterizing and modeling new magnetic shape memory alloys (MSMAs) and compositions to utilize field-induced phase transformation (FIPT) with the objective of obtaining large actuation stresses, large reversible actuation strains, work outputs, and operating temperature ranges. The novelty of the project arises from the utilization of a new magneto-mechanical mechanism in achieving high work output actuator materials (with the possibility of superior sensing and passive power generation capabilities) from the new MSMAs. The major accomplishments of the project include: 1) the design of a NiMnCoIn composition that resulted in reversible FIPT under magnetic field magnitudes much less than what has been reported in iron based alloys; 2) growth of large single crystals from this composition, 3) the demonstration of magnetostress levels larger than 20 MPa/Tesla in the designed composition utilizing FIPT whereas all previously reported magnetostress levels have been always less than 10MPa/Tesla regardless of the alloy system, composition, and magneto-microstructural mechanism; 4) the investigation of complex magneto-mechanical loading paths; and 5) the analysis of nonlinear magnetostatic boundary value problems for MSMAs using finite element method and taking into account FIPT.

1. Statement of the problem studied

Magnetic shape memory alloys (MSMAs) have attracted an increasing interest in the past 10 years due to their ability to combine the large strain output of conventional SMAs with the high frequency response of magnetostrictive materials [1-10]. However, their utility is partially limited because of low actuation stress levels achieved up to date [6-9]. The only mechanism that was utilized for the

field-induced shape change in these alloys has been the field-induced martensite reorientation (detwinning) which results in low actuation stresses [6,10]. Our recent works [10-12] on a selected NiMnGa MSMA suggested that it is possible to increase this stress level at least one order of magnitude by taking advantage of field-induced martensitic phase transformation under constant stress and low magnetic field strengths.

Thus, the goal of this project was to build on this previous work and current understanding of field-induced phase transformation in the NiMnGa system and identify, fabricate, characterize and model selected compositions of NiFeGa, CoNi(Al,Ga) and NiMn(In,Sn) alloys that allow for magnetic field-induced phase transformation, accompanied by large reversible actuation strains and work outputs. The right choice of combined bias stress and magnetic field led to an order of magnitude increase in the actuation stresses during the reversible field-induced phase transformation. The project goals were achieved by:

1. Formulating a framework based on microstructural, mechanical and magnetic requirements for field-induced phase transformation and identifying the parameter space in which field-induced phase transformation can be observed;
2. Focusing on specific compositions of NiFeGa and CoNi(Al,Ga) single crystals and determining whether these single crystals satisfy the set performance goals;
3. Developing thermodynamically based compositional and magneto-microstructural parameter selection and design principles and implementing them to fabricate single crystals from a “designed” composition in a new NiMn(In,Sn) alloy system with the addition of Co alloying;
4. Building a microstructure motivated and thermodynamics based material constitutive model for field-induced phase transformation to predict the evolution of field-induced strain and magnetization under complex magneto-mechanical loading conditions
5. Incorporating the constitutive model into a magneto-thermo-mechanical Finite Element (FEM) code to solve actual boundary-value problems for practical actuator design applications.

The compositional and microstructural design strategies focus on optimizing the three energy terms important for the thermoelastic martensitic transformation under magnetic field: Zeeman energy, magnetocrystalline anisotropy energy (MAE) and dissipated work. Temperature, stress, heat treatment (order and precipitation) and composition dependence of these energy terms in the aforementioned compositions are being studied carefully to satisfy and validate the design principles.

Our recent work on solving boundary value problems considering field-induced martensite reorientation in Ni_2MnGa showed that the specimen size and shape significantly affect the observed materials behavior. Indeed, measured materials properties were found not to be the exact indication of the materials real response. Therefore, analysis of the experimental results is necessary using the constitutive model development and solving the boundary value problems for the extraction of the true material response. This is one of the areas where the collaborative effort between the experimental work and model development was found to be beneficial for this project.

The research tasks in the present project with respect to materials development, fabrication, and materials characterization can be categorized into four progressive steps in addition to the modeling task:

- 1) Magneto-thermomechanical (MTM) and microstructural characterization of existing single crystals with the selected compositions from NiMnGa, CoNi(Al,Ga), and NiFeGa alloy systems

as a function of temperature, stress and magnetic field level, load and field directions, crystal orientation, heat treatment, etc.. These investigations were directed towards understanding how these single crystal compositions and selected heat treatments affect the aforementioned energy terms and determining whether the single crystals satisfy our targeted design parameters and property goals.

- 2) Using the same design principles that we have used to select existing single crystals or modifying them, if necessary, selection of a composition in the Ni-(33-38at.%)Mn-(12-17at.%) (In,Sn) alloy system, with ferromagnetic-paramagnetic structural phase transformation and small dissipation, via fabricating small arc-melted buttons and measuring their properties to find the one best satisfying the design criteria. Adding Co to increase the saturation magnetization of one phase and increasing the Zeeman Energy difference between the transforming phases. Growing of single crystals from this composition which would have a large Zeeman energy difference between transforming phases.
- 3) Magneto-thermo-mechanical and microstructural characterization of the single crystals of new alloys, especially investigating the mechanical properties such as pseudoelastic stress hysteresis as a function of temperature and magnetic field.
- 4) The domain structure characterization of selected magnetic shape memory alloys under stress and magnetic field application in order to develop more accurate demagnetization energy term for the Gibbs Free Energy formulation.
- 5) Constitutive model development and implementation for the MSMA behavior considering field-induced phase transformation and loading history dependence. Energy calculations in quest for deriving Claussius-Clapeyron Relationships under the application of stress, magnetic field, and temperature. Theoretical framework was developed to predict the effect of simultaneous application of magnetic field and stress on the phase transformation temperatures through this relationship. The theoretical framework starts from the Gibbs Free Energy formulation and it includes the demagnetization energy term which is important for magnetic shape memory alloys. The inclusion of this term required a fundamental understanding of the domain structure in these alloys which were tackled with in Task 4 above. Once the demagnetization energy was introduced in the Gibbs Free Energy formulation, it was possible to derive and validate the Claussius-Clapeyron relationship in the presence of simultaneous stress and magnetic field. Such relationship revealed the additional materials parameters important for the field-induced phase transformation and resulted in more refined material design guidelines.

2. Summary of Important Results

The major accomplishments for the project include:

- 1) A new magnetic shape memory alloy that transforms from a ferromagnetic austenite to an antiferromagnetic martensite is identified. It has been known that some of the near Heusler magnetic shape memory alloys (MSMAs) can experience a magnetic transition at the same time with a structural phase transformation. Therefore, they are also called as meta-magnetic SMAs. This gives the opportunity to utilize the Zeeman energy for triggering phase transformation. For this purpose, we have focused on NiMnIn alloys and identified a composition that transforms from a ferromagnetic austenite into an antiferromagnetic martensite phase. Then, we have added Co to increase the saturation magnetization, thus the Zeeman energy, while keeping martensite start temperature at a reasonable level, reaching to the composition $\text{Ni}_{45.7}\text{Mn}_{35.6}\text{Co}_{4.8}\text{In}_{13.8}$. Subsequently, ***we have grown large single crystals of $\text{Ni}_{45.7}\text{Mn}_{35.6}\text{Co}_{4.8}\text{In}_{13.8}$ for the first time in the world.***

- 2) **Reversible magnetic field induced phase transformation** in $\text{Ni}_{45.7}\text{Mn}_{35.6}\text{Co}_{4.8}\text{In}_{13.8}$ single crystals is achieved ***without the need for a stress bias***. This is a unique finding considering that in NiMnGa alloys field-induced phase transformation can only be achieved with an external stress assistance.
- 3) We have conducted extensive magneto-thermo-mechanical characterization of few meta-magnetic SMAs including NiMnCoIn, NiMnCoSn and NiMnCoAl SMAs in single crystalline, polycrystalline, and porous forms. We have investigated: 1) conventional shape memory properties of NiMnCoIn single crystals, 2) achievable actuation stress and work output levels in these single crystals, 3) in-situ evolution of the crystal structures of the magnetically transforming phases in the NiMnCoIn alloy under magnetic field and during in-situ cooling and heating, 4) thermodynamic formulation during martensitic phase transformation to better understand the energetic of magnetic-field induced shape memory effect, 5) the effects of orientation and temperature on the meta-magnetic shape memory effect, 6) the effects of simultaneous applications of external stress and magnetic field, while varying temperature, on the magnetization evolution and martensitic phase transformation, 7) the effects of aluminum replacement of indium in NiMnCoIn alloys on conventional and magnetic shape memory properties, and 8) shape memory response in porous meta-magnetic NiMnCoSn SMAs.
- 4) The magnetostress levels, which are a direct indication of actuation stress levels of MSMAs, as high as 23MPa/Tesla were experimentally achieved in $\text{Ni}_{45}\text{Mn}_{36.5}\text{Co}_5\text{In}_{13.5}$ oriented along the [100] direction. Comparison of magnetostress levels achieved in the present work with the literature data and our previous work demonstrates that no matter what the mechanism for the field-induced shape change is (field-induced martensite reorientation or field-induced martensitic phase transformation) in NiMnGa alloys, the magnetostress level is less than 10MPa/Tesla and levels off with increasing magnetic field. However, the NiMnCoIn alloy exhibits 23MPa/Tesla magnetostress which linearly increases with the applied field. Such magnetostress levels were achieved at transformation strain levels as high as 6.3%. ***This three to four fold increase in the magnetostress levels in the present NiMnCoIn composition is one of the main achievements in this project.*** This indicates that NiMnCoIn alloys are promising meta-magnetic SMAs with high actuation stress output. It is important to note that there is no limit for maximum magnetostress in NiMnCoIn alloys and it increases with the field. In addition, ***this mechanism does not depend on the orientation of the single crystals; all orientations can experience field-induced phase transformation*** because of the source of the magnetic energy, ***ceasing the need for single crystals or textured polycrystals.*** ***Additional experimental results and calculations showed that the magnetostress level can easily be increased to more than 100 MPa levels by sacrificing from the transformation strain.*** It was also demonstrated that the magnetostress levels are temperature dependent due to the temperature dependence of the Zeeman energy. Zeeman energy is the responsible magnetic energy for the magnetic actuation in meta-magnetic SMAs.
- 5) The shape memory characteristics of $\text{Ni}_{45}\text{Mn}_{36.5}\text{Co}_5\text{In}_{13.5}$ single crystals were investigated under compression along the [100] orientation. The effects of temperature and bias stress on the pseudoelastic response and the shape memory effect were explored. Critical stress for the onset of phase transformation vs. temperature phase diagrams were determined which is important for identifying the stress-temperature space at which stress, temperature, and magnetic field-induced shape changes can take place in these materials for potential actuation and sensing applications. The crystals demonstrated large stress and temperature hysteresis with a fully reversible transformation strain of 5.4%, the ramifications of which on the field requirement for FIPT were revealed.

- 6) In the new NiMnCoIn alloy, large magnetic and stress hysteresis and brittleness were identified as two potential road blockers. We have determined the reason of these two issues as large volume fraction of second phase particles which are not transformable. The elimination of these second phases was proven to be difficult, however, we have found out a heat treatment that now we can dissolve these second phases.
- 7) Lattice structures and parameters of parent and martensite phases of the NiMnCoIn alloy were revealed using synchrotron-based high-energy x-ray diffraction technique at Argonne National Laboratory. A new 6-layered monoclinic martensitic phase is found for the first time in a NiMnIn based magnetic SMA. *In-situ* temperature and magnetic field-induced phase transformations were demonstrated using the synchrotron-based XRD technique to study the microstructural details of phase transformations. This observation proved that exceptional magnetization response of this alloy is a consequence of structural phase transformation instead of a non-structural magnetic transition solely.
- 8) Using the Energy Minimization Theory, we have predicted the transformation shear, direction, and transformation strain in the NiMnCoIn alloy as a function of single crystal orientations using the lattice parameters and phase structures determined with the high energy XRD measurements. It was found that the maximum transformation strain in this material between L₂₁ austenite and 6-layered monoclinic martensite is 6.61% along the [001] orientation which is very close to the experimentally observed value of 6.3%.
- 9) We have designed a miniature mechanical loading frame with a 8 mm diameter that can fit in any commercially available superconducting magnetometer. This test frame allows us to monitor magnetic field-induced structural changes in meta-magnetic SMAs via field-induced magnetization variations under constant stress levels as a function of temperature. We have used this loading frame in an 18 Tesla magnetometer at the High Field Laboratory of The Institute of Materials Research in Japan, to study the effect of external stress on the field-induced kinetic arrest of martensitic phase transformation. This was *the first study* in meta-magnetic SMAs investigating the effects of simultaneous application of stress and field on field-induced phase transformation. It was revealed that while external stress and magnetic field oppose each other in promoting martensitic transformation and stress increases the critical field level required for the onset of martensite to austenite phase transformation.
- 10) In collaboration with our Japanese colleagues, we have studied the effect of aluminum in NiMnCoIn alloys, replacing indium, on the conventional shape memory properties of these meta-magnetic SMAs. The reason for such an effort was to replace expensive indium with inexpensive aluminum. It was revealed that NiMnCoAl is considerably tougher than NiMnCoIn alloys. As an example, the Ni₄₀Mn₃₃Co₁₀Al₁₇ polycrystalline samples can demonstrate perfect pseudoelasticity in a wide temperature range even at stress level above 400 MPa, NiMnCoIn polycrystals, on the other hand, usually fails around 50 to 100 MPa during stress-induced phase transformation or during isobaric thermal cycling experiments.
- 11) One of the major issues in meta-magnetic SMAs and the road blocker for using polycrystalline materials instead of using expensive single crystals is their brittleness due to intergranular fracture. To circumvent this problem, we looked into the possibility of fabricating these materials in polycrystalline form using powder metallurgy approaches in collaboration with our Japanese colleagues. We have demonstrated that *NiMnCoSn meta-magnetic SMAs can be fabricated in powder form*, mostly in single crystalline particle forms, and they *can be sintered into near fully dense and porous meta-magnetic SMA polycrystals*. The preliminary results at TAMU on both NiMnCoAl and NiMnCoSn polycrystals showed that: 1) NiMnCoAl alloys are much tougher and more ductile than NiMnCoIn meta-magnetic SMAs, 2) powder fabrication via high pressure gas atomization process does not deteriorate meta-magnetic SME in NiMnCoSn alloys, 3) the pressureless

sintering technique is capable of controlling the porosity size and achieving near full density compacts, and 4) the consolidation approach results in bulk samples that demonstrates perfect SME under stress levels much higher than those for ingot metallurgy samples.

- 12) To better understand the magneto-microstructural coupling in magnetic SMAs, an in-situ mechanical load frame has been developed for a commercially available atomic force microscope. This frame allows examining changes in topography and magnetic domain configuration under a given constant load or strain. *The in-situ evolution of the microstructure and the associated magnetic domain morphology was investigated as a function of applied strain level during the stress-induced martensite (SIM) transformation in Co₄₉Ni₂₁Ga₃₀ and during the stress-induced martensite detwinning in Ni₅₀Mn₃₀Ga₂₀ single crystals.* The magnetic force microscopy (MFM) measurements under different strain levels confirm the one-to-one correspondence, i.e. the magneto-microstructural coupling between the martensite twins and the magnetic domains in the NiMnGa alloy. Additionally, the growth of the twin variant with favorable orientation to the compression axis during martensite detwinning was observed. It was shown that this load frame can be used for the investigation of the relationship between the microstructure and the magnetic domain structure in magnetic SMAs by MFM. In addition, this is *the first study*, to the best of the PIs' knowledge, on magnetic SMAs monitoring magneto-microstructural evolution during SIM and attempting to reveal the effect of thermo-mechanical training on the magneto-microstructural coupling in a representative CoNiGa alloy. The results demonstrated that thermomechanical training procedures can change the magneto-microstructure of the crystals from one-to-one corresponding magnetic domains with martensite nano twins to the one with the large magnetic domains on the order of several micrometers without the one-to-one correspondence.
- 13) Complete stress-temperature phase diagram of Ni_{51.1}Mn_{24.0}Ga_{24.9} single crystals along the [100] orientation is constructed to determine the stress-temperature regions where different magnetic field induced shape changes can occur either by field-induced martensite reorientation or by field-induced phase transformation. Considering the multi-stage martensitic phase transformations, this task is critical for identifying the application space for these materials as actuators.
- 14) The shape memory and pseudoelastic response of Ni₅₄Fe₁₉Ga₂₇ single crystals along the [100], [123] and [110] orientations were investigated. We characterized their compressive and tensile conventional shape memory response to understand the microstructure and hysteretic behavior to identify the conditions for low thermal and stress hysteresis, which is a critical condition for meta-magnetic shape memory effect. It was shown that transformation strain, and temperature and stress hysteresis are orientation, temperature, and stress level dependent. We focused on identifying the range of temperature and stresses for low transformation hysteresis and on understanding the mechanisms responsible for temperature and orientation dependence of transformation strain and transformation hysteresis. *It was demonstrated that there are two main parameters dictating the temperature and stress dependence of transformation hysteresis which are the change in lattice constants with temperature and stress, and uneven change in Young's modulus of transforming phases with temperature.*
- 15) Effect of heat treatment on the tensile pseudoelastic response of the CoNi₃₃Al₂₇ single crystals along the [100] orientation as a function of temperature is determined. *High temperature pseudoelasticity at temperatures as high as 350°C is detected for the first time under tension in a shape memory alloy. These cobalt base SMAs demonstrate more than 5% fully recoverable pseudoelastic strain at stress levels as high as 800 MPa at 350°C. The*

highest temperature at which pseudoelasticity was observed in SMAs previously is only 200°C.

- 16) The CoNi₃₃Al₂₉ was subjected to a detailed heat treatment study to map out the precipitation behavior. The aim was to find out which heat treatment leads to ductile γ phase precipitation, the size, distribution, volume fraction and morphology of the second phase and how these second phase particles affect the shape memory response of these MSMA. The formation of ductile second phase along grain boundaries is the key to increase the ductility of these alloys.

Accomplishments in Modeling of Magnetic SMAs

- 16) **Magnetostatic Boundary Value Problem.** A major complication in measuring material properties of ferromagnetic materials is the influence of the demagnetization effect. The demagnetization effect and the resulting shape-dependent difference between the applied field and the internal field make measurements of MSMA properties difficult to interpret. Since for non-ellipsoidal specimen the internal magnetic field and thus induced magnetization is nonuniform, the approximation of uniform magnetization is usually adopted. In this work, nonuniform magnetization inside the MSMA specimen is taken into account to find out the demagnetization effect by explicitly solving the magnetostatic problem for relevant geometries. This work also describes a methodology by which experimental data can be interpreted more accurately. An iterative solution technique is described to obtain the relation between the applied magnetic field and the magnetic field inside the specimen.
- 17) **Maxwell Stress, Magnetic Body Force and Magnetic Body Couple.** The Maxwell (magnetic) stress, magnetic body force and magnetic body couple are evaluated using finite element analysis over the domain of the magnetic shape memory alloy (MSMA) specimen. We found that the axial component of the Maxwell stress, which acts along the direction of the applied traction, is compressive. The magnitude of this particular magneto stress component, at the end of the reorientation process, is nearly equal to 21% of the applied traction. This suggests that the axial component of the Maxwell stress favors the stress assisted variant. The magnitude of magnetic body force and magnetic body couple are calculated. It is observed that, due to the presence of the magnetic field gradient inside the material, the magnetic body force is not negligible.
- 18) **Magneto-Mechanical Coupled Finite Element Analysis.** We already found that the intensity of Maxwell stress is significant compared to the applied traction. As a next step, we analyze the behavior of the Cauchy stress in a magneto-mechanical coupled problem. The objective of the magneto-mechanical coupled finite element analysis is to investigate the variation of Cauchy stress due to field induced variant reorientation. In the model, we assume constant and uniform Cauchy stress inside the material. We also assume that the magnetization constitutive equation and the magnetic conservation equations do not depend on stress. Under these assumptions, we found that for the coupled problem Cauchy stress is associated with the magnetic body force, magnetic body couple and reorientation strain and has strong influence on the magnetic field and magnetization.
- 19) **Magnetostatic Stability Analysis.** The interesting feature of the studied magnetostatic boundary value problem is the appearance of banded zones in the spatial distribution of the magnetic field variables when the magnetization constitutive response becomes highly nonlinear. In the performed finite element analysis, the appearance of band like regions is observed and are explained by the loss of ellipticity of the magnetostatic system of equations. The analytic approach of stability analysis shows that the magnetostatic problem becomes unstable during the martensitic variant reorientation mechanism. A parametric stability

analysis reveals the conditions under which loss of ellipticity occurs and quantifies the influence of the nondimensional material parameters in the stability of the material.

- 20) **Magnetic Field Induced Phase Transformation.** The magnetic field associated with field induced phase transformation is nearly nine times higher than the magnetic field required for variant reorientation mechanism. This implies that the magnetic stress is very high compared to the variant reorientation mechanism. A non-linear continuum mechanics based finite deformation formulation is developed to consider the strong coupling of high magnetic field with the mechanical media.
- 21) **Finite Deformation and Non-Linear Kinematics.** The finite deformation analysis is an essential tool to know the decomposition of the total stress into a mechanical and a magnetic part. The contribution of the mechanical and the magnetic part to the total stress is very difficult to find out experimentally, because in most of the cases we measure the total stress. By following a systematic non-linear kinematic approach, we find out the relation between mechanical part and the magnetic part with the total stress. This decomposition is crucial due to the fact that the mechanical constitutive relation is associated only with the mechanical part of the total stress.
- 22) **Constitutive Modeling.** Motivated by experiments, a constitutive model is proposed to account for temperature, magnetic field and stress induced phase transformation from martensitic to austenitic phase. The constitutive equations are derived in a consistent thermodynamic way. The model is calibrated from experimental data. The strain versus temperature constitutive response is simulated and the constitutive responses of magnetization versus magnetic field is then predicted and compared with experimental results. Magnetization versus temperature response is also presented. The proposed model has the ability to predict the nonlinear, hysteretic strain and magnetization response caused by martensitic phase transformation due to temperature and magnetic field effect. The model is able to capture the magneto-thermo-mechanical coupling effect and simulate quite accurately the experimental results.

Technical Accomplishments

PART I. Experimental Work

1.1. NiMnCoIn META-MAGNETIC SHAPE MEMORY ALLOY

1.1.1 Motivation

The potential for high actuation stress levels in meta-magnetic SMAs is exciting; however, the necessity of relatively high magnetic field magnitudes for FIPT restricts their immediate utility in applications. Thus, it is of utmost importance to characterize the magnetic shape memory properties of NiMnCoIn alloys in terms of magnetostress levels, magneto-mechanical control of phase transformation temperatures, MFIS levels, and the critical stress levels for phase transformations as a function of temperature, field, and crystallographic orientation. These are required to eventually determine the full potential of NiMnCoIn alloys for actuator applications.

The main mechanisms that result in the field-induced external strain in MSMAs are: i) martensite variant reorientation as a result of the magnetic field-induced twin boundary motion [6], and ii) the field-induced phase transformation [10]. In the former mechanism, if the magnetocrystalline anisotropy energy (MAE) of a magnetic field-favored martensite variant is larger than the energy required for twin boundary motion, that variant will grow in expense of others, resulting in a field-induced macroscopic shape change. In NiMnGa single crystals, this mechanism results in high recoverable magnetic field-induced strains (MFIS) of up to 10% but with actuation stress levels of less than 5 MPa [6].

Fig. 1.a demonstrates a schematic with the definition of maximum MAE (K_u) in Ni_2MnGa , which is the area between the magnetization response of ferromagnetic single martensite variants along the easy and hard axes. It is important to note that the MAE is orientation dependent and limited with a saturation magnetic field above which MAE does not increase with the field [1, 6]. Similar to the MAE, the MFIS is also orientation dependent [6]. Since MAE provides only a few MPa of stress for twin boundary motion and both MAE and MFIS are orientation dependent, the field-induced variant reorientation mechanism is currently limited to single crystals. It is quite difficult, if not impossible, to experience such mechanism in polycrystals. Thus, the high cost of single crystals and low actuation stress levels restrict the potential applications of MSMAs utilizing this mechanism.

The second mechanism for MFIS is magnetic field-induced martensitic phase transformation. This mechanism is analogous to stress or temperature-induced martensitic transformations in conventional SMAs. In addition to the MAE, the Zeeman energy (ZE) play an important role for magnetic field-induced phase transformations (FIPTs) [10-11]. ZE stems from the difference in the saturation magnetizations of transforming phases and increases continuously with the field [13] as shown in Fig. 1.b. Unlike MAE, ZE does not strongly depend on crystal orientation, which provides an opportunity to utilize polycrystals for actuator applications [10, 13]. It can be maximized by increasing the difference between the saturation magnetizations, such as when a ferromagnetic phase transforms to a paramagnetic or antiferromagnetic phase, or vice versa.

Recently, we have shown that stress-assisted FIPT is possible in some NiMnGa alloys under certain thermal conditions [5, 10-11]. By utilizing only MAE, almost an order of magnitude increase in actuation stress (~20 MPa) was achieved with reversible MFIS of 0.5 % under low magnetic field magnitudes [10-11]. Moreover, one-way MFIS of up to 3.1% were attained under different stress magnitudes as high as 110 MPa in Ni_2MnGa single crystals [10-11]. It was revealed that if the superelastic stress hysteresis is lower than the magnetostress, which is defined as the amount of change in the critical stress for phase transformation under a given field, then

reversible stress-assisted FIPT is possible. Similarly, if the transformation thermal hysteresis is lower than the change in transformation temperatures under the field, reversible FIPT can be observed.

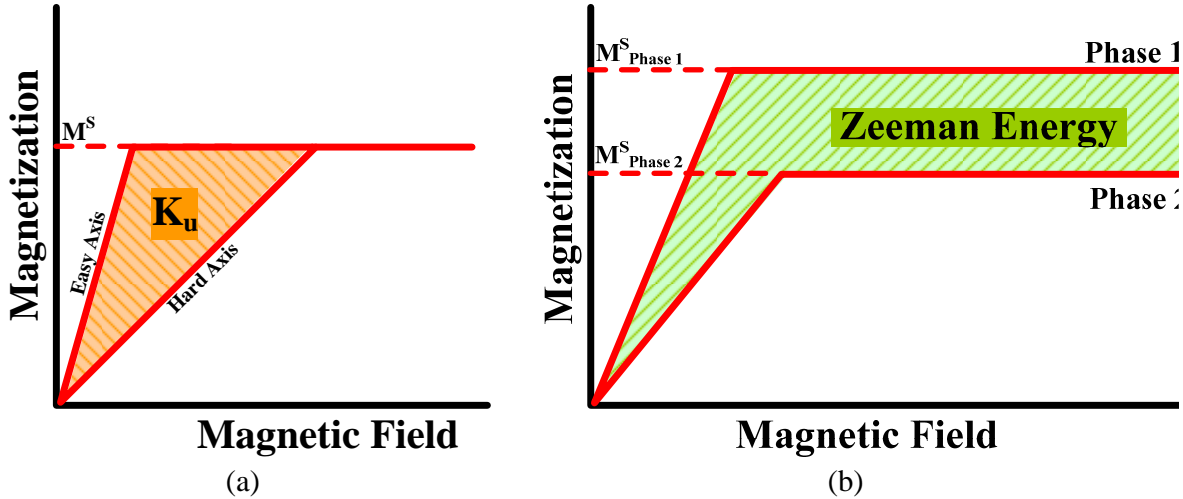


Figure 1. Schematics showing (a) the maximum magnetocrystalline anisotropy energy (K_u) for ferromagnetic martensite in Ni_2MnGa responsible for the field-induced martensite variant reorientation, (b) Zeeman energy difference between two phases martensitically transforming into each other, which can be responsible for field-induced phase transformation. M^S : Saturation magnetization.

FIPT is also observed in other families of MSAs, called meta-magnetic SMAs such as NiMnX alloys ($X=\text{In}, \text{Sn}, \text{Sb}$), where the ferromagnetic austenite transforms to a paramagnetic or antiferromagnetic martensite [14-20]. In these alloys, ZE is the responsible magnetic energy for FIPT since it is higher than the MAE as opposed to the NiMnGa alloys. Moreover, Co addition is usually employed to increase the Curie temperature and saturation magnetization in these alloys, which in turn increases the ZE. Kainuma *et al.* [17] reported that the transformation temperatures of NiMnCoIn alloys decrease with the magnetic field. In these quaternary alloys, magnetoelastic magnetization response, where martensite transforms to austenite above a critical field and then transforms back to martensite upon field unloading, can be obtained at certain temperatures. They have also shown that 4 T field is sufficient to recover 3% of pre-applied strain in martensite at room temperature. This work triggered several recent studies on metamagnetic SMAs [18, 20-30] but these have mainly focused on the magnetocaloric properties and compositional effects on the transformation temperatures [21-22, 26, 28-30]. There was no systematic study on the conventional shape memory properties of metamagnetic SMAs until our recent study on the compressive response of $\text{Ni}_{45}\text{Mn}_{36.5}\text{Co}_5\text{In}_{13.5}$ single crystals along the [100] orientation [25]. **We have reported a fully reversible superelastic response with strain levels more than 6%, and with large stress and temperature hysteresis.** We concluded that the relatively high magnetic field requirement for FIPT in NiMnCoIn alloys partially stems from their large transformation hysteresis and we discuss possible ways to decrease transformation hysteresis.

Kainuma *et al.* [17] predicted that the magnetostress levels in NiMnCoIn alloys should be on the order of tens of MPa, but there has been no systematic experimental study to prove this prediction. Wang *et al.* [31] reported reversible FIPT under 50 MPa with the application of 5 T in $\text{Ni}_{45}\text{Mn}_{36.6}\text{Co}_5\text{In}_{13.4}$ alloys with unknown MFIS values using in-situ high energy XRD measurements. The actuation stress level achieved in the study of Wang *et al.* [31] is an order of

magnitude higher than that in NiMnGa alloys obtained via field-induced martensite reorientation [6].

1.1.2. Preparation of NiMnCoIn Specimens

An ingot of $\text{Ni}_{45}\text{Mn}_{36.5}\text{Co}_5\text{In}_{13.5}$ (at %) was prepared using vacuum induction melting. Single crystals were grown using the Bridgman technique in He atmosphere. The single crystals were cut into rectangular prisms with dimensions of 4 mm x 4 mm x 8 mm using wire electro discharge machining. In the austenite phase ($\text{L}2_1$ ordered structure), the normal vectors of the prism faces were along the [100], [011], and [01 $\bar{1}$] directions. Compressive stress and magnetic field were applied along the [100] and [011] directions, respectively. Throughout this report, these austenite orientations will be used to describe the directions of the single crystal samples even if the sample might be in martensitic phase, as [100] indicating the long axis of the rectangular prisms. After homogenization at 900 °C for 24 hours in vacuum and water quenching, second-phase particles inherited from the as-grown crystals are detected in the microstructure [25]. Wavelength-dispersive spectroscopy was used to determine the composition of the matrix and the second phase as $\text{Ni}_{45.7}\text{Mn}_{35.6}\text{Co}_{4.8}\text{In}_{13.8}$ and $\text{Ni}_{42.0}\text{Mn}_{40.3}\text{Co}_{16.0}\text{In}_{1.6}$, respectively.

1.1.3. Isothermal and Constant Field Magnetization Response of NiMnCoIn

Isothermal stress-strain response of the crystals was determined at various temperatures with and without the presence of different constant magnetic field levels. The latter experiments provided the evolution of magnetostress as a function of the magnetic field level in addition to verifying and extending the stress–temperature phase diagram partially constructed using the first type experiments. The mechanical loading rate in strain control was $5 \times 10^{-4} \text{ s}^{-1}$, while the field loading-unloading rate was 250 Gauss/second in these experiments.

Figure 2 shows the effect of applied magnetic field on the magnetization response of $\text{Ni}_{45}\text{Mn}_{36.5}\text{Co}_5\text{In}_{13.5}$ single crystals as a function of temperature. First, a magnetic field of 0.05 T was applied at 390 K and the sample is cooled down to 100 K and heated back to 390 K. Then, the field was incrementally increased to 3, 5 and 7 T and the thermal cycling was repeated in each case. Under 0.05 T, the austenite to martensite transformation starts at 230 K (M_s : martensite start temperature) and finishes at 205 K (M_f : martensite finish temperature) upon cooling. The reverse transformation starts at 225 K (A_s : austenite start) and finishes at around 250 K (A_f : austenite finish) upon heating. The transformation is reversible with a small thermal hysteresis (~20 K). As the applied magnetic field increases, the transformation temperatures shift to lower temperatures, e.g. M_s decreases from 230 K to 165 K as the field increases from 0.05 to 5T. This is due to the fact that applied magnetic field favors the phase with the higher saturation magnetization (austenite in this case). Additional undercooling is needed to supply the required chemical energy to overcome the magnetic energy opposing phase transformation.

Figure 2.b shows the change in transformation temperatures as a function of magnetic field extracted from the experiments partially shown in Fig. 2.a. The change in A_s is approximately -12.6 K/T. The same value is around +6 K/T for NiMnGa alloys [32] since martensite has slightly higher saturation magnetization than that of austenite in NiMnGa alloys leading to a positive temperature change.

For applied magnetic fields higher than 3 T, the magnetization of austenite is saturated and does not increase with the field. During forward transformation, the magnetization of the single crystal drops from 130 emu/g to 30 emu/g under 3T and to 100 emu/g under 5T upon transformation. Under 7 T, there was no change in magnetization for this particular sample and thus, no transformation down to 100 K.

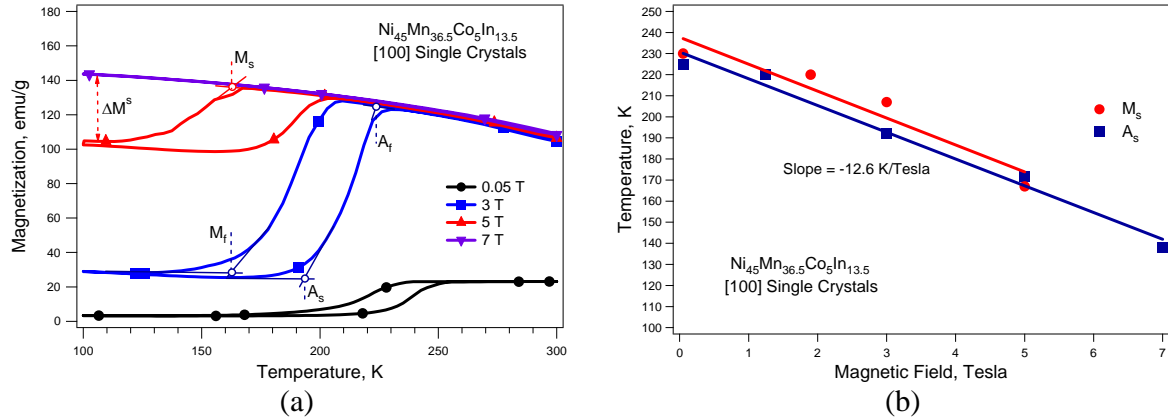


Figure 2. (a) Change in magnetization of $\text{Ni}_{45}\text{Mn}_{36.5}\text{Co}_5\text{In}_{13.5}$ single crystals oriented along the [100] orientation as a function of temperature under different constant applied magnetic fields. (b) Change in transformation temperatures as a function of magnetic field extracted from the experiments partially shown in Fig. 2a.

The increase in magnetization at low temperatures with increasing constant field upon the transformation can be due to either partial transformation of austenite to martensite or an anomalous increase in the magnetization of martensite. Ito *et al.* [33] observed a similar behavior in a $\text{Ni}_{45}\text{Mn}_{36.7}\text{Co}_5\text{In}_{13.3}$ alloy and they attributed this behavior to the former, i.e. to the kinetic arrest of martensitic transformation. They argued that there is an abnormal change in entropy and extremely low mobility of phase interfaces, resulting in lack of complete phase transformation at low temperatures. However the reason for such low mobility under high fields and at low temperatures is not known. Interestingly, a similar work on $\text{Ni}_{50}\text{Mn}_{34}\text{In}_{16}$ polycrystals by Krenke *et al.* [28] did not report a similar increase in low temperature magnetization after transformation under high magnetic fields.

The degree of change in magnetization due to martensitic transformation (i.e. ΔM^s : the difference between the magnetization right below M_f and the magnetization right above M_s as shown in Fig. 2.a) continuously increases with increasing magnetic field in the $\text{Ni}_{50.3}\text{Mn}_{33.8}\text{In}_{15.9}$ alloy polycrystals and then it saturates above 1 T (Figure 3). However, it first increases and then decreases with increasing field in the present single crystals with Co addition due to the partial transformation of austenite to martensite. The comparison in Figure 3 indicates the strong influence of Co addition on the kinetic arrest of martensitic transformation in NiMnIn alloys which requires further investigation.

Figure 4.a shows the magnetization vs. temperature cooling curve under 7 T (the curve between points 1 and 2) with only a small amount of martensitic transformation below 150 K. When the field is reduced down to 0 T at 50 K, the magnetization vs. field curve (the curve between points 2 and 3) in Fig. 4.b demonstrates that the magnetization starts to decrease at a field level considerably above the saturation fields of both austenite and martensite. Thus, this should be a consequence of an austenite to martensite phase transformation upon field removal. When the field is increased to 7 T again at 50 K, the magnetization vs. field curve (between points 3 and 4) shows a typical saturation curve of martensite.

Heating the specimen to room temperature under 7 T (the curve between the points 4 and 6) causes martensite to austenite reverse transformation above 150 K with the austenite magnetization level being exactly the same as during the cooling response under 7 T. Apparently, cooling under 7 T causes the kinetic arrest of the transformation even if the temperature level is much lower than what one would expect for the transformation start temperature under the field, according to Fig. 2. On the other hand, martensite is the stable phase under zero field upon

removal of the field. Reloading up to 7 T is not sufficient to induce the reverse transformation at 50 K. The reverse transformation temperature (A_s) upon heating under 7 T is close to what one would expect from Figure 2.b according to the linear slope shown earlier.

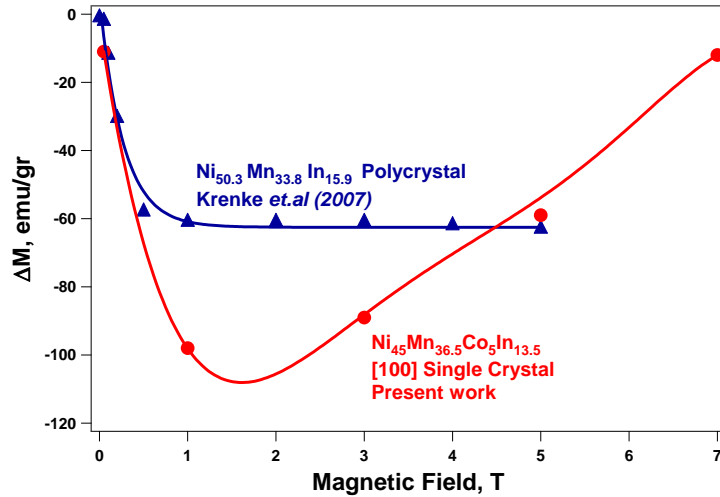


Figure 3. Comparison of the change in magnetization levels between austenite and martensite upon transformation (defined in Fig. 2.a) in Ni_{50.3}Mn_{33.8}In_{15.9} and Ni₄₅Mn_{36.5}Co₅In_{13.5} alloys showing the effect of Co addition on the kinetic arrest of martensitic transformation.

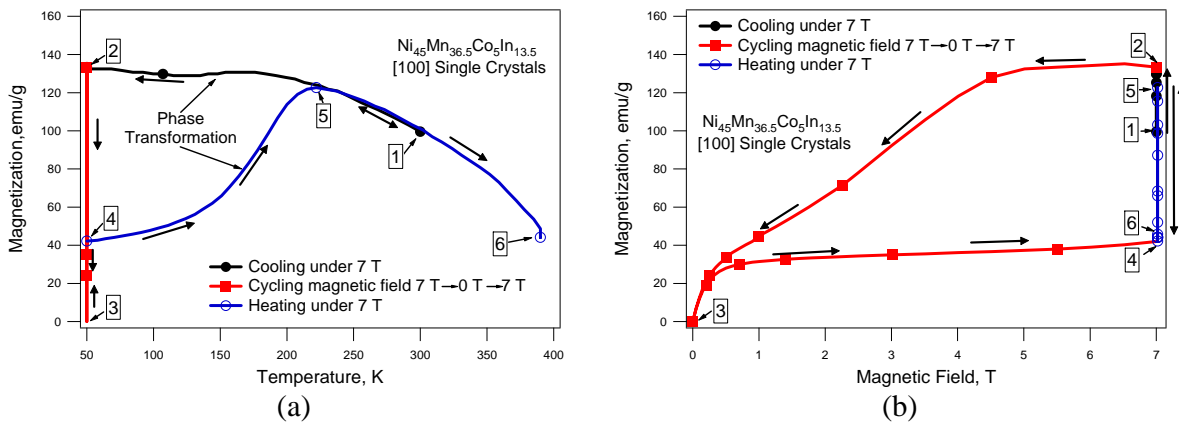


Figure 4. Magnetization vs. temperature (a) and magnetization vs. field (b) responses of Ni₄₅Mn_{36.5}Co₅In_{13.5} single crystals during the cooling under 7 T (path 1 to 2), unloading to 0 T at 50 K (path 2 to 3), loading to 7 T again at 50 K (path 3 to 4), and heating to 390 K under 7 T (path 4 to 6) indicating the kinetic arrest phenomenon for the martensitic transformation.

The shift in transformation temperatures with magnetic field provides a unique opportunity to induce reversible phase transformation at a certain temperature interval. Figure 5 shows the change in magnetization of the [100] single crystal as a function of applied magnetic field at 350, 250, 220 and 140 K. At 350 and 250 K, the single crystal is in the austenitic phase and it shows a typical response of a ferromagnetic material where the magnetization increases quickly and saturates at low fields (<0.5 T). At 220 K, most of the material is in the martensite state with a small amount of coexisting austenite according to Fig. 2. The initial magnetization response up to 1T that seems to saturate at 25 emu/g is due to the magnetization of martensite and residual austenite. Further increase in the applied field results in an abrupt change in magnetization due to phase transformation from martensite to austenite.

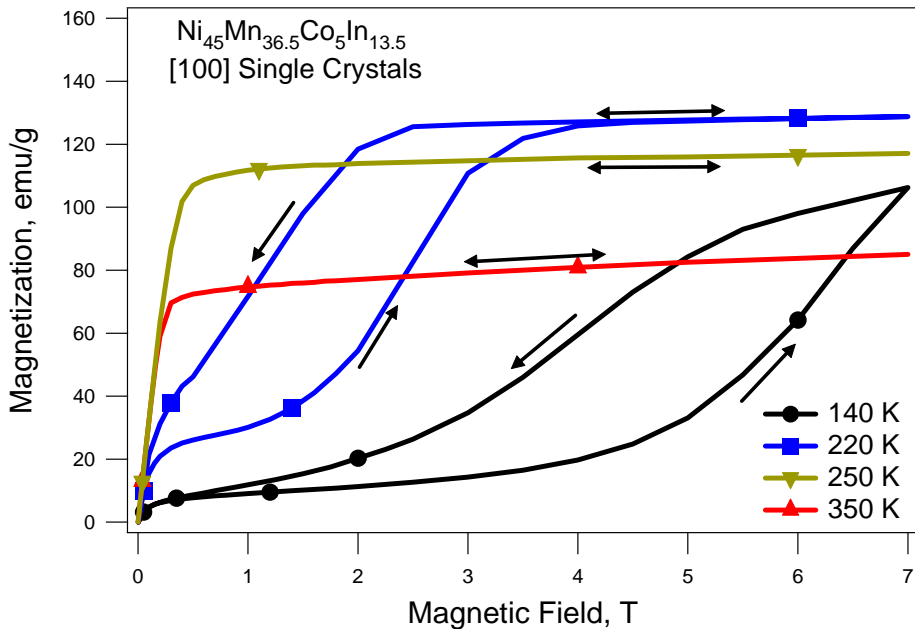


Figure 5. Change in magnetization of $\text{Ni}_{45}\text{Mn}_{36.5}\text{Co}_5\text{In}_{13.5}$ single crystals oriented along the [100] orientation as a function of applied magnetic field at different temperatures demonstrating fully reversible magnetic field-induced phase transformation.

At 4T, the magnetization saturates again where the structure is fully austenite. Removal of the magnetic field results in reverse transformation from austenite to martensite with a hysteresis of about 1.5T. At 140K, the magnetization response is similar to the one at 220K where the initial saturation magnetization is lower since the sample is fully martensitic. The required magnetic field for the reverse phase transformation at 140K is higher than the one at 220K since the sample temperature is much lower than the A_s under zero field and more magnetic energy is needed for the transformation. In this case, the reverse transformation is not complete up to 7T. Upon unloading, austenite to martensite transformation starts immediately, continues at a faster rate below 5.5T and is completed just below 1T. Clearly, ***the field loading-unloading can trigger fully reversible phase transformation without any stress-assistance which is promising for actuator applications.***

1.1.4. In-Situ Changes in the Lattice Structure during Phase Transformation Induced by Temperature under Constant Magnetic Field

In order to determine the crystal structure and lattice parameters of austenite and martensite phases of the NiMnCoIn single crystals, 2D diffraction patterns were collected as a function of temperature using a synchrotron-based high-energy x-ray diffraction technique. The high-energy (115 keV) XRD experiments were carried out at the 11-ID-C beam line at the Advanced Photon Source, Argonne National Laboratory, USA, with a wavelength of $\lambda=0.010756$ nm. The diffraction spots were recorded using a two-dimensional (2D) image plate detector (Mar345).

The in-situ high magnetic field experiments were conducted using a superconducting magnet (7 T, Oxford Instrument) installed on the beam line with a temperature range of 4–320 K. The magnetic field was applied parallel to the incident X-ray beam, i.e. along the longitudinal direction of the specimens. Figure 6.a shows the 2D diffraction pattern of the austenite phase captured using a Mar345 image plate at 300 K. A mask is placed at the center to remove the

effect of a residual peak in the image plate. The peaks are indexed for a selected rectangular region shown in Figure 6.a and the corresponding intensity versus 2θ graph is plotted in Figure 6.b. **Analyzing the peaks, the crystal structure of austenite is determined to be L₂₁ with the lattice constant of $a = 0.5979 \text{ nm}$.**

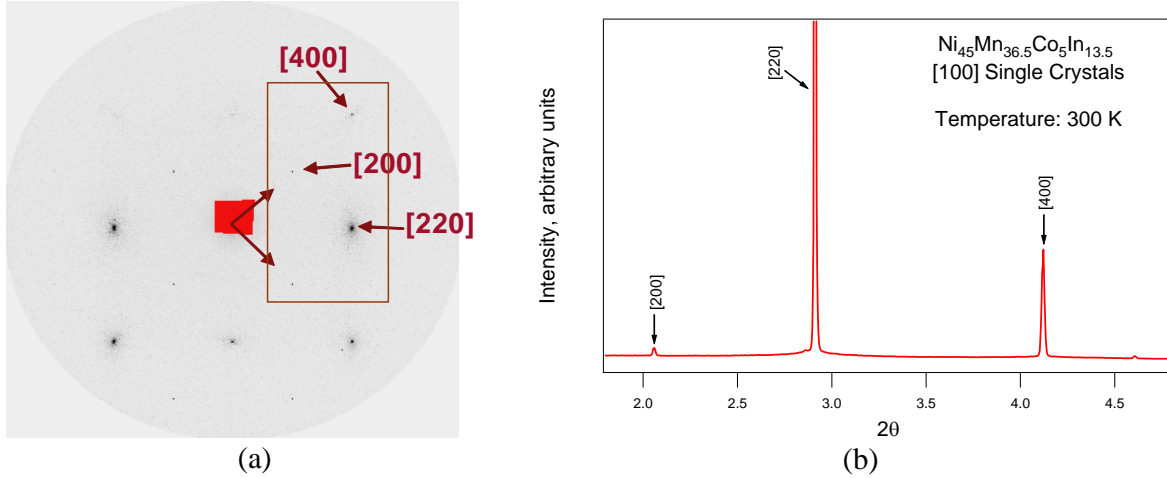


Figure 6. (a) The diffraction from the image plate and (b) the corresponding 2-D intensity versus 2θ graph of the Ni₄₅Mn_{36.5}Co₅In_{13.5} single crystal from the rectangular region shown in (a) at 300 K. The crystal structure is determined to be L₂₁ austenite.

The single crystal was then cooled down to 180 K ($< M_f$) where it became completely martensitic. The 2D diffraction pattern shown in Figure 7.a was collected at this temperature. It is clearly seen that the martensite has a modulated and more complex structure than austenite. The intensity versus 2θ graph of the same rectangular region shown in Fig. 6.a is presented in Figure 7.b. **The crystal structure of the martensite is determined to be six layered 12M monoclinic with lattice parameters of $a = 0.439 \text{ nm}$, $b = 0.557 \text{ nm}$, $c = 2.593 \text{ nm}$ and $\beta = 93.82^\circ$.**

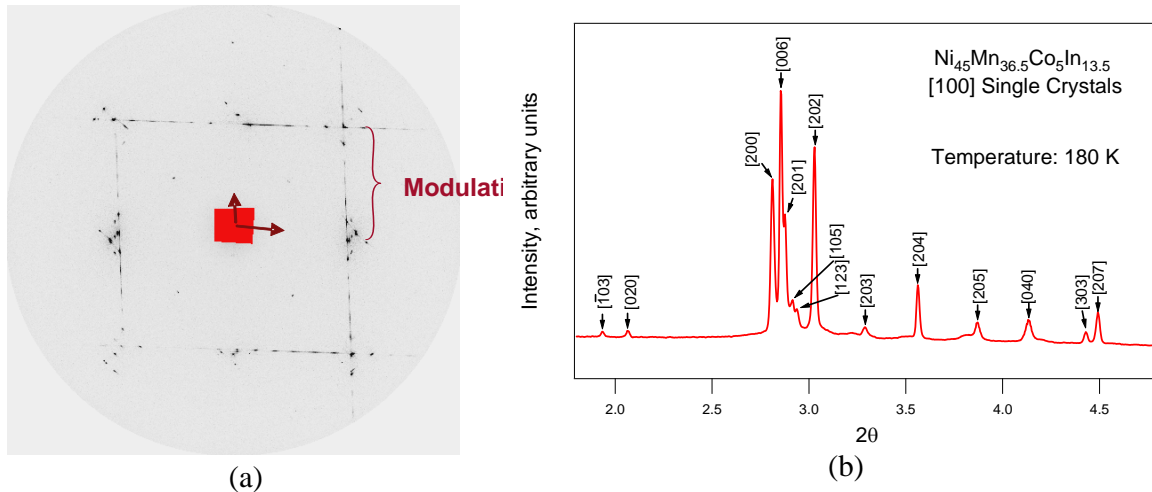


Figure 7. (a) The diffraction pattern from the image plate and (b) the corresponding 2-D intensity versus 2θ graph of the Ni₄₅Mn_{36.5}Co₅In_{13.5} single crystal at 180 K. The crystal structure determined to be six layered 12M monoclinic where the modulations are marked.

Subsequently, temperature and magnetic field-induced phase transformations were studied under high-energy x-ray beams to reveal the *in-situ* microstructural evolution during the phase

transformation. Initially, the single crystal sample was cooled down to 10 K and heated back up to 300K under zero field. At every 10 K increments, the x-ray diffraction data was recorded. Figure 8 shows the intensity versus 2θ response during cooling down to 200 K. At 240 K, the structure was completely austenite, at 230 K, martensite peaks started to emerge, and at 200 K, it completely transformed to martensite. These temperatures are consistent with those in Fig. 2. Further cooling to 10 K resulted only in minor changes in the peaks. During heating (Figure 8.b), the reverse transformation started below 250 K, and at 260 K the martensite transformed completely to austenite. The slight difference in the reverse transformation temperatures between Fig. 2 and Fig. 8.b can be attributed to the effect of the small field in Fig. 2, sample size difference, and sample to sample variation in NiMnCoIn alloys due to Mn volatility and macro-segregation during single crystal growth.

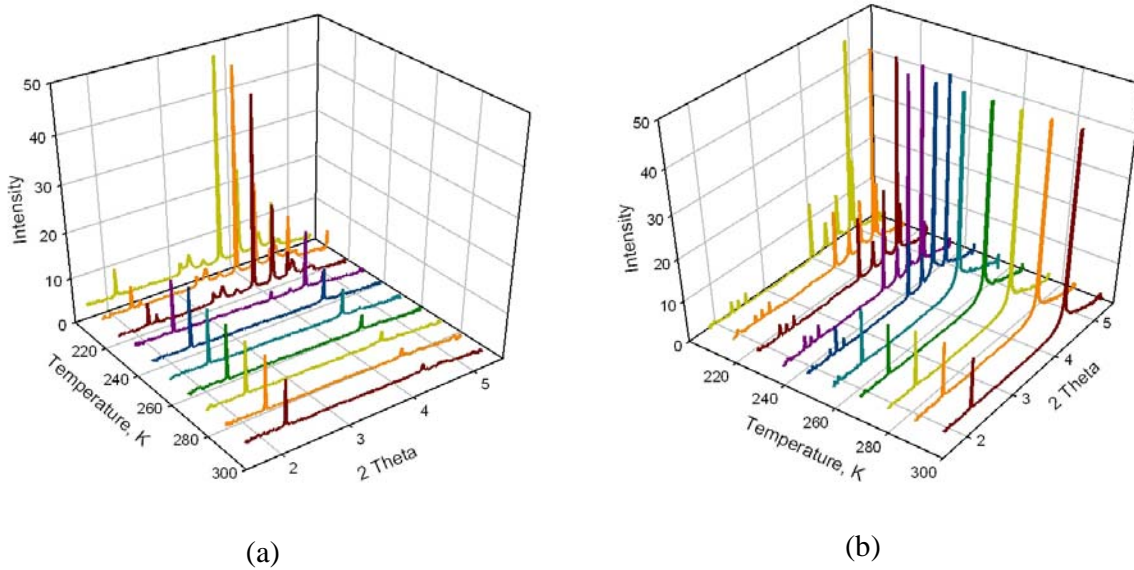


Figure 8. Intensity versus 2θ plots for the $\text{Ni}_{45}\text{Mn}_{36.5}\text{Co}_5\text{In}_{13.5}$ single crystals between 200 K and 300 K during a) cooling and b) heating under zero field.

To reveal the effect of applied magnetic field on the structural evolution during phase transformation, the same cooling/heating experiments were conducted under applied fields of 3 and 7 T between 100 K and 300 K. At every 10 K, the X-Ray diffraction data were recorded.

Figure 9 presents the structure of the sample as a function of temperature during cooling under different field magnitudes and the change in martensitic transformation temperature as a function of field, supporting the observations in Fig. 2.

Figure 10 shows the change in lattice parameters as a function of temperature and magnetic field. For clarity, the results are shown only for the temperature range from 150 K to 300 K during cooling and under applied magnetic fields of 0, 3 and 7 T. For better comparison, unit parameters are plotted as $a_m/\sqrt{2}$, $b_m/2$, $c_m/6\sqrt{2}$, and $a_a/2$ where the subscripts a and m show austenite and martensite, respectively. As shown in the figure, austenite to martensite phase transformation starts at 240 K under 0 T which is shown as M_s^{0T} . When the cubic austenite phase transformed to the monoclinic structure, a and c axes are elongated while the b axis is shortened as can be seen in Figure 10. When the applied field is increased to 3 T, the phase transformation start temperature decreases about 30 K to 210 K as shown by M_s^{3T} in the figure. When the sample is cooled down under 7 T, no phase transformation is detected. These results are in good

agreement with the results shown in Fig. 2.a where a high magnetic field results in austenite stabilization.

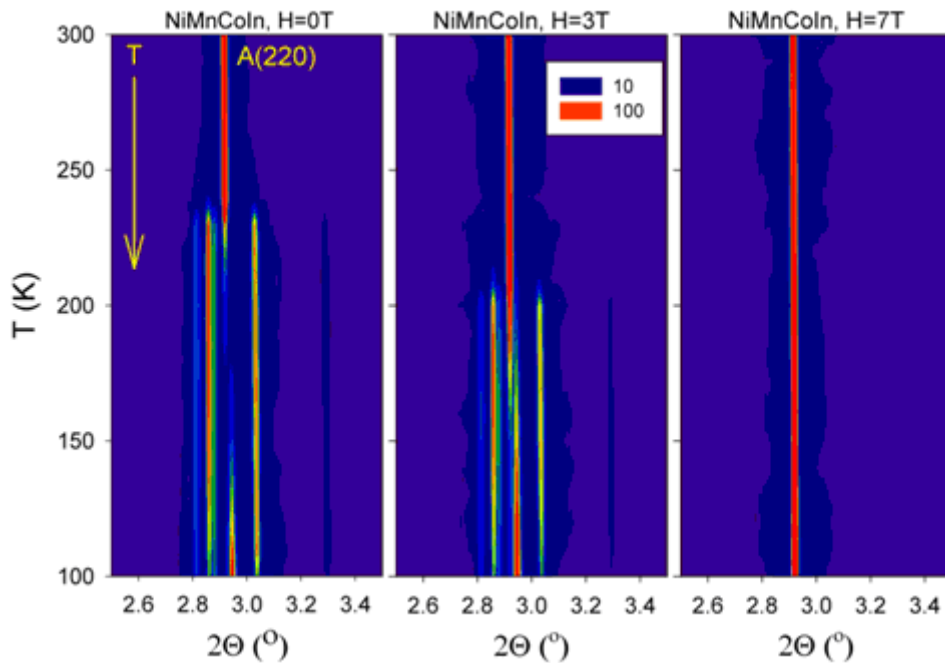


Figure 9. Temperature vs. 2θ plots for a $\text{Ni}_{45}\text{Mn}_{36.5}\text{Co}_5\text{In}_{13.5}$ single crystal during cooling under 0 T, 3 T, and 7 T fields showing the reduction in M_s temperature with field.

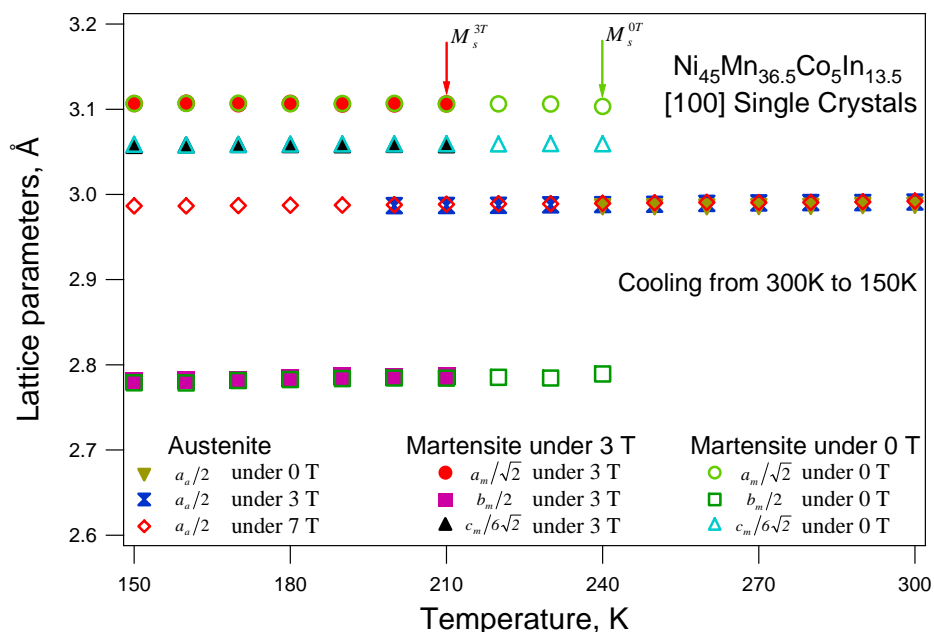


Figure 10. Change in lattice parameters of NiMnCoIn single crystal from 300 K to 150 K upon cooling, under 0, 3 and 7 T.

Figure 10 shows that when the sample is cooled down to 200 K under zero field and a high field, the stable phase changes from martensite to austenite with the field. Reversible FIPT can be achieved by cycling the magnetic field at 200 K as confirmed using the in-situ XRD measurements, which demonstrated reversible changes in the crystal structure (not shown here). Next, the sample was cooled down from 300 K to 200 K to obtain a fully martensitic sample under zero field and then, a magnetic field was applied with 1 T increments up to 7 T. No phase transformation was detected between 0-2 T and only a small amount of austenite formed at 3 T. The sample was completely austenite at 6 T. When the field was removed, austenite transformed back to martensite since it was no longer stable at that temperature. A small volume fraction of austenite transformed to martensite at 4 T, most of the sample was martensite at 3 T, and the structure was completely martensite at 2 T.

1.1.5. Isobaric Cooling/Heating Experiments on NiMnCoIn

In order to determine the shape memory response and the effect of applied stress on the transformation temperatures, isobaric cooling/heating experiments were conducted [25] and the results are shown in Figure 11.

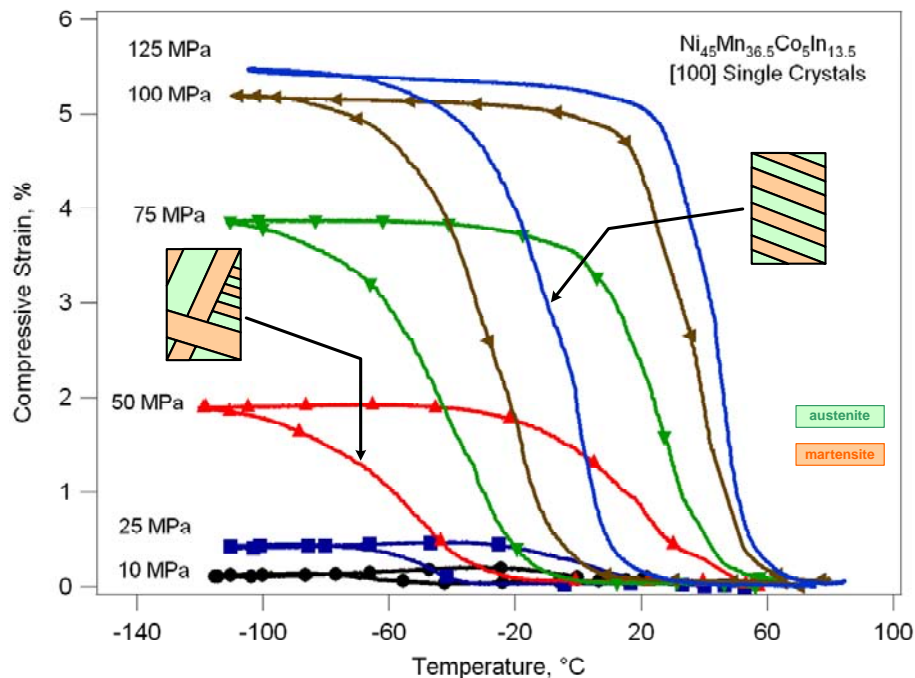


Figure 11. The strain vs. temperature response of Ni₄₅Mn_{36.5}Co₅In_{13.5} single crystals under constant compressive stress levels applied along the [100] orientation [25]. The insets show the possible microstructural evolution under the different stress levels as discussed in the main text.

The stress was isothermally applied in austenite and the sample thermally cycled between a temperature below M_f and a temperature above A_f under this stress. After the cycle was completed, the stress was increased further and thermal cycling repeated. In Fig. 11, the transformation strain (ε_{tr}) increases with stress from 0.2% under 10 MPa to 5.4% under 125 MPa. Such progression in ε_{tr} is a consequence of the evolution of martensite variants as a function of external stress. During cooling under low stresses, the measured low ε_{tr} levels imply that the stress is not sufficient to bias the formation and propagation of only a single martensite variant, and a self-accommodating martensite structure partially forms. Under high stress levels, the

volume fraction of the stress-biased martensite variant increases, so does the ε_{tr} level [25]. The possible evolution of martensite variants in two cases, *i.e.* under applied stresses of 50 and 125 MPa, during the forward transformation is also depicted in Fig. 11.

1.1.6. Effects of Magnetic Field on the Compressive Superelastic Response of a NiMnCoIn Single Crystal

Superelastic response of the present NiMnCoIn single crystals along the [001] orientation is shown in Figure 12.a. The experiments were conducted above A_f , resulting in a transformation strain of about 5.2 % in the plateau region at 0 °C. If the initial part of the unloading curve is extrapolated to zero stress, transformation strain can be determined as 6.3 %.

Figure 12.b presents the M_s temperature as a function of applied stress, determined from the isobaric thermal cycles in Fig. 11 and also the critical stress for the forward transformation as a function of test temperature, extracted from Fig. 12.a. It is clear that the critical stress for the transformation increases linearly with temperature, with a rate of 2.1 MPa/°C. The linear dependence between the critical stress and temperature can be expressed following the Clausius-Clapeyron (CC) relation:

$$\frac{\Delta\sigma}{\Delta T} = -\frac{\Delta H}{T_o \varepsilon_{tr}^{max}} \quad (1)$$

where $\Delta\sigma$ is the change in the critical stress, ΔT is the change in temperature, ΔH is the transformation enthalpy, T_o is the equilibrium temperature, and ε_{tr}^{max} is the transformation strain from a single crystal austenite to a single variant martensite.

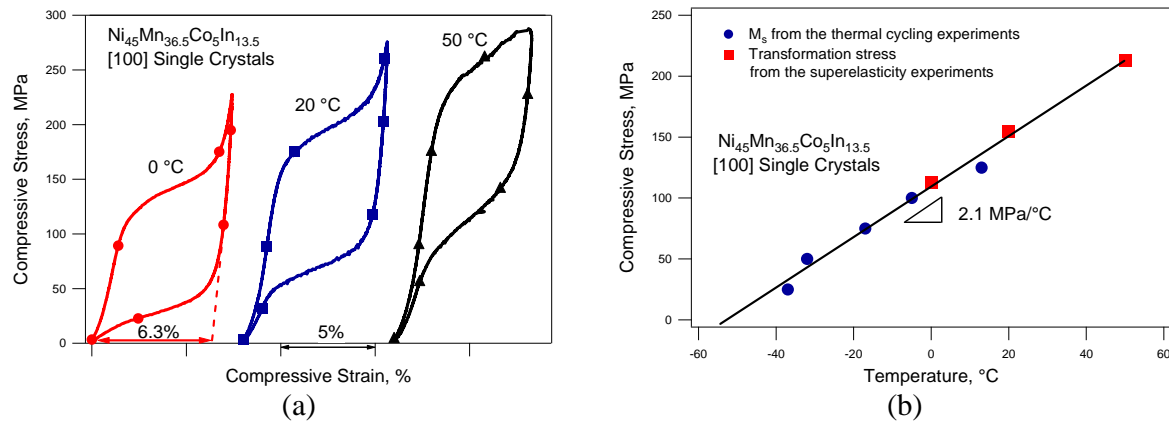


Figure 12. (a) Superelastic response of the $\text{Ni}_{45}\text{Mn}_{36.5}\text{Co}_5\text{In}_{13.5}$ single crystals along the [100] orientation under compression at 0 °C, 20 °C and 50 °C. (b) Critical stress for phase transformation vs. temperature phase diagram constructed using the data extracted from Figs. 11 and 12.a.

In order to reveal the effect of a magnetic field on the compressive superelastic response, the compressive behavior along the [100] orientation was investigated under constant magnetic fields at 0 °C. The field was applied along the [011] orientation, perpendicular to the applied stress direction prior to the loading, and kept constant throughout the experiment. Field magnitudes ranging from 0 T to 1.6 T with increments of 0.4 T were applied in order to capture the magnetostress levels as a function of field as shown in Figure 13. It is clear that the superelastic response exhibited a shift to higher stress levels with increasing magnetic field magnitudes. The magnitude of this shift is determined at 4% strain (the center of the superelastic loop) and plotted

as a function of the field level in Figure 13.b. The crystal exhibits approximately ~30 MPa magnetostress under 1.6 T which is much higher than other MSMA (2 to 8 MPa for NiMnGa alloys [10]). The magnetostress increases from 2.5 MPa to 30 MPa when the applied magnetic field increases from 0.4 T to 1.6 T. In these alloys, the magnetization of martensite and austenite saturates at an applied field of around 0.5 T according to Fig. 5. In order to determine the rate of increase in the transformation stress with field without considering the initial non-linear region due to saturation, the points for 0.4 T and above are taken into account and the transformation stress (or magnetostress) vs. magnetic field ($\Delta\sigma / \Delta H$) slope is determined as 22.9 MPa/T. In other words, up to the saturation field, the difference between MAEs of austenite and martensite is responsible for magnetostress. On the other hand, above the saturation field, a linear field dependence is expected as can be seen in Figs. 1 and 5 due to the Zeeman energy being the responsible energy contribution for the increase in transformation stress level.

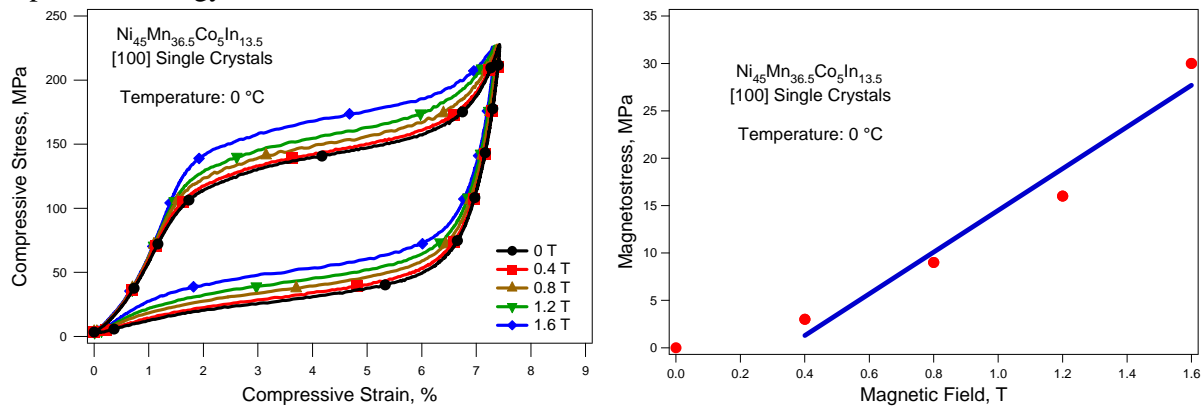


Figure 13. Effect of magnetic field on the superelastic response of $\text{Ni}_{45}\text{Mn}_{36.5}\text{Co}_5\text{In}_{13.5}$ [100](011) single crystals. The magnetic field was applied along the [011] orientation, perpendicular to the applied stress direction of [100], prior to the loading and kept constant throughout the experiment. (a) Experimental results at 0°C, and (b) the increase in transformation stress (determined at 4% strain) vs. magnetic field plot, showing a linear relationship above the saturation field.

1.1.7. Prediction of Theoretical Transformation Strains

In the present alloy, the parent phase has L2₁ structure while martensite has 12M monoclinic structure as mentioned in Section I.1.4. The lattice parameters determined from synchrotron high energy X-ray diffraction (Fig. 10) were used to find out the volume fractions of favorable lattice correspondence variants among the possible correspondence variant pairs (CVP), habit plane normal, transformation shear and twinning directions as shown in Table 1, utilizing “Energy Minimization Theory”. Once the habit plane normal and transformation shear direction are determined, it is possible to calculate the transformation strain (ε_{tr}) assuming the formation of the most favorable CVP [34-35]. Furthermore, the detwinning strain (ε_{dt}) can be calculated assuming the growth of the variant with the larger volume fraction in expense of the one with the smaller volume fraction within the CVP [34-35].

The contour plots of the calculated theoretical ε_{tr} and ε_{tr}^{max} ($=\varepsilon_{tr} + \varepsilon_{dt}$) values for tension and compression loading are shown in Figure 14 as a function of crystallographic orientation. The $\varepsilon_{tr} + \varepsilon_{dt}$ magnitudes under tension are a slightly higher than the ones under compression. The ε_{dt} values are very small due to the low volume fraction of one of the favored variants (0.075%, Table 1). In addition, the theoretical ε_{tr} and $\varepsilon_{tr} + \varepsilon_{dt}$ strains along the [100], [123], [110] and [111] orientations are summarized in Table 2 for both tension and compression.

Table 1. Theoretical volume fraction of the variants in the most favorable CVP, habit plane normal, transformation shear and twinning directions for Ni₄₅Mn_{36.5}Co₅In_{13.5} single crystals determined using the energy minimization method.

	Volume fraction of variants	Habit plane normal	Transformation shear direction	Twinning direction
12M	0.075	(-0.714 0.110 0.690)	<0.0985 0.0134 0.0836>	<0 -0.707 0.707>
12M	0.493	(-0.681 0.676 - 0.281)	<0.0069 0.0053 0.0103>	<0.707 0 -0.707>

Table 2. Theoretical transformation and detwinning strains of Ni₄₅Mn_{36.5}Co₅In_{13.5} single crystals loaded along the [100], [123], [011], and [111] orientations under compression and tension.

% Theoretical Strain for L2 ₁ to 12M martensitic phase transformation				
Compression		Tension		
Transformation strain (ε_{tr})	Transformation + Detwinning strain ($\varepsilon_{tr} + \varepsilon_{dt} = \varepsilon_{tr}^{max}$)	Transformation strain (ε_{tr})	Transformation + Detwinning strain ($\varepsilon_{tr} + \varepsilon_{dt} = \varepsilon_{tr}^{max}$)	
[100]	-6.61	-6.61	6.24	6.74
[123]	-4.04	-4.14	4.39	4.58
[011]	-3.25	-3.47	4.16	4.16
[111]	-1.22	-1.22	0.57	0.57

The maximum transformation strain along the [100] orientation is obtained as 6.61% and 6.24% for compression and tension, respectively. The former theoretical strain is larger than the 5.2% plateau strain experimentally obtained from the superelastic response at 0 °C (Fig. 12), but is close to 6.3 % strain determined by extrapolating the unloading curve to zero stress. Apparently, the transformation does not end at the end of the plateau region and continues during the second apparent elastic region. Under stress, the transformation strain of 5.2% is significantly lower than 6.3% under zero stress.

The difference between the theoretical and measured transformation strains in the superelastic response can be attributed to the differences in elastic moduli of transforming phases that eventually result in a change in lattice parameters of these phases under stress unevenly, and in turn, a change in transformation strain under stress. A similar difference between the theoretical and experimental transformation strains is also observed in Ni₅₁Fe₁₉Ga₃₀ single crystals [36]. The theoretical predictions described above utilized the lattice parameters determined under zero stress. Under stress, cubic austenite becomes more like a tetragonal phase before the transformation, which should affect the transformation strain. In addition, temperature can play a role in lattice parameters of austenite and martensite. Although the temperature dependence of austenite lattice parameters was considered in the calculations, it was not possible to determine the martensite lattice parameters at 0°C, which can only be induced under stress. However, from the trends in Fig. 10, the temperature effect is not pronounced.

1.1.8. Magnetostress Levels as a Function of Crystallographic Orientation

For magnetic actuator applications, in addition to actuation strain, i.e. MFIS for MSMAs, magnetostress is another key parameter that should be known *a priori*. Magnetostress levels together with MFIS are what dictate the work output of MSMA actuators. If transformation

strains and magnetostress levels are known as a function of crystallographic orientation, the response of polycrystals with known textures could be predicted.

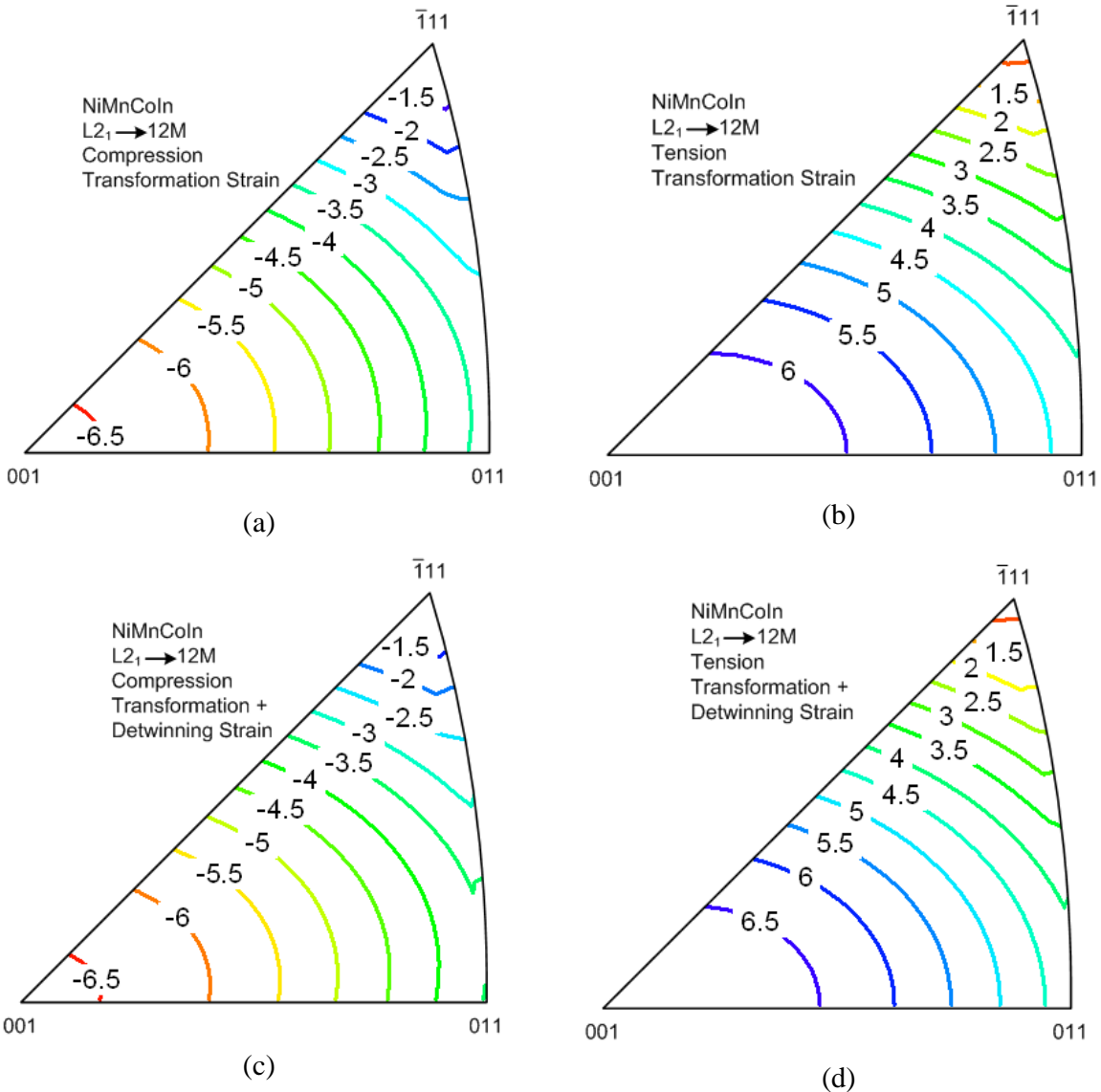


Figure 14. Contour plots of theoretical transformation strains ((a), (b)) and transformation + detwinning strains ((c), (d)) under compression ((a), (c)) and tension ((b), (d)) in $Ni_{45}Mn_{36.5}Co_5In_{13.5}$ single crystals calculated using the Energy Minimization Theory [34-35]. The lattice parameters were obtained using a synchrotron-based high-energy x-ray diffraction technique.

It is possible to predict magnetostress as a function of applied field if the change in critical stress for phase transformation with temperature (the slope of Clausius-Clapeyron curves) and the change in transformation temperature with applied field are known. The change in critical stress with temperature ($\Delta\sigma / \Delta T$) is expressed using the CC relation in eqn. 1. For the CC relation, the transformation strains of single crystals can be calculated utilizing Energy Minimization Theory as shown in Fig. 14 or it can be determined from superelasticity (Fig. 12) and/or isobaric thermal cycling experiments (Fig. 11). The change in transformation temperatures

with applied field ($\Delta T / \Delta H$) can be determined from the magnetization results shown in Figs. 2, 4, and 5. Then the magnetostress as a function of field can be approximated as;

$$\frac{\Delta\sigma}{\Delta H} = \frac{\Delta\sigma}{\Delta T} \times \frac{\Delta T}{\Delta H} \quad (2)$$

From Figure 12, the change in critical stress with temperature is determined as 2.1 MPa/K. The CC slopes for other orientations can be calculated using the calculated ε_{tr}^{max} values for each orientation and assuming ΔH and T_0 in eqn. 1 are not functions of orientation. $\Delta T / \Delta H$ for the M_s temperature is determined using the results from Figs. 2, 4, and 5 as -12.6 K/T. This value can be considered to be orientation independent neglecting the effect of MAE differences between martensite and austenite, if there is any. Thus, the reduction in the transformation temperatures originates from the difference between the saturation magnetizations of austenite and martensite, which is usually orientation independent. Table 3 shows the calculated magnetostress levels per 1 T applied field along the [100], [123], [110] and [111] orientations. The experimental values are indicated with “**” in the table.

Table 3. Orientation dependence of magnetostress as a function of applied field. * indicates the values obtained experimentally.

	ε_{tr}^{max} , %	$\frac{\Delta\sigma}{\Delta T}$ MPa/K	$\frac{\Delta T}{\Delta H}$ K/T	$[\frac{\Delta\sigma}{\Delta H}]_{theoretical}$ MPa/T	$[\frac{\Delta\sigma}{\Delta H}]_{experimental}$ MPa/T
[100]	6.61	2.1*	12.6*	26.5	22.9*
[123]	4.14	3.35	12.6*	42.2	
[110]	3.47	4.0	12.6*	50.4	
[111]	1.22	11.3	12.6*	143.4	

Note that these magnetostress levels are for compression; in other words, the magnetic field is doing work against compressive loading. The magnetostress levels for tension loading would be different due to the different ε_{tr}^{max} values under tension (Table 2).

The $[\frac{\Delta\sigma}{\Delta H}]_{theoretical}$ value calculated using eqn. 2 and shown in Table 3 for the [100] orientation is 26.5 MPa/T which is in good agreement with $[\frac{\Delta\sigma}{\Delta H}]_{experimental}$ which is 22.9 MPa/T.

The difference between the experimental and theoretical values is attributed to the demagnetization effect [37] that would result in lower magnetic field inside the material, and to the difference between the theoretical calculations and experimental observations of the transformation strain. Still, the above calculations provide a clear picture of the overall trends in the attainable actuation stress levels in Ni₄₅Mn_{36.5}Co₅In_{13.5} MSMA.

Figure 15 shows the contour plot of the magnetostress values calculated for the orientations in the standard stereographic triangle. It is evident that the magnetostress level of 143.4 MPa is maximum along the [111] orientation where the transformation strain (Fig. 14) is minimum, and the magnetostress is minimum along the [100] orientation where the transformation strain is maximum. These calculations suggest that if the actuation stress is the critical parameter for an application, then it is better to choose an orientation with small transformation strain, e.g. near the [111] orientation, and if the actuation strain is more important, an orientation with a large

transformation strain, e.g. [100] orientation, should be chosen. Magnetic work output, however, is nearly orientation independent (neglecting the MAE differences between austenite and martensite) due to Zeeman energy being the responsible major energy contribution.

Additionally, it would be possible to induce a reversible stress-assisted field-induced phase transformation at lower magnetic fields in the [111] orientation compared to the [100] orientation if the stress hysteresis does not change substantially with orientation. Since the magnetostress level per Tesla is significantly higher in the [111] orientation, the superelastic loops under field and without field (Fig. 13) could be separated at a lower field level as compared to other orientations making it possible to obtain field-induced phase transformation at lower magnetic field magnitudes. A similar mechanism (i.e. stress-assisted field induced phase transformation) has been observed in Ni₂MnGa single crystals along the [100] orientation during the I \leftrightarrow X transformation [6, 10-11], however, the transformation strain was only 0.5% and the magnetic energy contribution stemmed only from the difference between MAEs of the transforming phases. Brewer [38] reported that the thermal hysteresis along the [123] and [100] orientations is similar, which might also be the case for the [111] orientation and for the orientation dependence of the stress hysteresis. However, the latter argument needs to be validated experimentally since it has been reported in other SMAs [34-36, 39-43] that stress hysteresis can be a function of orientation and stress state.

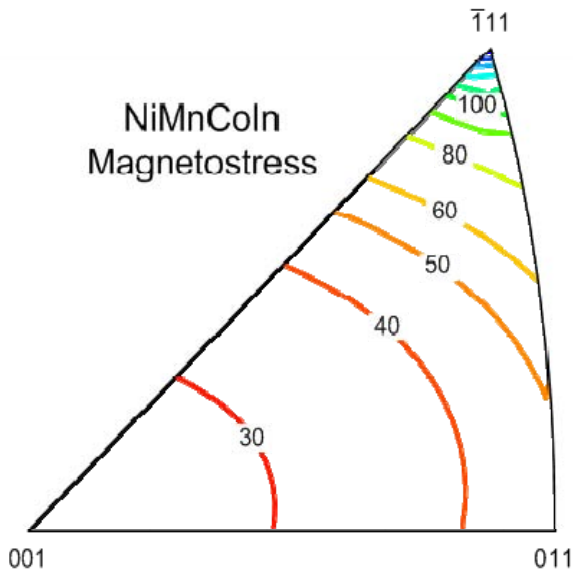


Figure 15. Predicted magnetostress levels in Ni₄₅Mn_{36.5}Co₅In_{13.5} MSMA as a function of crystallographic orientation presented in a standard stereographic triangle.

1.1.9. Magnetic Work Output of the Present NiMnCoIn Alloy

The magnetic work output of the NiMnCoIn alloy in hand was determined to be 1620 kJm⁻³ under 1.6 T. In contrast to NiMnGa alloys, the work output of these new alloys is not limited by a saturation magnetic field, increasing continuously with the applied field. Magnetostress is directly related to the actuation stress and is one of the key parameters to assess the potential of SMAs for actuator applications. It is determined by the change in the critical stress levels for phase transformation as in the present case or for martensite variant reorientation, when the field is applied. Figure 16 shows a comparison plot on the magnetostress levels as a function of field from the present study for phase transformation along the [100] (experimental) and [111] (predicted) orientations in the NiMnCoIn alloy, and from the literature on NiMnGa alloys for both phase transformation and variant reorientation [6, 10-11, 44-47]. In NiMnGa alloys, magnetostress initially increases linearly with the field and then saturates above a certain field

since MAE is the magnetic energy responsible for magnetostress (Fig. 1), and thus, is limited with the saturation field.

However, magnetostress always increases with field in the NiMnCoIn alloy since there is no limit for the contribution of the ZE (Fig. 1). It is clear from Fig. 16 that for magnetic fields above 0.7 T magnetostress of NiMnCoIn alloys is larger than for the other systems. When a magnetic field of 1.6 T is applied, the magnetostress for phase transformation in the NiMnCoIn alloy is 30 MPa while it is 5.7 [6] and 1.5 MPa [47] for variant reorientation in the 10 M and 14M martensites of NiMnGa alloys, respectively, and is 7.6 MPa for the phase transformation to 10 M martensite in the $\text{Ni}_{51.1}\text{Mn}_{24}\text{Ga}_{24.9}$ alloy [10, 12].

Another important measure of the actuation performance for MSMA is the magnetic work output per unit volume, $W = \sigma \times \varepsilon$, where σ is the magnetostress and ε is the strain induced by the magnetic field. The maximum work output for variant reorientation in NiMnGa alloys was reported to be 156 kJ m^{-3} by Karaca *et al.* [12]. The work outputs for the field-induced two-stage martensitic phase transformation in the $\text{Ni}_{51.1}\text{Mn}_{24}\text{Ga}_{24.9}$ alloy were determined as 36.4 kJ m^{-3} and 160 kJ m^{-3} , respectively for each stage, in our recent work [10].

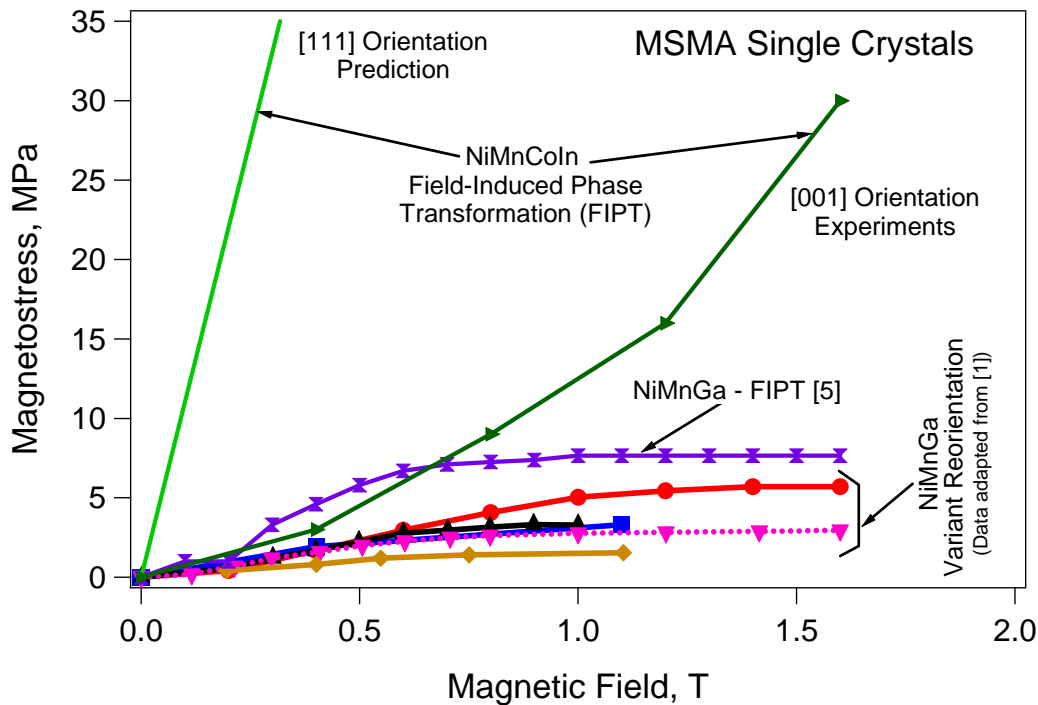


Figure 16. Magnetostress levels as a function of applied magnetic field for the martensitic phase transformation in the present $\text{Ni}_{45}\text{Mn}_{36.5}\text{Co}_5\text{In}_{13.5}$ single crystals, obtained from Fig. 13 and the predictions introduced in Section 4.2, and for the phase transformation and variant reorientation of 10M and 14M martensite structures in several NiMnGa alloys extracted from the literature [6, 10-11, 44-47].

It is important to note that the maximum work output for variant reorientation and phase transformation in the NiMnGa alloys are similar since in both mechanisms magnetostress stems from the MAE of martensite. The saturation magnetizations of austenite and martensite phases are about the same in the NiMnGa alloy compositions for which the magnetostress levels were reported; thus the ZE is negligible. The magnetic work output of the present NiMnCoIn alloy, on the other hand, is about 1600-1800 kJ m^{-3} which is one order of magnitude higher than the work output of NiMnGa alloys [10].

Figure 17 compares the aforementioned magnetostress, MFIS, and magnetic work output levels for NiMnGa alloys from the literature and the present NiMnCoIn alloy [6, 10, 44, 48-50]. Clearly, the NiMnCoIn alloy demonstrates a significantly enhanced work output level, which can open new opportunities for MSMAs in actuator applications. Figure 18 compares the experimentally reported actuation stress, strain, and work outputs for the several different actuator materials including MSMAs. The data presented in this figure for the materials other than MSMAs are adapted from [51] and [52]. We have also included in this figure, magnetostress level, MFIS, and magnetic work output for the NiMnCoIn alloy for 1 T applied field. The work output levels for the NiMnCoIn alloy are not the experimental actuation work outputs but instead the magnetic work output per 1 T observed in the present study. Part of the magnetic work output would be spent for dissipation during the forward and reverse phase front motion, and the remaining could be used as mechanical work output.

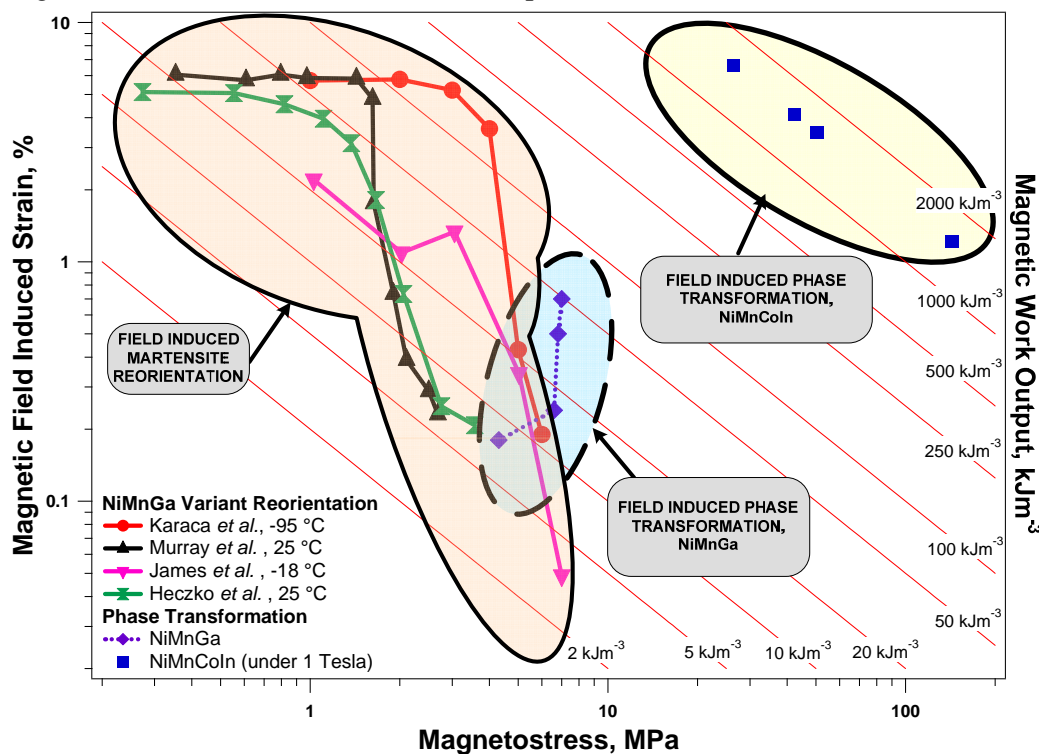


Figure 17. MFIS and magnetic work output vs. the magnetostress plots showing the literature data obtained to date in NiMnGa MSMAs utilizing field-induced martensite reorientation and field-induced phase transformation mechanisms, and the present results on the $\text{Ni}_{45}\text{Mn}_{36.5}\text{Co}_5\text{In}_{13.5}$ single crystals. A grid of constant magnetic work output hyperbolas ranging from 2 and 2000 kJ m^{-3} has been superimposed. Logarithmic scale is used for both axes for easy comparison [6, 10, 44, 48-50].

Considering that slightly higher magnetic field levels can be applied to overcome the dissipation, the work output levels for the NiMnCoIn alloy in Fig. 18 show a realistic estimate of the actuation work output levels that can be easily achieved in these new alloys. In the figure, MSMAs utilizing the field-induced phase transformation mechanism for actuation fill a gap between conventional SMAs and other actuator materials. It should be kept in mind that, one advantage of MSMAs over conventional SMAs is notably faster actuation frequency which makes these materials prime candidate for future high work output, high stroke, and medium frequency actuators.

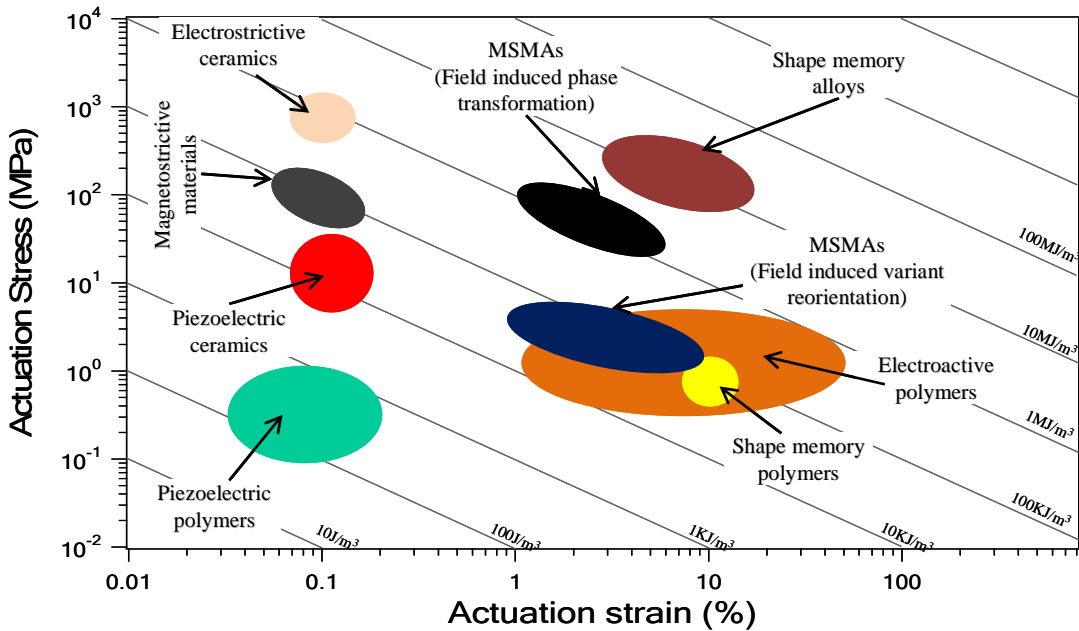


Figure 18. Comparison of actuation stress, actuation strain, and actuation work output levels that are reported for different active materials [51-52] with those from MSMA. The values resulting from the field-induced variant reorientation and phase transformation are presented separately. The results for the MSMA showing field-induced phase transformation include experimental observations in NiMnGa alloys and the realistic estimates for the new NiMnCoIn alloys which are predicted in the present work.

1.1.10. Thermodynamic Framework for the Magnetic Field-Induced Phase Transformation

We introduced a thermodynamic framework to better understand the effect of two possible magnetic energy contributions discussed earlier on the field-induced phase transformation and the origin of high magnetostress levels in the NiMnCoIn alloys. The Gibbs free energy difference between the parent and product phases during a thermoelastic martensitic transformation under applied magnetic field can be expressed as [10, 53];

$$\Delta G_{total}^{P \rightarrow M}(T, \sigma, H) = \Delta G_{ch}^{P \rightarrow M} - \Delta E_{mech}^{P \rightarrow M} + \Delta G_{el}^{P \rightarrow M} + \Delta E_{irr} + \Delta G_{mag}^{P \rightarrow M} - \Delta G_{MAE}^{P \rightarrow M} \quad (3)$$

where $\Delta G_{total}^{P \rightarrow M}(T, \sigma, H)$ is the total Gibbs free energy difference that needs to be less than zero to trigger the transformation. ΔG_{ch} is the chemical free energy difference between martensite and parent phases ($P \rightarrow M$ represents the direction of the transformation, *i.e.* from parent phase to martensite). ΔE_{mech} is the mechanical energy provided by the externally applied load during the phase transformation. ΔG_{el} is the stored elastic energy and ΔE_{irr} is the dissipation energy due to defect and dislocation generation and frictional energy spent on the movement of phase fronts. ΔG_{mag} is the Zeeman energy difference which can be expressed as [10, 13];

$$\Delta G_{mag}^{P \rightarrow M} = H \cdot M_{parent}^s - H \cdot M_{martensite}^s \quad (4)$$

where H is the externally applied magnetic field and M^s is the saturation magnetization. Similar to the chemical energy difference between transforming phases, the $\Delta G_{mag}^{P \rightarrow M}$ term provides an additional barrier such that further external mechanical work or overcooling needs to be provided for the phase transformation to take place. This term is more pronounced when the transformation occurs between a paramagnetic parent phase and a ferromagnetic martensite (or

vice versa). $\Delta G_{MAE}^{P \rightarrow M}$ is the difference between the magnetocrystalline anisotropy energies of parent and martensite phases and can be expressed as;

$$\Delta G_{MAE}^{P \rightarrow M} = (K_u \sin \theta)_{parent} - (K_u \sin \theta)_{martensite} \quad (5)$$

where K_u represents the MAE and θ is the angle between the applied field direction and the easy axis of magnetization of each phase domain. Magnetoelastic effects can be taken into account in the $\Delta G_{el}^{P \rightarrow M}$ term in eqn. 3, however, they are usually negligible as compared to $\Delta G_{mag}^{P \rightarrow M}$ and $\Delta G_{MAE}^{P \rightarrow M}$ [32, 53]. ΔG_{el} and ΔE_{irr} are also referred to as non-chemical energy terms.

The saturation magnetizations and MAE differences of the phases determine the effect of the applied magnetic field on phase transformation. If the saturation magnetization of austenite is higher than the saturation magnetization of martensite, the magnetic field favors austenite resulting in austenite stabilization and a decrease in transformation temperatures or an increase in critical stress for transformation at constant temperature. Similarly, if the MAE of martensite is larger than that of austenite, austenite stabilization will again be observed. The net effect of the magnetic field depends on whether $\Delta G_{mag}^{P \rightarrow M} - \Delta G_{MAE}^{P \rightarrow M}$ term is positive or negative. If it is positive then the parent phase is more stable under a magnetic field, in other words, a magnetic field can be used to trigger the martensite to parent phase transformation as in the case of NiMnCoIn alloys. If it is negative, the parent to martensite phase transformation can be activated with application of a magnetic field, which is the case for the NiMnGa alloys. It is important to note that $\Delta G_{mag}^{P \rightarrow M}$ term is more pronounced when the transformation occurs between a paramagnetic parent phase and a ferromagnetic martensite (or vice versa), as in NiMnCoIn alloys, where $\Delta G_{MAE}^{P \rightarrow M}$ is more pronounced if transforming phases are ferromagnetic with similar saturation magnetizations and one of them has larger MAE, as in the case of NiMnGa alloys. It is also important to note that the MAE is orientation dependent whereas the ZE is not.

In the present NiMnCoIn alloy, the MAE of martensite is negligible since martensite is weakly magnetic at best, and the MAE of austenite is very low, which is the case for most MSAs with cubic structure. Thus, $\Delta G_{mag}^{P \rightarrow M}$ is the only contributing energy term. In this case, according to eqn. 3 the field should favor austenite which in turn results in an increase in the critical stress for phase transformation or in a decrease in transformation temperatures. This is in good agreement with our experimental findings shown in Figs. 2, 9, and 13, and usually valid for all recently invented metamagnetic SMAs.

In NiMnGa alloys, composition can be adjusted to have a paramagnetic austenite to ferromagnetic martensite phase transformation [32, 54]. If paramagnetic austenite transforms to ferromagnetic martensite, the MAE of martensite might no longer be negligible but the MAE of austenite can still be neglected for most MSAs with cubic structure. In this case, the magnetic field favors formation of martensite due to a negative $\Delta G_{mag}^{P \rightarrow M}$, however, $\Delta G_{MAE}^{P \rightarrow M}$ might play a role depending on the stress state and the relative direction of easy axis with respect to the stress direction. If $\Delta G_{MAE}^{P \rightarrow M}$ is negligible compared to $\Delta G_{mag}^{P \rightarrow M}$, then, the field favors martensite, which means a decrease in the critical stresses for phase transformation and an increase in transformation temperatures.

If $\Delta G_{mag}^{P \rightarrow M}$ can be neglected and $\Delta G_{MAE}^{P \rightarrow M}$ term is negative, then, the critical stress increases if the stress is applied perpendicular to the field under compression or parallel to the field under tension for the NiMnGa alloys in which the easy axis of martensite is along the short axis. If the

easy axis of martensite is along the long axis as in NiFeGa and NiFeCoGa MSMAs [55-56], the critical stress increases if the stress is applied parallel to the field under compression or perpendicular to the field under tension.

Table 4 summarizes the possible effects of magnetic fields on the critical stress (σ_c) for phase transformation under compression and transformation temperatures (i.e. M_s) depending on the magnetic properties of the transforming phases and the relative direction of the uniaxial stress and magnetic field.

Table 4. Possible effects of externally applied magnetic field on the compressive critical stress (σ_c) for phase transformation and martensite reorientation, and on M_s temperature as a function of the magnetic states of transforming phases and relative direction of uniaxial compressive stress and the field. Para: paramagnetic, Ferro: ferromagnetic, Antiferro: antiferromagnetic.

Example alloys	Austenite	Martensite	Relative direction of σ and H	Assumptions	σ_c	M_s
NiMnGa [10, 48, 57]	Ferro-magnetic	Ferro-magnetic	$\sigma // H$	$\Delta G_{mag}^{P \rightarrow M}$ is negligible. Short axis of martensite is the easy axis	no effect	no effect
			$\sigma \perp H$		increases	decreases
NiFeGa [56] NiFeGaCo [55]	Ferro-magnetic	Ferro-magnetic	$\sigma // H$	$\Delta G_{mag}^{P \rightarrow M}$ is negligible. Long axis of martensite is the easy axis	increases	decreases
			$\sigma \perp H$		no effect	no effect
NiMn(In,Sn,Sb) [15, 18-19, 26] NiMnCo(In,Sn) [16-17]	Ferro-magnetic	Weakly magnetic (Para or antiferro)		$\Delta G_{MAE}^{P \rightarrow M}$ is negligible	increases	decreases
NiMnGa [32, 54]	Para-magnetic	Ferro-magnetic	$\sigma // H$		decreases	increases
			$\sigma \perp H$	$ \Delta G_{mag}^{P \rightarrow M} > \Delta G_{MAE}^{P \rightarrow M} $	decreases	increases
			$\sigma \perp H$	$ \Delta G_{mag}^{P \rightarrow M} < \Delta G_{MAE}^{P \rightarrow M} $	increases	decreases

For each case, example alloy systems are also listed in the table where NiMnGa represents the alloys that have magnetic hard and easy axes along the long and short axes of martensite, respectively, NiFeGa stands for the alloys which have magnetic hard and easy axes along the short and long axes of martensite, respectively, and NiMnIn stands for the alloys that transforms

from ferromagnetic austenite to weakly magnetic martensite with a negligible MAE of martensite.

In summary, $\Delta G_{mag}^{P \rightarrow M}$ and $\Delta G_{MAE}^{P \rightarrow M}$ depend on the magnetic properties of transforming phases that can be altered by composition and temperature. Additionally, $\Delta G_{MAE}^{P \rightarrow M}$ depends also on the relative orientation of applied stress and magnetic field, and on the stress state. The change in critical stress for phase transformation and M_s depends on the total contribution of these two magnetic terms where the critical stress increases and M_s decreases when the sum of two magnetic terms is positive.

1.1.11. Requirements to Achieve Reversible Field-Induced Actuation

Magnetic FIPT using the change in magnetization or structure under a magnetic field does not provide direct information on the actuation strain. The actuation strain values reported in Figs. 17 and 18 for the NiMnCoIn alloy are indeed the transformation strain levels. To induce the phase transformation, transform the martensite completely to austenite, and obtain MFIS levels as high as transformation strain levels, a critical field level should be applied, which is a function of temperature as shown in Fig. 2.b.

In conventional SMAs, in order to observe external shape change, martensite structure formation during phase transformation must be biased either by an applied stress or internal residual stresses. In other words, simple thermal cycling thru transformation temperatures will not result in large external shape changes even though the material can completely transform to another phase. Temperature cannot bias specific martensite variants, therefore, either thermo-mechanical training should be performed to obtain the so-called “two-way shape memory effect” or a constant external stress should be applied during thermal cycles to bias a martensite variant. The same should hold for MSMA during field-induced phase transformation during magnetic cycling. Since the MAE of martensite is negligible in the present NiMnCoIn alloy and the martensite is weakly magnetic, the magnetic field should not favor any martensite variant nor result in external strain. Thus, to be able to obtain reversible field-induced phase transformation accompanied with MFIS, one needs to either built up internal local stress thru thermo-mechanical or magneto-mechanical training, or a simultaneous stress, high enough to bias a variant, should be applied. From this point of view, a magnetic field in the present case is analogous to temperature, as both do not have a significant effect on the microstructure formation of martensite, but martensite transforms to austenite when they are increased, and austenite transforms back to martensite when they are reduced. Therefore, it is of utmost importance to understand the effect of bias stress levels on the field-induced phase transformation during field cycling which is currently being studied. This is due to the fact that such a loading condition constitutes what is used for many practical actuator applications.

For desirable actuation properties, in addition to high reversible actuation strain, the field requirement for actuation must also be low. Although actuation stress, strain and work output values of NiMnCoIn alloys are very promising, the requirement for relatively high magnetic field (1.5-3T) for phase transformation may place a barrier for their practical use. Therefore, it is essential to decrease the critical field for martensite to austenite transformation and transformation hysteresis. Low transformation hysteresis will assure austenite to martensite back transformation upon field unloading. This problem is somewhat similar to the earlier issues in conventional SMAs to obtain stable pseudoelasticity or to the problem to reduce the thermal hysteresis for increasing the efficiency and response frequency of SMAs. The critical magnetic field and transformation hysteresis for reversible actuation can possibly be reduced by:

- i) Increasing the compatibility between transforming phases and enhance the strength of phases against transformation plasticity to reduce dissipation. There are several

- approaches reported for conventional SMAs, which can also be utilized in MSMAs, such as compositional modifications, coherent precipitation, and thermo-mechanical processing.
- ii) Increasing $\Delta G_{mag}^{P \rightarrow M}$ and Curie temperature by additional alloying.
 - iii) Employing stress or temperature assisted transformation. Stress favors austenite to martensite transformation while temperature favors martensite to austenite transformation. They can be used to assist FIPT.
 - iv) Using textured polycrystals or certain single crystal orientations. It has been shown in Section I.1.8 that magnetostress per Tesla is maximum along the [111] orientation. Using single crystals or textured polycrystals along this orientation might result in low magnetic field requirement.

Clearly, metamagnetic SMAs including NiMnCoIn alloys are promising new materials for actuator applications, however, there are few issues mentioned above that the materials science community need to address for their rapid insertion into practical applications.

1.1.12. Crystallographic Orientation Dependence of Stress vs. Temperature Phase Diagram

Figure 19 shows the results from an extended study on the martensitic transformation start temperature as a function of applied stress, extracted from the thermal cycles, and critical stress for forward transformation as a function of test temperature, extracted from the pseudoelastic responses. For all orientations, as temperature increases critical stress for phase transformation increases and vice versa. The linear correlation between stress and temperature is known as

Clausius-Clapeyron (CC) Relation and can be written as $\frac{\Delta\sigma}{\Delta T} = -\frac{\Delta H}{T_o \varepsilon_t}$ where $\Delta\sigma$ is the change

in critical stress, ΔT is the change in temperature, ΔH is the transformation enthalpy, T_o is the equilibrium temperature, and ε_t is the transformation strain. Since we are using the same material along different directions, only ε_t is orientation dependent among all the aforementioned.

1.1.13. The effect of Simultaneous Application of Stress and Magnetic Field on the Magnetic Field-Induced Reversible Phase Transformation

In May 2008, we have started a joint research effort on synthesis, development, magneto-thermo-mechanical and metallurgical characterization of meta-magnetic SMAs with Professor Ryosuke Kainuma from Institute of Multidisciplinary Research for Advanced Materials, Tohoku University, Japan. Professor Kainuma is a renowned pioneer in the magnetic shape memory research and the inventor of the Ni-Sn, Ni-Sb and Ni-In based meta-magnetic SMAs.

Dr. Karaman and his student visited their ‘Institute of Multidisciplinary Research for Advanced Materials’ for two weeks, under the full sponsorship of Tohoku University. In the course of this visit, besides setting the foundations of a promising partnership through fruitful discussions on current and prospective MSMA systems, Mr. Basaran and Prof. Kainuma’s students carried out a set of experiments at the High Field Laboratory for Superconducting Materials, a part of Institute for Materials Research of the same university. These experiments were conducted on either bulk or powdered specimens of $Ni_{45.7}Mn_{35.6}Co_{4.8}In_{13.8}$, both of which were heat treated with sequential steps of 900°C, 24 hours, water quenching and 500°C, 1 hour, water quenching. Prior to the experiments, the transformation temperatures and the change in temperature hysteresis at different levels of applied magnetic field for all specimens were determined by SQUID magnetometer.

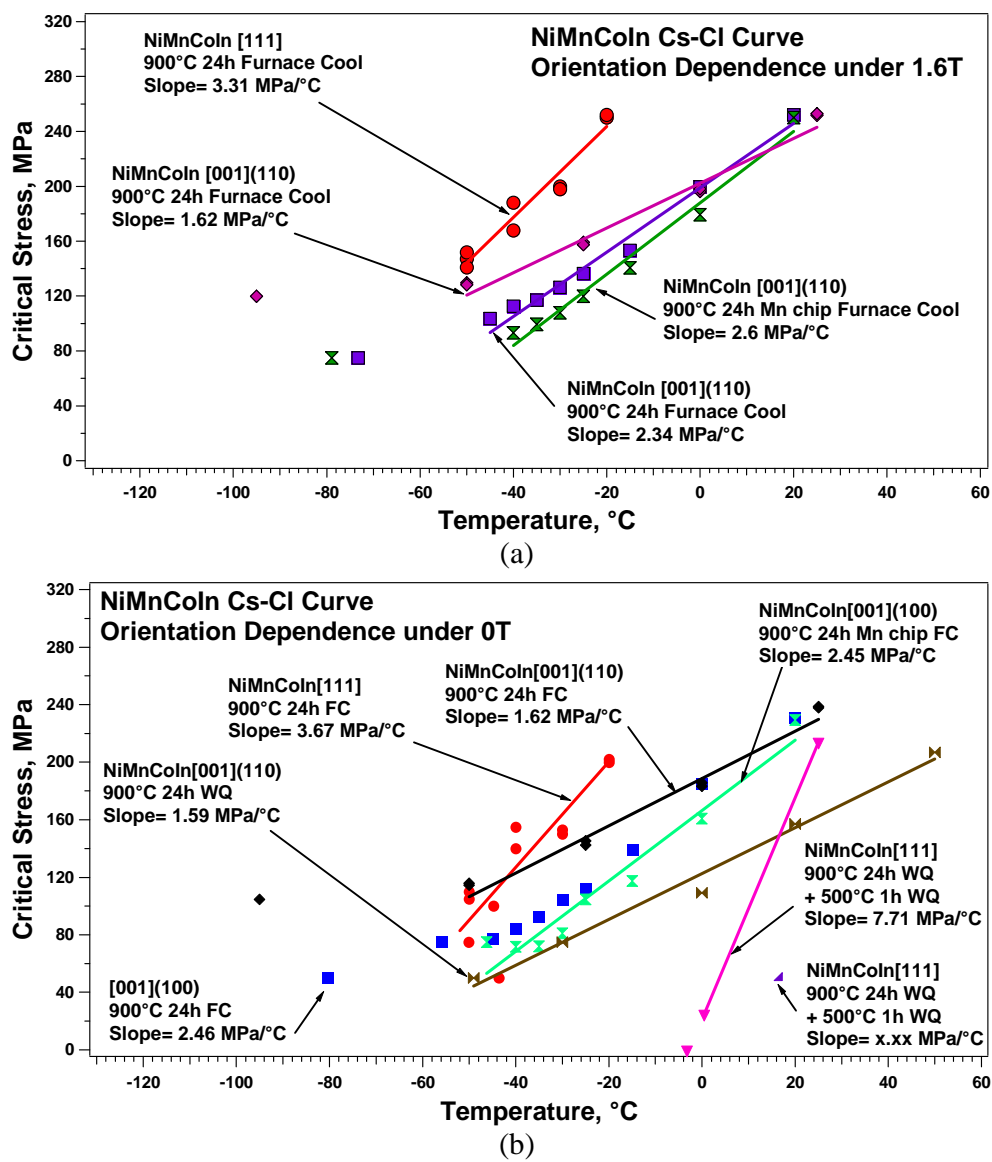


Figure 19. Clausius-Clapeyron relationship showing orientation dependence and effect of magnetic field.

On the powderized specimen, an X-Ray Diffraction examination was carried out with and without an applied magnetic field up to 3 Tesla. The setup utilized was a special design, high field superconducting magnet equipped XRD machine. The aim of this test was to find out the change in lattice parameters of both austenite and martensite phases at different temperatures and applied magnetic field levels, i.e. to track the evolution of martensitic transformation. The martensite manifests itself with emerging extra peaks as the temperature decreases. The applied magnetic field of 3T suppresses the martensite start temperature and helps the austenite peaks persist even at colder temperatures than martensite finish temperature as an indication of kinetic arrest of martensitic transformation (Figure 20).

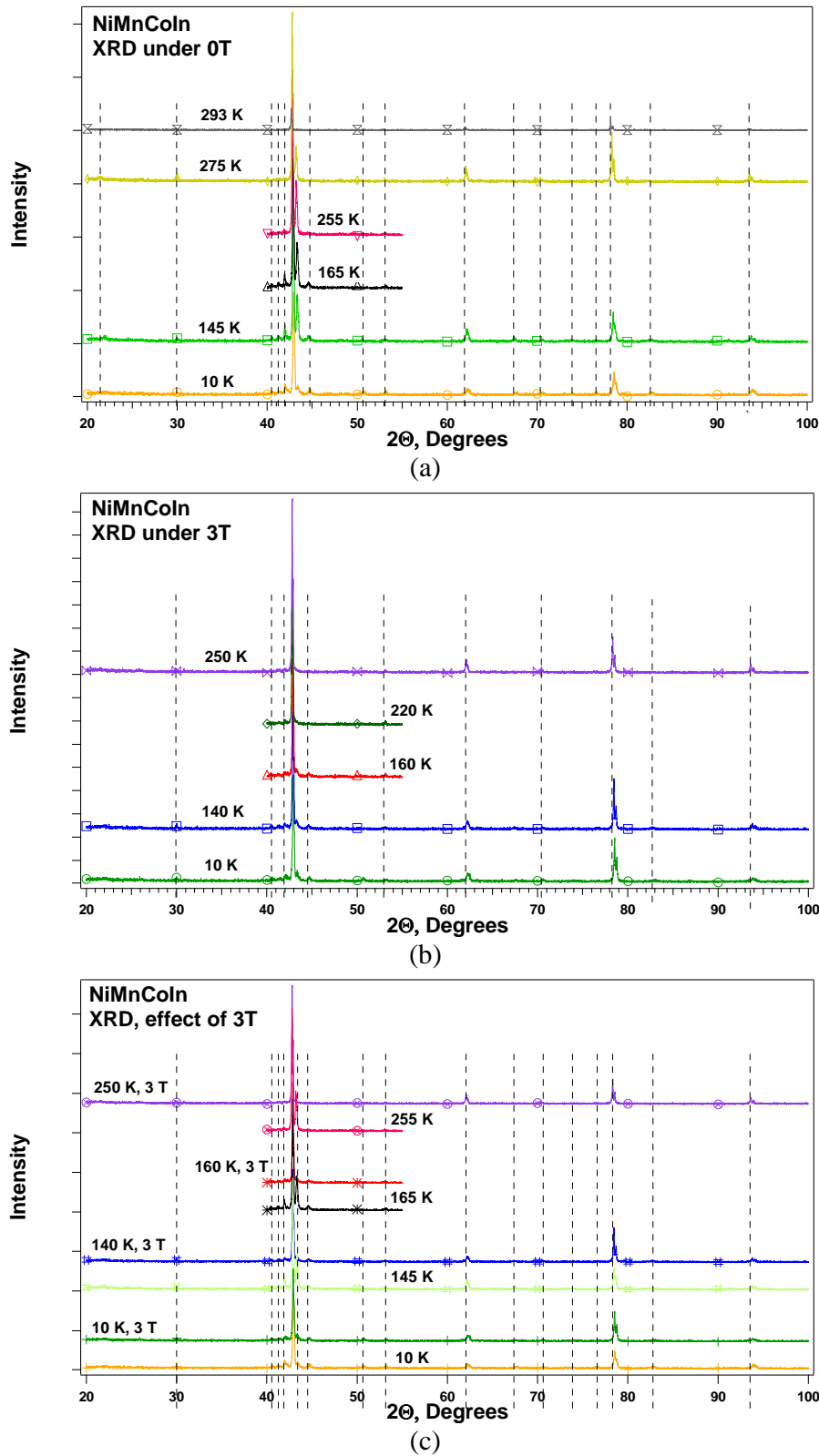


Figure 20. X-ray diffraction patterns indicating change in lattice structure as a function of temperature during phase transformation a) without magnetic field, b) under 3T, c) comparison of same temperature levels with and without magnetic field.

Figure 21 displays the magnetization response (M-T curves) of our bulk $\text{Ni}_{45.7}\text{Mn}_{35.6}\text{Co}_{4.8}\text{In}_{13.8}$ specimen after the aforementioned two step heat treatment by SQUID magnetometer.

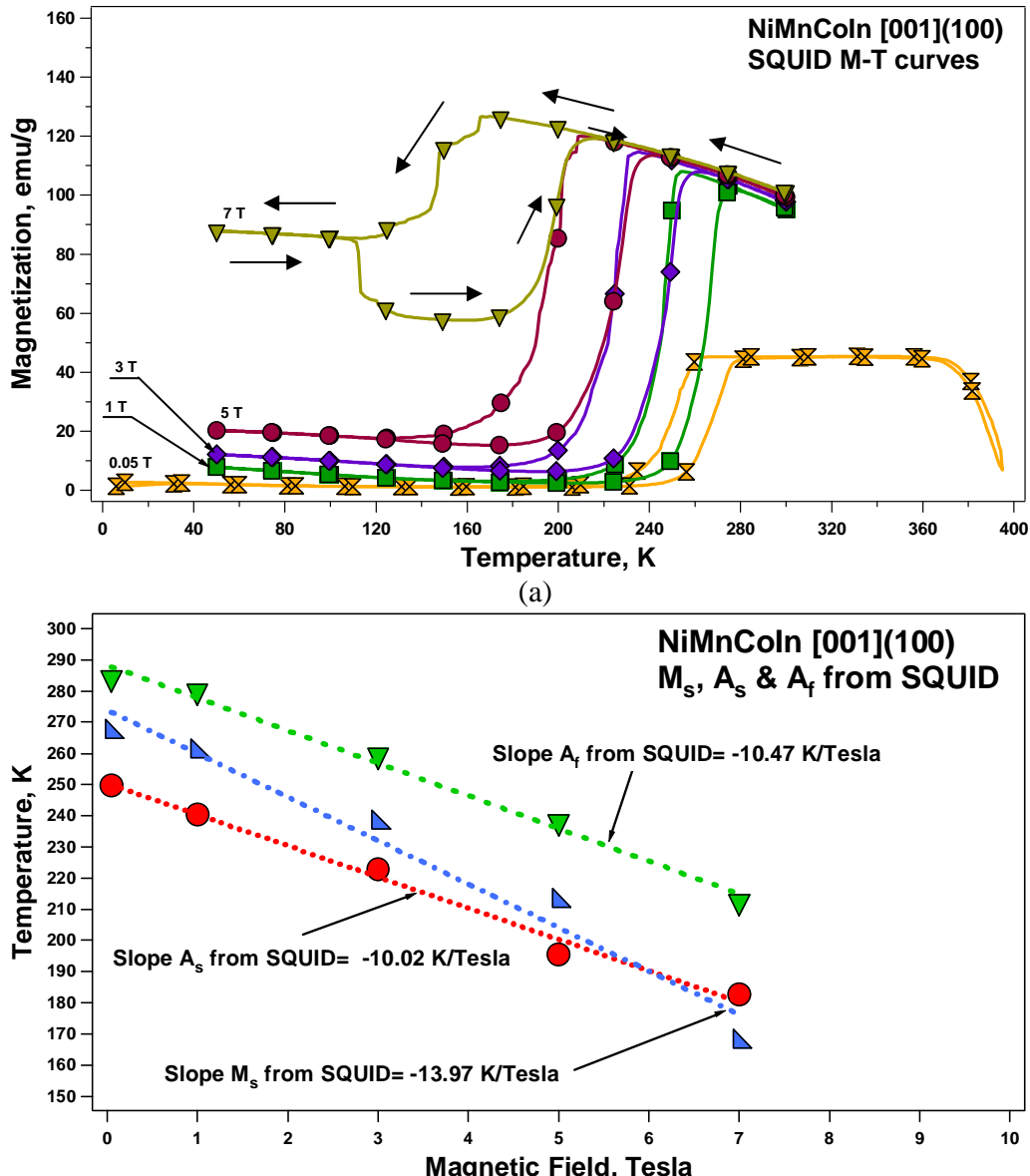


Figure 21. a) Change of magnetization with temperature cycling under different constant magnetic field levels, b) evolution of M_s (martensite start), A_s (austenite start) and A_f (austenite finish) transformation temperatures as a function of applied magnetic field.

From the 0.05 Tesla curve, the approximate values of the forward and reverse transformation temperatures, M_s (martensite start), M_f (martensite finish), A_s (austenite start) and A_f (austenite finish) are observed as 267, 225, 250 and 284 K, respectively. Also, the Curie temperature, T_C , can be approximated as 376 K. It is evident that, with increasing magnetic field, all transformation temperatures are suppressed further from the Curie temperature. Magnetic field

promotes the reverse transformation (P to M, parent to martensite) by making it harder for the weakly magnetic (paramagnetic) martensite to nucleate and/or the martensitic phase front to propagate. Magnetic field promotes the reverse transformation through the magneto-mechanical coupling since it first aligns and eventually merges different magnetic domains in the ferromagnetic austenite. At that point, temperature is the only driving force favoring the martensite for forward transformation (M to P, martensite to parent) to take place. The temperature hysteresis increases linearly up to 5 Tesla with increasing applied magnetic field. Hysteresis is a measure of compatibility between austenite and martensite phases. As stated before, magnetic field energy wise favors the ferromagnetic austenite and makes it harder for weakly magnetic martensite to nucleate and propagate, thus deteriorating the compatibility in between. However, at 7 Tesla, it shows a sudden, much larger increment. This rise can be taken as a sign of the magnetic field reaching at a critical point where incompatibility between magnetic field favored austenite and temperature favored martensite gets pronounced. Furthermore, a sudden, burst like transformation is observed during, P to M, forward transformation right after cooling at around 160K. In SQUID measurements, since stress is not involved, the only driving force for forward transformation is heat. At this relatively colder temperature with respect to $M_s = 225\text{K}$ under 0.005 Tesla, the mobility of the habit plane (that is, the interface between P and M phases) might be decreasing [58], hence causing the intermittent transformation behavior under 7 Tesla. Below M_f temperature, one usually assumes that a shape memory alloy converts into a structure of 100% martensite. On the 0.05 Tesla curve, from 225 K down, the magnetization level of martensite stays fixed at around 1.5 emu/g. This magnetization level value can be taken as granted for the 100% martensitic phase for this NiMnCoIn composition. As the applied field increases, the level of magnetization coinciding at the portions of the M-T curves which remain below M_f , also increases. Aforementioned increment in level of magnetization suggests an incomplete forward transformation even below M_f temperatures, completeness of which is also proportionate to the volume fraction of the remnant austenite. The portrayed phenomenon is called as the kinetic arrest of the austenitic phase and it manifests itself as a result of cooling under magnetic field.

The equilibrium magnetic field H_o , can be given as the arithmetic mean of magnetic martensite start, H^{M_s} and magnetic austenite finish, H^{Af} values. At H_o , the Gibbs Free Energies of P and M are equal to each other. The change of H_o is given as a function of temperature, with and without applied bias stress, in Figure 22.

The magnetic Clausius-Clapeyron relationship can be written as $\frac{dT}{dH} \approx \frac{-\Delta M}{\Delta S}$. Here, ΔM

and ΔS are the differences between austenite and martensite in terms of Magnetization (M) and Entropy (S), respectively. ΔS changes sign from positive to negative, meaning that austenite becomes more stable thermodynamically than martensite in the course of cooling.

This strange development might be due to the (magnetic) contribution by applied magnetic field in the Gibbs Free Energy. Assuming ΔM to be constant, it is possible to argue that a substantial decrease that almost makes ΔS zero is the reason that the quantity, $-\frac{dH_0}{dT}$ approaches to zero. On these terms, the explanation for Kinetic Arrest to happen is the driving force for martensitic transformation, ΔG , to amount to nil, seeing that it is described as $\Delta G = \Delta T \cdot \Delta S$.

On the bulk specimen, the combined effects of changes in temperature, high magnetic field and stress were sought after via a range of magnetization tests, for the first time in magnetic shape memory research. The test setup utilized was an 18 Tesla Extraction Type Magnetometer, in the High Field Laboratory for Superconducting Materials of the Institute for Materials Research, Tohoku University, Japan. In order to apply the required bias stress under the high

magnetic field provided by the 18 Tesla superconducting magnet at a broad test temperature range of 4.2K–245K, we designed a micro stress-stage. This portable, spring loaded, screw driven gadget was precisely manufactured out of a precipitation hardened copper-beryllium alloy and was attached at the end of the extraction train of the magnetometer. Bias stress levels of 75 and 125 MPa were exerted on the specimen subsequent to a set of tests under no stress.

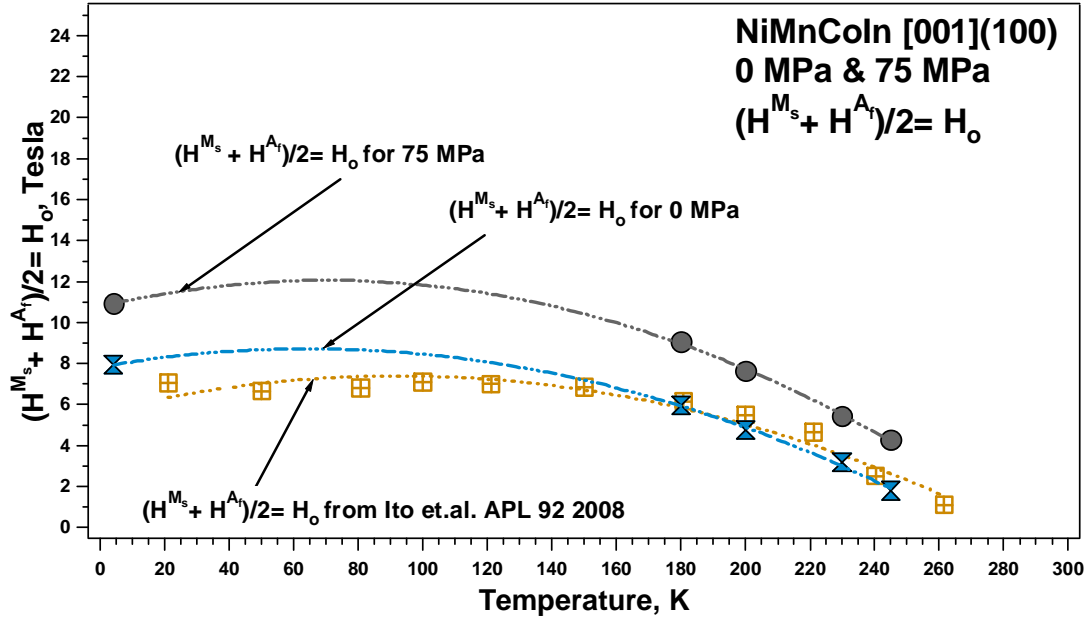


Figure 22. Effect of applied stress on the change of equilibrium magnetic field as a function of temperature.

All the experiments, with and without stress, were conducted at temperatures of 4.2, 180, 200, 230 and 245K, respectively. During each test, the magnetization response of the specimen was recorded while the applied magnetic field changed from 0.05 Tesla up to 18 Tesla and back. In case that full recovery of the magnetization loop was not accomplished in the previous experiment, prior to application of magnetic field the specimen was first cooled down to 100K under zero field to restore the fully martensitic structure and then was heated up to the designated temperature for the next M-H curve.

Figure 23 shows the magnetization response of the [100] oriented NiMnCoIn single crystal under compressive stress levels of 0 and 75MPa at the above mentioned temperatures. In Figure 23a, it is clearly seen that saturation levels of magnetization for austenite decreases with increasing temperature. When compared to SQUID results (since both are under 0MPa), it is in good agreement. As the test temperature nears the Curie temperature, the capability of austenite to get magnetized (i.e., level of its ferromagnetism) weakens. This explains the reduction in the level of saturation magnetization of austenite. Furthermore, increasing temperature suppresses critical magnetic field points of transformation (which are austenite start, H^{A_s} ; austenite finish, H^{A_f} ; martensite start, H^{M_s} and martensite finish, H^{M_f} , respectively) towards lower values. This is expected since rise in temperature provides extra chemical energy to help magnetic field favored reverse (M to P) transformation take place earlier.

At the beginning of each M-H curve, in the segments prior to H^{A_s} , magnetization levels of martensite alter from 10 emu/g to almost 30 emu/g as the temperature goes up from 180K to 245K. This change happens in a monotonic trend for all temperature levels, except for the 4.2K test. The rise in magnetization level of martensite indicates that a very small volume fraction of it

is starting to transform into austenite because of the going up test temperature. Magnetic hysteresis (refer to Figures 25 and 26) also displays a monotonic decrease and almost saturates at 2T for 0MPa.

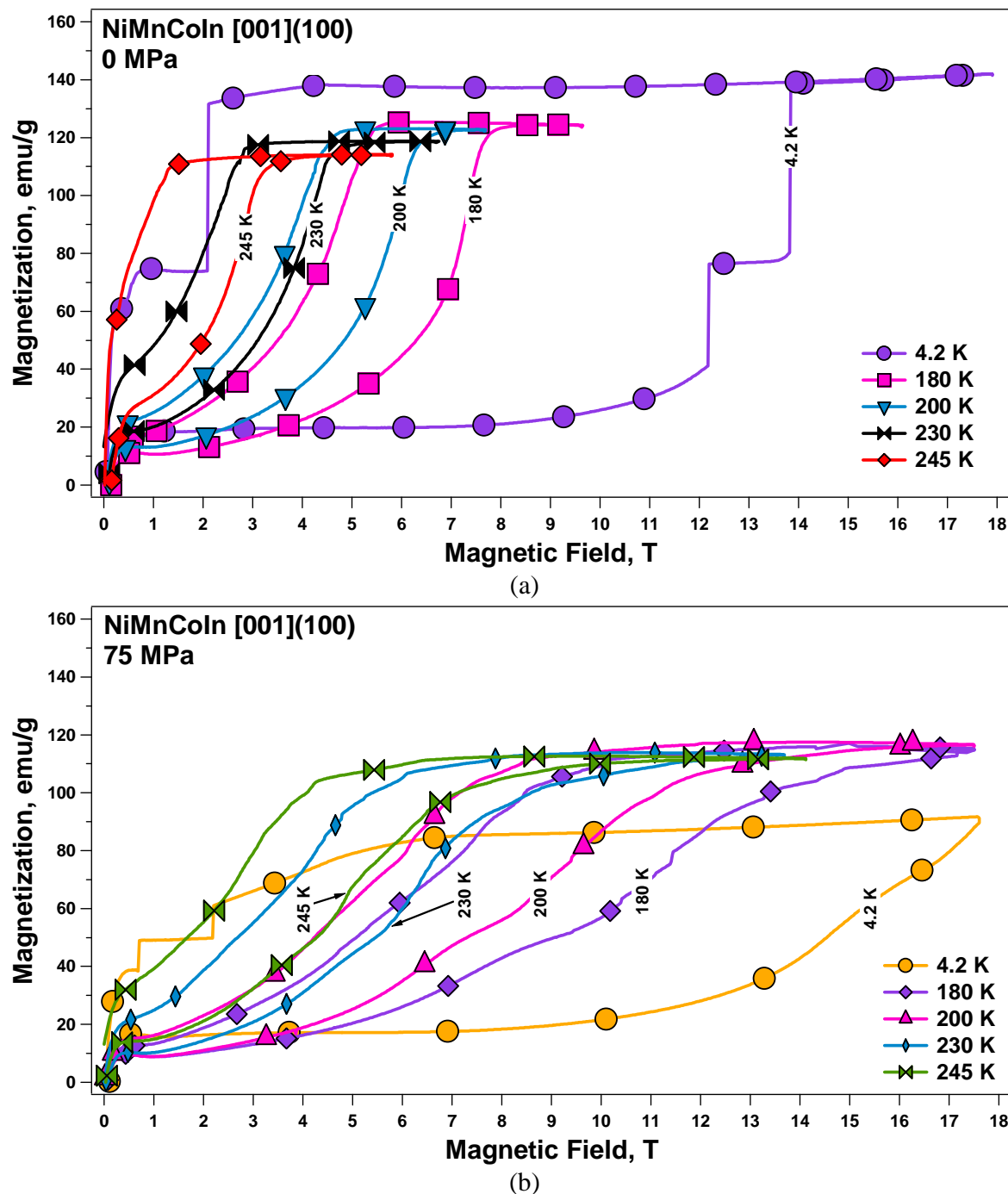


Figure 23. a) M-H curve showing the change in magnetization as a function of applied magnetic field at different levels of constant temperature from 4.2K to 245K, b) effect of applied stress included to the former.

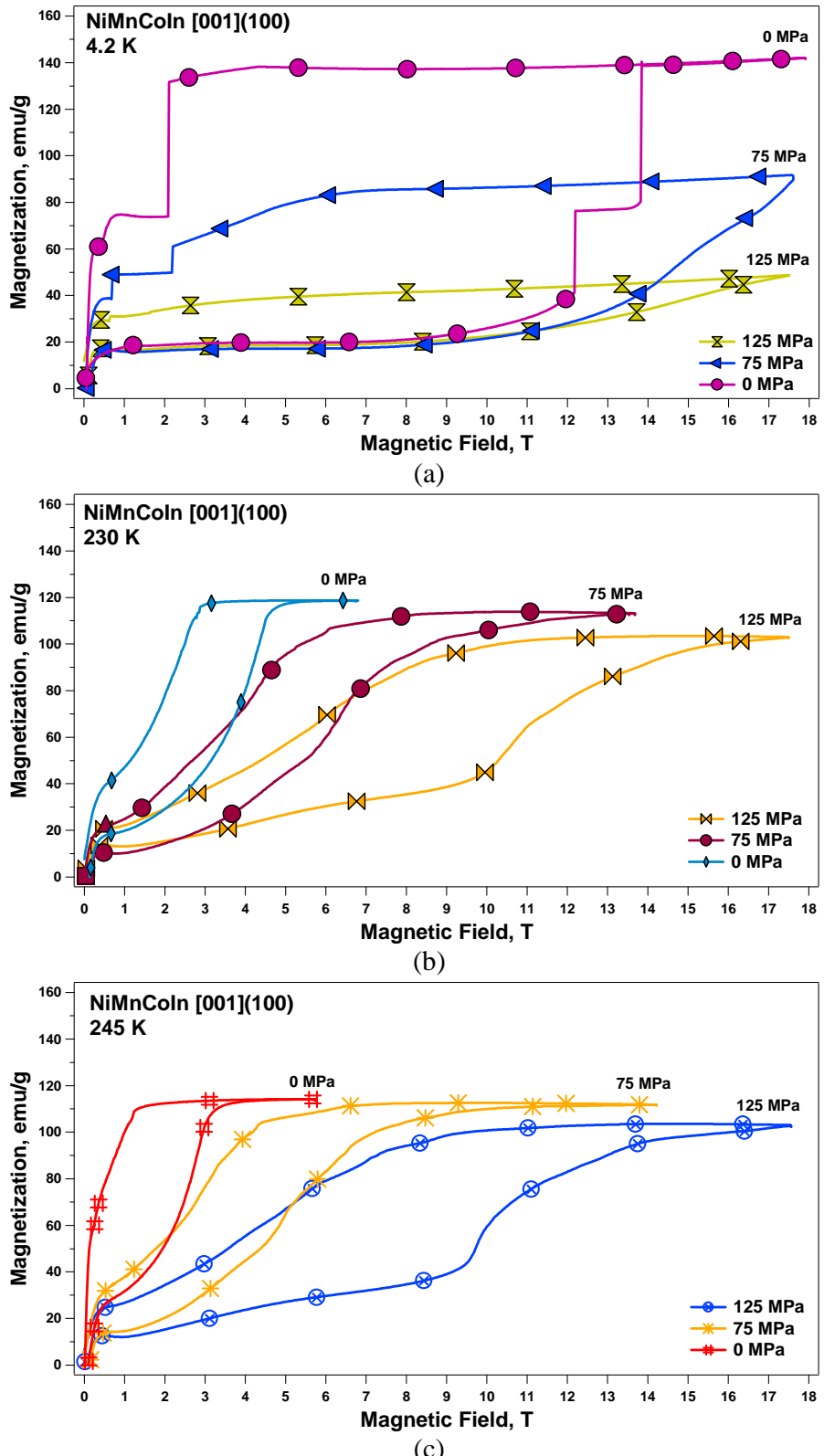


Figure 24. M-H curves showing the change in magnetization as a function of applied magnetic field under different levels of applied stress at; a) 4.2K b) 230K and c) 245K.

At all levels of temperature, it is evident from Figure 24 that stress suppresses the magnetization levels of both austenite and martensite. On the side of austenite, this declination can be attributed to an incomplete reverse transformation (M to P) since stress favors forward (P to M) transformation. Finally, after H^{Af} , the product that mainly consists of austenite saturates at a lower magnetization value compared to that of stress free reverse transformation.

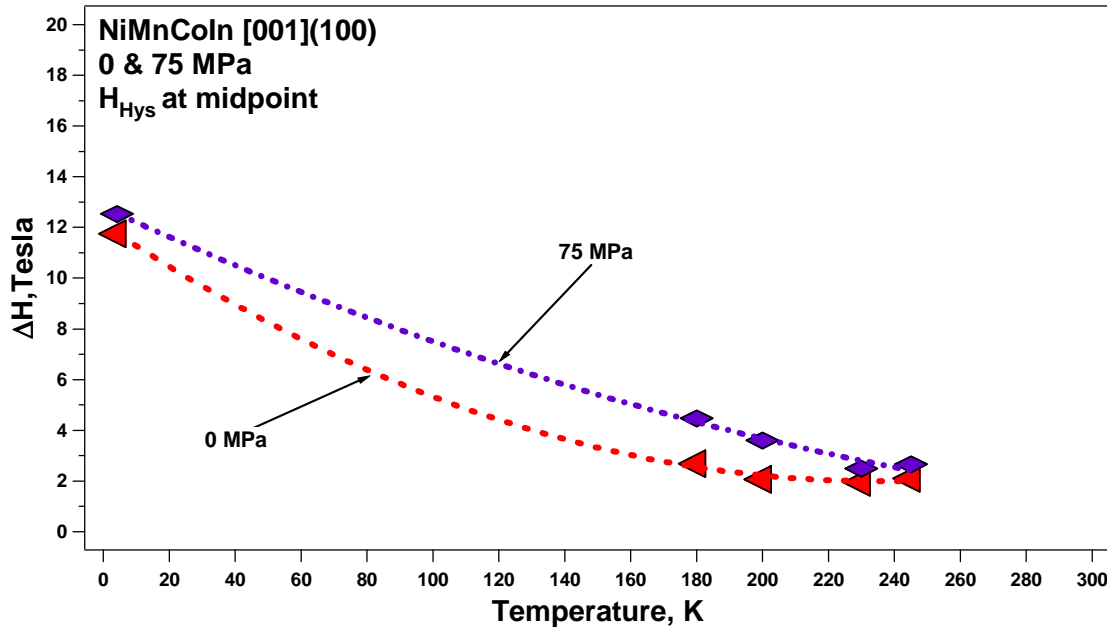


Figure 25. Change in magnetic field hysteresis as function of temperature under 0MPa and 75MPa applied stress.

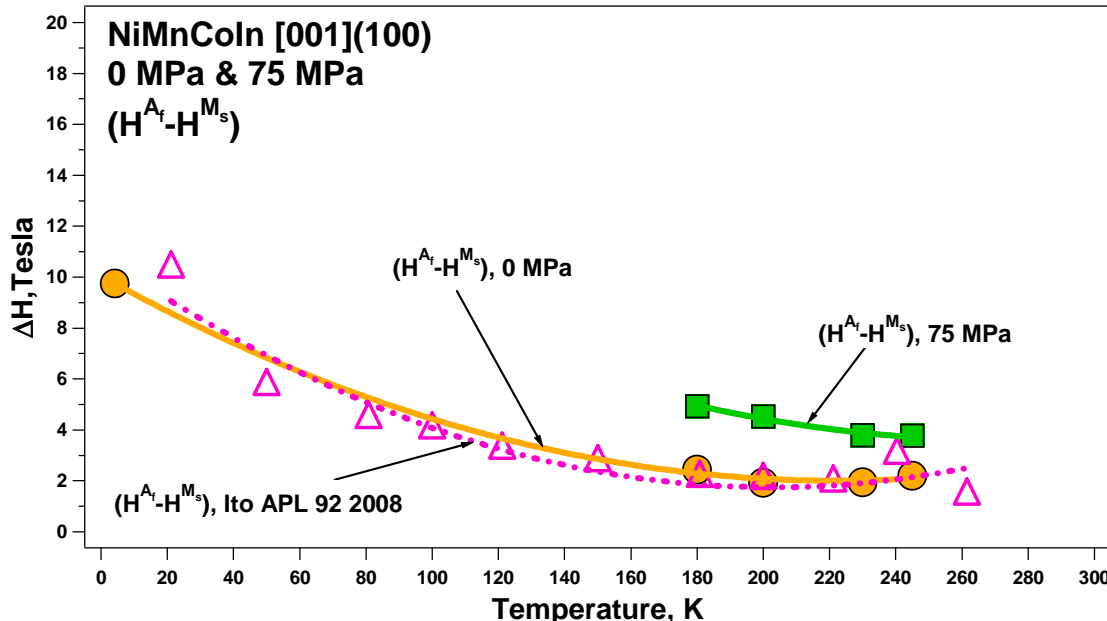


Figure 26. Change in magnetic field hysteresis as function of temperature under 0MPa and 75MPa applied stress.

The martensitic structures which form under influence of stress, both at the beginning of reverse transformation and at the end of forward transformation, are detwinned. It was recently revealed that the martensite phase is paramagnetic in NiMnIn based alloys [58]. Application of stress detwinds the self accommodated initial structure and as can be easily seen in Figure 24b and c. It seems that self accommodated martensite is more compatible with austenite than stress biased detwinned martensite is. This is evident from increasing magnetic hysteresis in Figure 24b and c. Figure 25 and Figure 26 are derived from the M-H curves and represent the tendency of magnetic hysteresis as a function of temperature under applied bias stress. They are plotted using two different techniques in order to have a comparative idea. Both figures agree that bias stress enlarges the magnetic hysteresis since it raises the level of incompatibility between martensite and austenite due to rising internal friction.

Figure 27 shows the magnetic Clausius-Clapeyron. It simply represents the trend of change in critical magnetic field points of transformation, H^{Af} , H^{Ms} , H^{As} as a function of temperature, respectively, and the effect of stress on this tendency. These results are also listed in Table 5. It can be seen that stress increases the relative slope for all, i.e., makes it especially harder for reverse transformation to occur.

Table 5. Clausius-Clapeyron Slopes under stress

	Slope, H^{Af}	Slope, H^{Ms}	Slope, H^{As}
0 MPa	-10.47 K/Tesla	-13.97 K/Tesla	-10.02 K/Tesla
75 MPa	-11.46 K/Tesla	-14.71 K/Tesla	-11.85 K/Tesla
125 MPa	-17.24 K/Tesla	-17.47 K/Tesla	-14.26 K/Tesla

1.1.14. In-situ Neutron Diffraction Measurements

In order to understand the change in lattice parameters during kinetic arrest of martensitic transformation, we recently started collaboration with Los Alamos National Lab. $\text{Ni}_{45.7}\text{Mn}_{35.6}\text{Co}_{4.8}\text{In}_{13.8}$ single crystalline specimen was exposed to neutron beams in the presence of a magnetic field ranging from 0 to 1.85T. In order to observe Kinetic Arrest, the specimen was cooled under the mentioned magnetic field levels. Neutron diffraction patterns were acquired at various temperatures during both heating and cooling. Figures 28-30 below show the preliminary results achieved from the first attempts.

Figure 28a and 28b present the fitted curves to austenite and martensite raw data, respectively. Very similar to x-ray diffraction, austenite has fewer neutron diffraction peaks compared to those of martensite.

Figure 29 shows the evolution in austenite phase fraction as a function of temperature, with or without a bias magnetic field, by tracking a selected peak (400). Likewise, Figure 30 depicts the progression in martensite phase fraction as a function of temperature, with or without a bias magnetic field, by tracking another selected peak. Both results confirm suppression of transformation temperatures by applied magnetic field. We will continue the same experiments including the bias stress in the near future to shed light on the change in lattice parameters of austenite and martensite phases during transformation hence understand the volume fractions of remnant austenite in martensite due to kinetic arrest in the M-H curves from the experiments in Japan.

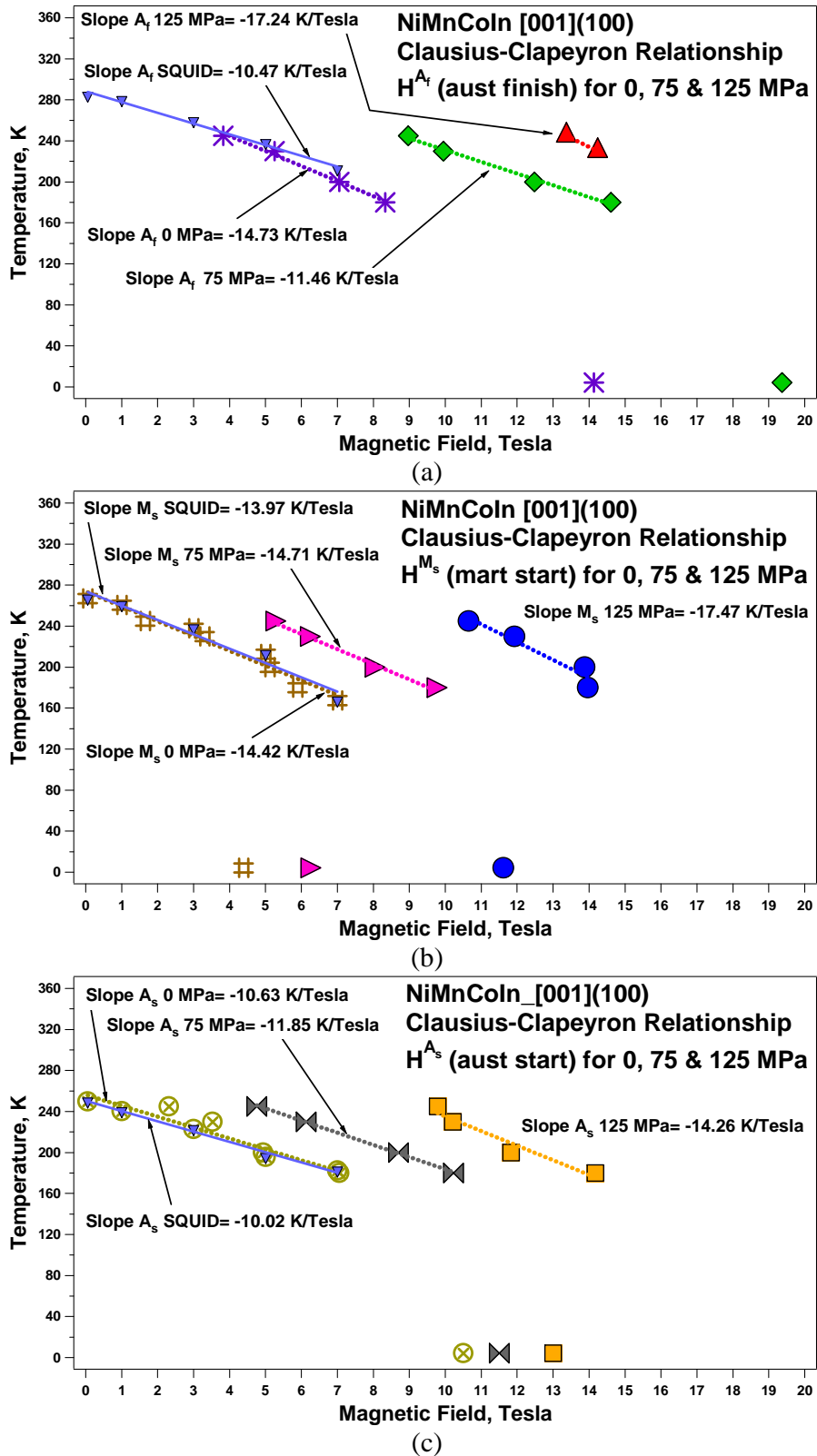


Figure 27. Clausius-Clapeyron relationship under stress for; a) H^{A_f} , magnetic field for austenite finish b) H^{M_s} , magnetic field for martensite start c) H^{A_s} , magnetic field for austenite start.

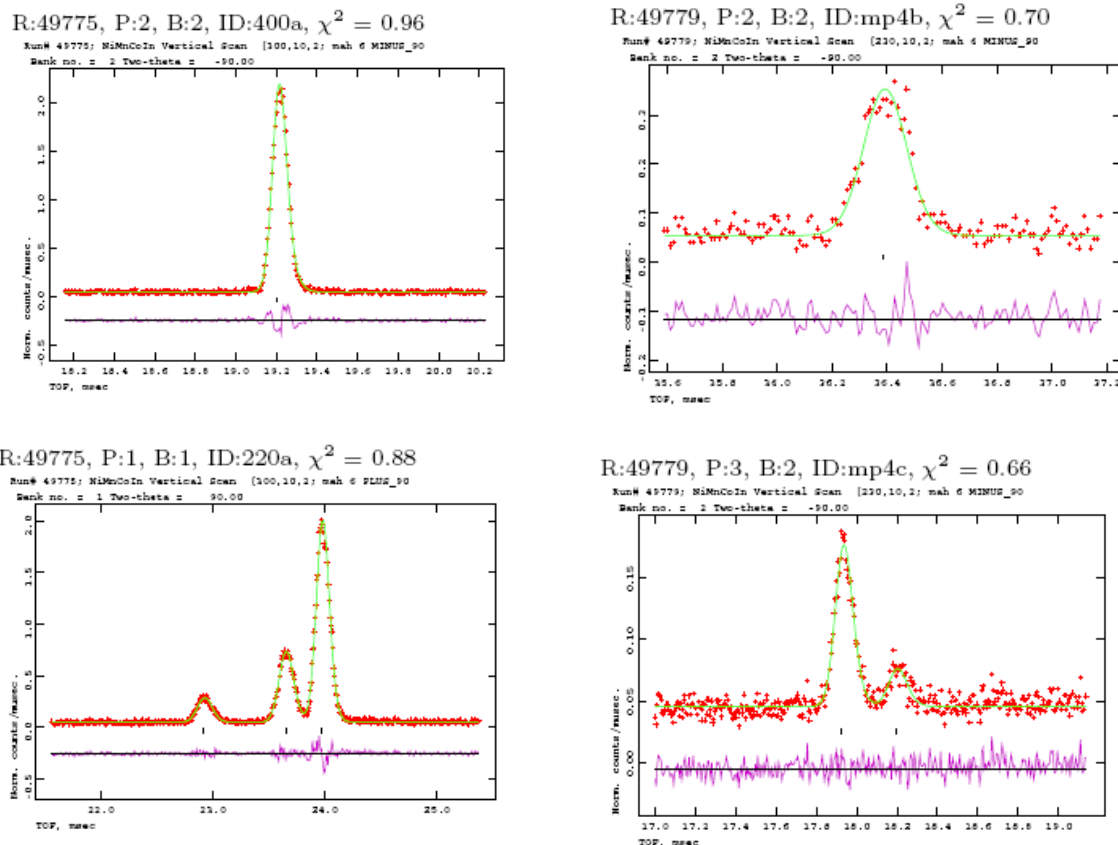


Figure 28. Examples of a) austenite peak fits, b) martensite peak fits.

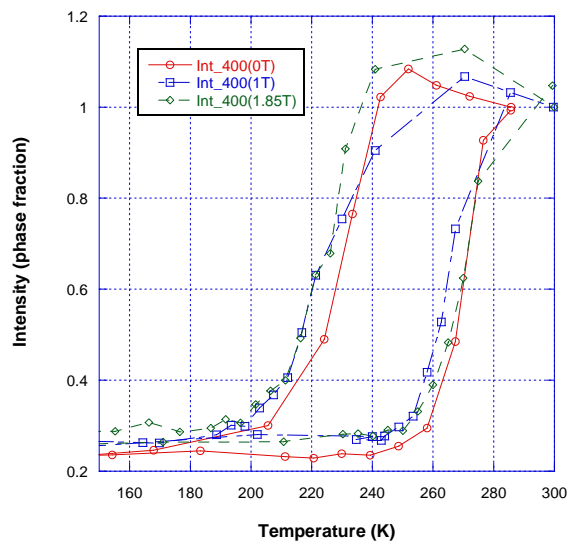


Figure 29. Comparison of Austenite phase fraction with magnetic field

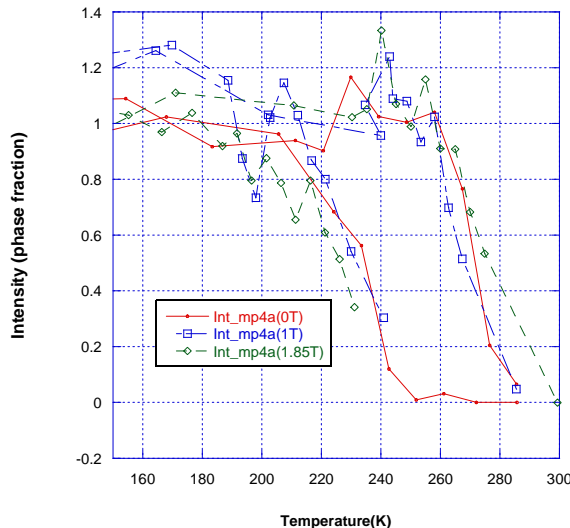


Figure 30. Comparison of Martensite phase fraction with magnetic field

1.2. NiFeGa MAGNETIC SHAPE MEMORY ALLOYS

1.2.1. Specimen Preparation

An ingot of NiFeGa with a nominal composition of $\text{Ni}_{54}\text{Fe}_{27}\text{Ga}_{19}$ (at. %) was prepared using vacuum induction melting. Single crystals were grown using Bridgman technique in He atmosphere. Samples were cut into 4 mm x 4 mm x 8 mm rectangular prisms by EDM. Compressive stress was applied along [001], [123] and [011] directions of the parent phase. Differential scanning calorimetry (DSC) response of $\text{Ni}_{54}\text{Fe}_{27}\text{Ga}_{19}$ single crystal is given in Figure 31. The transformation temperatures; Martensite start (M_s), martensite finish (M_f), austenite start (A_s) and austenite finish (A_f) can be determined as 3.5, -7, 7 and 14°C, respectively. Note that thermal hysteresis $\{(A_f - M_s)/2\}$ is very low (8.75°C).

1.2.2. Shape Memory Effect (SME) under Constant Stress

Figure 32a, b and c show the strain vs. temperature response of [100], [123] and [110] orientations, respectively, under constant applied compression stress. The stress is isothermally applied when the sample is in austenite phase. Next, the sample is thermally cycled between a temperature below M_f and a temperature above A_f under applied constant stress. When the cycle is completed, the stress is increased further and thermal cycling is repeated. During cooling if null or a low level stress is applied then a self accommodating structure appears which results in a net axial strain of zero. However, if cooling is realized under high applied stress levels, one favorable martensite variant forms and consequently grows at the expense of the other rival variants outcome of which is a net shape change.

From Figure 32, it is clear that as applied stress increases transformation occurs at higher temperatures. This behavior is expected and is governed by Clausius-Clapeyron (CC) equation. The following can be clearly seen in Figure 32:

- i) Temperature hysteresis and shape memory strain levels are orientation dependent,
- ii) Temperature hysteresis is narrow,

- iii) Shape memory strain level decreases as a function of applied stress.

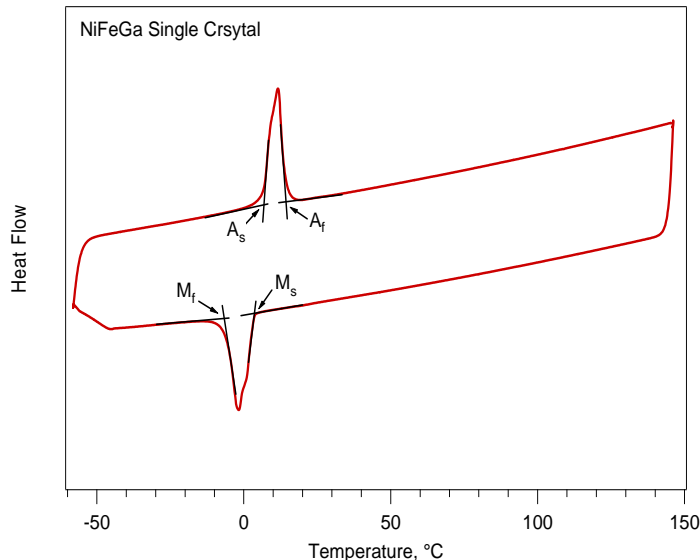


Figure 31. DSC response of a NiFeGa single crystal, displaying transformation temperatures; M_s , M_f , A_s and A_f determined by line intersection method.

In [110] orientation, temperature hysteresis is narrower compared to those of [100] and [123] orientations at low stress levels; however, it increases considerably with stress and a burst type transformation occurs at high stress levels in comparison with gradual transformation at low stress levels. On the other hand, for [110] orientation, transformation strain first decreases in a similar fashion as in the other two orientations, but when a critical level of applied stress is reached it increases from that point on.

1.2.3. Pseudoelastic Response as function of Temperature

Figure 33a, b and c display the incremental pseudoelastic response as a function of temperature along the [100], [123] and [110] orientations, respectively. For all these three orientations, the critical stress for phase transformation increases with increasing temperature and perfect pseudoelastic behavior is possible to observe along all. It is also evident from Figure 33 that stress hysteresis raises with increasing transformation strain. Also, as the test temperature gets higher, the transformation takes place with a more pronounced hardening. The critical stress for slip can be determined as 1100, 320, 450 MPa for [100], [123] and [110] orientations, respectively (not shown). The high strength for dislocation slip along the [100] orientation is attributed to the curtailing of active slip systems, $\{1\bar{1}0\}\langle001\rangle$ and $\{100\}\langle001\rangle$ slip systems in B2 structure [59]. The compression along the [100] orientation results in high strength and M_d temperature in NiFeGa alloy similar to Co based shape memory alloys [60-61].

It is also important to note that, there is a two-stage phase transformation along the [110] orientation at 22°C. At 22°C austenite transforms to the 1st martensitic phase around 76MPa. Subsequently, an intermartensitic transformation starts at 200 MPa followed by the elastic deformation of the 2nd martensitic phase. During unloading, 2nd martensitic phase transforms back to the initial martensitic phase which also transforms back to austenite as the stress diminishes. Multiple phase transformations in NiFeGa has already been reported [62-64] and it is a well-known phenomena that occurs in many conventional shape memory alloys [65-67]. For test temperatures higher than 22°C, it is harder to distinguish the fore mentioned two stage

transformation. Yet, the transformation strain levels indicate that the final product is the 2nd martensitic phase at all other test temperatures. The variation in transformation behavior observed during shape memory effect experiments as a consequence of the applied stress can as well be attributed to creation of these different martensitic structures.

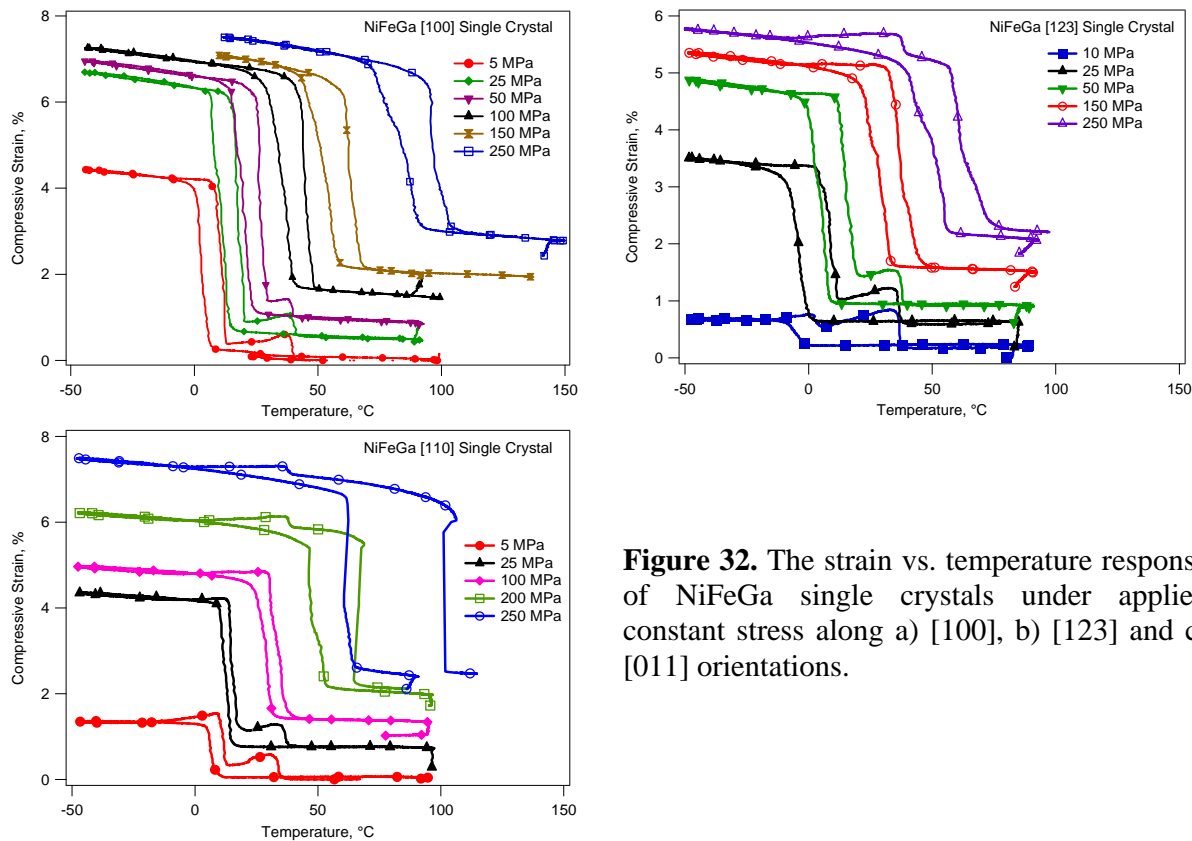


Figure 32. The strain vs. temperature response of NiFeGa single crystals under applied constant stress along a) [100], b) [123] and c) [011] orientations.

1.2.4. Shape Memory Characteristics of NiFeGa Alloys as Function of Stress, Temperature and Orientation

To begin with, we demonstrate the techniques how to determine:

- i) Critical stress for phase transformation (σ_c),
- ii) M_s and M_f temperatures,
- iii) Transformation Strain for shape memory effect (ε_{SME}),
- iv) Transformation strain for pseudoelasticity (ε_{PE}),
- v) Temperature hysteresis,

The schematic in Figure 34a illustrates how the pseudoelastic strain (ε_{PE}) is determined for the pseudoelastic response experiments as a function of temperature. Linear lines are drawn to the loading portion of the curve in austenite phase and to the unloading portion of the curve in martensite phase to determine Young's Modulus of austenite (E_A) and martensite (E_M), respectively. Another line parallel to the plateau portion of the curve is drawn between these two lines representing the moduli. This way, as portrayed in the schematic, it is possible to determine the pseudoelastic strain values both in the plateau region (ε_{PE}) and under zero stress (ε_{PE}^0). In order to determine the level of the Critical Stress for forward transformation, the line drawn to

represent E_A is offset 0.2% to the right to intersect the pseudoelastic curve, so that the intersection gives the critical level which is sought for.

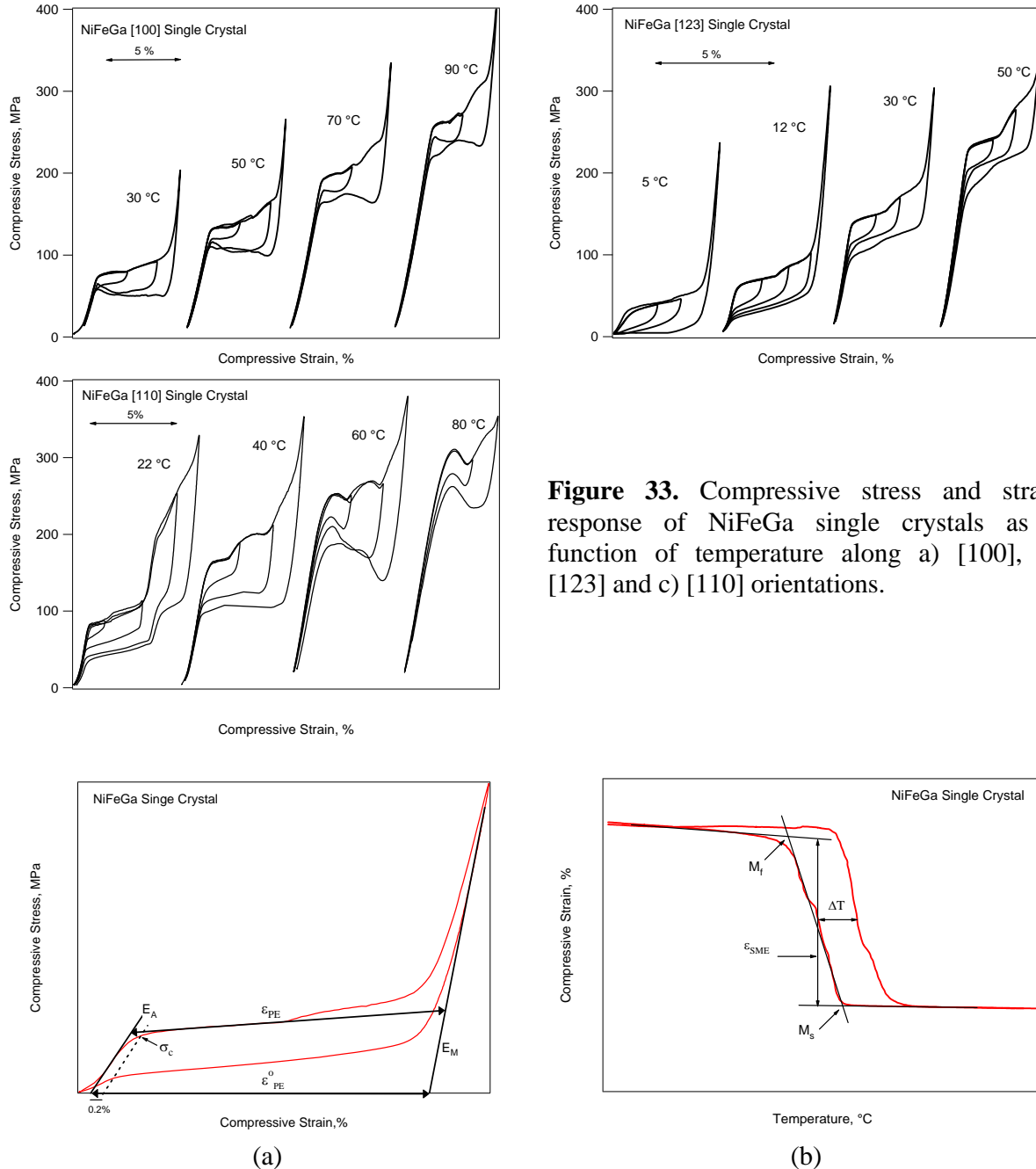


Figure 33. Compressive stress and strain response of NiFeGa single crystals as a function of temperature along a) [100], b) [123] and c) [110] orientations.

Figure 34. a) A schematic showing how the Young's modulus of austenite and martensite, pseudoelastic strain at the plateau region and under no stress is determined from the pseudoelastic response, b) A schematic for determining transformation strain and temperature hysteresis, martensite start and finish temperatures from cooling-heating curves under stress.

The schematic in Figure 34b describes the way to determine the transformation strain (ε_{SME}) and temperature hysteresis (ΔT) from shape memory effect (heating/cooling) experiments under constant applied stress. The shape memory strain as a function of applied stress level is measured

at $(M_s + M_f)/2$ between the extrapolated thermal expansion strain lines of parent and martensite phases. The temperature hysteresis is determined by drawing a tie line between the forward and backward transformations at which 50% of the phase transformation is completed.

Following these guidelines listed above, the information below were deduced from the experimental results:

1.1.5. Stress vs. Temperature Phase Diagram for the NiFeGa Alloy

Figure 35 shows the martensitic transformation start temperature as a function of applied stress, extracted from thermal cycles shown by Figure 32, and critical stress for forward transformation as a function of test temperature, extracted from pseudoelastic responses shown by Figure 33. For all orientations, as temperature increases critical stress for phase transformation increases and vice versa. The linear correlation between stress and temperature is known as Clausius-Clapeyron (CC) Relation. From SME experiments, the maximum transformation strains are determined to be 5.57%, 3.68% and 3.38% along [100], [123] and [110] orientations, respectively. The CC slope along [100] orientation is the lowest, 2.97 MPa/ $^{\circ}$ C, since it has the highest transformation strain. The CC slopes are 4.39 MPa/ $^{\circ}$ C and 4.64 MPa/ $^{\circ}$ C along [123] and [110] orientations, respectively.

In Figure 35, the critical stress values for 2nd transformation along [110] orientation are also shown. The first martensitic phase transforms to another martensitic phase when the applied stress is increased further and it transforms back to initial martensitic phase when the applied stress is removed. The 1st stage transformation has a negative CC slope of -0.65 MPa/ $^{\circ}$ C. The negative slope for intermartensitic transformations has already been reported and it is due to negative enthalpy change during phase transformation [68].

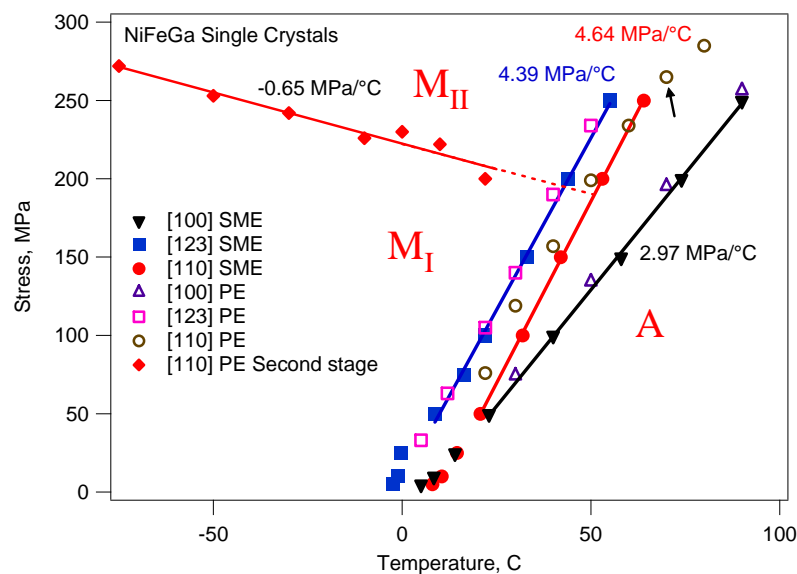


Figure 35. Stress vs. temperature phase diagram of NiFeGa single crystals. Transformation start temperatures and critical stress values are extracted from Figures 32 and 33, respectively, by following the guidelines shown in Figure 34. The stable phase regions along [100] orientation are also presented in this stress vs. temperature phase diagram.

The stable phases for [110] are depicted as: M_I, the 1st martensitic phase; M_{II}, the 2nd martensitic phase and A, austenite phase. It should be noted that a few points towards the end of the 1st stage [110] PE curve (open circles), slightly deviate from the general tendency (slope) of

that imaginary line right after the CC lines for 1st and 2nd stages intersect each other. The start of the deviation is marked clearly by an arrow in the figure and is attributed to the fact that after this certain critical stress level, austenite directly transforms to the 2nd martensitic phase which has a higher transformation strain resulting in a lower CC slope in magnitude.

1.2.6. Transformation Strain from SME and PE Curves

From Figure 32, it is possible to pull out transformation strain of shape memory effect, ϵ_{SME} as a function of applied stress following the methods described in Figure 34b. Similarly, transformation strain of pseudoelasticity, ϵ_{PE} , can be extracted from Figure 33 and determined after Figure 34a. In order to be able to compare ϵ_{SME} with ϵ_{PE} , they are plotted together in Figure 36. Since it is difficult to determine the critical stress level and transformation strain for the 2nd martensitic transformation along [110] orientation separately, the total pseudoelastic transformation strain after the 2nd stage transformation is plotted against critical stress for the 1st stage transformation.

Shape memory effect strains for all orientations increase with increasing applied stress at lower region of stress due to formation of single variant instead of multiple variants. The transformation strain reaches peak values of 5.57% at 25MPa, 3.38% at 50MPa and 3.68% at 25MPa along [100], [123] and [110] orientations, respectively. The differences in these peak stresses are attributed to the need of different bias stress values for single variant formation in each orientation. After the peak value is reached, the transformation strain decreases linearly with increasing stress for all three orientations. The reduction is more pronounced along [100] orientation as transformation strain decreases from 5.57% to 3.78% when stress increases from 25MPa to 250MPa. In [110] orientation, the transformation strain increases after 150MPa which is attributed to the formation of 2nd martensitic phase.

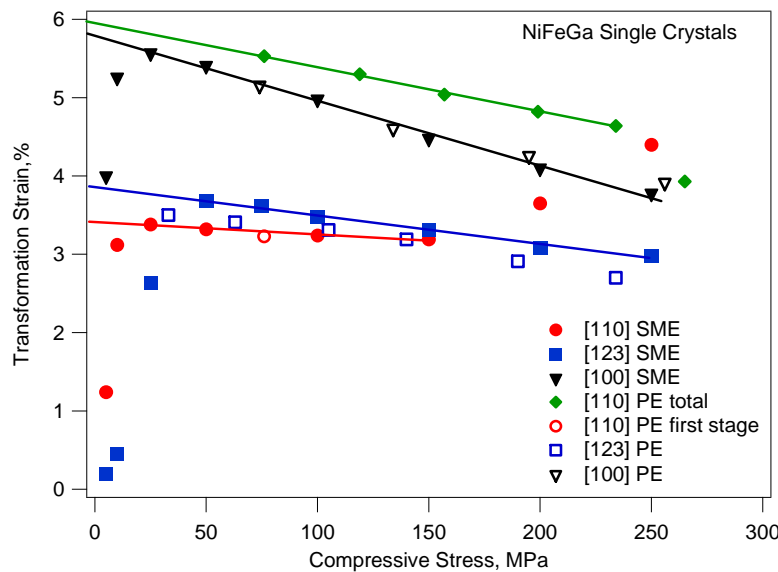


Figure 36. Transformation strain vs compressive stress for three orientations determined by using schematics shown in Figure 33a.

The superposed ϵ_{PE} values fit nicely to ϵ_{SME} values along [100] and [123] orientations where they also decrease with increasing stress (or temperature). For [110] orientation, ϵ_{PE} for the 1st stage is the same ϵ_{SME} as expected and the ϵ_{PE} for the 2nd stage transformation is the highest amongst all orientations. Also note that, around 150 MPa, the ϵ_{SME} and ϵ_{PE} have almost the same

values. This may be a sign of the fact that as applied stress increases, austenite transforms to 2nd martensitic phase instead of 1st martensitic phase along [110] orientation.

In order to obtain the transformation strain under zero stress, a linear fit line is drawn for ε_{SME} values along the three orientations and ε_{PE} for the total transformation strain along the [110] orientation. It is found that phase transformations under 0 MPa are expected to be 5.78% for [100], 3.86% for [123], 3.4% after the first stage transformation and 5.95% for the total strain along [110] orientation. Moreover, the decrease in strain with temperature is determined to be 0.0082, 0.0037, 0.0015 and 0.0056 %/MPa along the [100], [123], 1st stage [110] and 2nd stage [110] orientations, respectively.

The change in pseudoelastic transformation strain with temperature has not attracted enough attention so far. It has been reported that pseudoelastic strain increases with temperature in NiTi alloys while it decreases considerably in Co based alloys [60-61, 69-70]. In our study, as shown in Figure 36, transformation strain decreases with temperature in pseudoelastic response and with applied stress in shape memory response, in both cases independent of orientation. Nevertheless, decrease in transformation strain is crystal structure dependent since the decrease in transformation strain with temperature is different for the transformation after 1st and 2nd stages along [110] orientation.

The decrease in transformation strain under the influence of stress or temperature can be attributed to two different causes:

- i) Change in lattice constants with temperature and stress
- ii) Change in Young's Modulus of transforming phases with temperature.

If the change in lattice parameters with temperature is neglected, we can approximate the observed pseudoelastic transformation strain as;

$$\varepsilon_{PE} = \varepsilon_o - \frac{\sigma_c}{E_A^T} + \frac{\sigma_c}{E_M^T} \quad (6)$$

where ε_o is the transformation strain under no stress, E_A^T is the Young's Modulus of austenite and E_M^T is the Young's Modulus of martensite at temperature T and σ_c is the critical stress for transformation. The change in Young's Modulus with stress is also neglected in this equation. At 30 °C, for the [100] orientation Equation 6 can be written as

$$\varepsilon_{PE} = 5.78 - \frac{74 \text{ MPa}}{7.34 \text{ GPa}} - \frac{74 \text{ MPa}}{30.2 \text{ GPa}} = 5.02 \% \quad (7)$$

The experimental value of ε_{PE} is 5.16% which is close to the calculated value. The error can be attributed to the assumption of no change in lattice parameters with temperature and probably an inaccurate determination of transformation strain due to hardening behavior in the plateau region.

From Equation 6 the orientation dependence of decrease in transformation strains with stress is attributed to the difference in Young's modulus of austenite and martensite phases. E_A is determined to be 7.34, 19.7 and 12.6 GPa where E_M is 30.2, 45 and 38.4 (second stage) GPa along the [100], [123] and [110] orientations, respectively.

If we calculate

$$\frac{\varepsilon_o - \varepsilon_{PE}}{\sigma} = \frac{1}{E_A^T} - \frac{1}{E_M^T} \quad (7)$$

for three orientations we will get, 0.0103, 0.0028, 0.0053%/MPa along [100], [123] and [110] orientations, respectively. These rates correlate with the experimentally observed trends as shown

by Figure 36. The decrease of transformation strain with temperature reaches a maximum along [100] orientation and a minimum along [123] orientation.

The observed rise in pseudoelastic strain with temperature in some alloys (e.g. NiTi) can be explained by Equation 6. If austenite has higher Young's modulus than martensite as in the case of NiTi alloy [71] then ε_{PE} will be larger than ε_o . The more pronounced change in pseudoelastic strain in NiFeGa and Co based SMAs is due to their very low Young's Modulus of austenite where in some cases more than 2% of elastic strain can be obtained prior to transformation. Figure 32a shows that for [100] orientation which possesses the lowest Young's modulus, the elastic strain reaches to a level of 3% at 150°C prior to cooling under an applied stress of 250 MPa. This elastic strain value is good enough to be utilized for practical applications and is an indication that even without any phase transformation NiFeGa can find employment along with some conventional highly elastic materials.

Another method to determine the actual transformation strain from pseudoelastic experiments might be using ε_{PE}^o instead of ε_{PE} . The schematic in Figure 34a shows how to measure ε_{PE}^o , which is by removing the elastic contributions of austenite and martensite phases from ε_{PE} . Actually, this method is similar to what we have calculated using Eq.6 but, this time we don't use constant critical stress but just determine the transformation strain graphically at zero stress level.

The ε_{PE}^o values that are extracted from Figure 33a are plotted in Figure 37 with ε_{PE} and ε_{SME} from Figure 36 for [100] orientation. it is clear that the corrected transformation strains have less dependence on temperature and closer values to the theoretical strain. The small decrease in ε_{PE}^o is attributed to the change in lattice parameters and the error from the drawing of the modulus lines due to nonlinearity of loading/unloading curves.

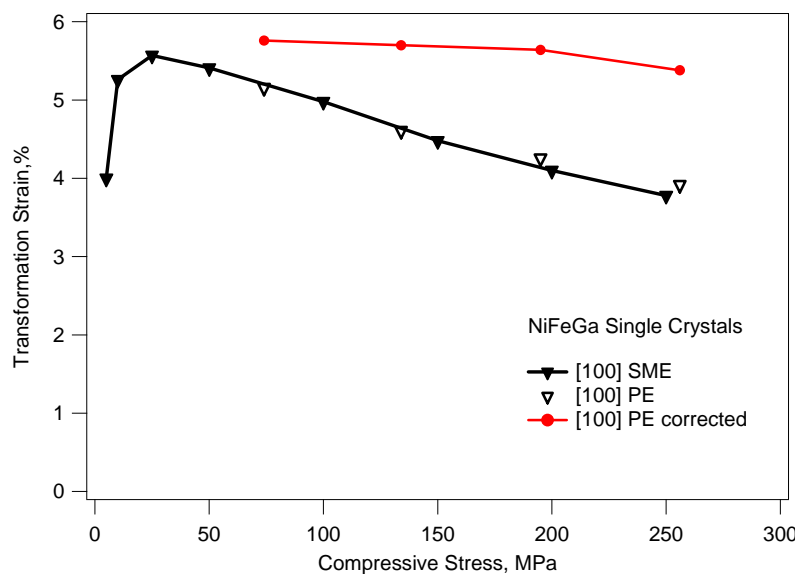


Figure 37. Transformation strain as a function of stress along [100] orientation determined by the methods shown by Figure 33a.

1.2.7. Thermal Transformation Hysteresis

Temperature hysteresis is an important shape memory characteristic where low temperature hysteresis indicates good compatibility between transforming phases and is desired for actuator applications. Figure 38 shows the temperature hysteresis as a function of applied stress along the

three orientations. For [100] and [123] orientations, temperature hysteresis is around 10°C and it increases slightly with increasing applied stress. For [110] orientation, the temperature hysteresis is around 5°C when austenite transforms to 1st martensitic phase and it increases substantially after 150MPa due to the aforementioned increase in transformation strain and formation of 2nd martensitic phase. Low temperature hysteresis suggests good compatibility between austenite and martensite. It can also be a sign of low stress hysteresis in pseudoelastic response. For NiTi single crystals in solutionized and overaged state, the SME strain and thermal hysteresis increase with applied stress [72].

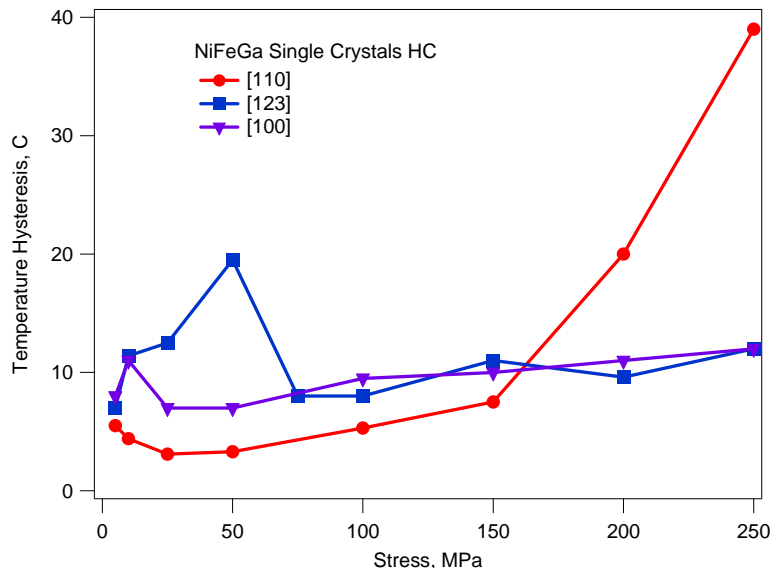


Figure 38. Temperature hysteresis as a function of applied stress and orientation extracted from the curves shown in Figure 32. The schematic shown in Figure 34b presents how the temperature hysteresis is determined.

Large hysteresis in NiTi originates from the partial accommodation of martensitic transformation with dislocations instead of internal twins and elastic distortion of the matrix [26]. When the stress levels are increased, dislocation formation becomes easier and thermal hysteresis increases.

Cui *et. al.* [73] reported that transformation hysteresis is based on crystal symmetry and geometric compatibilities, in other words; lattice parameters of the transforming phases. Low temperature hysteresis in NiFeGa alloys suggests the good compatibility of transforming phases. The change in transformation (temperature) hysteresis with stress can be attributed to the change in lattice parameters with stress. Hysteresis has a minimum at an optimum stress level and to increase the stress further also increases hysteresis. this phenomenon can be observed along [100] and [123] orientations as shown by Figure 38.

Another important factor for low temperature hysteresis is whether the martensite formed is composed of internal twins or not. Formation of internal twins stores additional elastic and interfacial energies. If we examine the heating cooling curves, storage of elastic energy can be determined by the gradual change of strain with temperature. For [110] orientation, under low stress magnitudes, the transformation occurs gradually. Nevertheless, upon the increase in applied stress, at some point, the phase transformation takes place in a very sudden manner; burst type response. This behavior might be attributed to the fact that the first transforming phase has internal twins; yet, the second phase has detwinned structure. In the first case, thanks to the internal twins, it is easier for the martensite phase to achieve good compatibility with the

austenite phase. However, the second martensitic phase with detwinned structure may not be as compatible with the austenite and in this case an additional energy is required through further undercooling. Whilst transformation starts for a detwinned martensite structure, it happens in a very sudden manner. This is because the energy required for nucleation is greater than the energy required for phase front motion, thus the strain curve assumes shape of a square wave. In course of heating with a large elastic energy, the back transformation occurs gradually as in the case of first martensitic transformation along [110] orientation. In the absence of elastic energy, further heating is necessary to add to the chemical energy, hence help the back transformation. A similar approach can be taken to forward transformation; when the energy needed for nucleation of austenite is achieved, back transformation occurs in a sudden manner. As well, the strength of phases for dislocation motion must be taken into account in order to understand the change in temperature hysteresis with stress. Seeing that the applied stress level increases, it is easier to form defects such as dislocations in the habit plane (austenite-martensite interface) during phase transformation. For NiFeGa single crystals, [100] orientation has high strength for dislocation slip (\sim 1000MPa); however [123] and [110] orientations have lower strengths (\sim 300-400MPa). Therefore, as the applied stress levels increases more dislocation activity would be expected along [123] and [110] orientations than along [100] orientation. This might explain the increase in hysteresis for [123] and [110] orientations.

1.2.8. Stress Hysteresis

Stress hysteresis increases with ϵ_{PE} for all orientations as evident by the incremental strain responses shown in Figure 33. It is hard to determine stress hysteresis due to lack of plateau regions for forward and reverse transformations. As temperature increases, unloading curve (reverse transformation) shifts to lower stress values during unloading, therefore widening the stress hysteresis of the $\sigma-\epsilon$ curve along [100] and [110] orientations. This behavior can be called as the stabilization of martensite and is also observed in NiMnGa single crystal along [110] orientation and in CuAlNi alloys [74-75]. The stabilization degree is directly related to the amount of deformation applied as seen in Figure 33. The increase in stress during back transformation is attributed to the difference between the speeds of austenite phase front and the cross head motion of the test setup [75]. The phase boundary moves faster than the cross head and this difference inflicts itself in the form of a stress increase due to ongoing transformation. Accordingly, the cross head tries to compensate and increases the level of applied stress. This is the case if the experiment is conducted under displacement control. Should force control be used instead of displacement control or the cross head speed was increased, the transformation would be very sudden and the increase in stress would not be observed [75].

The second point we need to clarify is the orientation dependence of stabilization of martensite. Clearly seen in Figure 33 that, the reverse transformation occurs gradually along [123] orientation; while along [100] and [110] orientations the martensite stabilization behavior is pronounced. The difference might be attributed to the formation of detwinned martensite structure along [100] and [110] orientations while; the martensite formed is of twinned structure along [123] orientation. Sittner et. al. [76] reported that just before the reverse transformation of detwinned γ' martensite back to austenite, a twinning wave appeared and moved in jumps along the specimen, leaving behind γ' plates full of internal twins. These γ' plates were then immediately retransformed to the parent phase. They witnessed these phenomena by optical microscopy during in-situ heating experiments on CuAlNi alloys. The internal twins must be formed at the interface to satisfy the compatibility of transforming phases which requires additional energy and corresponds to a decrease in stress [75-76]. After formation of twins the transformation occurs in a sudden manner. Additionally, when higher external stresses are applied, meaning that when the temperature increases in pseudoelastic response, it becomes

harder to form the twinning wave, thus increasing the degree of martensite stabilization. In [123] orientation, the martensite might be internally twinned and the elastic energy stored during forward transformation helps the reverse transformation result in a gradual progression, that is, as stress decreases phase front moves. The difference in the rank of martensite stabilization between [100] and [110] orientations can be linked to the higher strength for dislocation motion along [100] orientation compared to that of [110] orientation and different resolved shear stress factors for phase transformation. Formation of dislocations during forward transformation impedes the formation of twinned martensite during reverse transformation, thus resulting in large stress hysteresis.

The structure of martensite might also affect the stabilization behavior. It has been reported that 10M and 14M structures in NiMnGa alloys have very thin internal twin structure where L1₀ structure has larger twin width [77-78]. This might suggest that it would be easier for detwinned 14M transform back to austenite than the L1₀ martensite. Chernenko *et. al.* [75] attributed the martensite stabilization along [110] orientation to the formation of L1₀ martensite and the lack of stabilization along [100] orientation to the formation of modulated martensite.

1.2.9. Calculation of Theoretical Transformation Strains

The origin of the orientation dependence of the shape memory strain is mainly the crystallographic relation between the applied stress direction and possible crystallographic systems (transformation shear plane - also known as habit plane - and direction) for parent to martensite transformation. By using “Energy Minimization Theory”, it is possible to determine habit plane and direction as well as twinning shear and direction for given lattice parameters.

In NiFeGa alloys; parent phase has L2₁ structure while martensite has 10M, 14M or L1₀ crystal structures [62-63]. The 10M and 14M structures are monoclinic while L1₀ is tetragonal. For cubic to tetragonal transformation, there are a total of 3 variants. As for cubic to monoclinic phase transformation the number of possible variants is 12. In the parent phase coordinate system, the deformation matrices to obtain these variants can be designated as \mathbf{U}_i .

For a given variant pair, the twin plane \mathbf{n} and twin shear \mathbf{a} can be determined provided that the plane is an invariant plane (unrotated and undistorted) using

$$\mathbf{R}_{ij}\mathbf{U}_j - \mathbf{U}_i = \mathbf{a} \otimes \mathbf{n} \quad (8)$$

where \mathbf{R}_{ij} is an orthogonal tensor and represents the relative rotation between the two variants satisfying $\mathbf{R}_{ij}^T \mathbf{R}_{ij} = \mathbf{I}$ (\mathbf{I} is second rank identity tensor and the superscript T represents the transpose of a matrix). The \otimes represents a dyadic product. The twinned martensite is composed of variant pairs with a certain volume ratio. When there is finite number of twin layers, the deformation of martensite is represented as

$$\mathbf{F}_M = \mathbf{R}_h [f\mathbf{R}_{ij}\mathbf{U}_j + (1-f)\mathbf{U}_i] \quad (9)$$

where \mathbf{U}_i and \mathbf{U}_j are two variants in the twinned martensite and $(1-f)$ and f are respective volume fractions. The tensor \mathbf{R}_h is the relative rotation between the twinned martensite and the parent phase. The habit plane \mathbf{m} and transformation shear \mathbf{b} can be obtained using

$$\mathbf{F}_M - \mathbf{I} = \mathbf{b} \otimes \mathbf{m} \quad (10)$$

where \mathbf{I} is the identity tensor representing the undeformed austenite. In these equations, the known parameters are \mathbf{U}_i , \mathbf{U}_j , and all the other unknowns can be solved from the equations.

Sutou *et. al.* [62] reported the lattice parameters for different martensite phases and they are used to determine volume fraction, habit plane, transformation shear and twinning direction as shown by Table 6.

Once the habit plane normal and transformation shear are determined, it is possible to find the transformation strain as

$$\boldsymbol{\varepsilon} = \frac{1}{2} (\mathbf{F}_M^T \cdot \mathbf{F}_M - \mathbf{I}) = \frac{1}{2} [\mathbf{b} \otimes \mathbf{m} + \mathbf{m} \otimes \mathbf{b} + (\mathbf{b} \cdot \mathbf{b}) \mathbf{m} \otimes \mathbf{m}] \quad (11)$$

Table 6. Volume fraction, habit plane, transformation shear and twinning direction for NiFeGa alloys determined by energy minimization method.

	Volume Fraction, f	Habit plane , m	Transformation shear, b	Twinning, a
L1 ₀	0.3516	(0.101 0.704 -0.703)	<0.012 0.084 0.095>	{0 1 -1}
10M	0.2126	(0.078 0.693 -0.716)	<0.010 0.065 0.692>	{-0.126 -0.021 0.115}
10M	0.2138	(-0.110 0.693 -0.712)	<-0.006 0.065 0.069>	{-0.127 0.001 0.117}
14M	0.055	(0.081 0.717 -0.692)	<0.009 0.084 0.092>	{0.096 0.019 0.104}

The detwinning strain can be found by considering the conversion of the small fraction variant to the large one. The deformation can be determined as

$$F_M^{dt} = R_h U_i \quad \text{for } f < 0.5 \quad (12)$$

$$F_M^{dt} = R_h \cdot (U_i + a \otimes n) \quad \text{for } f > 0.5 \quad (13)$$

The total strain by detwinning can be determined similar to Eq. 9 once F_M^{dt} is known. It is important to note that for NiMnGa and NiFeGa alloys the stress required for detwinning is very low compared to NiTi and for these alloys it is better to compare the experimental results with the theoretical results with detwinning. The resolved shear stress factor (RSSF) is calculated using

$$\text{RSSF} = (\mathbf{b} \cdot \mathbf{e})(\mathbf{m} \cdot \mathbf{e}) / |\mathbf{b}|$$

where e denotes the single crystal loading direction. RSSF can be used to calculate the stress required for SIM along different orientations if the critical RSSF is known. The RSSF for cubic to L1₀ transformation are 0.525, 0.262 and 0.323 for [100], [011] and [123] orientations, respectively. From these values, one would expect a lower level of applied stress to start stress induced martensite (SIM) in [100] orientation than that required in other orientations provided that the materials are in the same thermal condition. Figure 39 shows the resolved shear stress factors, transformation strain and detwinning strain calculated by energy minimization theory for all three possible martensite structures.

For all martensite types, [100] orientation has the highest and [111] orientation has the lowest transformation strain values. The effect of detwinning is more pronounced in L1₀ martensitic transformation.

Table 7 gives the experimental and theoretical transformation strains along the three orientations for three possible martensite phases obtained from Figure 39. Along [123] orientation, the experimental value of 3.86% and the lack of martensite stabilization in pseudoelastic response suggest that the transformed martensite is in twinned state which might be 14M or L1₀. For [110] orientation, the first stage might be 14M transformation where the second stage is definitely due to detwinned L1₀ martensite formation.

For [100] orientation, it is difficult to predict the transforming phase by just comparing the experimental and theoretical strain values since they are very close. However, the change in stress hysteresis behavior with temperature in pseudoelastic response suggests that at low temperatures or under low applied stress levels the structure transforms to twinned martensite which might be 14M and at high temperatures it transforms to L1₀ or detwinned 14M. Sutou *et al.*[62] also reported that in pseudoelastic response the sample transforms to 14M initially and then to L1₀ martensite and as temperature increases it only transforms to L1₀ in tension along [105] orientation which is close to [100] orientation. Since the second stage transformation along

[110] orientation might be only due to L₁₀ transformation and martensite stabilization in pseudoelastic response at the high temperatures is well pronounced, it is strongly suggested that the final martensite product should also be L₁₀ martensite.

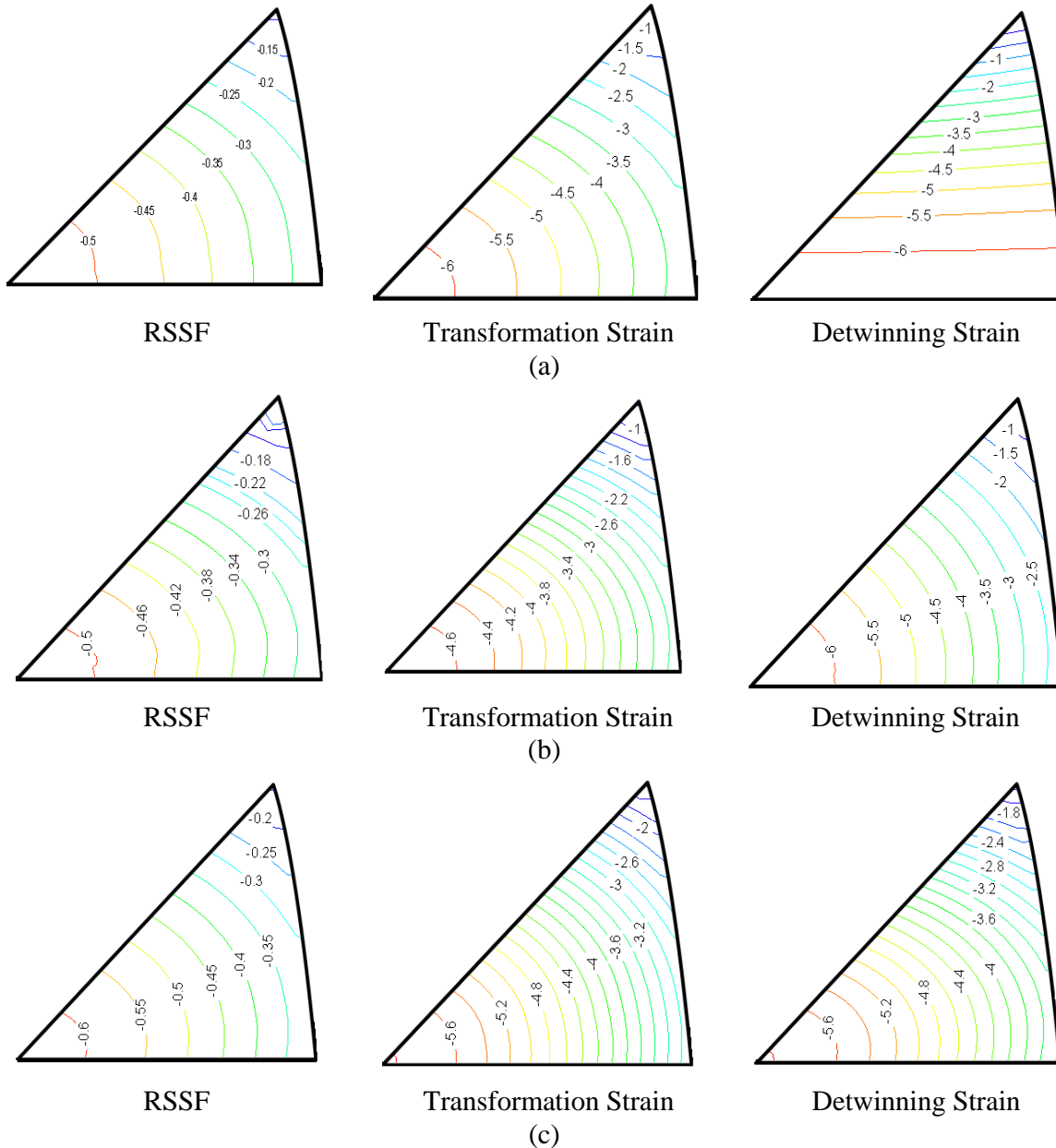


Figure 39. Resolved shear stress (RSSF) factor, transformation strain and detwinning strain contours for L₂₁ to (a) L₁₀, (b) 10M and (c) 14M phase transformations of NiFeGa alloy under compression.

1.2.10. Potential of NiFeGa alloys for Magnetic Field Induced Transformation

The recently discovered reversible field-induced phase transformation in NiMnGa alloys is a very promising method to increase the actuation stress levels of about one order of magnitude with respect to variant reorientation method [10-12]. The main requirement for field-induced phase transformation is that the stress hysteresis must be smaller than magnetostress [11]. Since

the magnetocrystalline anisotropy energy of NiFeGa alloys is similar to NiMnGa alloys, magnetostress for NiFeGa alloys must be in the order of a few MPa's [79].

Table 7. Comparison of experimentally observed strains with theoretically calculated strains for three martensite types, 10M and 14M and L₁ along [100], [123] and [110] orientations.

Experimental SME	Theoretical					
	Transformation Strain			Detwinning Strain		
	10M	14M	L10	10M	14M	L10
100	5.78	4.73	6.03	6.25	6.38	6.25
123	3.86	3.01	3.63	3.79	3.43	3.72
110 First Stage	3.4	2.44	3	3.06	2.2	2.95
110 Second Stage	5.95	2.44	3	3.06	2.2	2.95
						6.25

Figure 40 shows the pseudoelastic response along [100], [110] and [123] orientations as a function of temperature with a fixed total strain of 2%. For all orientations, transformation strain decreases with temperature since the elastic strain increases due to the need of higher critical stress for phase transformation. The decrease of transformation strain along [100] orientation is more pronounced with respect to other orientations since it has the lowest Young's Modulus. The stress hysteresis decreases with temperature for all orientations due to the decreasing transformation strain with increasing temperature. Also, note the low stress hysteresis in [110] orientation which can be correlated with the low temperature hysteresis shown by Figure 32c.

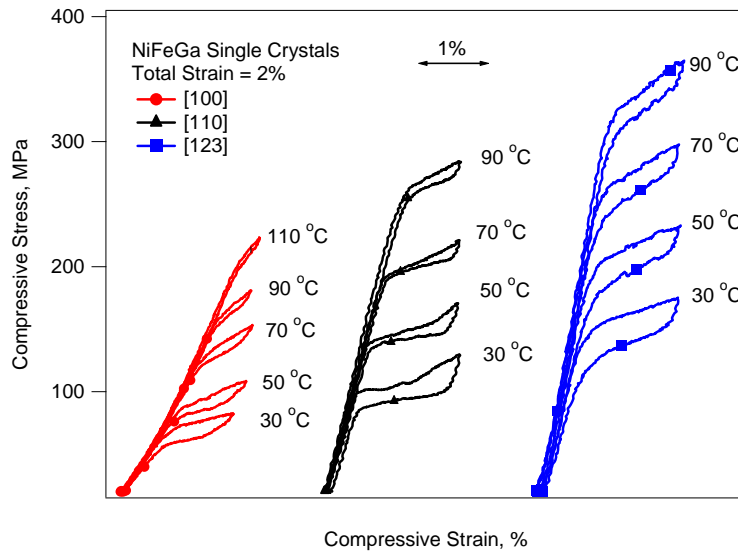


Figure 40. Compressive stress-strain response of NiFeGa single crystals as function of temperature along [100], [123] and [110] orientations, respectively with total strain of 2%.

From Figure 40, we can conclude that stress hysteresis is highly dependent on transformation strain and stress hysteresis less than 5MPa can be obtained in NiFeGa alloys. Similar to NiMnGa alloys, this low stress hysteresis might result in reversible field-induced transformation with the application of magnetic field along the hard axis of martensite. The field induced transformation strain values might be small since they can't reach the full transformation strain due to low stress hysteresis requirement. However, by using the technique Cui *et. al.* [62] reported, alloys can be

designed with low stress hysteresis which might result in high reversible field-induced phase transformation strain.

1.2.12. Summary of Findings on NiFeGa Single Crystals

In this part of the study, the shape memory and pseudoelastic response of NiFeGa single crystals along [100], [123] and [110] orientations were determined. It has been shown that transformation strain, temperature hysteresis and stress hysteresis are all orientation dependent. Transformation strain, detwinning strain and resolved shear stress factors were calculated by using energy minimization theory. The following major results were obtained:

- 1) The transformation strains of 5.78% and 3.86% are obtained along the [100] and [123] orientations, respectively.
- 2) Two-stage transformation in pseudoelasticity is observed along the [110] with 3.4 % transformation strain for the first stage and 5.95 % total transformation strain.
- 3) The experimental transformation strains fits well with the theoretical strains, however it is difficult to differentiate the forming martensite types.
- 4) Stress hysteresis in pseudoelasticity is determined to be a function of orientation, transformation strain, crystal structure of martensite and whether martensite has internal twins or not.
- 5) The decrease in transformation strains with stress in shape memory experiments and with temperature in pseudoelasticity experiments can be attributed to the difference in Young's modulus of transforming phases.
- 6) Stress-temperature phase diagram under compression is constructed for NiFeGa single crystals. CC slope of 2.97 MPa/°C, 4.39 MPa/°C, 4.64 MPa/°C is obtained along the [100], [123] and [110] orientations respectively. Also CC slope of -0.65 MPa/°C is obtained for the intermartensitic phase transformation in [110] orientation
- 7) Low stress hysteresis might result in field-induced phase transformation in NiFeGa alloys.

1.3. CoNiGa MAGNETIC SHAPE MEMORY ALLOYS

1.3.1. High Temperature Pseudoelasticity (PE) of $\text{Co}_{49}\text{Ni}_{21}\text{Ga}_{30}$ Single Crystals in Tension along the [100] Orientation

Figure 41 shows select PE responses at various temperatures between 40 and 300°C. This is the first time a transformation range of 260°C with full recoverability has been observed in an SMA. The specimen shows fully recoverable strains of 8% at every temperature with a small decrease then increase in stress hysteresis. The increase in stress hysteresis is a result of large dissipation mechanisms at high temperatures.

The terminology in Figure 42 was developed to define the stress drop upon transformation, transformation strain and stress hysteresis. The peak stress, σ_{peak} , is accompanied by large strains therefore martensitic transformation occurs prior to the load drop, $\sigma_{\text{peak}} - \sigma_{\text{plateau}}$. The σ_{peak} is a result of multiple martensite variant nucleation. The variants interact and compete with one another until one variant spans the cross section of the specimen and dominates. Transformation then occurs at a steady lower stress in a Lüders type transformation. The multiple variants created prior to transformation are consumed by the dominant martensite variant resulting in almost full theoretical transformation strains of the specimen.

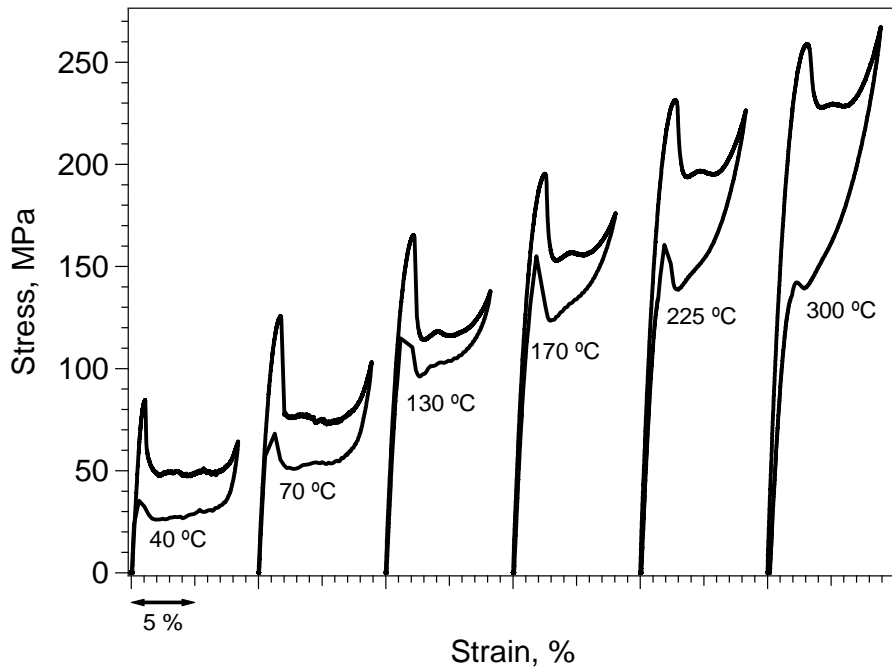


Figure 41. Select curves displaying the pseudoelastic response of CoNiGa single crystals in tension loaded along the [100] direction. PE tests were performed between 40°C and 300°C.

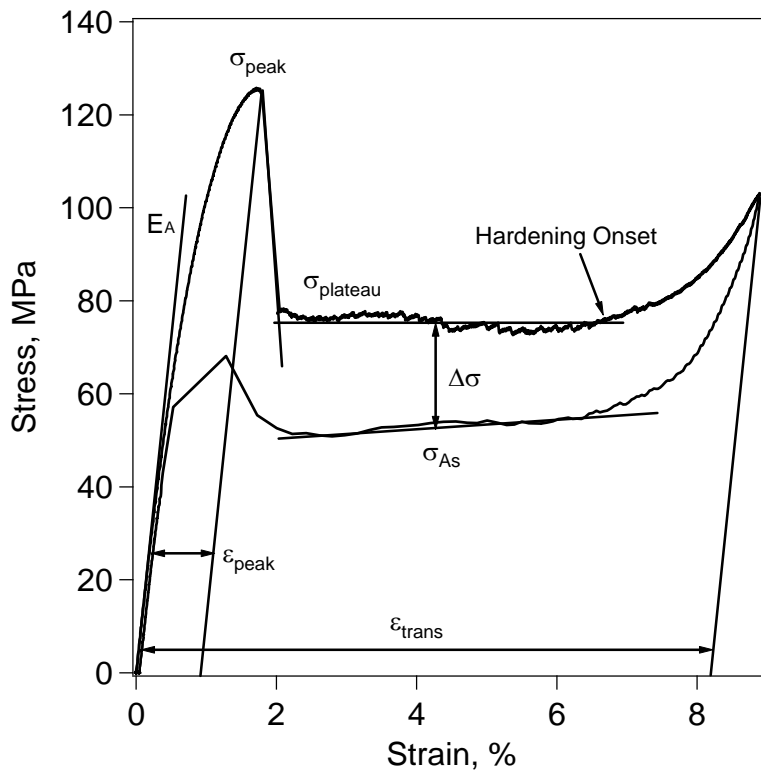


Figure 42. The pseudoelastic response of a CoNiGa single crystal in tension at 40 °C. The terminology displayed is used to describe the pseudoelastic response of CoNiGa. E_A is used as shown to separate the peak and transformation strains from the elastic deformation of austenite. Stress hysteresis is taken in the center of the plateau stress as shown.

The subsequent hardening at the end of σ_{plateau} is a result of interaction between the root and the gauge length of the specimen. Larger stress is required to de-twin the martensite CVPs/transform the austenite in contact with the specimen roots.

1.3.2. Stress-Temperature Phase Diagram of $\text{Co}_{49}\text{Ni}_{21}\text{Ga}_{30}$ under Tension along the [100] Orientation

Using the PE results combined with previously gathered DSC data, we have constructed the stress-temperature phase diagram show in Figure 43. The slope of the plateau σ_{Ms} transformation is $0.76 \text{ MPa}/^\circ\text{C}$. The σ_{As} follows the same slope closely, but begins to deviate from the $0.76 \text{ MPa}/^\circ\text{C}$ slope above $200 \text{ }^\circ\text{C}$. This shows an increase in stress hysteresis due to martensite stabilization at elevated temperatures. A similar stabilization effect has been observed in compression and is attributed to the creation of multiple martensite variant generation and interaction [61].

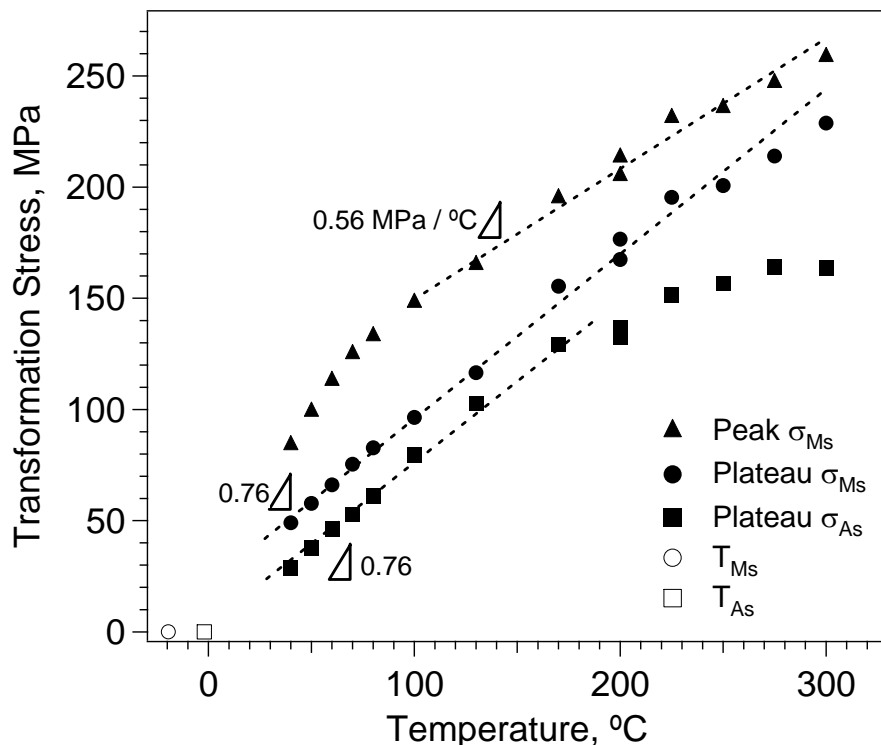


Figure 43. Peak stress, and plateau stresses of σ_{Ms} and σ_{As} as a function of testing temperature from pseudoelastic tests and T_{Ms} and T_{As} from DSC tests at 0 MPa . The plot follows a Clausius-Clapeyron relationship with a slope of 0.76 for the plateau stresses and 0.56 for peak stress.

The peak σ_{Ms} points represent the peak stress values for the forward transformation. There is a rapid increase in the $\sigma_{\text{peak}} - \sigma_{\text{plateau}}$ between 40 and $100 \text{ }^\circ\text{C}$. After $100 \text{ }^\circ\text{C}$ the slope stabilizes at $0.56 \text{ MPa}/^\circ\text{C}$. This curve fit line intersects with the plateau σ_{Ms} curve fit line at $400 \text{ }^\circ\text{C}$ and it is expected the $\sigma_{\text{peak}} - \sigma_{\text{plateau}}$ phenomena will disappear. The dissipation of the $\sigma_{\text{peak}} - \sigma_{\text{plateau}}$ allows the T_M value to be estimated with the 0.76 slope of σ_{Ms} .

1.3.3. Cyclic Stability of $\text{Co}_{49}\text{Ni}_{21}\text{Ga}_{30}$ Single Crystals

Figure 44 displays the results of 1000 cycle tests at 40 , 100 and $200 \text{ }^\circ\text{C}$. The as grown condition shows excellent stability at 40 and $100 \text{ }^\circ\text{C}$ with little more than lower critical

transformation stresses with increasing cycle number. At 200 °C the PE response degrades and turns to a purely elastic response by cycle 1000. This is a result pinning of the martensite by dislocation stacking at second phase boundaries and possibly the formation of additional γ and/or γ' second phases.

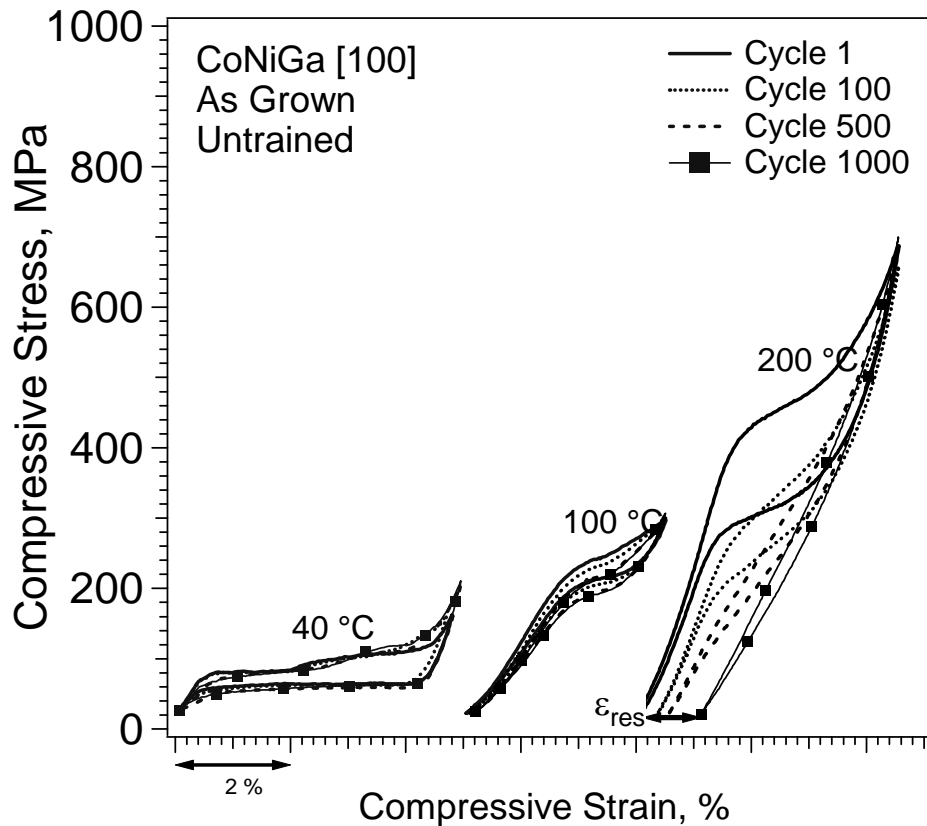


Figure 44. Cyclic deformation response of the [100] oriented as grown $\text{Co}_{49}\text{Ni}_{21}\text{Ga}_{30}$ under compression at 40, 100 and 200°C. Degradation and ratcheting occurs at 200 °C.

1.3.4. Effect of Training on High Temperature Cyclic Stability of $\text{Co}_{49}\text{Ni}_{21}\text{Ga}_{30}$ Single Crystals

Training the specimens consists of performing PE tests in 20 °C increments between 20 and 300 °C. The stability of the critical transformation stress at 60 °C in Figure 45 shows that training improves low temperature cyclic stability. High temperature cyclic stability is improved when comparing the 200 °C tests of the untrained and trained specimens. The specimen then shows full degradation and a purely elastic response at 300 °C. This is due pinning of the martensite from diffusion related phenomena such as martensite aging and precipitation of coherent γ and/or γ' second phases.

1.3.5. Effect of Precipitates on the High Temperature Cyclic Stability of $\text{Co}_{49}\text{Ni}_{21}\text{Ga}_{30}$ Single Crystals

The specimens were first homogenization heat treated at 1200 °C then heat treated at 1100 °C for 4 hours or 900 °C for 24 hours. Figure 46 shows the normalized residual strain at the 1000th cycle, $\varepsilon_{\text{res}}/\varepsilon_{\text{Tr}}$, as a function of testing temperature for the as grown, trained and heat treated specimens.

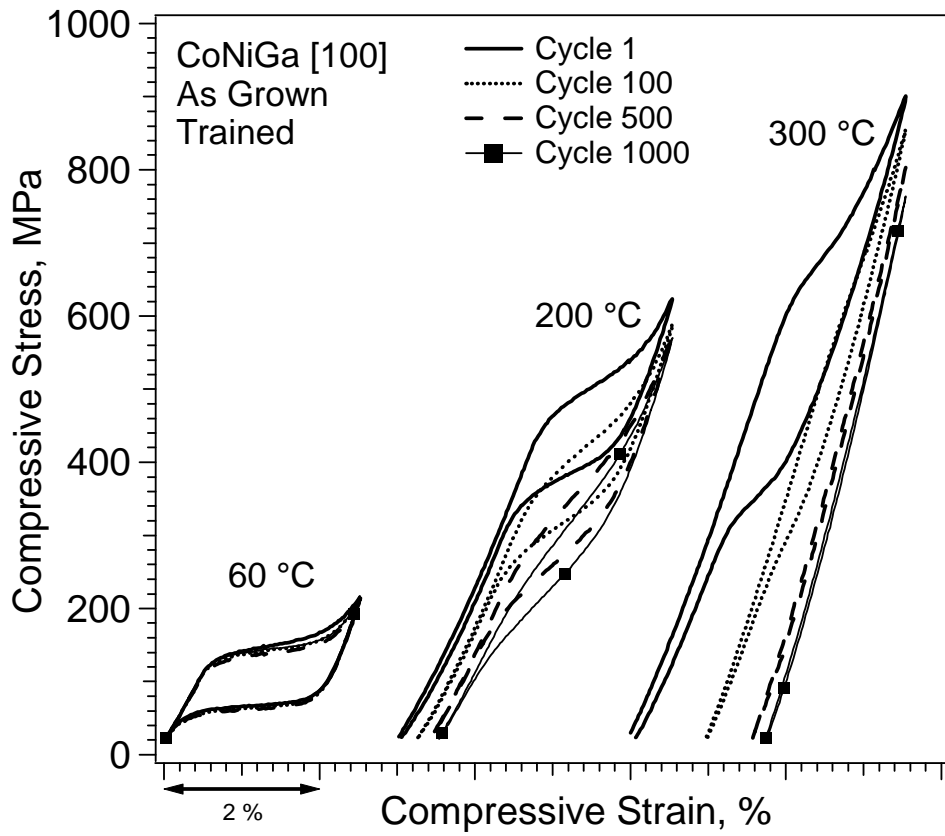


Figure 45. Cyclic deformation response of [100] oriented trained $\text{Co}_{49}\text{Ni}_{21}\text{Ga}_{30}$ in compression at 60, 200 and 300 °C. Improved cyclic stability is observed at 200 °C while complete degradation occurs at 300 °C.

The 1100 °C heat treatment shows great improvement compared to those trained in the 200 and 300 °C tests with a $\epsilon_{\text{res}}/\epsilon_{\text{Tr}}$ of 0.13 and 0.53 respectively. The 900 °C heat treatment shows better cyclic stability at 300 °C, but worst stability at 200 °C when compared to the 1100 °C heat treatment. The 900 °C heat treatment causes large γ phase precipitates to form thereby decreasing the initial cyclic stability, but these large precipitates, $\sim 10 \mu\text{m}$, also allow greater cyclic stability at high temperatures after cycling at lower temperatures. This shows that large randomly distributed γ phase allows a high level of training. Such good cycle stability is rarely seen in high temperature shape memory alloys.

1.3.6. Stress-Temperature Phase Diagram Obtained from Tensile and Compressive Pseudoelastic and Heating-Cooling Response of $\text{Co}_{49}\text{Ni}_{21}\text{Ga}_{30}$ Single Crystals

Figure 47 shows the pseudoelastic responses in tension and compression at 30, 100, 200 and 260 °C. Notable dissimilarities include the transformation strain (ϵ_{trans}), residual strain (ϵ_{res}), critical transformation stress (σ_{Ms}), and stress hysteresis ($\Delta\sigma$). The compressive and tensile stress states suppress and promote, respectively, martensite correspondent variant pair (CVP) detwinning. This results in larger ϵ_{trans} in tension, ~8%, than in compression, ~6%. Full recoverability is observed at every temperature except 260 °C in compression. The ϵ_{res} is from reaching the temperature required for plastic deformation of austenite before martensitic transformation can occur (T_M). As a result, the T_M for tension will be much higher than for

compression. Figure 48 compares the tensile and compressive transformation stresses (σ_{Ms} , M_s and σ_{As}) and stress hysteresis ($\Delta\sigma$) at various temperatures. The tensile and compressive σ_{Ms} slopes for martensitic transformation are 0.76 and 2.19 MPa/ $^{\circ}$ C respectively. Figure 48b shows both curve fit lines for martensitic transformation intersect close to zero stress as expected. The low slope for tension confirms TM will be much higher than the compressive case. The σ_{As} deviates from linear behavior above 100 $^{\circ}$ C in compression and 200 $^{\circ}$ C in tension. This martensite stabilization effect is a result of multiple martensite variant generation and interaction at elevated temperatures. The $\Delta\sigma$ values for tension and compression, Figure 48a, fluctuate around ~25MPa below 100 $^{\circ}$ C. Above this temperature the tension and compression $\Delta\sigma$ increases linearly with slopes of 0.24 and 0.94 MPa/ $^{\circ}$ C respectively. The increase in compressive stress hysteresis at high temperatures is a result of multiple martensite variant interaction.

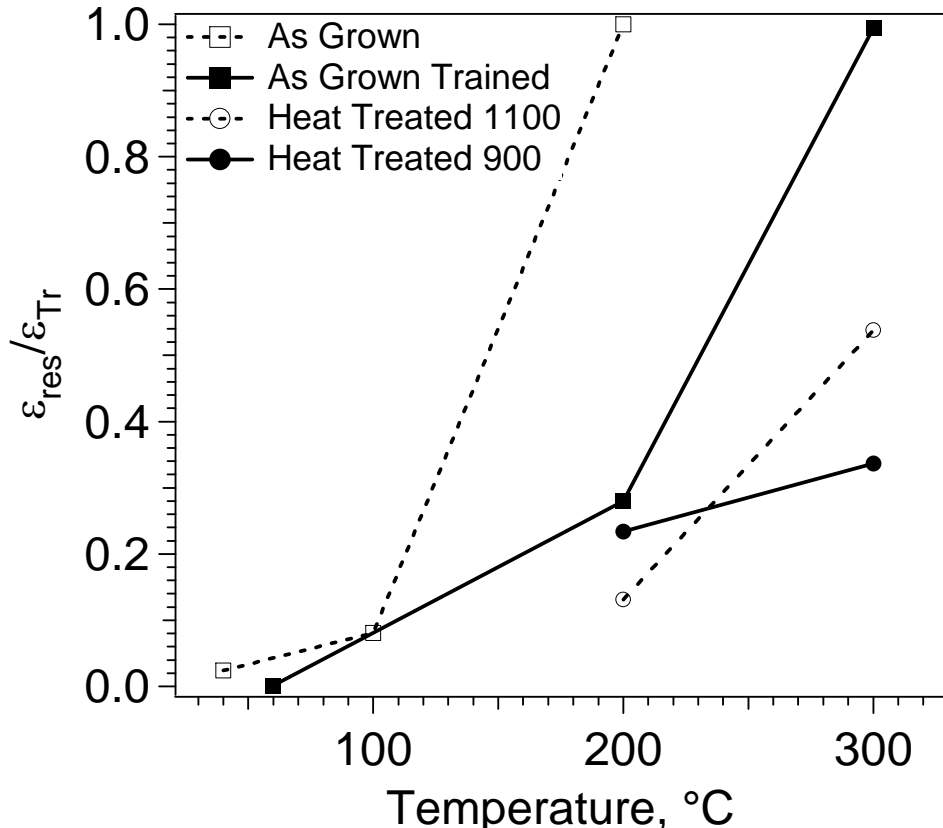


Figure 46. Normalized residual strain at cycle 1000 as a function of cycling temperature for as grown, trained, 1100 and 900 $^{\circ}$ C heat treated specimens.

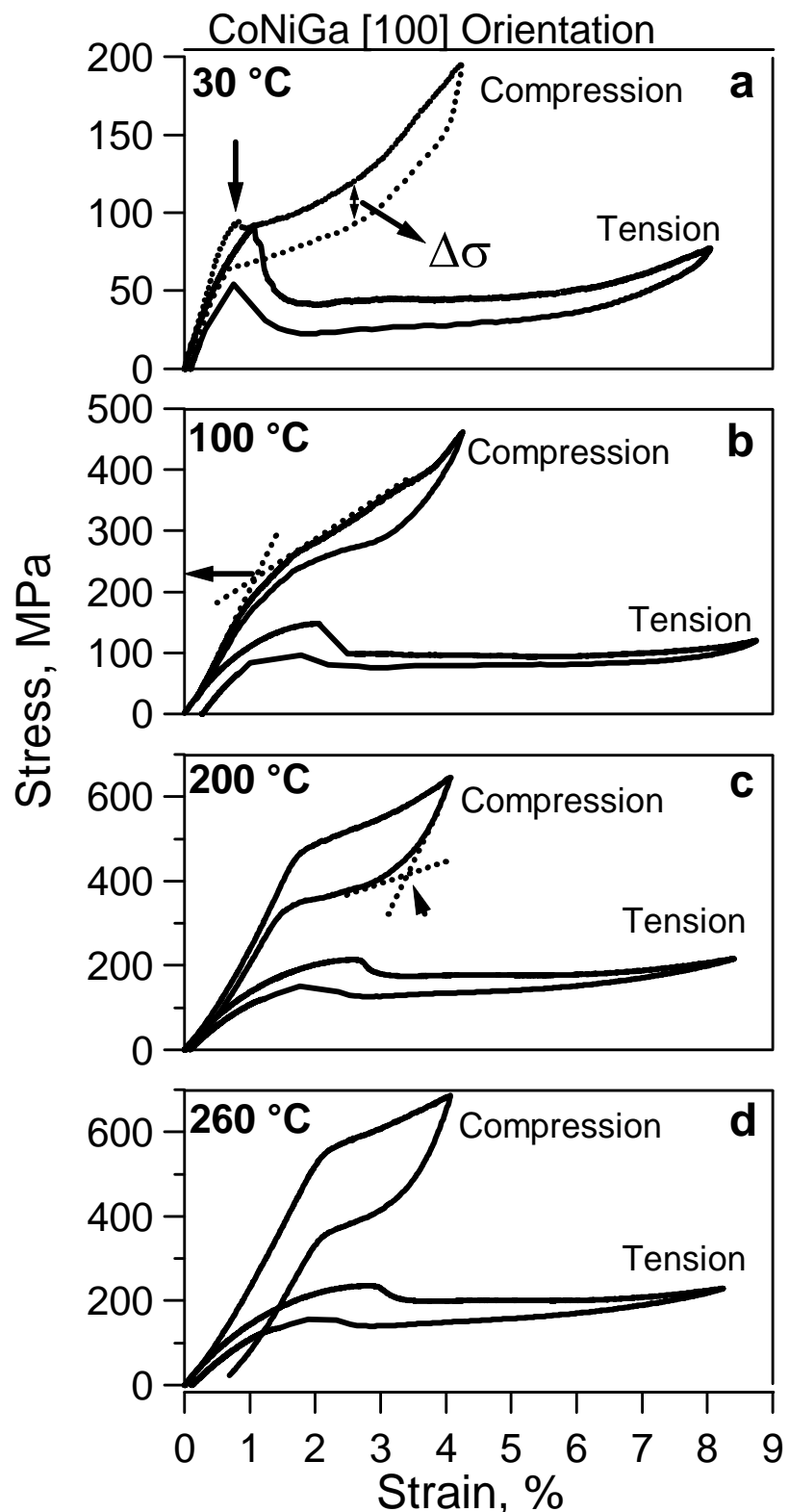


Figure 47. The tensile and compressive (a) stress hysteresis ($\Delta\sigma$), (b) martensite transformation stress (σ_{Ms} and M_s) and (c) austenite transformation stress (σ_{As}) as a function of temperature.

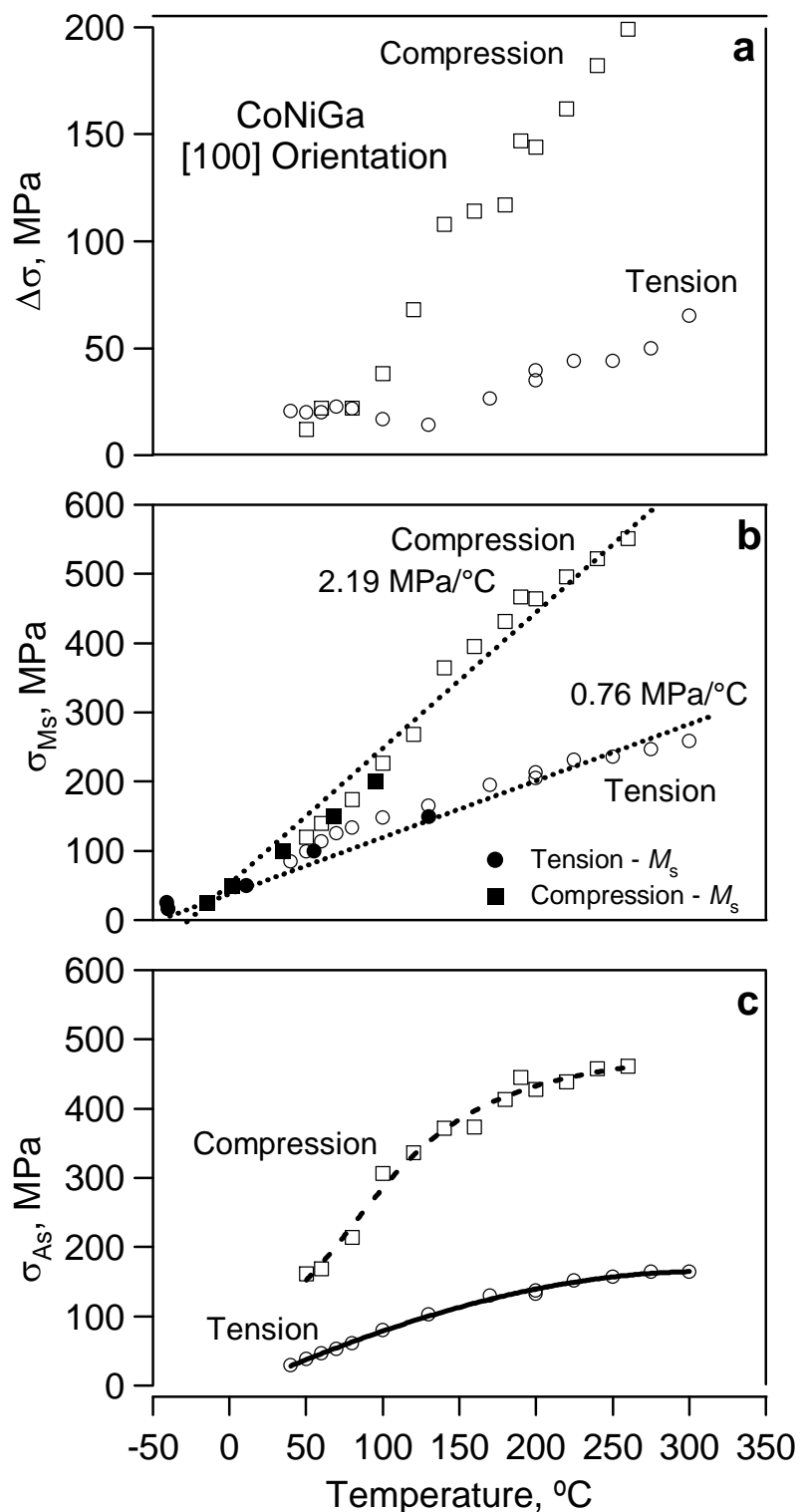


Figure 48. The tensile and compressive (a) stress hysteresis ($\Delta\sigma$), (b) martensite transformation stress (σ_{Ms} and M_s) and (c) austenite transformation stress (σ_{As}) as a function of temperature. Note: σ_{Ms} corresponds to critical stress for transformation from pseudoelastic tests while M_s is the martensite start temperature taken from heating-cooling experiments.

1.4. IN-SITU OBSERVATION of MAGNETO-MICROSTRUCTURAL COUPLING

The in-situ evolution of the microstructure and the associated magnetic domain morphology were investigated as a function of applied strain level during the stress-induced martensite (SIM) transformation in $\text{Co}_{49}\text{Ni}_{21}\text{Ga}_{30}$ single crystals. This is the first study, to the best of the PIs' knowledge, on MSMA monitoring magneto-microstructural evolution during SIM and attempting to reveal the effect of thermo-mechanical training on the magneto-microstructural coupling. This material is selected as our first material to investigate in-situ microstructure-magnetic domain coupling for understanding the mechanism of stress-assisted field-induced phase transformation. The effect of thermo-mechanical history on the SIM transformation and the magnetic domain configuration is also examined. The results demonstrated a significant influence of thermo-mechanical training on the characteristics of SIM and its domain morphology. The magnetic domains were found to be superimposed on the nano-scaled martensite twins in the as-grown crystal, whereas the training brought about the formation of micro-domains on the order of a few microns ($<10 \mu\text{m}$) without showing the one-to-one correspondence between domains and twin structure observed in the as-grown condition. The observations in this study imply that the stress-assisted magnetic field-induced strain can result from the growth of the SIM in the as-grown crystal or from the martensite rearrangement of self-accommodated martensite after thermomechanical training. The magnitude of the required magnetic field for phase-boundary motion should be low within the pseudoelasticity plateau. Provided that the volume fraction of detwinned martensite could be increased, a magnetic field-induced strain could also be obtained in detwinned areas, since the internally detwinned martensite variants are among themselves twin-related and show stripe-like patterns with anti-parallel magnetization vectors. Some of the results can be summarized as follows:

- a. Figure 49 shows MFM-images of the as-grown crystal (a) without applied stress and (b) at 1% compressive strain. The stress-free austenite phase has single magnetic domain morphology as seen in Figure 49.a. The precipitates in the matrix give rise to some magnetic contrast due to their ferromagnetic nature. These precipitates contain higher Co content than the matrix according to energy dispersive X-ray (EDX) analysis (results are not shown). After the formation of martensite at 1% strain (Figure 49.b) small micro domains ($< 0.5 \mu\text{m}$) with dark and bright parts generate a distinct magnetic contrast that are aligned as domain lines almost parallel to the compression axis. Depending on the local magnetization direction of the sample surface, attractive or repulsive forces act on the MFM-tip resulting in the dark and bright parts of the image, respectively. Note that these domain-lines also proceed into regions of untransformed austenite. Clearly the single-domain morphology of the stress-free state as shown in Figure 49.a does no longer exist at 1% strain.

It should be noted, that the micro domains are not uniformly distributed in Figure 49.b. The non-uniformity result from the Moiré-effect, which can arise in atomic force microscopy, when there is a mismatch between the sample (i.e. magnetic domain structure) and the scanning line grating. Therefore, the resolution of the scan was successively increased until the actual domain structures were captured. Figure 50.a shows these domain structures in a completely transformed region in the as-grown condition. The domain structures are on the order of the twin size observed by TEM. The fact that one twin is wider than the other is also visible in the magnetic domain structure. Clearly, there is a one-to-one correspondence between the magnetic domain structure and the twins in the as-grown crystal. A schematic of the magnetic domain structure of the as-grown crystal is given in Figure 50.b. Each twin is internally divided into magnetic domains with anti-parallel magnetization. These magnetic domains within the twins are separated by 180° walls, whereas the twins themselves form 90°

walls. It is assumed from the contrast in the MFM-image, that twin 1 has out-of-plane, whereas twin 2 has in-plane magnetization.

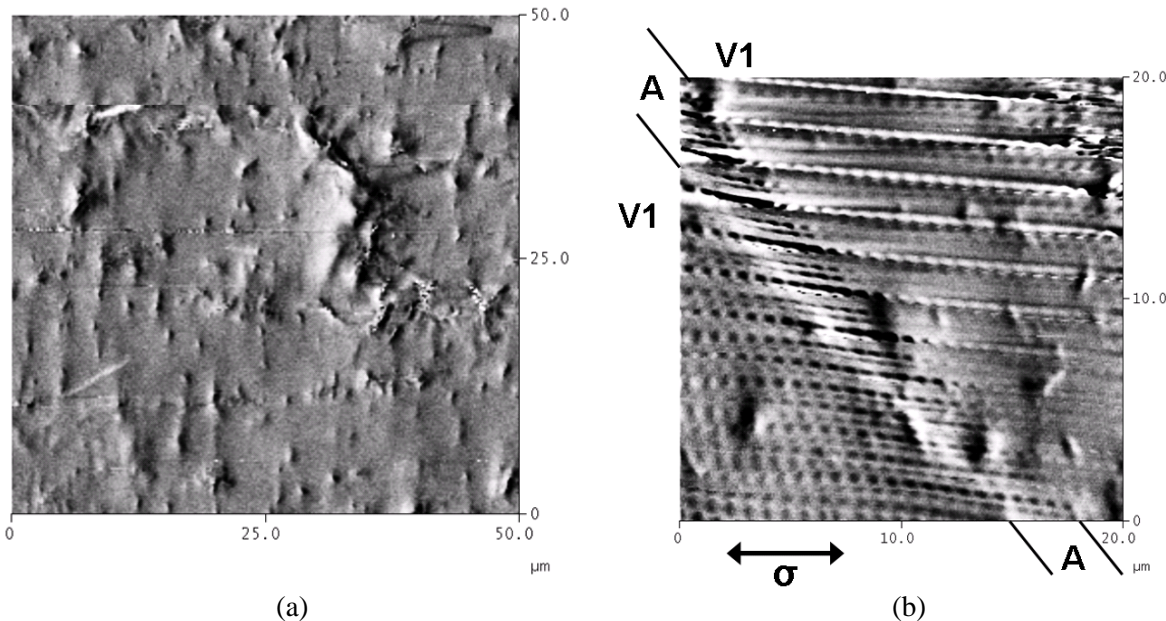


Figure 49. MFM images of the as-grown $\text{Co}_{40}\text{Ni}_{21}\text{Ga}_{30}$ crystal showing (a) austenite phase and (b) two-phase region of austenite (A) and martensite variant V1 at 1 % strain.

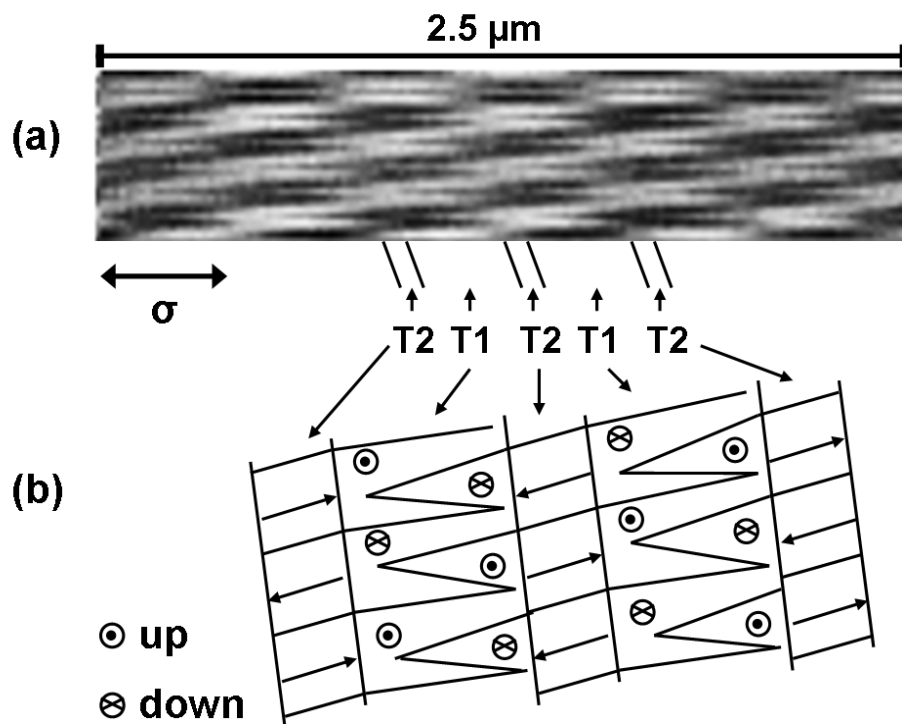


Figure 50. (a) Actual magnetic domain structure as obtained by high resolution MFM-scans within a martensite variant of the as-grown crystal and (b) corresponding schematic showing a one-to one correspondence between twins T1 and T2 and the magnetic domain structure.

b. The differences in microstructure due to the thermo-mechanical training also affect the magnetic domain structure. The small sub-micron domains seen in the as-grown crystal do not appear in the trained condition. In contrast, domains on the order of several micrometers are observed at 1% strain (Figure 51). The interfaces of the martensite variants and the austenite coincide with the main domain walls. Figure 51.a displays supplementary domains at the interfaces between austenite and a martensite variant (V3). The supplementary domains form a type of fir tree pattern, in which the magnetic flux is distributed by 90° domains. In contrast to this, in areas, in which austenite and martensite variant V2 coexist, 180° domain structures are present (Figure 51.b). In this case the transitions (domain walls) show up as fine black or white lines. This kind of domain pattern was also found at the interfaces between austenite and the martensite variants V1.

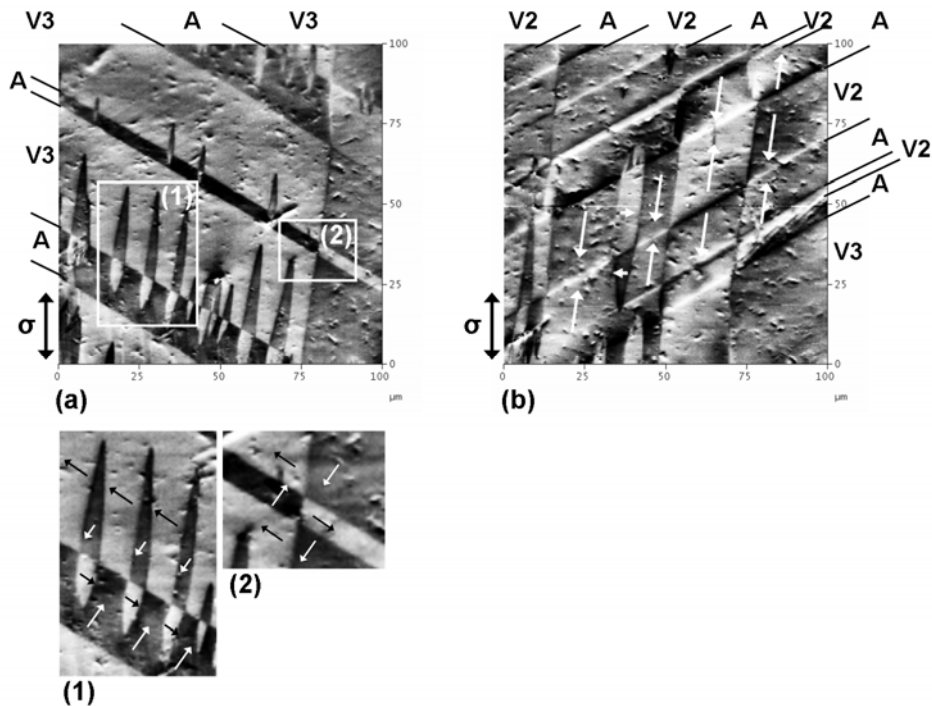


Figure 51. MFM images of the thermo-mechanically trained crystal at 1 % strain: (a) two-phase region of austenite (A) and martensite variant V3, (c), (b) austenite (A) and martensite variants V2 and V3. The arrows represent the direction of magnetization.

The magnetic domain structure after thermo-mechanical training is very different as compared to the structure in the as-grown condition. The results demonstrated a significant influence of thermo-mechanical training on the characteristics of SIM and its domain morphology. The magnetic domains were found to be superimposed on the nano-scaled martensite twins in the as-grown crystal, whereas the training brought about the formation of micro-domains on the order of a few microns ($<10 \mu\text{m}$) without showing the one-to-one correspondence between domains and twin structure observed in the as-grown condition. The one-to-one correspondence of the twin variants with the magnetic domains is not observed, although the martensite variants are still internally twinned. The size of the magnetic domains is much larger, *i.e.* on the order of micrometers, and 180° domain walls coincide with the interfaces of martensite variants and residual austenite phases. The one-to-one correspondence was found to

be dependent on the thickness of twin plates. The twin plates must reach a critical thickness to have micro-domains, which is determined by exchange interactions and magnetic anisotropy. If this criterion is not fulfilled relatively large magnetic domains separated by 180° domain walls are energetically favored instead of the small magnetic domains separated by 90° domain walls. This criterion is also supported by electron holography studies in a Fe-Pd-alloy. As the one-to-one-correspondence was not observed in the self-accommodated martensite after training, it is concluded that the twin size is smaller than the critical thickness.

The as-grown crystal showed a one-to-one correspondence between the twin structure and the magnetic domains within the pseudoelastic plateau. Thus, the magnetic domain structure is magneto-elastically coupled with the twin structure. The magnetocrystalline anisotropy energy is high in this case, because the magnetization direction changes across the twin boundary. When this variation in magnetic anisotropy energy is sufficiently large, an application of a magnetic field can cause twin boundary motion. The twin variant having the easy magnetization axis along the applied field would grow at the expense of the other. However, no detwinning was observed in the as-grown crystal. The stress within the PE-plateau seems to be not sufficiently high for twin boundary motion. Therefore, the energy needed to move a twin boundary appears to be larger than the magnetic anisotropy energy and thus MSME will hardly be obtained.

A stress-assisted magnetic field-induced strain can result from the growth of the SIM in the as-grown crystal or from the martensite rearrangement of self-accommodated martensite after thermo-mechanical training. The magnitude of the required magnetic field for phase-boundary motion should be low within the pseudoelasticity plateau. Provided that the volume fraction of detwinned martensite could be increased by training, a magnetic field-induced strain could also be obtained in detwinned areas, since the internally detwinned martensite variants are among themselves twin-related and show stripe-like patterns with anti-parallel magnetization vectors.

Figure 52 shows the stress-strain response of the [001]-oriented Ni-Mn-Ga single crystal at room temperature when loaded to 5 % strain.

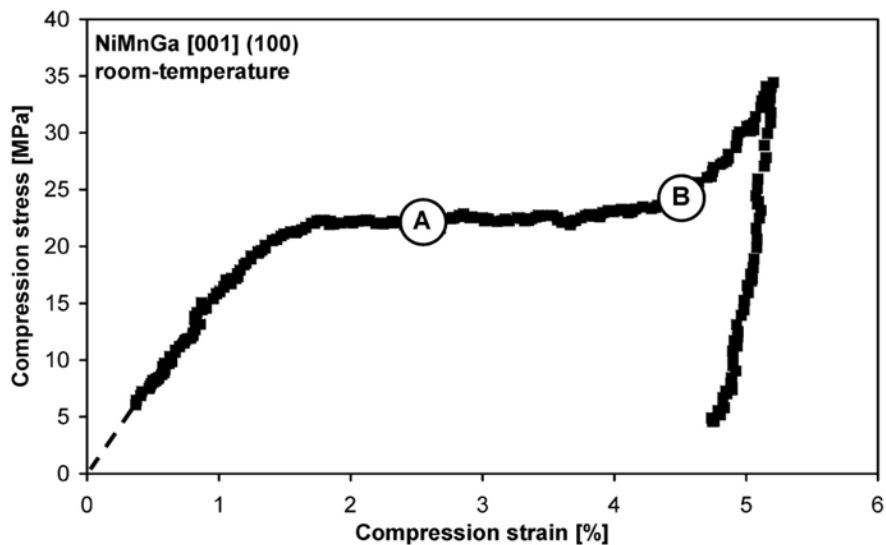


Figure 52. Stress-strain response of the [001]-oriented Ni-Mn-Ga single crystal at room temperature. Points A and B on the curve correspond to the strain levels of the *in-situ* tests shown in Figures 53 and 54.

The reorientation strain level substantiates the presence of 10M martensite. After exceeding the critical stress for transformation, 22 MPa, martensitic transformation continues at a constant

stress. In-situ magnetic force microscopy (MFM) tests were performed at constant strains of 2.5 and 4.5 %, points A and B respectively, which correspond to the onset and ending of transformation.

The topography and the corresponding magnetic domain structures at 2.5 % strain are shown in Figure 53 (a) and (b). Dust particles on the surface create bright spots in the topography images marked by the arrow in Figure 53(a). The martensite needle structures, labeled T1 and T2, are not aligned along the [001] compression axis, Figure 53(a). The comparison with the MFM-image, Figure 53, demonstrates there is a direct relationship between the needle structures and the magnetic domain structures. The high contrast needles, T2 in Figure 53 (b), shows the magnetic domain structures are perpendicular to the (100) plane. The remaining needles, T1, have in-plane domain structures as shown by their low contrast. The domain structures, T1 and T2, are separated by 90° domain walls at the boundaries of the needle structures. This kind of domain pattern is typical for alternating twin and proves a one-to-one correspondence, i.e. magneto-microstructural coupling between the martensite twins and the magnetic domains. The twins are divided into magnetic domain structures with alternating magnetization directions shown by the grey boxes superimposed on Figure 53 (b). These internal domain structures are to balance the magnetocrystalline and the magnetostatic energies.

Figure 54 shows AFM results at 2.5 and 4.5 % strain in a different location from Figure 53. A second twin pair exists that runs perpendicular to the [001] loading axis, Figure 54(a). Again, a magneto-microstructural coupling between the needle and the domain structure is observed in Figure 54 (b). It is therefore necessary to examine different areas to observe all martensite variants. The effect of straining the alloy to 4.5 % on the magneto-microstructure is exemplarily shown in Figure 54 (c) for the same area as in Figure 54 (b). The same domain structures seen at 2.5 % strain are present at 4.5 % strain; however, the volume fraction of in-plane magnetic domain structures has significantly increased. The favorable compressive twin variant, in this case the in-plane magnetic domain structures, grows at the expense of the others. This twin variant will also grow when applying a magnetic field along the [001] direction. To conclude, in-situ MFM measurements under load are a powerful new tool that allows examining the stress-induced martensite and the corresponding magnetic domain structures to understand the mechanism during MSME and to identify the influence of external applied stress on the magneto-microstructural coupling.

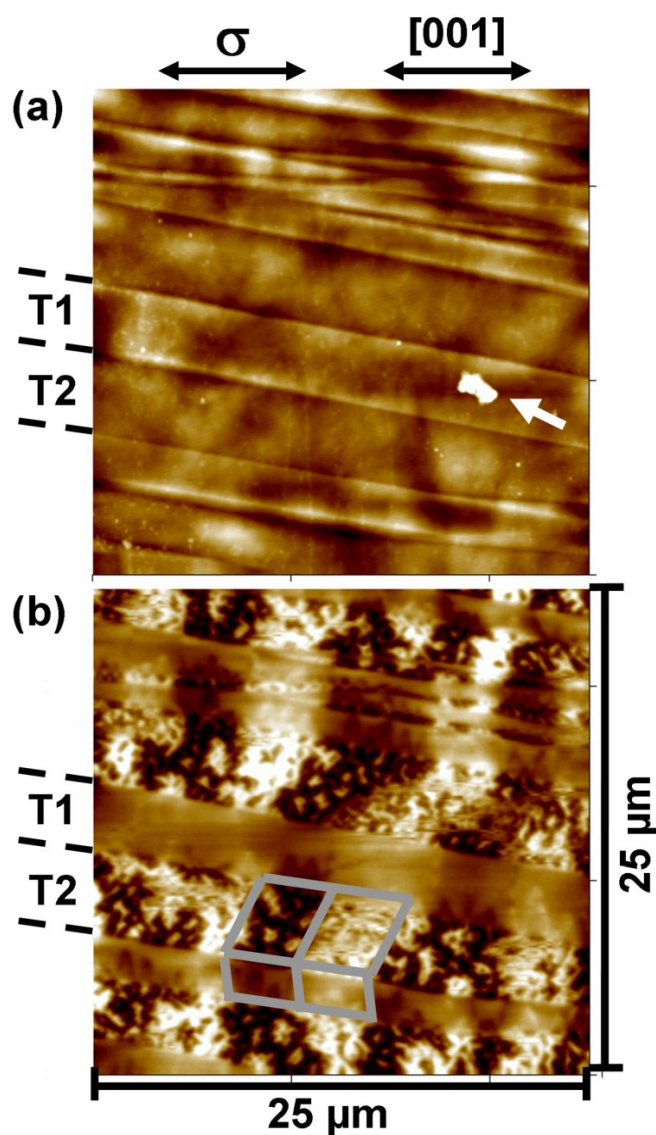


Figure 53. AFM images of NiMnGa at 2.5 % strain where (a) is the topography and (b) shows magnetic domain structures recorded with MFM. The bright spot on the topographical image, indicated by the white arrow, is due to dust particles.

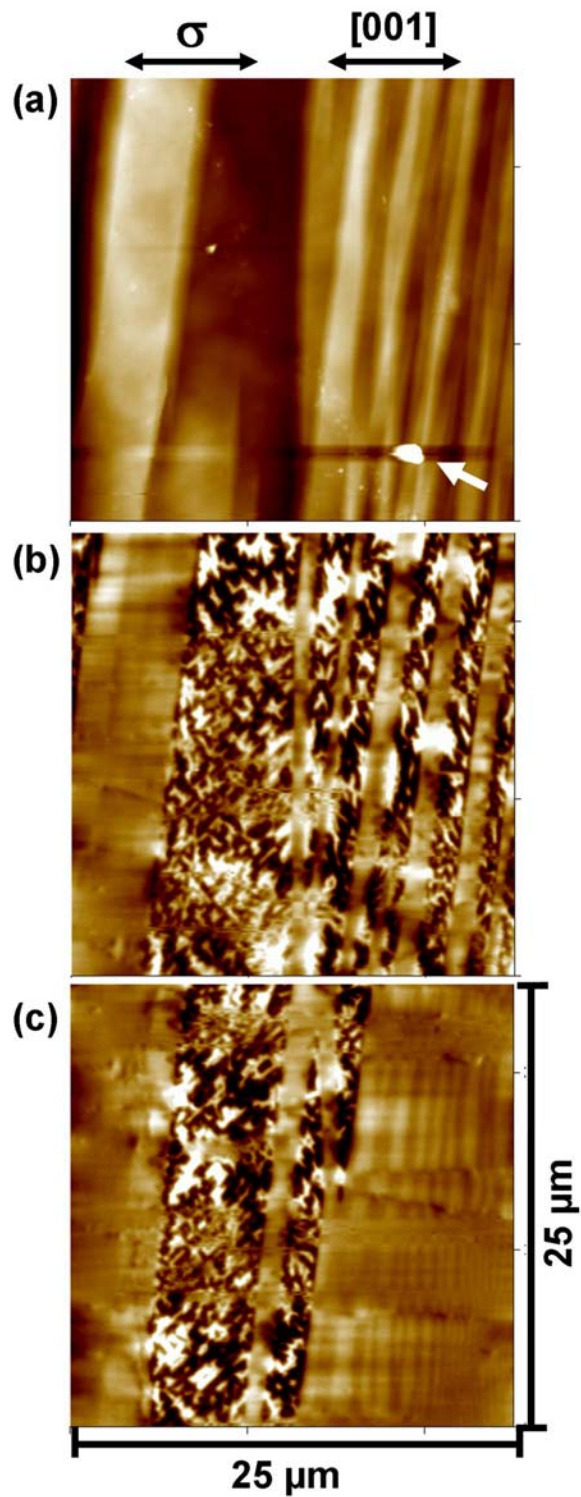


Figure 54. AFM images of: (a) topography at 2.5 % strain, (b) magnetic domain structures at 2.5 % and (c) Magnetic domain structures at 4.5 % strain. Note all images in this figure are of the same area.

References

1. Ullakko K, Huang JK, Kantner C, O'Handley RC, Kokorin VV. *Appl Phys Lett* 1996;69:1966.
2. Murray SJ, Marioni MA, Kukla AM, Robinson J, O'Handley RC, Allen SM, *J. Appl Phys* 2000;87:5774.
3. Sozinov A, Likhachev AA, Lanska N, Ullakko K. *Appl Phys Lett* 2002;80:1746.
4. Marioni MA, O'Handley RC, Allen SM, Hall SR, Paul DI, Richard ML, Feuchtwanger J, Peterson BW, Chambers JM, Techapiesancharoenkij R, *J Magn and Magn Mater* 2005;290:35.
5. O'Handley RC, *J. Appl Phys* 1998;83:886.
6. Karaca HE, Karaman I, Basaran B, Chumlyakov YI, Maier HC, *Acta Mater* 2006;54:233.
7. Murray SJ, Marioni M, Allen SM, O'Handley RC, Lograsso TA, *Appl Phys Lett* 2000;77:886.
8. Heczko O, Straka L, *Mater Sci and Eng A* 2004;378:394.
9. Heczko O, Sozinov A, Ullakko K, *IEEE Trans on Magn* 2000;36:3266.
10. Karaca HE, Karaman I, Basaran B, Lagoudas DC, Chumlyakov YI, Maier HJ, *Acta Mater* 2007;55:4253.
11. Karaman I, Karaca HE, Basaran B, Lagoudas DC, Chumlyakov YI, Maier HJ, *Scripta Mater* 2006;55:4036.
12. Karaca HE, Karaman I, Basaran B, Lagoudas DC, Chumlyakov YI, Maier HJ, *Scripta Mater* 2006;55:803.
13. R. C. O'handley, *Modern Magnetic Materials: Principles and Applications*, John Wiley & Sons, New York, NY 2000.
14. X. Moya, L. Manosa, A. Planes, T. Krenke, M. Acet, E. F. Wassermann, *Materials Science and Engineering A* 2006, 438-440, 911.
15. Y. Sutou, Y. Imano, N. Koeda, T. Omori, R. Kainuma, K. Ishida, K. Oikawa, *Applied Physics Letters* 2004, 85, 4358.
16. R. Kainuma, Y. Imano, W. Ito, H. Morito, Y. Sutou, K. Oikawa, A. Fujita, K. Ishida, S. Okamoto, O. Kitakami, T. Kanomata, *Applied Physics Letters* 2006, 88.
17. R. Kainuma, Y. Imano, W. Ito, Y. Sutou, H. Morito, S. Okamoto, O. Kitakami, K. Oikawa, A. Fujita, T. Kanomata, K. Ishida, *Nature* 2006, 439, 957.
18. K. Oikawa, W. Ito, Y. Imano, Y. Sutou, R. Kainuma, K. Ishida, S. Okamoto, O. Kitakami, T. Kanomata, *Applied Physics Letters* 2006, 88.
19. T. Krenke, E. Duman, M. Acet, E. F. Wassermann, X. Moya, L. Manosa, A. Planes, *Nature Materials* 2005, 4, 450.
20. R. Kainuma, K. Oikawa, W. Ito, Y. Sutou, T. Kanomata, K. Ishida, *Journal of Materials Chemistry* 2008, 18, 1837.
21. M. K. Chattopadhyay, V. K. Sharma, S. B. Roy, *Applied Physics Letters* 2008, 92.
22. Z. D. Han, D. H. Wang, C. L. Zhang, H. C. Xuan, B. X. Gu, Y. W. Du, *Applied Physics Letters* 2007, 90.

23. W. Ito, Y. Imano, R. Kainuma, Y. Sutou, K. Oikawa, K. Ishida, Metallurgical and Materials Transactions A 2007, 38A, 759.
24. R. Kainuma, W. Ito, K. Oikawa, K. Ishida, in Proc. International Conference on Martensitic Transformations, Santa Fe, NM 2008.
25. H. E. Karaca, I. Karaman, A. Brewer, B. Basaran, Y. I. Chumlyakov, H. J. Maier, Scripta Materialia 2008, 58, 815.
26. M. Khan, N. Ali, S. Stadler, Journal of Applied Physics 2007, 101.
27. K. Koyama, T. Igarashi, H. Okada, K. Watanabe, T. Kanomata, R. Kainuma, W. Ito, K. Oikawa, K. Ishida, Journal of Magnetism and Magnetic Materials 2007, 310, 994.
28. T. Krenke, E. Duman, M. Acet, E. F. Wassermann, X. Moya, L. Manosa, A. Planes, E. Suard, B. Ouladdiaf, Physical Review B 2007, 75.
29. V. K. Sharma, M. K. Chattopadhyay, R. Kumar, T. Ganguli, P. Tiwari, S. B. Roy, Journal of Physics-Condensed Matter 2007, 19.
30. V. K. Sharma, M. K. Chattopadhyay, S. B. Roy, Journal of Physics D: Applied Physics 2007, 40, 1869.
31. Y. D. Wang, E. W. Huang, Y. Ren, Z. H. Nie, G. Wang, Y. D. Liu, J. N. Deng, H. Choo, P. K. Liaw, D. E. Brown, L. Zuo, Acta Materialia 2008, 56, 913.
32. S. Jeong, K. Inoue, S. Inoue, K. Koterazawa, M. Taya, K. Inoue, Materials Science and Engineering A 2003, 359, 253.
33. W. Ito, K. Ito, R. Y. Umetsu, R. Kainuma, K. Koyama, K. Watanabe, A. Fujita, K. Oikawa, K. Ishida, T. Kanomata, Applied Physics Letters 2008, 92.
34. H. Sehitoglu, I. Karaman, R. Anderson, X. Zhang, K. Gall, H. J. Maier, Y. Chumlyakov, Acta Materialia 2000, 48, 3311.
35. J. Dadda, H. J. Maier, D. Niklasch, I. Karaman, H. E. Karaca, Y. I. Chumlyakov, Metallurgical and Materials Transactions A, Vol. 39, pp. 2026-2039, 2008.
36. H. E. Karaca, I. Karaman, B. Basaran, Y. I. Chumlyakov, H. J. Maier, Submitted to Acta Materialia, 2008.
37. D. C. Lagoudas, B. Kiefer, A. J. Broederdorf, Proceedings of ASME, International Mechanical Engineering Congress and Exposition 2006, 1.
38. A. Brewer, M.S. Thesis, Texas A&M University, 2007.
39. H. E. Karaca, I. Karaman, Y. I. Chumlyakov, D. C. Lagoudas, X. Zhang, Scripta Materialia 2004, 51, 261.
40. D. Canadinc, J. Dadda, H. J. Maier, I. Karaman, H. E. Karaca, Y. I. Chumlyakov, Smart Mater. Struct. 2007, 16, 1006.
41. Y. Chumlyakov, E. Panchenko, I. Kireeva, I. Karaman, H. Sehitoglu, H. J. Maier, A. Tverdokhlebova, A. Ovsyannikov, Materials Science and Engineering A 2008, 481-482, 95.
42. R. F. Hamilton, H. Sehitoglu, C. Efstathiou, H. J. Maier, Y. Chumlyakov, Acta Materialia 2006, 54, 587.
43. K. Gall, H. Sehitoglu, Y. I. Chumlyakov, I. V. Kireeva, Acta Materialia 1999, 47, 1203.

44. O. Heczko, A. Sozinov, K. Ullakko, IEEE Transactions on Magnetics 2000, 36, 3266.
45. L. Straka, O. Heczko, IEEE Transactions on Magnetics 2003, 39, 3402.
46. P. Mullner, V. A. Chernenko, G. Kostorz, Journal of Magnetism and Magnetic Materials 2003, 267, 325.
47. A. Sozinov, A. A. Likhachev, N. Lanska, O. Soderberg, K. Ullakko, V. K. Lindroos, Materials Science and Engineering A 2004, 378, 399.
48. S. J. Murray, M. Marioni, S. M. Allen, R. C. O'Handley, T. A. Lograsso, Applied Physics Letters 2000, 77, 886.
49. R. D. James, R. Tickle, M. Wuttig, Materials Science and Engineering A 1999, 273-275, 320.
50. R. Tickle, R. D. James, T. Shield, M. Wuttig, V. V. Kokorin, IEEE Transactions on Magnetics 1999, 35, 4301.
51. D. C. Lagoudas, Shape Memory Alloys: Modeling and Engineering Applications, Springer, New York 2008.
52. D. J. Leo, Engineering Analysis of Smart Material Systems John Wiley & Sons, New Jersey 2007.
53. O. Heczko, Journal of Magnetism and Magnetic Materials 2005, 290-291, 787.
54. I. E. Dikshtein, D. I. Ermakov, V. V. Koledov, L. V. Koledov, T. Takagi, A. A. Tulaikova, A. A. Cherechukin, V. G. Shavrov, JETP Letters 2000, 72, 373.
55. H. Morito, A. Fujita, K. Oikawa, K. Ishida, K. Fukamichi, R. Kainuma, Applied Physics Letters 2007, 90.
56. H. Morito, A. Fujita, K. Fukamichi, R. Kainuma, K. Ishida, K. Oikawa, Applied Physics Letters 2003, 83, 4993.
57. R. C. O'Handley, J Appl Phys 1998, 83, 886.
58. R.Y. Umetsu et al., Scripta Mater. 2008, article in press.
59. Chumlyakov YI, Kireeva IV, Karaman I, Panchenko EY, Zakharova EG, Tverskov AV, Ovsyannikov AV, Nazarov KM, Kirillov VA. Russian Phys J 2004;47:893.
60. Karaca HE, Karaman I, Chumlyakov YI, Lagoudas DC, Zhang X. Scripta Mater 2004;51:261.
61. Dadda J, Maier HJ, Karaman I, Karaca HE, Chumlyakov YI. Scripta Mater 2006;55:663.
62. Sutou Y, Kamiya N, Omori T, Kainuma R, Ishida K, Oikawa K. Appl Phys Lett 2004;84(8):1275
63. Todd Heil, PhD Dissertation, Virginia Polytechnic Institute and State University, 2007
64. Masdeu F, Pons J, Segui C, Cesari E, Dutkiewicz J, J. Magn. Magn. Mater., 2005;290:816.
65. Chernenko VA, Pons J, Cesari E, Ishikawa K, Acta Mater. 2005;53:5071
66. Otsuka K, Sakamoto H, and Shimizu K, Acta Metall., 1979;27:585.
67. Kainuma R, Nakano H and Ishida K, Met. Mat. Trans. A. 1996;27A:4153.
68. Otsuka K, Wayman CM, Nakai K, Sakamoto H, Shimizu K. Acta Metall 1976;24(3):207.
69. Dadda J, Maier HJ, Karaman I, Karaca HE, Chumlyakov YI. Scripta Mater 2006;55:663.
70. Shaw JA, Kyriakides S, J. Mech. Phys. Solids 1995;43:1243.

71. Huang WM, Wu JA, Lim BY, Vahhi IE, J. Alloy Compd. 2005; 390: 175.
72. Liu ZH, Wu GH, Liu Y , Intermetallics 2006;14(12):1493.
73. Cui J, Chu YS, Famodu OO, Furuya Y, Hattrick-Simpers J, James RD, Ludwig A, Thienhaus S, Wuttig M, Zhang ZY, Takeuchi I, Nature Materials 2006;5(4):286.
74. Chernenko VA, L'vov V, Pons J, Cesari E, Journal of Applied Physics 2003;93:2394.
75. Picornell C, Pons J, Cesari E, Scripta Mater.2006; 54:459.
76. Sittner P, Novák V, Zarubová N, Acta Mater 1998; 46: 1265.
77. Ge Y, Jiang H, Sozinov A, Söderberg O, Lanska N, Keränen J, Kauppinen EI, Lindroos VK, Hannula SP, Mat. Sci. Eng. A 2006; 438: 961.
78. Pons J, Chernenko VA, Santamarta R, Cesari E, Acta Mater. 2000; 48(12): 3027.
79. Oikawa K, Ota T, Ohmori T, Tanaka Y, Morito H, Fujita A, Kainuma R, Fukamichi K, Ishida K, Appl Phys Lett 2002; 81(27): 5201.

Listing of all publications and technical reports supported under this grant or contract**(a) Book Chapters**

1. Kiefer B., and Lagoudas D. C., *Modeling of Magnetic SMA*. In: Lagoudas, D.C. (Editor), Introduction to Modeling and Engineering Applications of Shape Memory Alloys, Springer-Verlag, New York, 2008.

(b) Papers published in peer reviewed journals

1. Dadda, J., Maier, H.J., Karaman, I., and Chumlyakov, Y.I., "High Temperature In-Situ Microscopy during Stress-Induced Phase Transformations in $\text{Co}_{49}\text{Ni}_{21}\text{Ga}_{30}$ Shape Memory Alloy Single Crystals," *International Journal of Materials Research*, in press, 2010.
2. Monroe, J.A., Karaman, I., Karaca, H.E., Chumlyakov, Y.I., and Maier, H.J., "High Temperature Superelasticity and Competing Microstructural Mechanisms in $\text{Co}_{49}\text{Ni}_{21}\text{Ga}_{30}$ Shape Memory Alloy Single Crystals Under Tension," *Scripta Materialia*, Vol.62, pp. 368-371, 2010.
3. Ito, W., Basaran, B., Umetsu, R.Y., Karaman, I., Kainuma, R., and Ishida, K., "Shape Memory Response in the $\text{Ni}_{40}\text{Co}_{10}\text{Mn}_{33}\text{Al}_{17}$ Polycrystalline Alloy," *Materials Transactions JIM*, Vol. 51, pp. 525-528, 2010.
4. Dadda, J., Maier, H.J., Karaman, I., and Chumlyakov, Y.I., "Cyclic Deformation and Austenite Stabilization in $\text{Co}_{35}\text{Ni}_{35}\text{Al}_{30}$ Single Crystalline High-temperature Shape Memory Alloys," *Acta Materialia*, Vol. 57, pp. 6123-6134, 2009.
5. Karaca, H.E., Karaman, I., Basaran, B., Chumlyakov, Y.I., and Maier, H.J., "Magnetic Field-Induced Martensitic Phase Transformation in NiMnCoIn Ferromagnetic Shape Memory Alloys," *Advanced Functional Materials*, Vol. 19, pp. 983-998, 2009.
6. Kiefer B., and Lagoudas D. C., "Modeling the Coupled Strain and Magnetization Response of Magnetic Shape Memory Alloys under Magneto-mechanical Loading Paths," *Journal of Intelligent Material Systems and Structures*, Vol. 20, pp. 143-170, 2009.
7. Chumlyakov, Y.I., Panchenko, E.Y., Ovsyannikov, A.V., Chusov, S.V., Kirillov, V.A., Karaman, I., and Maier, H.J., "High-Temperature Superelasticity and the Shape-Memory Effect in [001] Co-Ni-Al Single Crystals," *Physics of Metals and Metallography*, Vol. 107, pp. 194-205, 2009.
8. Kireeva, I.V., Pobedennaya, Z.V., Chumlyakov, Y.I., Pons, J., Cesari, E., and Karaman, I., "Effect of Orientation on the High-Temperature Superelasticity in $\text{Co}_{49}\text{Ni}_{21}\text{Ga}_{30}$ Single Crystals," *Technical Physical Letters*, Vol. 35, pp. 186-189, 2009.
9. Niklasch D., Dadda J., Maier H.J., and Karaman I., "Magneto-Microstructural Coupling During Stress-Induced Phase Transformation in $\text{Co}_{49}\text{Ni}_{21}\text{Ga}_{30}$ Ferromagnetic Shape Memory Alloy Single Crystals," *Journal of Materials Science*, Vol. 43, pp. 6890-6901, 2008.
10. Karaca H.E., Karaman I., Brewer A., Basaran B., Chumlyakov Y.I., Maier H.J., "Shape Memory and Pseudoelasticity Response of NiMnCoIn Magnetic Shape Memory Alloy Single Crystals", *Scripta Materialia*, Vol. 58, Issue 10 pp. 815-818, 2008.
11. Kiefer B., and Lagoudas D.C., "Modeling of the Variant Reorientation in Magnetic Shape-Memory Alloys under Complex Magneto-mechanical Loading," *Materials Science and Engineering A*, Vol. 481-482, pp.339-342, 2008.
12. Kart S.O., Uludogan M., Karaman I., and Cagin T., "DFT Studies on Structure, Mechanics and Phase Behavior of Magnetic Shape Memory Alloys: Ni₂MnGa," *Physica Status Solidi A*, Vol. 205, pp. 1026-1035, 2008.

13. Niklasch D., Maier H.J., and Karaman I., "Design and Application of a Mechanical Load Frame for In-situ Investigation of Ferromagnetic Shape Memory Alloys by Magnetic Force Microscopy," *Review of Scientific Instruments*, Vol. 79, p. 113701, 2008.
14. Dadda J., Maier H.J., Niklasch D., Karaman I., Karaca H.E., and Chumlyakov Y.I., "Pseudoelasticity and Cyclic Stability in Co₄₉Ni₂₁Ga₃₀ Shape Memory Alloy Single Crystals at Ambient Temperature," *Metallurgical and Materials Transactions A*, Vol. 39, pp. 2026-2039, 2008.
15. Chumlyakov Y.I., Panchenko E., Kireeva I.V., Karaman I., Sehitoglu H., Maier H.J., Tverdokhlebova A., and Ovsyannikov A., "Orientation dependence and tension/compression asymmetry of shape memory effect and superelasticity in ferromagnetic Co₄₀Ni₃₃Al₂₇, Co₄₉Ni₂₁Ga₃₀ and Ni₅₄Fe₁₉Ga₂₇ single crystals," *Materials Science and Engineering A*, Vol. 481-482, pp. 95-100, 2008.
16. Chumlyakov, Y.I., Kireeva, I.V., Panchenko, E.Y., Timofeeva, E.E., Pobedennaya, Z.V., Chusov, S.V., Karaman, I., Maier, H.J., Cesari, E., and Kirillov, V.A., "High Temperature Superelasticity in CoNiGa, CoNiAl, NiFeGa, and TiNi Monocrystals," *Russian Physics Journal*, Vol. 51, pp. 1016-1036, 2008.
17. Karaca HE, Karaman I, Basaran B, Lagoudas DC, Chumlyakov YI, and Maier HJ, "On the Stress-Assisted Magnetic Field-Induced Phase Transformation in Ni₂MnGa Ferromagnetic Shape Memory Alloys," *Acta Materialia*, Vol. 55, pp. 4253-4269, 2007.
18. Kiefer B, Karaca HE, Lagoudas DC, and Karaman I, "Characterization and Modeling of the Magnetic Field-Induced Strain and Work Output in Ni₂MnGa Magnetic Shape Memory Alloys," *Journal of Magnetism and Magnetic Materials*, Vol. 312, pp. 164-175, 2007.
19. Karaman I, Basaran B, Karaca HE, Karsilayan AI, and Chumlyakov YI, "Energy Harvesting Using Martensite Variant Reorientation Mechanism in a NiMnGa Magnetic Shape Memory Alloy," *Applied Physics Letters*, Vol. 90, 172505, 2007.
20. Dadda J, Canadinc D, Maier HJ, Karaman I, Karaca HE, and Chumlyakov YI, "Stress-Strain-Temperature Behavior of [001] Single Crystals of Co₄₉Ni₂₁Ga₃₀ Ferromagnetic Shape Memory Alloy under Compression," *Philosophical Magazine*, Vol. 87, No.16, pp. 2313-2322, 2007.
21. Canadinc D, Dadda J, Maier HJ, Karaman I, Karaca HE, and Chumlyakov YI, "On the Role of Cooling Rate and Crystallographic Orientation on the Shape Memory Properties of CoNiAl Single Crystals Under Compression," *Smart Materials and Structures*, Vol. 16, pp. 1006-1015, 2007.
22. Karaman I, Karaca HE, Basaran B, Lagoudas DC, Chumlyakov YI, and Maier HJ, "Stress-Assisted Reversible Magnetic Field-Induced Phase Transformation in Ni₂MnGa Magnetic Shape Memory Alloys," *Scripta Materialia*, Vol. 55, pp. 403-406, 2006.
23. Karaca HE, Karaman I, Basaran B, Lagoudas DC, Chumlyakov YI, and Maier HJ, "One-way Shape Memory Effect due to Stress Assisted Field-Induced Phase Transformation in Ni₂MnGa Magnetic Shape Memory Alloys," *Scripta Materialia*, Vol. 55, pp. 803-806, 2006.
24. Meyer D, Maier HJ, Dadda J, Karaman I, and Karaca HE, "Thermally and Stress-Induced Martensitic Transformation in CoNiAl Ferromagnetic Shape Memory Alloy Single Crystals," *Materials Science and Engineering A*, Vol. 438-440, pp. 875-878, 2006.
25. Dadda J, Maier HJ, Karaman I, Karaca HE, and Chumlyakov YI, "Pseudoelasticity at Elevated Temperatures in [001] Oriented Co₄₉Ni₂₁Ga₃₀ Single Crystals under Compression," *Scripta Materialia*, Vol. 55, pp. 663-666, 2006.

(c) *Papers published in non-peer-reviewed journals or in conference proceedings*

1. Haldar K., Lagoudas D. C., Basaran, B., and Karaman, I., "Constitutive Modeling of Magneto-Thermo-Mechanical Response of Field Induced Phase Transformation in NiMnCoIn Magnetic Shape Memory Alloy," Proceedings of ASME, International Mechanical Engineering Congress and Exposition 2010, Accepted, September 28-October 01, 2010, Philadelphia, PA, 2010.
2. Haldar K., Lagoudas D. C., Basaran, B., and Karaman, I., "Constitutive Modeling of Magneto-Mechanical Coupling Response of Magnetic Field Induced Phase Transformations in NiMnCoIn Magnetic Shape Memory Alloys," Proc. Of SPIE 2010, Vol.7644, March 07-11, 2010, San Diego, CA, 2010.
3. Chatzigeorgiou G., Haldar K., and Lagoudas D. C., "Stability of Magnetomechanical Problem in Magnetic Shape Memory Alloys," Proc. Of SPIE 2010, Vol.7644, March 07-11, 2010, San Diego, CA, 2010.
4. Lagoudas D. C., Haldar K., Basaran, B., and Karaman, I., "Constitutive Modeling of Magnetic Field Induced Phase Transformation in NiMnCoIn Shape Memory Alloys," Proceedings of ASME, International Mechanical Engineering Congress and Exposition 2009, Paper SMASIS09-1469, September 21-23, 2009, Oxnard, CA, 2009.
5. Lagoudas D. C., Kiefer B., and Haldar K., "Magneto-mechanical Finite Element Analysis of Magnetic Shape Memory Alloys with Body Force and Body Couple," Proceedings of ASME, International Mechanical Engineering Congress and Exposition 2008, Paper SMASIS08-533.
6. Dadda, J., Maier, H.J., and Karaman, I., "Pseudoelasticity of $\text{Co}_{49}\text{Ni}_{21}\text{Ga}_{30}$ High-Temperature Shape Memory Alloy Single Crystals under Compression," SMST-2007: Proceedings of the International Conference on Shape Memory and Superelastic Technologies, December 2-5, 2007, Tsukuba, Japan, Edited by S. Miyazaki, ASM International, Materials Park, OH 44073, p. 659, 2008.
7. Lagoudas, D.C., Kiefer, B., and Broederdorff, A.J., "Accurate Interpretation of Magnetic Shape Memory Alloy Experiments Utilizing Coupled Magnetostatic Analysis", ASME International Mechanical Engineering Congress and Exposition 2006, November 5-10, 2006, Chicago, IL, 2006.
8. Lagoudas, D., Kiefer, B. and Broederdorff, A., "Constitutive Modeling of Magnetic Shape Memory Alloys with Magneto-Mechanical Coupling," Comp-07 (International Symposium on Advanced Composite Technology), May 16-18, 2007, Corfu, Greece, 2007.

(d) *Papers presented at meetings, but not published in conference proceedings*

1. Haldar K., Lagoudas D.C., Basaran, B., and Karaman, I., "Modeling of Magnetic Field Induced Phase Transformation in NiMnCoIn Magnetic Shape Memory Alloys," The 2009 joint ASCE-ASME-SES conference on Mechanics and Materials, June 24-27, 2009, Blaksburg, VT, 2009.
2. Lagoudas D.C., Kiefer B., and Haldar K., "Magnetic Field-Induced Reversible Phase Transformations in Magnetic Shape Memory Alloys," Conference on Behavior and Mechanics of Multifunctional and Composite Materials III, The International Society for Optical Engineering (SPIE) 16th Annual International Symposium on Smart Structures and Materials & Nondestructive Evaluation and Health Monitoring, March 9-12, 2009, San Diego, CA, 2009.
3. Karaman, I., Basaran, B., Zhu, R., Karaca, H.E., and Chumlyakov, Y.I., "Crystallographic Orientation and Heat Treatment Effect on Magnetic Field-Induced

- Phase Transformations of NiMnCoIn Metamagnetic Shape Memory Alloys," Symposium on Magnetic Shape Memory Alloys, MRS Fall Meeting, November 30 - December 4, 2009, Boston, MA, 2009.
4. Karaca, H.E., Karaman, I., Basaran, B., and Chumlyakov, Y.I., "Magnetic Field-Induced Phase Transformations in NiMn-based Shape Memory Alloys," Symposium on Active Materials, Mechanics and Behavior, ASME 2009 Conference on Smart Materials, Adaptive Structures and Intelligent Systems, September 21-23, 2009, Oxnard, CA, 2009.
 5. Basaran, B., Karaman, I., Zhu, R., Karaca, H.E., and Chumlyakov, Y.I., "The Effect of Simultaneous Stress and Magnetic Field on the Actuator Type Response of NiMnCoIn and NiMnCoSn Metamagnetic Shape Memory Alloys," Symposium on Active Materials, Mechanics and Behavior, ASME 2009 Conference on Smart Materials, Adaptive Structures and Intelligent Systems, September 21-23, 2009, Oxnard, CA, 2009.
 6. Lagoudas, D.C., Haldar, K., Basaran, B., and Karaman, I., "Constitutive Modeling of Magnetic Field-Induced Phase Transformations in NiMnCoIn Magnetic Shape Memory Alloys," Symposium on Active Materials, Mechanics and Behavior, ASME 2009 Conference on Smart Materials, Adaptive Structures and Intelligent Systems, September 21-23, 2009, Oxnard, CA, 2009.
 7. Karaca, H.E., Karaman, I., Basaran, B., Chumlyakov, Y.I., and Maier, H.J., "Characterization of Ferromagnetic CoNiAl and NiFeGa Alloys for High Temperature Shape Memory Applications," Symposium on Active Materials, Mechanics and Behavior, ASME 2009 Conference on Smart Materials, Adaptive Structures and Intelligent Systems, September 21-23, 2009, Oxnard, CA, 2009.
 8. Karaca, H.E., Basaran, B., Karaman, I., and Chumlyakov, Y.I., "Characterization of Magnetic Field-Induced Phase Transformations in NiMnCoIn Meta-magnetic Shape Memory Alloys," Symposium on Domain Microstructures and Mechanisms for Advanced Properties in Phase Transforming Materials, Materials Science & Technology 2009 Conference, October 25-29, 2009, Pittsburgh, PA, 2009.
 9. Kireeva, I.V., Pobedennaya, Z.V., Chumlyakov, Y.I., Kretinina, I.V., Cesari, E., Pons, J., and Karaman, I., "Characteristics of Superelasticity in Ferromagnetic <001> Single Crystals of a CoNiGa Alloy during Compressive Deformation," The 8th European Symposium on Martensitic Transformations, September 7-11, 2009, Prague, Czech Republic, 2009.
 10. Ren, Y., Wang, Y.D., Nie, Z.H., Karaman, I., Karaca, H.E., Gama, S., and Brown, D.E., "High-Energy Synchrotron X-Ray Diffraction for In-Situ Study of Structural Phase Transformations," Symposium on Domain Microstructures and Mechanisms for Advanced Properties in Phase Transforming Materials, Materials Science & Technology 2009 Conference, October 25-29, 2009, Pittsburgh, PA, 2009.
 11. Chumlyakov, Y.I., Kireeva, I.V., Panchenko, E.Y., Maier, H.J., Karaman, I., Timofeeva, E.E., Pobedennaya, Z.V., and Kirillov, V.A., "High Temperature Superelasticity in Ferromagnetic Single Crystals with Thermoelastic Martensitic Transformation," The 8th European Symposium on Martensitic Transformations, September 7-11, 2009, Prague, Czech Republic, 2009.
 12. Karaman I., Karaca H.E., Basaran B., and Chumlyakov Y.I., " Magnetic Field-Induced Phase Transformation in NiMnCoIn Metamagnetic Shape Memory Alloys," The Symposium on Shape Memory Alloys - Mechanisms, Multifunctionalities, and Applications, The 45th Annual Technical Meeting of Society of Engineering Science (SES), Urbana, IL, October 12 – 15, 2008.

13. Basaran B., Karaman I., Karaca H.E., and Karsilayan, A.I., "Utilization of Magnetic Shape Memory Alloys in Energy Harvesting," The International Conference on Martensitic Transformations (ICOMAT 08), June 29 – July 4, 2008, Santa Fe, NM, 2008.
14. Karaman I., Karaca H.E., Basaran B., Chumlyakov Y.I., and Maier, H.J., "Magnetic Field-Induced Phase Transformation in NiMnCoIn Shape Memory Alloys," The International Conference on Martensitic Transformations (ICOMAT 08), June 29 – July 4, 2008, Santa Fe, NM, 2008.
15. Karaca, H.E., Karaman, I., Badakhshan, S., Basaran, B., Chumlyakov Y.I., Niklasch D., and Maier H.J., "Shape Memory Behavior of NiFeGa(Co) Ferromagnetic Shape Memory Single Crystals," The International Conference on Martensitic Transformations (ICOMAT 08), June 29 – July 4, 2008, Santa Fe, NM, 2008.
16. Niklasch, D., Maier, H.J., Karaman, I., and Chumlyakov, Y.I., "In-Situ Characterization of Stress-Induced Martensite and Related Magnetic Domain Structure in Ni-Fe-Ga Ferromagnetic Shape Memory Alloy Single Crystals," International Conference on Martensitic Transformation (ICOMAT) 2008, June 29 – July 5, 2008, Santa Fe, NM, 2008.
17. Dadda, J., Maier, H.J., Karaman, I., and Karaca, H.E.*, "Functional Degradation of CoNiAl and CoNiGa High-Temperature Shape Memory Alloy Single Crystals at Elevated Temperatures upon Cyclic Deformation," International Conference on Martensitic Transformation (ICOMAT) 2008, June 29 – July 5, 2008, Santa Fe, NM, 2008.
18. Maier H.J., Niklasch D., and Karaman I., "Magneto-Microstructural Characterization of Magnetic Shape Memory Alloys," The 3rd International Conference on Smart Materials, Structures and Systems (CIMTEC 2008), Symposium A: Smart Materials and Micro/Nanosystems, June 8-13, 2008, Acireale, Sicily, Italy, 2008.
19. Karaman I., Karaca H.E., Basaran B., Chumlyakov Y.I., and Maier H.J., "Magnetic Field-Induced Phase Transformation in NiMnGa and NiMnCoIn Shape Memory Alloys," Conference on Behavior and Mechanics of Multifunctional and Composite Materials II, The International Society for Optical Engineering (SPIE) 15th Annual International Symposium on Smart Structures and Materials & Nondestructive Evaluation and Health Monitoring, March 9-13, 2008, San Diego, CA, 2008.
20. Karaca, H.E., Karaman, I., Chumlyakov, Y.I., and Maier, H.J., "Shape Memory Behavior of NiFeGa(Co) Ferromagnetic Shape Memory Single Crystals," Conference on Behavior and Mechanics of Multifunctional and Composite Materials, The International Society for Optical Engineering (SPIE) 15th Annual International Symposium on Smart Structures and Materials & Nondestructive Evaluation and Health Monitoring, March 9-13, 2008, San Diego, CA, 2008.
21. Karaman I., Karaca H.E., Basaran B., Chumlyakov Y.I., and Maier H.J., "Crystallographic Orientation Dependence of Magnetic Field-Induced Phase Transformation in NiMnCoIn Single Crystals," The Symposium on "Magnetic Shape Memory Alloys," 2007 Materials Research Society (MRS) Fall Meeting, November 26-30, 2007, Boston, MA, 2007.
22. Karaca H.E., Basaran B., Karaman I., Chumlyakov Y.I., Niklasch D., and Maier H.J., "Compressive response of NiFeGa Ferromagnetic Shape Memory Single Crystals," The Symposium on Shape Memory Alloys - Mechanisms, Multifunctionalities, and Applications, The 44th Annual Technical Meeting of Society of Engineering Science (SES), College Station, TX, October 21 – 24, 2007.
23. Basaran, B., Karaca H.E., Karaman I., and Chumlyakov Y.I., "Enhancing Actuator Properties of NiMnCoIn Magnetic Shape Memory Alloys by Field-Induced Phase

- Transformation," The Symposium on Shape Memory Alloys - Mechanisms, Multifunctionalities, and Applications, The 44th Annual Technical Meeting of Society of Engineering Science (SES), College Station, TX, October 21 – 24, 2007.
- 24. Karaca HE, Karaman I, Basaran B, and Chumlyakov YI, "Magnetic Field-Induced Phase Transformation in NiMnGa and NiMnCoIn Shape Memory Alloys," ASME Applied Mechanics and Materials Conference, Phase Transformations and Mechanochemistry Symposium, June 3-7, 2007, Austin, TX, 2007.
 - 25. Karaman I, Karaca HE, and Basaran B, "Reversible field-induced phase transformation in Ni₂MnGa with large actuation stress and work output," Conference on Behavior and Mechanics of Multifunctional and Composite Materials, The International Society for Optical Engineering (SPIE) 14th Annual International Symposium on Smart Structures and Materials, March 18-22, 2007, San Diego, CA, 2007.
 - 26. Lagoudas, D.C. and Kiefer, B., "Modeling of Magnetic Shape Memory Alloys", , The International Society for Optical Engineering (SPIE) 14th Annual International Symposium on Smart Structures and Materials, March 18-22, 2007, San Diego, CA, 2007
 - 27. Basaran B, Karaca HE, Karaman I, Chumlyakov YI, and Maier HJ, "Effect of Magnetic Field on the Multi-Stage Martensitic Phase Transformation in NiMnGa Magnetic Shape Memory Alloys," Symposium on Fundamentals of Shape Memory and Related Transitions, TMS 2007 Annual Meeting, February 25 – March 1, 2007, Orlando, FL, 2007.
 - 28. Lagoudas, D., Kiefer, B. and Broederdorff, A., "Constitutive Modeling of Magnetic Shape Memory Alloys with Magneto-Mechanical Coupling," Comp-07 (International Symposium on Advanced Composite Technology), May 16-18, 2007, Corfu, Greece, 2007.
 - 29. Lagoudas, D.C., Kiefer, B., and Broederdorff, A.J., "Accurate Interpretation of Magnetic Shape Memory Alloy Experiments Utilizing Coupled Magnetostatic Analysis", ASME International Mechanical Engineering Congress and Exposition 2006, November 5-10, 2006, Chicago, IL, 2006.
 - 30. Kart SO, Uludogan M, Karaman I, and Cagin T, "DFT Studies on Magnetic Shape Memory Alloys," 62nd Southwest Regional Meeting of the American Chemical Society, October 19-22, 2006, Houston, Texas, 2006.
 - 31. Karaman I, Karaca HE, Basaran B, Lagoudas DC, Chumlyakov YI, and Maier HJ, "Reversible Field-Induced Phase Transformation in Ni₂MnGa with Large Actuation Stress and Work Output," The 7th European Symposium on Martensitic Transformations and Shape Memory Alloys, September 10-15, 2006, Bochum, Germany, 2006.
 - 32. Karaca HE, Karaman I, Basaran B, Chumlyakov YI, and Maier HJ, "Remarkable Pseudoelastic Response of Co₄₈Ni₃₃Al₉ and Ni₅₄Ga₂₇Fe₁₉ Ferromagnetic Shape Memory Alloys under Tension and Compression," The 7th European Symposium on Martensitic Transformations and Shape Memory Alloys, September 10-15, 2006, Bochum, Germany, 2006.
 - 33. Basaran B, Karaca HE, Karaman I, Chumlyakov YI, and Maier HJ, "Guidelines to Increase Actuation Stress in NiMnGa Magnetic Shape Memory Alloys," The 7th European Symposium on Martensitic Transformations and Shape Memory Alloys, September 10-15, 2006, Bochum, Germany, 2006.
 - 34. Dadda J, Maier HJ, Karaman I, Karaca HE, and Chumlyakov YI, "Pseudoelasticity in Co₄₉Ni₂₁Ga₃₀ Ferromagnetic Shape Memory Single Crystals Under Compression," The 7th European Symposium on Martensitic Transformations and Shape Memory Alloys, September 10-15, 2006, Bochum, Germany, 2006.

35. Chumlyakov YI, Panchenko E, Kireeva IV, Karaman I, Sehitoglu H, Maier H, Ovsyannikov A, and Tverdokhlebova A, "Orientation dependence of shape memory effect and superelasticity in ferromagnetic Co-Ni-Al, Co-Ni-Ga, Ni-Fe-Ga single crystals," The 7th European Symposium on Martensitic Transformations and Shape Memory Alloys, September 10-15, 2006, Bochum, Germany, 2006.

(e) *Manuscripts submitted but not published*

1. Karaca H.E., Karaman I., Basaran B., Chumlyakov Y.I., Maier H.J., "Compressive Response of NiFeGa Magnetic Shape Memory Alloys," submitted to *Acta Materialia*, 2010.
2. Haldar K., Chatzigeorgiou G., and Lagoudas D. C., "Stability Analysis of Magnetostatic Boundary Value Problems for Magnetic SMAs," *Journal of Intelligent Material Systems and Structures*, submitted, 2010.

(f) *Technical reports submitted to ARO*

Two interim progress reports.

5. List of all Participating Scientific Personnel showing any Advanced Degrees Earned by them while employed on the Project

- a) Dr. I. Karaman (PI): Texas A&M University – Materials design, fabrication, and characterization, and magneto-thermo-mechanical properties
- b) Dr. D.C. Lagoudas (Co-PI): Texas A&M University – Modeling
- c) Robert Barber (Research Associate/Engineer): Texas A&M University – Die/tool/fixture design and fabrication, materials processing
- d) Bjoern Kiefer (Graduate Research Assistant - Ph.D. Student): Texas A&M University – Modeling. He earned his Ph.D. degree working in this project. He is currently a faculty at the University of Stuttgart, Germany.
- e) Haluk Ersin Karaca (Graduate Research Assistant – Ph.D. Student): Texas A&M University – magneto-microstructural characterization, magneto-thermo-mechanical property characterization. He earned his Ph.D. degree working in this project. He is currently a faculty at the University of Kentucky.
- f) Burak Basaran (Graduate Research Assistant – Ph.D. Student): Texas A&M University – Magnetothermomechanical test set-up design, building and property characterization. He earned his Ph.D. degree working in this project. He is currently a post-doc at the University of Kentucky.
- g) Krishnendu Haldar (Graduate Research Assistant - Ph.D. Student): Texas A&M University – Modeling.
- h) Sadegh Badakhshan Raz (Graduate Research Assistant - Ph.D. Student): Texas A&M University – New alloy design, fabrication, and characterization, electrical resistivity set-up design and fabrication.
- i) Cengiz Yegin (Graduate Research Assistant - Ph.D. Student): Texas A&M University – Magneto-thermo-mechanical characterization.
- j) Andrew L. Brewer (Graduate Research Assistant – M.S. Student): Texas A&M University – Magneto-thermo-mechanical characterization of NiMnCoIn Metamagnetic Shape Memory Alloys. He earned his M.S. degree working in this project. He is currently working for CIA.

- k) Ruixian Zhu (Graduate Research Assistant – M.S. Student): Texas A&M University – Magneto-thermo-mechanical characterization, theoretical studies on elasticity modulus and mechanical and thermal hysteresis. He earned his M.S. degree working in this project. He is currently a Ph.D. student at Texas A&M University.
- l) Alicia Broederdorf (Undergraduate Research Assistant): Texas A&M University – Modeling. She earned her B.S. degree working in this project.
- m) James A. Monroe (Undergraduate Research Assistant): Texas A&M University – Physical property characterization, effect of heat treatment and precipitation on SMA characteristics. He earned his B.S. degree working in this project. He is currently a Ph.D. student at Texas A&M University.

6. Report of Inventions

None

Part-II: Modeling Accomplishment

1 MAGNETOSTATIC BOUNDARY VALUE PROBLEM FOR MSMAs

A major complication in measuring material properties of ferromagnetic materials is the influence of the demagnetization effect. The demagnetization effect and the resulting shape-dependent difference between the applied field and the internal field make measurements of MSMA properties difficult to interpret. Since for non-ellipsoidal specimen the internal magnetic field and thus induced magnetization is nonuniform, the approximation of uniform magnetization is usually adopted. In this work, nonuniform magnetization inside the MSMA specimen is taken into account to find out the demagnetization effect by explicitly solving the magnetostatic problem for relevant geometries. This work also describes a methodology by which experimental data can be interpreted more accurately. An iterative solution technique is described to obtain the relation between the applied magnetic field and the magnetic field inside the specimen.

1.1 Field and Constitutive Equations

In the following paragraphs we will provide the basic concepts of magnetostatics of MSMA materials. For static conditions in stationary magnetized bodies and negligible free currents, Maxwell's equations reduce to [1, 2]

$$\nabla \cdot \mathbf{B} = 0, \quad \text{and} \quad \nabla \times \mathbf{H} = \mathbf{0}. \quad (1)$$

The magnetization vector \mathbf{M} , the magnetic induction \mathbf{B} and the magnetic field \mathbf{H} are related through the following constitutive equation

$$\mathbf{B} = \mu_0(\mathbf{M} + \mathbf{H}). \quad (2)$$

Equations (1) are subject to the jump conditions

$$[\mathbf{B}] \cdot \mathbf{n} = 0, \quad [\mathbf{H}] \times \mathbf{n} = \mathbf{0}, \quad (3)$$

on all interfaces, if surface currents are negligible. Here, μ_0 is the permeability of the free space and in equation (3) \mathbf{n} denotes the unit vector normal to the surface of discontinuity.

For a MSMA, the magnetization vector is identified through an appropriate phenomenological model. The model is based on the Gibbs free energy function G , in which the Cauchy stress tensor $\boldsymbol{\sigma}$ and the magnetic field

strength \mathbf{H} are the independent state variables. The loading history dependence of the constitutive behavior, caused by dissipation associated with variant rearrangement, is introduced through the evolution of internal state variables. The chosen internal state variables are the variant volume fraction ξ , the magnetic domain volume fraction α and the magnetization rotation angles $\theta_i (i=1,4)$. These variables are motivated by experimentally observed changes ([3]) in the crystallographic and magnetic microstructure. An idealized microstructural representation of the twinned martensitic phase is given in Figure 1. Two martensitic variants, variant-1 with volume fraction, ξ , and variant-2 with volume fraction, $1 - \xi$, form 90° magnetic domain walls and each variant contains 180° domain walls. The volume fractions of 180° magnetic domain wall in variant-1 and variant-2 are represented in Figure 1 by domain-1 and domain-2 and denoted by α and $1 - \alpha$ respectively.

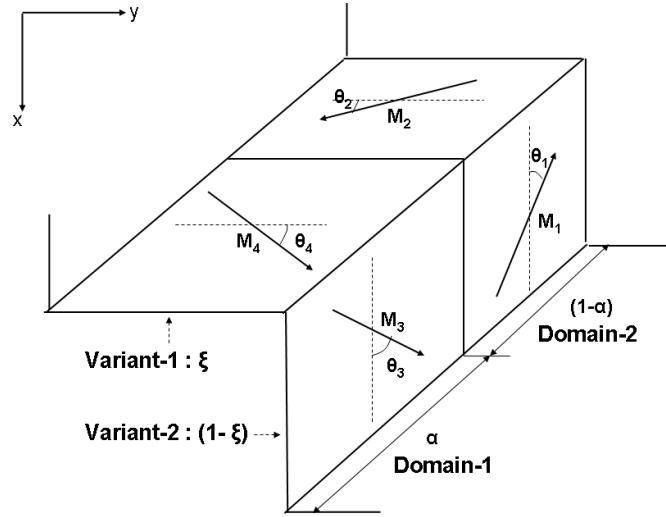


Figure 1: Schematic representation of the microstructure showing the coexistence of martensitic variants and magnetic domains ([4]).

The specific form of the Gibbs free energy is given by [4]

$$G(\boldsymbol{\sigma}, \mathbf{H}, T, \boldsymbol{\varepsilon}^r, \xi, \alpha, \theta_i) = -\frac{1}{2\rho} \boldsymbol{\sigma} : \mathcal{S} \boldsymbol{\sigma} - \frac{1}{\rho} \boldsymbol{\sigma} : \boldsymbol{\varepsilon}^r - \frac{\mu_0}{\rho} \mathbf{M} \cdot \mathbf{H} + \frac{1}{\rho} f(\xi, \alpha) + \{\xi(1-\alpha)G_2^{an}(\theta_2) + (1-\xi)(1-\alpha)G_1^{an}(\theta_1) + \xi\alpha G_4^{an}(\theta_4) + (1-\xi)\alpha G_3^{an}(\theta_3)\} + G_0(T), \quad (4)$$

where ρ , \mathcal{S} , $\boldsymbol{\varepsilon}^r$, f , G_k^{an} and G_0 are the density, the effective compliance tensor, the reorientation strain tensor, a hardening function, the magnetocrystalline

anisotropy energy of the k^{th} domain and a reference state energy respectively. The free energy function (4) is comprised of the elastic strain energy, the Zeeman energy, a mixing term, the magnetocrystalline anisotropy energy, and a reference state energy. The Zeeman or external field energy aims to align the internal magnetization with the externally applied magnetic field. The magnetocrystalline anisotropy energy can be viewed as the energy stored in the material due to the work done by an applied field in rotating the magnetization away from the magnetic easy axes.

The internal variables ξ , α and θ_i can in general be connected with energy dissipation. Experimental results ([5]) show that the hysteresis for the single variant MSMA crystal specimen with respect to the magnetic easy axis and hard axis are almost negligible. This observation was expected for the case of the hard axis magnetization response, since the dominant mechanism, related with the magnetization rotation θ_i , is a reversible process. With regard to the easy axis magnetization, magnetic domain wall motion is the most important mechanism that can be associated with dissipation. Permanent magnets, for example, exhibit large hysteresis effects due to micro-scale pinning sites and other phenomena [6, 7]. In MSMA, however, the magnetic domain wall motion appears to be associated with a very small amount of dissipation.

The dissipation in MSMAs is mainly due to variant reorientation mechanism which is caused due to the change in ξ , allowing to neglect the α dependency of the hardening function f . From the free energy expression (4) the constitutive equations are derived in a thermodynamically consistent manner, such that the magnetization constitutive equation becomes

$$\mathbf{M} = -\frac{\rho}{\mu_0} \frac{\partial G}{\partial \mathbf{H}}. \quad (5)$$

By using the Gibbs energy function (4) and the 1st law of thermodynamics, Coleman-Noll entropy principle obeys the following inequality

$$\boldsymbol{\pi}^r : \dot{\boldsymbol{\epsilon}}^r + \pi_\xi \dot{\xi} + \pi_\alpha \dot{\alpha} + \sum_i^4 \pi_{\theta_i} \dot{\theta}_i \geq 0 \quad (6)$$

where $\boldsymbol{\pi}^r = -\rho \frac{\partial G}{\partial \boldsymbol{\epsilon}^r}$, $\pi_\xi = -\rho \frac{\partial G}{\partial \xi}$, $\pi_\alpha = -\rho \frac{\partial G}{\partial \alpha}$, $\pi_{\theta_i} = -\rho \frac{\partial G}{\partial \theta_i}$ are the thermodynamic driving forces. As the rotation of magnetization vector and magnetic domain wall motion do not have any dissipation effect ([5]), we have $\pi_{\theta_i} = 0$, $\pi_\alpha = 0$.

1.2 Explicit Form of Magnetization Constitutive Equations

In this section we present a special reduced form of magnetization constitutive equations in 2-D, consistent with the experiment, to capture some main features of the MSMA. In a typical experiment, a martensitic MSMA sample is subjected to a constant mechanical load along the long axis, which is the x -axis, and subsequently to a perpendicular magnetic field in the y -axis. The stress is assumed to be uniaxial and uniform inside the specimen. The effects of magnetic body force and magnetic body couple are neglected in the present work and the magnetomechanical coupling will be studied in a subsequent paper. The x -component of the applied magnetic field is zero. However, the magnetic field along the x direction due to the magnetization of the body is assumed to be small and the dependence $\mathbf{M}(H_x)$ is neglected. So the magnetization components are assumed to have the form of $M_x = M_x(H_y)$ and $M_y = M_y(H_y)$. Under these conditions, the general 3-D magnetostatic problem can be reduced to a simpler 2-D problem by considering the components of the field variables in the following form

$$\mathbf{H} = \{H_x, H_y, 0\}, \mathbf{M} = \{M_x, M_y, 0\}, \mathbf{B} = \{B_x, B_y, 0\}. \quad (7)$$

We also assume that the only non-zero stress component is σ_{xx} , which is uniform and constant inside the specimen during the experiment.

In the martensitic phase (Figure 1), $\mathbf{M}_1, \mathbf{M}_2, \mathbf{M}_3, \mathbf{M}_4$ represent the magnetization vectors of variant-2 in domain-2, variant-1 in domain-2, variant-2 in domain-1 and variant-1 in domain-1 respectively. θ_i represents the corresponding rotation of the magnetization vector \mathbf{M}_i from the magnetic easy axis (dotted line). If \mathbf{M} is the total magnetization vector contributed from each variant and domain volume fraction, then

$$\mathbf{M} = (1 - \xi)\{(1 - \alpha)\mathbf{M}_1 + \alpha\mathbf{M}_3\} + \xi\{(1 - \alpha)\mathbf{M}_2 + \alpha\mathbf{M}_4\}, \quad (8)$$

where

$$\mathbf{M}_1 = M^{sat}(-\cos \theta_1 \mathbf{e}_x + \sin \theta_1 \mathbf{e}_y), \mathbf{M}_2 = M^{sat}(\sin \theta_2 \mathbf{e}_x - \cos \theta_2 \mathbf{e}_y), \quad (9)$$

$$\mathbf{M}_3 = M^{sat}(\cos \theta_3 \mathbf{e}_x + \sin \theta_3 \mathbf{e}_y), \mathbf{M}_4 = M^{sat}(\sin \theta_4 \mathbf{e}_x + \cos \theta_4 \mathbf{e}_y), \quad (10)$$

and M^{sat} represents the saturation magnetization. The rotation angles are directly related with the the anisotropy energy. An explicit form of magnetocrystalline anisotropy energy for uniaxial symmetry is usually given by ([8]),

$$G_i^{an} = K_1 \sin^2 \theta_i. \quad (11)$$

where K_1 is the coefficient to be determined from magnetization measurement and θ is the rotation angle between the magnetization and the easy axis.

We will now present the expressions of magnetization vector before reorientation, during reorientation and after reorientation.

1. Before Reorientation

Before reorientation starts we only have stress-favored variant in the initial configuration. Since the MSMA specimen does not have any remnant magnetization before applying the magnetic field, only 180° domain walls exist. When the magnetic field is applied along the y-direction, the hard axis of the stress-favored variant, the magnetization vectors start rotating in each domain. The domain walls do not move since there is no magnetic field acting along the easy axis of the stress-favored variant. The x component of the magnetization vector in the adjacent domain alters the direction and cancels out when added and gives zero resultant magnetization. On the other hand, the y components of the magnetization vectors are added up and give a resultant magnetization.

In this region, we have $\xi = 0$ and $\alpha = \frac{1}{2}$. Moreover, from $\pi_{\theta_1} = \pi_{\theta_3} = 0$ we get $\sin \theta_1 = \sin \theta_3 = \frac{\mu_0 M^{sat}}{2\rho K_1} H_y$.

Equation (8) gives the magnetization vector,

$$\mathbf{M} = \frac{1}{2}(\mathbf{M}_1 + \mathbf{M}_3) = M^{sat} \sin \theta_1 \mathbf{e}_y \quad \text{or} \quad \mathbf{M} = \frac{\mu_0 (M^{sat})^2}{2\rho K_1} H_y \mathbf{e}_y. \quad (12)$$

The above result shows that we only have y component of the magnetization vector in the macroscopic scale.

2. During Reorientation

Once the critical field for the variant reorientation has been reached, the field-favored variant nucleates and a sharp change in the slope of magnetization curve occurs. In this configuration the magnetic domain wall motion is initiated due to the formation of 90° domain and it is assumed that the unfavorable magnetic domains in the field-favored variant are eliminated simultaneously with the activation of the reorientation process due to comparative high magnetic field ([9, 10]).

Here, $\alpha = 1$ and equations $\pi_{\theta_3} = \pi_{\theta_4} = 0$ lead to $\sin \theta_3 = \frac{\mu_0 M^{sat}}{2\rho K_1} H_y$ and $\theta_4 = 0$. Considering the above results, the expression for the macroscopic magnetization vector \mathbf{M} (Equation (8)) is given below.

$$\begin{aligned}\mathbf{M} &= (1 - \xi) \mathbf{M}_3 + \xi \mathbf{M}_4 = \\ M^{sat}((1 - \xi) \cos \theta_3 + \xi \sin \theta_4) \mathbf{e}_x + M^{sat}((1 - \xi) \sin \theta_3 + \xi \cos \theta_4) \mathbf{e}_y,\end{aligned}\quad (13)$$

and by substituting the expression of θ_3 and θ_4 , we get

$$\mathbf{M} = (1 - \xi) \sqrt{1 - \left(\frac{\mu_0 M^{sat}}{2\rho K_1} H_y\right)^2} \mathbf{e}_x + (1 - \xi) \frac{\mu_0 M^{sat}}{2\rho K_1} H_y \mathbf{e}_y. \quad (14)$$

The expression of ξ can be obtained from the equation $\pi_\xi = 0$ by using Kuhn-Tucker loading conditions and a specific form of hardening function. More detail derivation is given in [4]. Here we will present the evolution equation of ξ for a constant applied traction during the forward reorientation process. The expression is given below,

$$\xi = \frac{1}{2} \cos \left[F_1 \left(\frac{(\mu_0 M^{sat})^2}{2\rho K_1} H_y^2 - \mu_0 M^{sat} H_y \right) + F_2 + \pi \right] + \frac{1}{2}. \quad (15)$$

The model parameters F_1 and F_2 are functions of M^{sat} , ρK_1 , $H_y^{s(1,2)}$, $H_y^{f(1,2)}$. Here we introduce two more new material parameters $H_y^{s(1,2)}$ and $H_y^{f(1,2)}$, which denote the beginning and the end of the reorientation process. These parameters can be found from experiments.

3. After Reorientation

After complete reorientation, only field induced martensitic variant is present and the magnetization process becomes saturated. The magnetization vectors are aligned along the applied magnetic field, which is the easy axis of the field-favored variant.

In this situation we have $\xi = 1$ and $\alpha = 1$. Equation $\pi_{\theta_4} = 0$ gives $\theta_4 = 0$ and the magnetization vector is given by

$$\mathbf{M} = \mathbf{M}_4 = M^{sat} \sin \theta_4 \mathbf{e}_x + M^{sat} \cos \theta_4 \mathbf{e}_y = M^{sat} \mathbf{e}_x. \quad (16)$$

Exemplary model predictions of the magnetic field-induced strain and the magnetization response are depicted in Figure 2 and 3 for different constant stress levels. This particular prediction is based on model parameters calibrated from data published by Heczko et al. 2003[11].

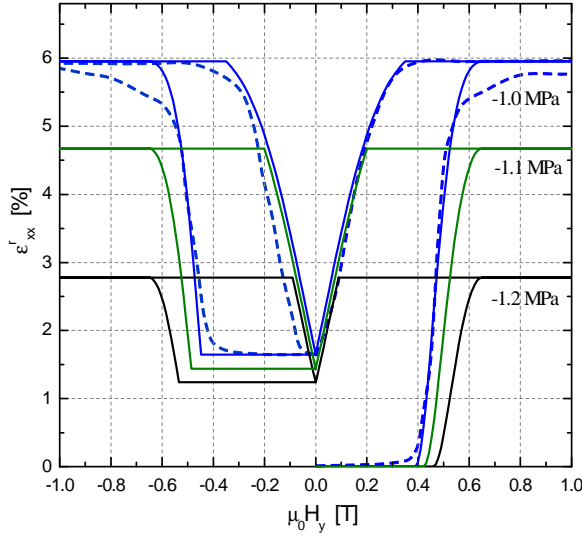


Figure 2: Predicted MFIS hysteresis curves at different stress levels (solid lines) and comparison to experimental data (dashed line) [11].

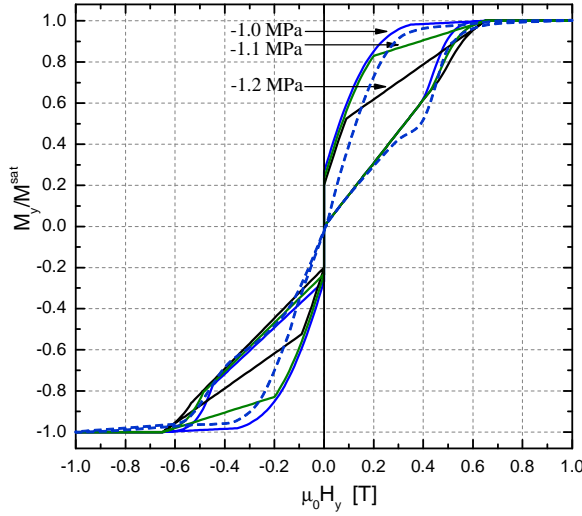


Figure 3: Predicted magnetization hysteresis curves at different stress levels (solid lines) and comparison to experimental data [11] at -1.0 MPa (dashed line).

1.3 Finite Element Analysis of the Magnetostatic Problem

A typical experiment consists of subjecting a martensitic MSMA sample to a constant mechanical load and subsequently to a perpendicular magnetic

field. This particular setup has motivated using the computational domain depicted in Fig. 4 to solve a relevant magnetostatic problem using the finite element method. All magnetostatic analysis was performed using the COMSOL Multiphysics (formerly Femlab) finite element software package in which the constitutive model was used to provide the magnetic properties of the MSMA sample.

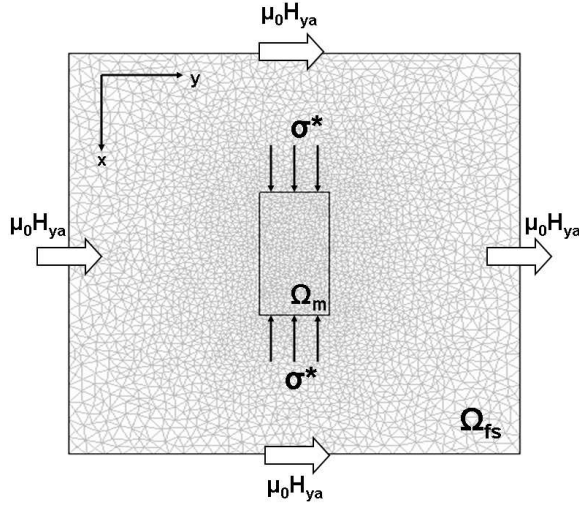


Figure 4: Schematic of the 2D domain geometry with magnetic and mechanical boundary conditions. The domain Ω_m denotes the specimen with an applied constant traction σ^* . Ω_{fs} denotes the free space surrounded by the specimen with the magnetic boundary conditions $\mu_0 H_y^a$.

According to the electromagnet's specifications, a uniform magnetic field can be assumed in the empty gap between the pole pieces of dimensions 26mm \times 26mm \times 26mm. Typical specimen dimensions are 8mm \times 4mm \times 4mm, or aspect ratios of 2:1:1, where the long axis is the x -direction.

A spatially constant magnetic flux is applied on all sides of the boundary, or, more precisely, the potential

$$\Phi_x^m = \Phi_y^m = 0 ; \quad \Phi_z^m = -\mu_0 H_y^a x , \quad (17)$$

is applied, such that with Eq. (45) it follows

$$\begin{aligned}\mu_0 H_x = B_x &= \frac{\partial \Phi_z^m}{\partial y} - \frac{\partial \Phi_y^m}{\partial z} = 0 ; \quad \mu_0 H_y = B_y = \frac{\partial \Phi_x^m}{\partial z} - \frac{\partial \Phi_z^m}{\partial x} = \mu_0 H_y^a ; \\ \mu_0 H_z = B_z &= \frac{\partial \Phi_y^m}{\partial x} - \frac{\partial \Phi_x^m}{\partial y} = 0 .\end{aligned}\tag{18}$$

This results is the desired homogeneous magnetic field in the computational domain if no specimen is included. The presence the MSMA sample in the gap of course perturbs the homogeneity of the computed field.

Table 1: Material parameters for the Ni_{51.1}Mn_{24.0}Ga_{24.9} composition [12] at -2 MPa.

Material Parameters					
Quantity	Value	Unit	Quantity	Value	Unit
ρK_1	700.0	kJm ⁻³	$\mu_0 H_y^{s(1,2)}$	0.9	T
M^{sat}	742.4	kAm ⁻¹	$\mu_0 H_y^{f(1,2)}$	1.85	T
$\varepsilon^{\text{r,max}}$	5.65	%	$\mu_0 H_y^{s(2,1)}$	0.75	T
σ^*	-2.0	MPa	$\mu_0 H_y^{s(2,1)}$	-0.17	T
ξ^{crit}	1.0				

Table 2: Hardening and hysteresis parameters for the Ni_{51.1}Mn_{24.0}Ga_{24.9} composition [12] at -2 MPa.

Model Parameters		
Quantity	Value	Unit
A^c	-60.807	kPa
B_1^c	75.411	kPa
B_2^c	96.736	kPa
C^c	-183.975	kPa
$Y^{\xi,c}$	223.572	kPa

For the calibration stress level of -2MPa the magnetic field-induced strain hysteresis loop depicted in Fig. 5 results from the material parameters and model parameters of Table 1 and Table 2 respectively. The corresponding magnetization behavior predicted by the model is shown in Fig. 6.

The following assumptions are made for using the magnetization data in the magnetostatic analysis

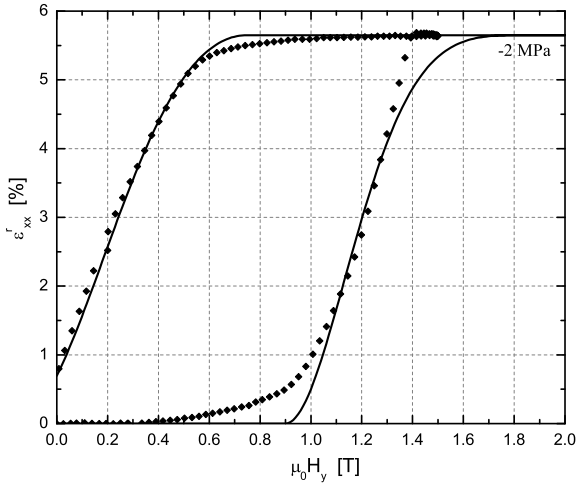


Figure 5: Model Calibration. Experimental data (diamonds) and model simulation (solid line). Data (taken from [12]) for a Ni_{51.1}Mn_{24.0}Ga_{24.9} alloy tested at -95°C under the compressive stress of 2 MPa.

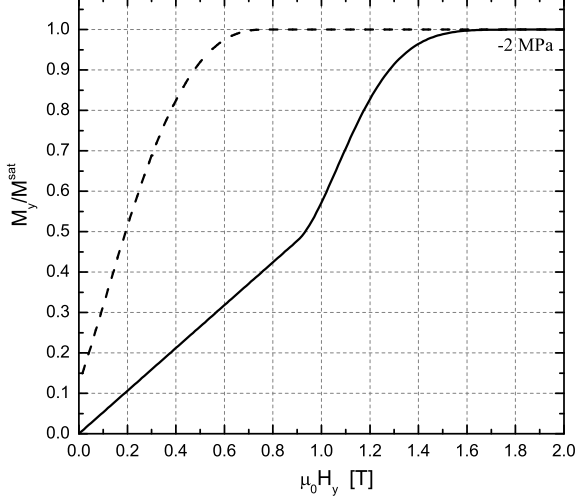


Figure 6: Predicted y-component of the magnetization at the compressive stress of 2 MPa. Only the solid portion of the curve is used in the magneto-static analysis.

1. The stress is assumed to be uniaxial, at a constant level and spatially homogeneous, since magnetic body forces and magnetic body couples are neglected. The only coupling between the mechanical and the mag-

netostatic problem at this point is given by the stress level dependence of the magnetic properties. Thus for each stress level the magnetostatic analysis has to be performed in a separate computation.

2. The magnetic field, and thus the magnetization, on the other hand vary spatially inside the prismatic specimen. The magnetic properties predicted by constitutive behavior are evaluated separately at every integration point in the finite element mesh. Since the magnetization depends on the applied field in a nonlinear fashion the magnetostatic problem is highly nonlinear¹. COMSOL Multiphysics provides an appropriate iterative nonlinear solver. The parametric version of this solver was used such that the magnetic field distribution could be computed, while scaling the applied magnetic field from 0 T to 2 T.
3. The component M_x is predicted to be zero at low fields, due to the magnetic domain structure, then to suddenly increase as the variant reorientation process sets in and to again decrease to zero as the material is saturated in the y -direction. It is always smaller than M^{sat} . The component $M_y = M_y(H_y)$ is therefore determined to be dominating the component $M_x = M_x(H_y)$. Furthermore, even though the x -component of the applied magnetic field is zero, the same does not hold for the internal field, due to the magnetization of the body and the shape of the specimen (corner effects). However, the dependence $\mathbf{M}(H_x)$, and $\mathbf{M}(H_z)$ is assumed to be small and thus neglected.
4. The hysteretic nature of the constitutive response is not addressed in the magnetostatic analysis at this point. To be precise, the hysteresis is not neglected, but the analysis is only carried out from 0 T to 2 T, for which the solid line part of the magnetic hysteresis in Fig. 6 applies, not for the removal of the magnetic field (dashed line).

The nonlinear magnetostatic problem is mathematically described by Eq. (45), the interface conditions (3) and the boundary conditions (60). The geometry of the computational domain was introduced in Fig. (??). The constitutive relations are reflected in the magnetization curve of Fig. (6). Numerical results of the finite element analysis are plotted in Fig. 7 in terms of the distribution of the y -component of the magnetic field for the exemplary applied magnetic flux level of 2 T.

¹Even if the relation between field and magnetization were linear the magnetostatic problem would be nonlinear, though numerically most likely easier to handle.

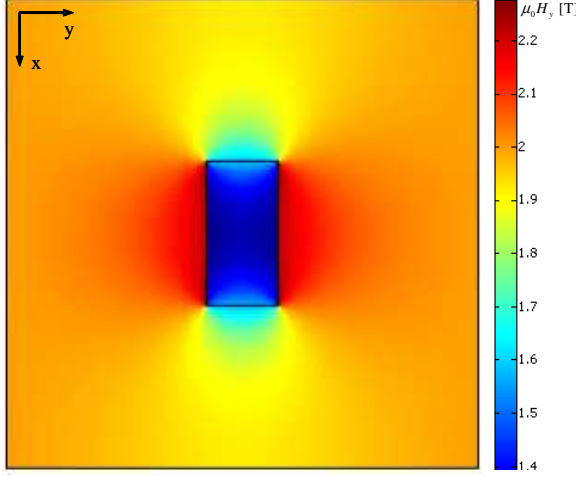


Figure 7: Distribution of H_y in the computational domain at the applied magnetic field of $\mu_0 H_y^a = 2.0$ T.

1.4 The Demagnetization Effect and Correct Interpretation of Experimental Data

Typical magnetic field distribution around a rectangular permanent magnet shows that the magnetic field stream lines emanate from the *north pole* of the specimen and end at the *south pole* [6, 7]. It is evident that the stream line pattern satisfies the interface conditions (3). While the tangential component of \mathbf{H} is continuous on all interfaces, its normal component can be discontinuous if there exist a discontinuity in the magnetization. Since the normal component of \mathbf{B} is continuous and therefore $[\mathbf{B}] \mathbf{n} = \mu_0 [\mathbf{H} + \mathbf{M}] \mathbf{n} = 0$, it is clear that the normal component of \mathbf{H} has to balance the jump in \mathbf{M} that occurs at the interface between the magnetized medium and free space. Inside the specimen the magnetic field opposes the direction of magnetization. The magnetostatic field caused by the body's own magnetization is therefore called the *demagnetizing field* \mathbf{H}^d [6]. The demagnetization field in a uniformly magnetized ellipsoidal sample is always uniform, while it is nonuniform in a rectangular body.

Permanent magnets exhibit substantial remnant macroscopic magnetization at zero applied fields and, within certain limits, the magnetization of the magnetic sample does not depend on the applied magnetic field [6]. For magnetostatic problems involving only permanent magnets the Poisson equations (22) are linear and the principle of superposition holds. Thus, if additionally an external magnetic field \mathbf{H}^a is applied, the total magnetic field

is then given by

$$\mathbf{H} = \mathbf{H}^a + \mathbf{H}^d . \quad (19)$$

Generic integral representations of the solution of the magnetostatic problem defined by Eqs. (45) exist [13, 14]. For uniformly magnetized bodies the magnetization vector can be taken outside the integral expressions for the magnetic field strength [14, 15], such that

$$\mathbf{H}^d(\mathbf{r}) = - \underbrace{\left[\frac{1}{4\pi} \iint_{\partial\Omega^m} \frac{\mathbf{r} - \mathbf{r}'}{|\mathbf{r} - \mathbf{r}'|^3} \otimes \mathbf{n}' dA' \right]}_{=: \mathbf{D}} \mathbf{M} = -\mathbf{DM} . \quad (20)$$

Therein \mathbf{r} is the position at which \mathbf{H} is evaluated in \mathbb{R}^3 and \mathbf{r}' the location of a point on the surface $\partial\Omega^m$, with unit outward normal \mathbf{n}' , of the region Ω^m occupied by the magnetized body. By applying the divergence theorem an equivalent volume integral representation of Eq. (20) can be obtained. \mathbf{D} is the demagnetization tensor, which only depends on the geometry of the body and can be computed by evaluating the bracketed integral expression in Eq. (20). For a spatially uniformly magnetized body the demagnetization field can thus be computed by simply multiplying the magnetization with an appropriate demagnetization factor. Such factors have been tabularized for ellipsoids of many different aspect ratios [6, 7, 16]. This procedure is analogous to using Eshelby tensors in elasticity theory to determine the strain field inside ellipsoidal inclusions [17, 18]. The demagnetization tensor has the following properties: i) it is independent of position inside an ellipsoidal body; ii) it is diagonal if its eigenvectors are aligned with the symmetry axes of the body; iii) its trace is 1, if evaluated inside the body. The demagnetization factor for a sphere is therefore 1/3 in any direction. For a prismatic cylinder with square or cylindrical cross-section the axial and transverse demagnetization factors are related by $D^t = 1/2(1 - D^a)$ [19].

The magnetic field inside a uniformly magnetized sample of non-ellipsoidal shape is always nonuniform. The demagnetization tensor in this case depends on the position inside the sample. It is customary to define average demagnetization tensors for samples of arbitrary shape, sometimes referred to as *magnetometric demagnetization tensors* [19, 20], in the following manner

$$\langle \mathbf{D} \rangle := \frac{1}{\Omega^m} \int_{\Omega^m} \mathbf{D}(\mathbf{r}) dV . \quad (21)$$

The average demagnetization field can then be written as

$$\langle \mathbf{H}^d \rangle = -\langle \mathbf{D} \rangle \mathbf{M} . \quad (22)$$

Numerical solution schemes have been developed to compute the demagnetization factors for uniformly magnetized bodies of arbitrary shape. For many standard geometries, such as prismatic bars with different types of cross-sections, these have also been tabularized [15, 19, 20].

By definition the demagnetization factor loses its meaning for bodies with nonuniform magnetization. Thus, the exact demagnetization field inside a non-ellipsoidal body, whose magnetization is induced by an external magnetic field and therefore not uniform unless complete saturation is reached at high fields, can not be computed with the help of demagnetization factors. Furthermore, if the magnetization is a function of the applied field the magnetostatic problem as described by Eqs. (45) becomes nonlinear and superposition no longer holds. In this case, which is always encountered in experiments unless ellipsoidal specimen are used, an explicit numerical solution of the magnetostatic boundary value problem has to be obtained. For MSMAs the problem is complicated by the fact that the magnetic properties are nonlinear, hysteretic and stress level dependent. Furthermore, the shape of the sample changes due to the magnetic field-induced strain. This effect, however, is expected to have negligible significance.

In this analysis the magnetic properties, which are initially only known in terms of the applied field, were used as if they were the true constitutive response of the material. Thus the relation between the internal and applied field computed in one run of the analysis can only serve as a first correction of the experimental data according to

$$\text{Known: } \langle M_y \rangle(H_y^a), H_y^a \Leftrightarrow \langle H_y^{\text{iter}1} \rangle.$$

$$\text{To be computed: } \langle M_y \rangle(H_y^a) \Rightarrow \langle M_y \rangle(\langle H_y^{\text{iter}1} \rangle). \quad (23)$$

Then the analysis is repeated with the magnetic properties given by $\langle M_y \rangle(\langle H_y^{\text{iter}1} \rangle)$ and with the result one can again correct the magnetization curve

$$\text{Known: } \langle M_y \rangle(H_y^a), H_y^a \Leftrightarrow \langle H_y^{\text{iter}2} \rangle.$$

$$\text{To be computed: } \langle M_y \rangle(H_y^a) \Rightarrow \langle M_y \rangle(\langle H_y^{\text{iter}2} \rangle). \quad (24)$$

By following this procedure, the relation between the applied field and the internal field is computed more accurately in each iteration step. This can be considered an *inverse problem*. One aims to determine the actual magnetic properties of the sample such that solving the magnetostatic problem for a sample of this geometry gives back the relation $\langle M_y \rangle(H_y^a)$ that is plotted in Fig. 6. The original and corrected magnetization curves resulting from this iterative procedure are depicted in Fig. 8 for the considered specimen with 2:1 length to width ratio.

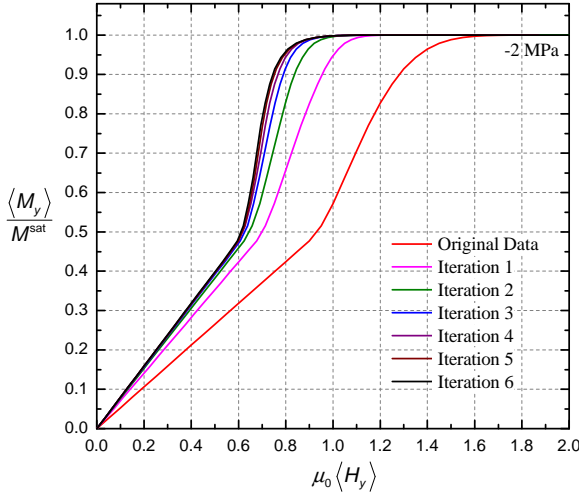


Figure 8: Magnetization data corrected for demagnetization. Specimen aspect ratio 2:1.

As described above, the corrected curves were plotted by using the same data for the vertical magnetization axes, while rescaling the magnetic field axis by means of the relation between the average internal and applied field at each iteration. One observes the relatively fast convergence of the solution. After six iterations the difference to the solution of the previous iteration is small enough to conclude that the solution has converged. The magnetization of curve of iteration six can thus be considered the "true" magnetization response, which is independent of the specimen geometry. The original data is the magnetization behavior that would be measured in an experiment using a prismatic sample of this aspect ratio. In an experiment that uses a sample of the same material, but different aspect ratio a different curve would be measured.

A parametric study has been performed to investigate the sample shape dependence of the demagnetization effect for the prismatic specimen with nonlinear magnetic properties. In Fig. 9 the corrected magnetization data has been plotted for four different aspect ratios of the prismatic specimen with square cross-section. The corresponding corrections of the magnetic field-induced strain data have been plotted in Fig. 10. It is clearly observed that the influence of the specimen aspect ratio on the difference between the apparent material behavior and the true constitutive response is very significant and must therefore be addressed when using data for model calibration. Once the MFIS data has been corrected for demagnetization, the

model parameters can be recalibrated.²

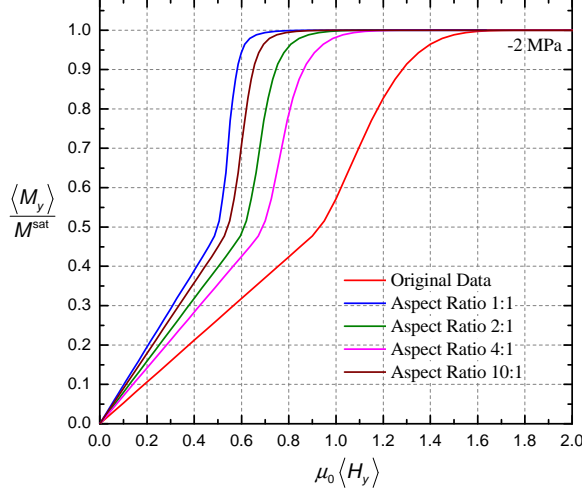


Figure 9: Influence of specimen aspect ratios on the correction of the magnetization data.

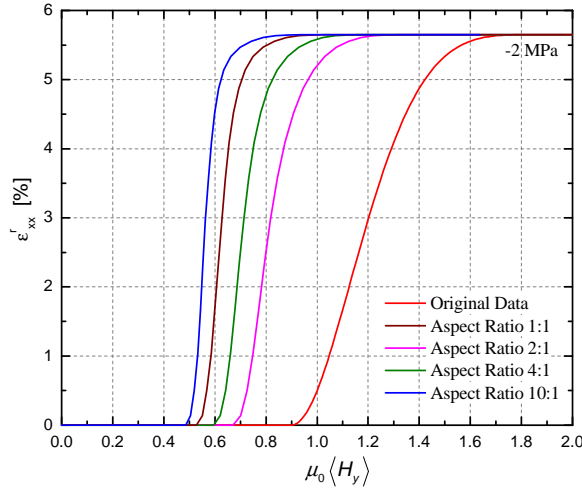


Figure 10: Influence of specimen aspect ratios on the correction of the magnetic field-induced strain data.

²The specific results presented here are based on solutions of 2-D boundary value problems and can thus only be used qualitatively. The procedure is the same for 3-D problems, which however are computationally much more involved.

One of the stated goals of this analysis was to investigate the error one can expect when using the demagnetization factor method instead of the finite element analysis of the nonlinear magnetostatic problem. The average demagnetization factor was defined in Eq. (21). Using Eqs. (19) and 22 one can compute the average internal magnetic field by

$$\langle H_y \rangle = H_y^a + \langle H_y^d \rangle = H_y^a - \langle D_{yy} \rangle \langle M_{yy} \rangle . \quad (25)$$

This relation is often applied in the literature [10, 21] to correct magnetization data. This procedure of course assumes that the magnetization in the sample is uniform and that superposition holds.

The demagnetization factor for the specimen of the 2:1 aspect ratio is $D_{yy} = 0.651$. Since a literature value was not available for this particular geometry, the factor was computed using finite elements for a sample of constant and spatially uniform magnetization placed in free space. This method has proven to yield very accurate demagnetization factors for other geometries for which literature data could be referred to [19].

If the magnetization response curve of the MSMA can not be measured and is also not predicted by a constitutive model Eq. (25) is sometimes used with a constant M_y , for example $M_y = M^{sat}$. This is expected to lead to a very crude approximation of the demagnetization effect. If the magnetization response is known or predicted as in Fig. 6 a much better approximation is obtained. The different correction methods are compared in Fig. 11.

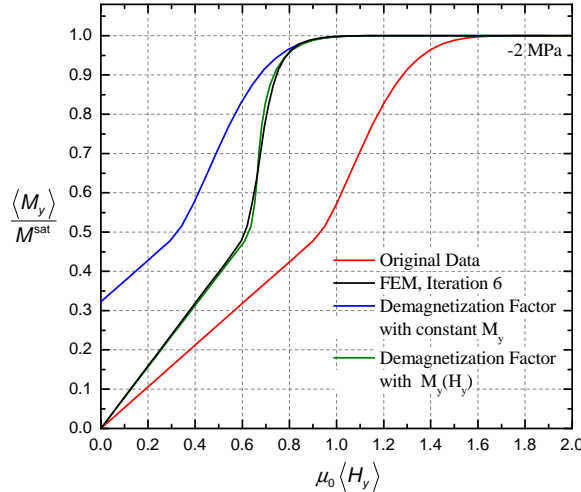


Figure 11: Comparison of the corrections through demagnetization factors and FEM analysis. Specimen aspect ratio 2:1.

These observations suggest that using the demagnetization factor method, which is based on the assumption of uniform magnetization in the specimen, one obtains essentially the same result as performing the FEM analysis of the nonlinear magnetostatic problem with nonuniform magnetization, if average field quantities are considered. This conclusion can be misleading, however, because it only holds for average quantities. As evident from Fig. ?? and Fig. ??, there exist a significant variation in the local magnetization. To further quantify this variation, Fig. 12 displays local values of the magnetic field at several points in the specimen as a function of the applied field.

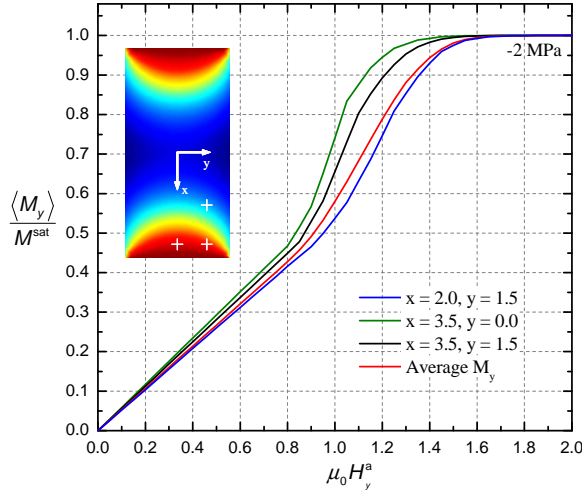


Figure 12: Position dependence of the magnetization response within the rectangular specimen.

For problems in which the knowledge of local magnetic field and magnetization is important, one can not avoid solving the magnetostatic problem explicitly, as done here. Such cases are certainly encountered if one is interested in solving magnetomechanical MSMA boundary value problems not just involving simple specimen shapes, but, for example, more complicated geometries of MSMA components in actuators and other applications.

After correcting the magnetization response data, the solution of the magnetostatic problem is presented here with the modified magnetic constitutive equation. The H_x and H_y components are given in Fig 13 and Fig 14. The magnitude of the H_y component is higher compared to the H_x component due to the applied boundary conditions along the y -direction (Fig 4). Moreover, magnetic field concentration is observed at the corners of the specimen.

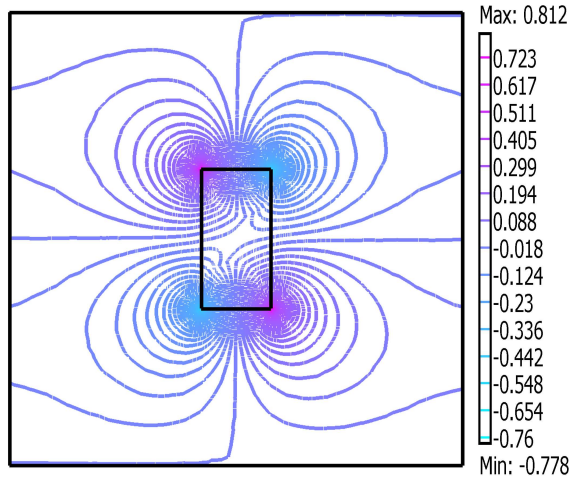


Figure 13: Distribution of H_x in the computational domain at the applied magnetic field of $\mu_0 \langle H_y \rangle = 0.97T$.

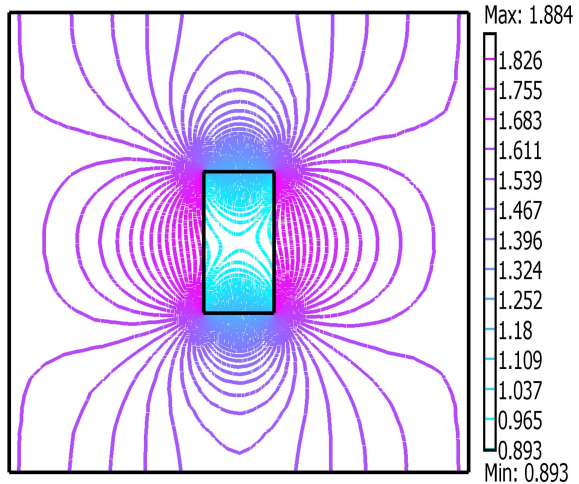


Figure 14: Distribution of H_y in the computational domain at the applied magnetic field of $\mu_0 \langle H_y \rangle = 0.97T$.

1.5 Maxwell (Magnetic) Stress, Magnetic Body Force and Body Couple

The Maxwell (magnetic) stress, magnetic body force and magnetic body couple are evaluated using finite element analysis over the domain of the magnetic shape memory alloy (MSMA) specimen. We found that the axial component of the Maxwell stress, which acts along the direction of the applied traction,

is compressive. The magnitude of this particular magneto stress component, at the end of the reorientation process, is nearly equal to 21% of the applied traction. This suggests that the axial component of the Maxwell stress favors the stress assisted variant. The magnitude of magnetic body force and magnetic body couple are calculated. It is observed that, due to the presence of the magnetic field gradient inside the material, the magnetic body force is not negligible.

The Maxwell stress, magnetic body force and magnetic body couple depend on the magnetic field and magnetization and they can be computed with the solution of the magnetostatic boundary value problem. Without solving the magneto-mechanical coupled problem, we can get an estimation of the Maxwell stress ($\boldsymbol{\sigma}^M$), magnetic body force ($\rho\mathbf{f}^m$) and magnetic body couple ($\rho\mathbf{L}^m$) by using the following expressions [2]

$$\boldsymbol{\sigma}^M = \mu_0 \mathbf{H} \otimes \mathbf{H} + \mu_0 \mathbf{H} \otimes \mathbf{M} - \frac{1}{2} \mu_0 (\mathbf{H} \cdot \mathbf{H}) \mathbf{I}, \quad (26)$$

$$\rho\mathbf{f}^m = \mu_0 (\nabla \mathbf{H}) \mathbf{M}, \quad \text{and} \quad \rho\mathbf{L}^m = \text{skw}(\mu_0 \mathbf{M} \otimes \mathbf{H}). \quad (27)$$

It should be noted that, for stationary magnetic materials, the body force and body couple are given by [2]

$$\nabla \cdot \boldsymbol{\sigma}^M = \rho\mathbf{f}^m, \quad \text{and} \quad \text{skw}(\boldsymbol{\sigma}^M) = -\rho\mathbf{L}^m. \quad (28)$$

We will study the behavior of Maxwell stress, magnetic body force and magnetic body couple at the magnetic field $\mu_0 < H_y > = 0.97T$. We take this point as it is close to the end of the reorientation process, where the intensity of the magnetic field is high. The spatial variation of the numerical results inside the specimen are demonstrated by selecting nine representative points (Fig 15) from P_0 to P_8 in the x-y plane.

The field induced martensitic variant volume fraction ξ is presented in Fig 16(a). The figure shows that the minimum value ξ is 0.93 and the maximum value is 1, which suggests that almost everywhere the new field favored variant is present. This is why the normalized magnetization vectors (Fig 16(b)) are parallel to the direction of the horizontally applied magnetic field.

The four components of the non symmetric Maxwell stress at $\mu_0 < H_y > = 0.97T$ are presented in Fig 17 and 18. The nonuniform Maxwell stress is observed due to presence of nonuniform distribution of magnetic field and magnetization vector. The numerical results at P_0 to P_8 are given in Table 3. The σ_{xx}^m component of the Maxwell stress is significant and compressive in

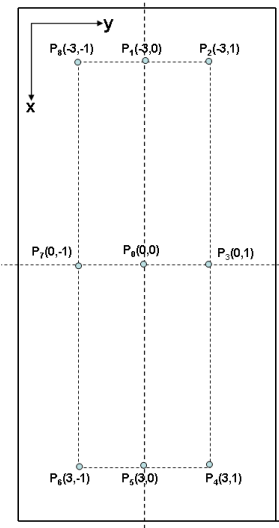


Figure 15: Location of nine representative points to explore the numerical analysis.

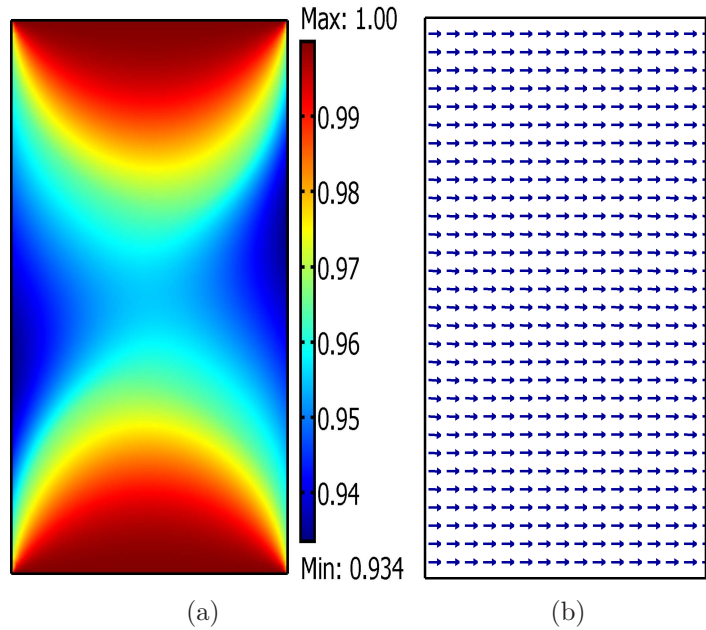


Figure 16: (a) Field induced martensitic volume fraction and (b) Magnetization vector(normalized) distribution at $\mu_0 < H_y > = 0.97T$.

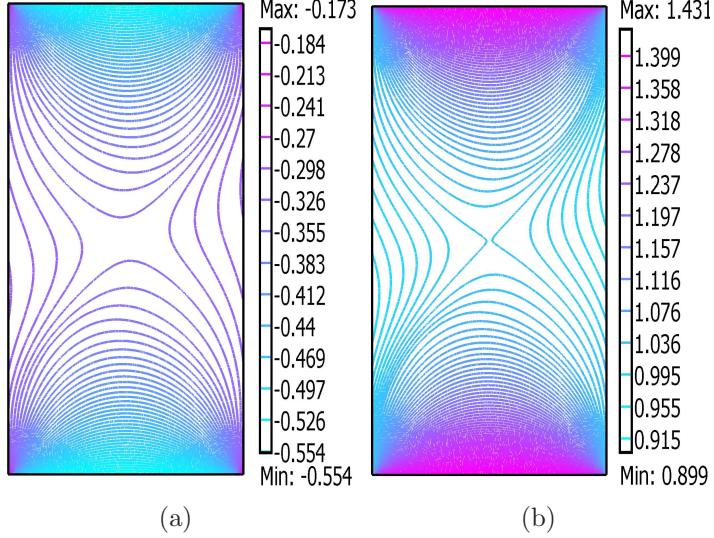


Figure 17: σ_{xx}^m and σ_{yy}^m -component distribution of Maxwell stress (MPa) at $\mu_0 < H_y > = 0.97T$.

	P_0	P_1	P_2	P_3	P_4	P_5	P_6	P_7	P_8
σ_{xx}^m	-0.336	-0.444	-0.416	-0.329	-0.416	-0.444	-0.416	-0.329	-0.416
σ_{yy}^m	1.011	1.227	1.178	0.996	1.178	1.227	1.178	0.996	1.178
σ_{xy}^m	-0.036	0.004	-0.163	-0.032	0.173	0.005	-0.163	-0.032	0.173
σ_{yx}^m	0.000	0.003	-0.085	0.001	0.090	0.002	-0.085	0.001	0.090

Table 3: Maxwell stress(MPa) at 0.97T.

nature. The values are nearly equal to the 21% of the applied traction, which is -2 MPa. This implies that x-component of the Maxwell stress favors the stress assisted variant. The σ_{yy}^m component has larger value than σ_{xx}^m component but in tension. The tensile characteristic of the σ_{yy}^m component does not facilitate to nucleate field favored variant along the y direction.

The σ_{xy}^m and σ_{yx}^m components of Maxwell stress depend on the magnetic body couple according to Eq 28(b) and so the shear stress distribution (Fig 18) is strongly influenced by the body couple. For example, if we select the point P_3 , the value of magnetic moment at this point is $0.039N - mm/mm^3$ (Table 4) and acts clockwise. The shear stress components at this point are $\sigma_{xy}^m = -0.163MPa$ and $\sigma_{yx}^m = -0.085MPa$ (Table 3) and they contribute to balance the magnetic body couple according to Eq 28(b). Fig 19(a) shows the nonuniform variation of magnetic body couple at $\mu_0 < H_y > = 0.97T$. The magnitude of the body couple is observed

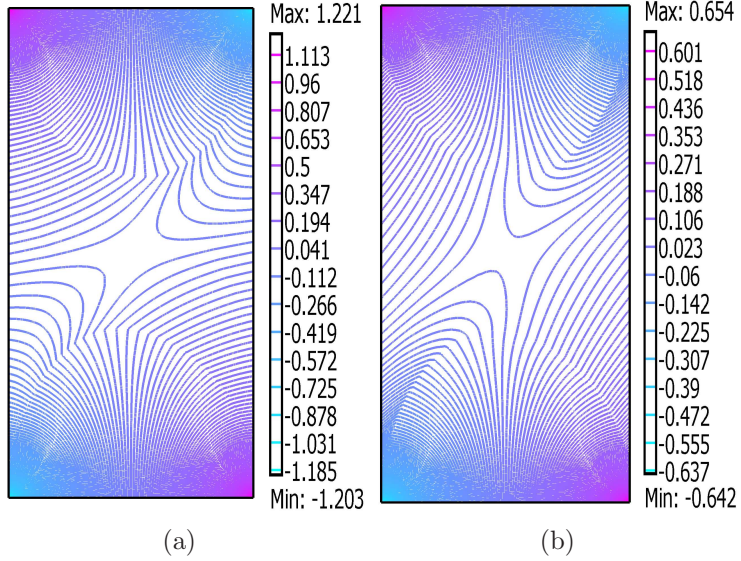


Figure 18: σ_{xy}^m and σ_{yx}^m -component distribution of Maxwell stress (MPa) at $\mu_0 < H_y \geq 0.97T$.

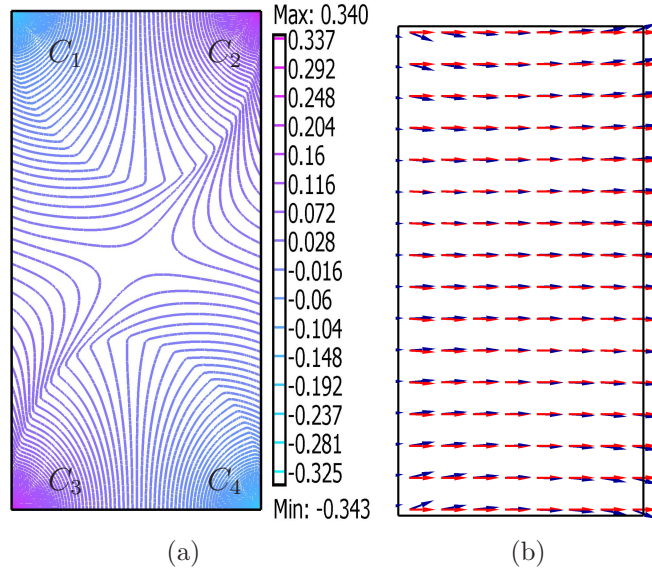


Figure 19: Magnetic body couple at $\mu_0 < H_y \geq 0.97T$ and orientation of magnetization vector and magnetic field vectors.

to have higher values near the corner regions compared to the body couple at the central region. As the body couple vector is the cross product of

magnetic field and magnetization vector, high value is observed close to the corners due to high magnetic field concentration and larger angle between field vectors and the magnetization vectors (Fig 19(b)). In the figure, the two arrows at a point represent magnetization vector(light arrow) and magnetic field vector(dark arrow) respectively. It should be noted that the magnetic field vector changes orientation from the corner region C_1 to C_2 and the sign of body couple changes (Fig 19(a)). Due to the cento-symmetry nature of the solution of the magnetostatic problem, an opposite trend of the sign change in the body couple is observed from C_3 to C_4 . The shear stress components show similar trend in the spatial distribution.

	P_0	P_1	P_2	P_3	P_4	P_5	P_6	P_7	P_8
ρL^m	0.018	-0.001	0.039	0.021	-0.041	-0.001	0.039	0.02	0.041

Table 4: Body couple($N - mm/mm^3$) 0.97T.

The intensity of the body force depends on the gradient of the magnetic field. The magnitude of the body force is demonstrated in Fig 20 and the numerical results for points P_0 to P_8 are given in Table 5. As the gradient of magnetic field is very high due to the corner effects, we observe high magnitude of body forces near the corners. The magnitude decreases at the central region of the specimen, where the magnetic field distribution is relatively more uniform.

	P_0	P_1	P_2	P_3	P_4	P_5	P_6	P_7	P_8
ρf_x^m	-0.001	-0.080	-0.077	0.005	0.078	0.080	0.077	-0.005	-0.080
ρf_y^m	0.000	0.000	-0.046	-0.012	-0.045	0.000	0.046	0.012	0.045

Table 5: Body force(N/mm^3) at 0.97T.

1.6 Magneto-Mechanical Coupled Finite Element Analysis

We already found that the intensity of Maxwell stress is significant compared to the applied traction. As a next step, we analyze the behavior of the Cauchy stress in a magneto-mechanical coupled problem. The objective of the magneto-mechanical coupled finite element analysis is to investigate the variation of Cauchy stress due to field induced variant reorientation. In the model, we assume constant and uniform Cauchy stress inside the material. We also assume that the magnetization constitutive equation and the

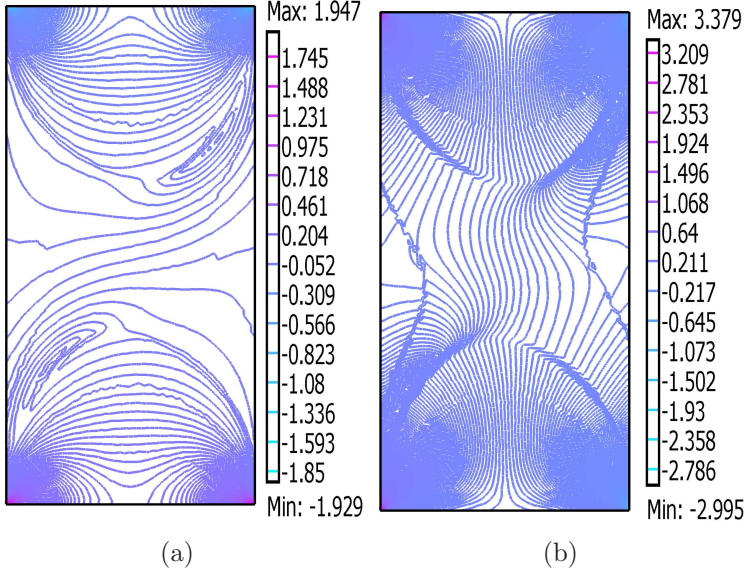


Figure 20: ρf_x^m and ρf_x^m -component distribution of body force (N/mm^3) at $\mu_0 < H_y \geq 0.97T$.

magnetic conservation equations do not depend on stress. Under these assumptions, we found that for the coupled problem Cauchy stress is associated with the magnetic body force, magnetic body couple and reorientation strain and has strong influence on the magnetic field and magnetization.

The results in the previous section show that the intensity of Maxwell stress are significant compared to the applied traction. This observation motivates us to solve a coupled magneto-mechanical problem to investigate the behavior of the Cauchy stress. In this section, the coupled magneto-mechanical problem is solved with magnetic and mechanical boundary conditions. The magnetic boundary conditions are the same as described for the magnetostatic process and are presented by Eq (3). The mechanical boundary conditions of the problem are illustrated in Fig 21 and they correspond to an experimental setup, proposed in [12]. This setup consists of a $2T$ electromagnet, which is adjustably mounted on a mechanical load frame, such that the applied force lies in the vertical plane and the direction remains perpendicular to the horizontally applied magnetic field. The specimen is held in place by non-magnetic grips with proper lubrication. In Fig 21, t_x and t_y denote the traction on the boundaries along x and y directions respectively. Moreover, U denotes the displacement along the x axis.

In addition to the magnetostatic problem, the elastostatic boundary value

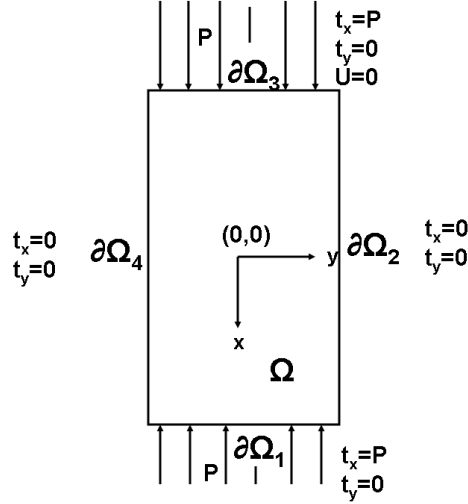


Figure 21: Imposed mechanical boundary conditions. Ω is the material domain and $\partial\Omega$ denotes the boundary.

problem is also defined in this section. The mechanical problem is described by the conservation of linear momentum and the conservation of angular momentum for the magnetic continuum [1, 2],

$$\nabla \cdot \boldsymbol{\sigma} + \rho \mathbf{f} + \rho \mathbf{f}^m = \mathbf{0} \quad \text{in } \Omega , \quad (29a)$$

$$\text{skw } \boldsymbol{\sigma} = \rho \mathbf{L}^m \quad \text{in } \Omega , \quad (29b)$$

where ρ is the mass density, $\boldsymbol{\sigma}$ the Cauchy stress tensor and \mathbf{f} the body force. The additional body force \mathbf{f}^m and the body couple \mathbf{L}^m are due to the magnetization of the body. The equilibrium equations (29) can be rewritten as

$$\nabla \cdot (\boldsymbol{\sigma} + \boldsymbol{\sigma}^M) + \rho \mathbf{f} = \mathbf{0} \quad \text{in } \Omega , \quad (30a)$$

$$\text{skw } (\boldsymbol{\sigma} + \boldsymbol{\sigma}^M) = \mathbf{0} \quad \text{in } \Omega , \quad (30b)$$

subject to the jump conditions on all interfaces between the specimen and vacuum

$$[\![\boldsymbol{\sigma} + \boldsymbol{\sigma}^M]\!] \cdot \mathbf{n} = \mathbf{0} . \quad (31)$$

The expressions for the magnetic body force, magnetic body couple and Maxwell stress are given in Eq. 27 and in Eq. 26. The detailed derivation of the magneto-mechanical boundary condition is given in the appendix.

The body couple due to magnetization causes asymmetry to the Cauchy stress tensor. The complete expression of the Cauchy stress is given by [2]

$$\boldsymbol{\sigma} = \boldsymbol{\sigma}^E - \mu_0(\mathbf{H} \otimes \mathbf{M}) , \quad (32)$$

where $\boldsymbol{\sigma}^E$ is symmetric and mechanical part of the Cauchy stress tensor. The constitutive relation holds between $\boldsymbol{\sigma}^E$ and the elastic strain $\boldsymbol{\varepsilon}^e$ and given by,

$$\boldsymbol{\sigma}^E = \mathbf{C} : \boldsymbol{\varepsilon}^e = \mathbf{C} : (\boldsymbol{\varepsilon} - \boldsymbol{\varepsilon}^r) \quad (33)$$

Here $\boldsymbol{\varepsilon} = \frac{1}{2}(\nabla \mathbf{u} + \nabla \mathbf{u}^T)$ is the total strain, $\boldsymbol{\varepsilon}^r = \Lambda \xi$ is the reorientation strain, \mathbf{u} is the total displacement vector, Λ is the reorientation tensor and ξ is the volume fraction of the field induced variant. The specific form of Λ for this 2-D problem is given in Tab 6.

Substituting (32) in (29b) and assuming that the non magnetic body force term $\rho \mathbf{f}$ is negligible, we get;

$$\nabla \cdot (\boldsymbol{\sigma}^E - \mu_0 \mathbf{H} \otimes \mathbf{M}) + \rho \mathbf{f}^m = \mathbf{0} . \quad (34)$$

The following steps show the simplified form of the above equation.

$$\begin{aligned} \nabla \cdot \boldsymbol{\sigma}^E + [\rho \mathbf{f}^m - \nabla \cdot (\mu_0 \mathbf{H} \otimes \mathbf{M})] &= \mathbf{0} , \\ \nabla \cdot \boldsymbol{\sigma}^E + [\mu_0(\nabla \mathbf{H})\mathbf{M} - (\mu_0 \mathbf{H}(\nabla \cdot \mathbf{M}) + \mu_0(\nabla \mathbf{H})\mathbf{M})] &= \mathbf{0} , \\ \nabla \cdot \boldsymbol{\sigma}^E + [-\mu_0 \mathbf{H}(\nabla \cdot \mathbf{M})] &= \mathbf{0} . \end{aligned} \quad (35)$$

The modified conservation of linear momentum equation (35) is expressed as a function of the mechanical part of the Cauchy stress. The Young modulus and the Poisson ratio of the martensitic phase are taken 2GPa and 0.3 respectively ([22],[23]). The material is assumed to have isotropic mechanical properties. Table 6 shows the magnetic and mechanical equations with different coupling terms when both magnetic body force and magnetic bodycouple are considered.

The objective of this numerical simulation is to investigate the variation of Cauchy stress due to field induced variant reorientation. In the model, we assume constant and uniform Cauchy stress inside the material. We also assume that the magnetization constitutive equation and the Maxwell equations do not depend on stress. Due to this reason, the magnetostatic solution of the coupled problem gives the same solution as obtained from the uncoupled magnetostatic problem. The numerical examples of the magnetic part,

Maxwell Equations:

$$\Delta \Phi^m = -\mu_0 \nabla \times \mathbf{M}.$$

Conservation of Linear and Angular Momentum:

$$\nabla \cdot \boldsymbol{\sigma} + \rho \mathbf{f}^m = \mathbf{0}.$$

$$\text{skw}(\boldsymbol{\sigma}) = \mu_0 \text{skw}(\mathbf{M} \otimes \mathbf{H}).$$

Cauchy Stress:

$$\boldsymbol{\sigma} = \boldsymbol{\sigma}^E - \mu_0 (\mathbf{H} \otimes \mathbf{M}).$$

Material Constitutive Equation:

$$\boldsymbol{\sigma}^E = \mathbf{C} : (\boldsymbol{\varepsilon} - \boldsymbol{\varepsilon}^r) \in \text{Sym}.$$

$$\text{Where, } \boldsymbol{\varepsilon} = \frac{1}{2}(\nabla \mathbf{u} + \nabla \mathbf{u}^T), \boldsymbol{\varepsilon}^r = \Lambda \xi$$

$$\Lambda = \varepsilon^{r,max} \begin{bmatrix} 1 & 0 & 0 \\ 0 & -1 & 0 \\ 0 & 0 & 0 \end{bmatrix},$$

and $\varepsilon^{r,max}$ = maximum reorientation strain.

Boundary Conditions:

$$[\![\boldsymbol{\sigma} + \boldsymbol{\sigma}^M]\!] \cdot \mathbf{n} = \mathbf{0}. \quad \text{Or}$$

$$\boldsymbol{\sigma}^E \mathbf{n} = \mathbf{t}_a + \frac{\mu_0}{2} (\mathbf{M} \cdot \mathbf{n})^2 \mathbf{n} + \mu_0 (\mathbf{H} \otimes \mathbf{M}) \mathbf{n}.$$

Coupling Terms:

$$\mathbf{M} = \mathbf{M}(\mathbf{H}, \xi), \quad \rho \mathbf{f}^m = \mu_0 (\nabla \mathbf{H}) \mathbf{M} \quad \text{and} \quad \rho \mathbf{L}^m = \mu_0 \text{skw}(\mathbf{M} \otimes \mathbf{H}).$$

Table 6: Summary of the field equations, constitutive equation and boundary conditions.

presented in the previous section, are still valid for this magneto-mechanical coupling problem. However, for the coupled problem Cauchy stress is associated with the magnetic body force, magnetic body couple and reorientation strain and has strong influence on the magnetic field and magnetization.

The traction boundary conditions are also influenced by the magnetic field and magnetization vector. The expression of the coupled magneto-

mechanical traction at the boundaries is given by Eq. 129 and at each boundary, the components of the traction vectors are given below,

$$\tilde{\mathbf{t}}_{\partial\Omega_1} = (-2 + \mu_0 M_x H_x + \frac{\mu_0}{2} M_x^2) \mathbf{e}_x + \mu_0 M_x H_y \mathbf{e}_y \quad (36)$$

$$\tilde{\mathbf{t}}_{\partial\Omega_2} = \mu_0 M_y H_x \mathbf{e}_x + (\mu_0 M_x H_y + \frac{\mu_0}{2} M_y^2) \mathbf{e}_y \quad (37)$$

$$\tilde{\mathbf{t}}_{\partial\Omega_3} = (-\mu_0 M_x H_x - \frac{\mu_0}{2} M_x^2) \mathbf{e}_x - \mu_0 M_x H_y \mathbf{e}_y \quad (38)$$

$$\tilde{\mathbf{t}}_{\partial\Omega_4} = -\mu_0 M_y H_x \mathbf{e}_x + (-\mu_0 M_x H_y - \frac{\mu_0}{2} M_y^2) \mathbf{e}_y. \quad (39)$$

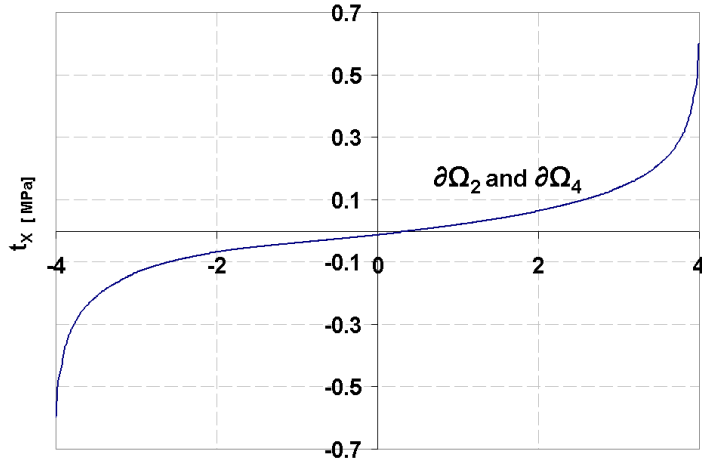
where we denote $\tilde{\mathbf{t}} = \sigma^E \mathbf{n}$. For $\mu_0 < H_y > = 0.97T$, the variant reorientation process is almost complete and M_x component is almost zero, as we described in the previous section. So, the traction at $\partial\Omega_1$ and $\partial\Omega_3$ are $\tilde{t}_{x,\partial\Omega_1} = -2MPa$ and $\tilde{t}_{y,\partial\Omega_3} = 0MPa$ respectively. The variation of the x-component of the magnetic traction on $\partial\Omega_2$ and $\partial\Omega_4$ is presented in Fig 22(a). The range varies from -0.6MPa to 0.6MPa and the two plots at each boundary coincide due to centro-symmetric behavior of H_x . The y-component of the magnetic traction on $\partial\Omega_2$ and $\partial\Omega_4$ is presented in Fig 22(b). In this case, the magnitude of the magnetic traction is more than 1MPa.

The Cauchy stress distribution at $\mu_0 < H_y > = 0.97T$ is given in Fig 23 and Fig 24. It should be noted that the Cauchy stress distribution is strongly nonuniform in the specimen. The detail numerical data at nine representative points (Fig 15) from P_0 to P_8 are given in the Table 7. We observe that the variation of the Cauchy stress along the axial direction with respect to -2MPa, which was assumed to be constant and uniform, is significant. The percent change of the Cauchy stress in the axial direction is presented in Table 8. The results show that the change in magnitude can be up to 80%. The maximum stress value occurs at the center of the specimen. The value of the stress gradually increases from the center towards the left and right edges, where the sign changes from negative to positive.

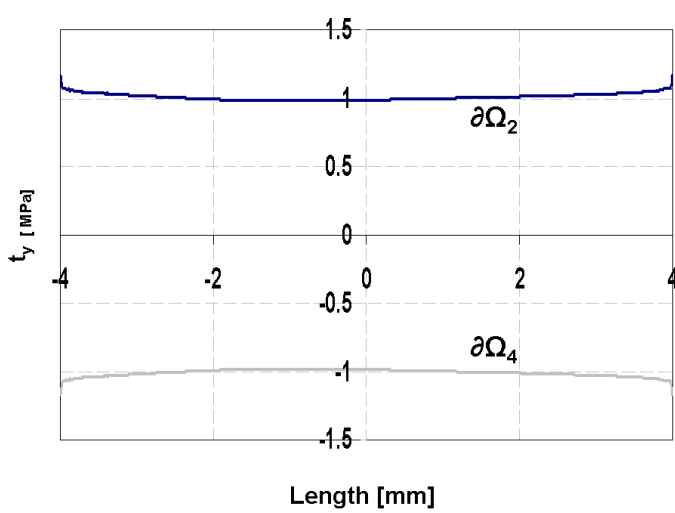
	P_0	P_1	P_2	P_3	P_4	P_5	P_6	P_7	P_8
σ_{xx}	-3.58	-2.31	-2.25	-2.30	-2.15	-2.32	-2.25	-2.32	-2.17
σ_{yy}	-0.39	-0.08	-0.10	-0.22	-0.11	-0.07	-0.11	-0.22	-0.11
σ_{xy}	0.11	-0.03	0.48	-0.04	-0.53	-0.04	0.52	-0.03	-0.49
σ_{yx}	0.07	-0.02	0.41	-0.08	-0.44	-0.04	0.45	-0.07	-0.41

Table 7: Cauchy stress(MPa) at 0.97T.

The horizontal component of the Cauchy stress is non zero and can have maximum value near -0.53MPa (Fig 23(b)). The σ_{yy} component is compres-



(a)



(b)

Figure 22: Variation of traction vectors on $\partial\Omega_2$ and $\partial\Omega_4$ at $\mu_0 < H_y \geq 0.97T$ (a) x-components and (b) y-components.

sive in most of the regions except the regions A and B (Fig 23(b)), where it has positive value. If we neglect the stress concentration near the corners (Fig 23(b)), the magnitude of the stress is high around the center and then radially decreases towards the edges. The solutions at the nine representative

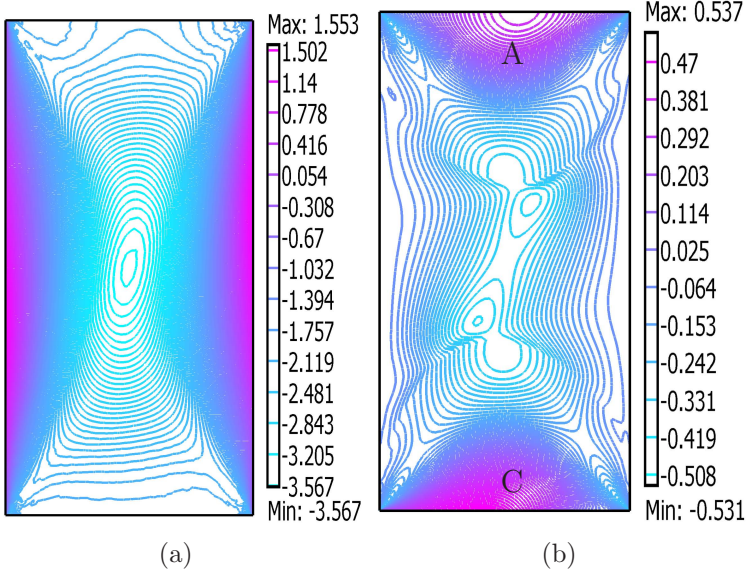


Figure 23: σ_{xx} and σ_{yy} -component distribution of Cauchy stress (MPa) at $\mu_0 < H_y > = 0.97T$.

	P_0	P_1	P_2	P_3	P_4	P_5	P_6	P_7	P_8
σ_{xx}	79.0%	15.5%	12.5%	15.0%	7.5%	16.0%	12.5%	16.0%	8.5%

Table 8: Percent difference in Cauchy stress(MPa) at 0.97T with and without magnetic coupling.

points, as presented in Table 8, show that the maximum magnitude among the nine points occurs at the center point, which is -0.39MPa.

The magnitude of the shear stress components is high near the corners, where the body couple is maximum due to the larger angle between the magnetization vectors and magnetic field vectors (Fig 19). We observe that, due to presence of body couple, the Cauchy stress is nonsymmetric (Fig 24). The numerical values are presented in Table 8.

The axial and horizontal component of the total stress $\boldsymbol{\sigma}^t = \boldsymbol{\sigma} + \boldsymbol{\sigma}^M$ is shown in Fig 25. The total stress is symmetric and the shear component is given in Fig 26. The value of total stress components are presented in the Table 9. We observe that the horizontal component becomes positive, while for the Cauchy stress the horizontal component was negative.

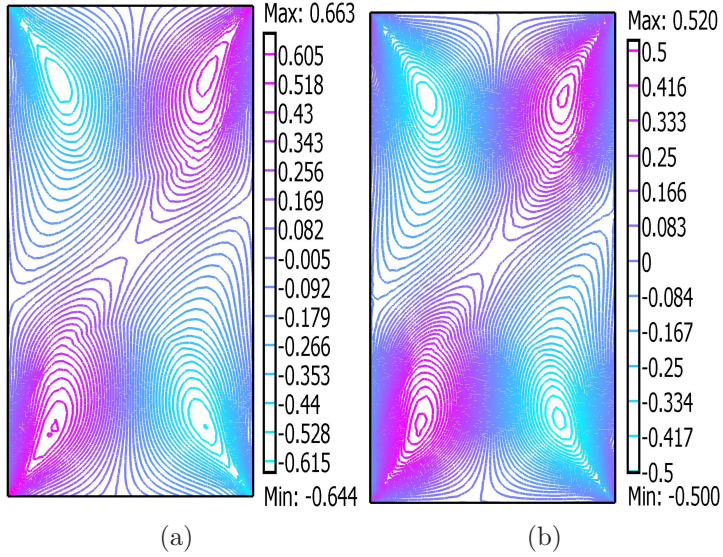


Figure 24: σ_{xy} and σ_{yx} -component distribution of Cauchy stress (MPa) at $\mu_0 < H_y > = 0.97T$.

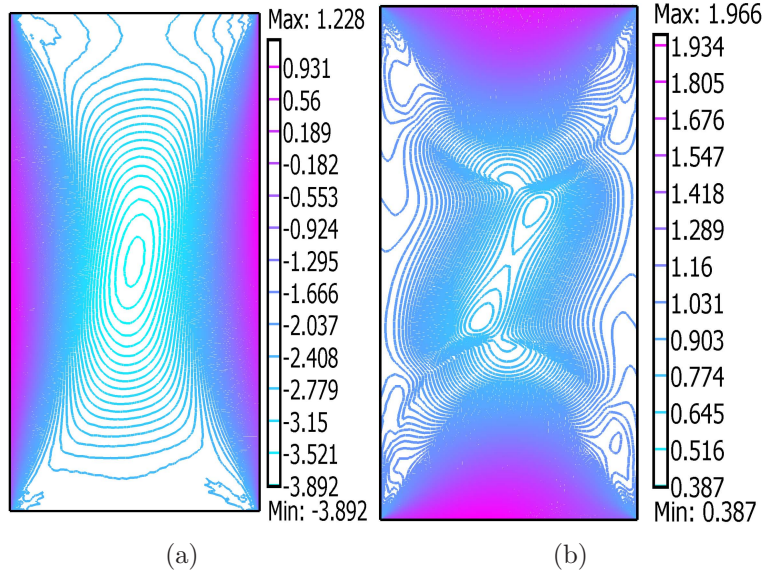


Figure 25: σ_{xx}^t and σ_{yy}^t -component distribution of Cauchy stress (MPa) at $\mu_0 < H_y > = 0.97T$.

2 MAGNETOSTATIC STABILITY ANALYSIS

The interesting feature of the studied magnetostatic boundary value problem is the appearance of banded zones in the spatial distribution of the magnetic

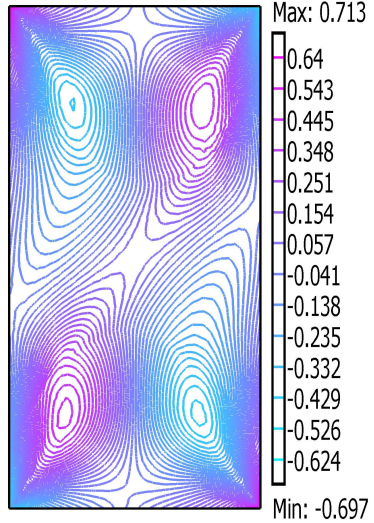


Figure 26: σ_{xy}^t -component distribution of Cauchy stress (MPa) at $\mu_0 < H_y \geq 0.97T$.

	P_0	P_1	P_2	P_3	P_4	P_5	P_6	P_7	P_8
σ_{xx}^t	-3.92	-2.75	-2.67	-2.63	-2.57	-2.67	-2.66	-2.65	-2.59
σ_{yy}^t	0.63	1.30	1.08	0.78	1.06	1.30	1.06	0.77	1.07
σ_{xy}^t	0.07	-0.02	0.32	-0.07	-0.35	-0.03	0.36	-0.06	-0.32

Table 9: Total stress(MPa) at 1.06T.

field variables when the magnetization constitutive response becomes highly nonlinear. In the performed finite element analysis, the appearance of band like regions are observed and are explained by the loss of ellipticity of the magnetostatic system of equations. The analytic approach of stability analysis shows that the magnetostatic problem becomes unstable during the martensitic variant reorientation mechanism. A parametric stability analysis reveals the conditions under which loss of ellipticity occurs and quantifies the influence of the nondimensional material parameters in the stability of the material.

2.1 Non-Dimensional Magnetostatic Equations

Based on the discussion in section 1.2, four material parameters, M^{sat} , ρK_1 , $H_y^{s(1,2)}$ and $H_y^{f(1,2)}$, are required to calibrate the constitutive equations. These are the saturation magnetization, the magnetic anisotropy constant, and the critical material parameters which denote forward reorientation start and

forward reorientation finish respectively. Nondimensionalization of the equations reduces the number of necessary parameters to 3, and allows an easier parametric study of the problem. For the nondimensional representation of the magnetostatic problem in the 2-D special case, we introduce the nondimensional spatial coordinates $\hat{x} = x/L$ and $\hat{y} = y/W$ where L and W are the characteristic lengths along the x and y axis respectively. The aspect ratio of the geometry is defined by

$$\ell = L/W. \quad (40)$$

The non-dimensional form of the 2-D Maxwell equations, using (1), are given by

$$\frac{\partial \hat{B}_x}{\partial \hat{x}} + \ell \frac{\partial \hat{B}_y}{\partial \hat{y}} = 0, \quad (41)$$

$$\ell \frac{\partial \hat{H}_x}{\partial \hat{y}} - \frac{\partial \hat{H}_y}{\partial \hat{x}} = 0, \quad (42)$$

while the constitutive relation (2) becomes

$$\hat{B}_x = \frac{1}{\hat{k}} \hat{H}_x + \hat{M}_x, \quad \hat{B}_y = \frac{1}{\hat{k}} \hat{H}_y + \hat{M}_y, \quad (43)$$

where

$$\begin{aligned} \hat{B}_x &= \frac{B_x}{\mu_0 M^{sat}}, & \hat{B}_y &= \frac{B_y}{\mu_0 M^{sat}}, & \hat{H}_x &= \frac{\hat{k} H_x}{M^{sat}}, & \hat{H}_y &= \frac{\hat{k} H_y}{M^{sat}}, \\ \hat{M}_x &= \frac{M_x}{M^{sat}}, & \hat{M}_y &= \frac{M_y}{M^{sat}}, & \hat{k} &= \frac{\mu_0 (M^{sat})^2}{2\rho K_1}. \end{aligned} \quad (44)$$

Taking advantage of the specific form of Equation (1), the magnetostatic problem is often reformulated by deriving the magnetic field strength from a scalar potential or the flux density from a vector potential \mathbf{A} . In the latter case $\mathbf{B} = \nabla \times \mathbf{A}$ identically satisfies the first of Equation (1). In nondimensional form, we are defining $\hat{\nabla} = L\nabla = \frac{\partial}{\partial \hat{x}} + \ell \frac{\partial}{\partial \hat{y}}$ and $\hat{\mathbf{A}} = \mathbf{A}/L\mu_0 M^{sat}$ such that $\hat{\mathbf{B}} = \hat{\nabla} \times \hat{\mathbf{A}}$. The vector potential $\hat{\mathbf{A}} = \hat{\mathbf{A}}(\hat{x}, \hat{y})$, in the component form can be written as $\hat{\mathbf{A}} = \{\hat{A}_x(\hat{x}, \hat{y}), \hat{A}_y(\hat{x}, \hat{y}), \hat{A}_z(\hat{x}, \hat{y})\}$. Using the identity $\hat{\nabla} \times (\hat{\nabla} \times \hat{\mathbf{A}}) = \hat{\nabla}(\hat{\nabla} \cdot \hat{\mathbf{A}}) - \hat{\Delta} \hat{\mathbf{A}}$, the Coulomb gauge $\hat{\nabla} \cdot \hat{\mathbf{A}} = 0$ and equation (1b), we get

$$\hat{\nabla} \times (\hat{\nabla} \times \hat{\mathbf{A}} - \hat{\mathbf{M}}) = \mathbf{0} \quad \text{or} \quad \hat{\Delta} \hat{\mathbf{A}} = -\hat{\nabla} \times \hat{\mathbf{M}}, \quad (45)$$

which is the vector-valued Poisson equation for the magnetic potential $\widehat{\mathbf{A}}$. Here we also used the nondimensional constitutive equation (43). Under the condition (7), the vector valued potential equation (45) reduces to

$$\widehat{\Delta} \widehat{A}_x = 0, \quad (46)$$

$$\widehat{\Delta} \widehat{A}_y = 0, \quad (47)$$

$$\widehat{\Delta} \widehat{A}_z = -\left(\frac{\partial \widehat{M}_y}{\partial \widehat{x}} - \ell \frac{\partial \widehat{M}_y}{\partial \widehat{y}}\right). \quad (48)$$

Using $\widehat{\phi} = \widehat{A}_z$, the spatial derivatives of \widehat{M}_x and \widehat{M}_y with respect to \widehat{y} and \widehat{x} respectively can be written in the following form.

$$\begin{aligned} \frac{\partial \widehat{M}_x}{\partial \widehat{y}} &= \frac{d \widehat{M}_x}{d \widehat{H}_y} \frac{\partial \widehat{H}_y}{\partial \widehat{y}} = \frac{d \widehat{M}_x}{d \widehat{H}_y} \left(\frac{\partial \widehat{B}_y}{\partial \widehat{y}} / \frac{d \widehat{B}_y}{d \widehat{H}_y} \right) = -\frac{d \widehat{M}_x}{d \widehat{H}_y} \left(\frac{\partial^2 \widehat{\phi}}{\partial \widehat{x} \partial \widehat{y}} / \frac{d \widehat{B}_y}{d \widehat{H}_y} \right), \\ \frac{\partial \widehat{M}_y}{\partial \widehat{x}} &= \frac{d \widehat{M}_y}{d \widehat{H}_y} \frac{\partial \widehat{H}_y}{\partial \widehat{x}} = \frac{d \widehat{M}_y}{d \widehat{H}_y} \left(\frac{\partial \widehat{B}_y}{\partial \widehat{x}} / \frac{d \widehat{B}_y}{d \widehat{H}_y} \right) = -\frac{d \widehat{M}_y}{d \widehat{H}_y} \left(\frac{\partial^2 \widehat{\phi}}{\partial \widehat{x}^2} / \frac{d \widehat{B}_y}{d \widehat{H}_y} \right). \end{aligned} \quad (49)$$

In the constitutive relation (43), \widehat{M}_y is a function only of \widehat{H}_y . Differentiating (43b) with respect to \widehat{H}_y we get

$$\frac{d \widehat{B}_y}{d \widehat{H}_y} = \frac{1}{\widehat{k}} + \frac{d \widehat{M}_y}{d \widehat{H}_y}. \quad (50)$$

Substituting equation (49) in (48) and using (50), we get

$$\frac{\partial^2 \widehat{\phi}}{\partial \widehat{x}^2} + \widehat{\ell k} \frac{d \widehat{M}_x}{d \widehat{H}_y} \frac{\partial^2 \widehat{\phi}}{\partial \widehat{x} \partial \widehat{y}} + \ell^2 \left(1 + \widehat{k} \frac{d \widehat{M}_y}{d \widehat{H}_y} \right) \frac{\partial^2 \widehat{\phi}}{\partial \widehat{y}^2} = 0. \quad (51)$$

For the expressions $\frac{d \widehat{M}_x}{d \widehat{H}_y}$ and $\frac{d \widehat{M}_y}{d \widehat{H}_y}$ one needs to use the constitutive relations of the previous section. In non-dimensional form we have

1. before reorientation

$$\widehat{M}_x = 0, \quad \widehat{M}_y = \widehat{H}_y, \quad (\widehat{H}_y \leq \widehat{H}_y^{s(1,2)}), \quad (52)$$

2. during reorientation

$$\widehat{M}_x = (1 - \xi) \sqrt{1 - \widehat{H}_y^2}, \quad \widehat{M}_y = \xi + (1 - \xi) \widehat{H}_y, \quad (\widehat{H}_y^{s(1,2)} \leq \widehat{H}_y \leq \widehat{H}_y^{f(1,2)}), \quad (53)$$

respectively with the condition $|\widehat{H}_y| \leq 1$ and

3. after reorientation

$$\widehat{M}_x = 1, \quad \widehat{M}_y = 0, \quad (\widehat{H}_y \geq \widehat{H}_y^{f(1,2)}). \quad (54)$$

Here, ξ is continuous and differentiable with respect to \widehat{H}_y . The expression of ξ with the nondimensional variables is derived from Equation (15) and one can rewrite ξ by,

$$\xi = \frac{1}{2} \cos \left[\widehat{F}_1 \left(\frac{1}{2} \widehat{H}_y^2 - \widehat{H}_y \right) + \widehat{F}_2 + \pi \right] + \frac{1}{2}, \quad \widehat{H}_y^{s(1,2)} \leq \widehat{H}_y \leq \widehat{H}_y^{f(1,2)}. \quad (55)$$

The non-dimensional magnetic field values $\widehat{H}_y^{s(1,2)}$ and $\widehat{H}_y^{f(1,2)}$ are the critical non-dimensional material parameters which denote forward reorientation start and forward reorientation finish respectively. The terms \widehat{F}_1 and \widehat{F}_2 are given by

$$\widehat{F}_1 = \frac{2\pi}{(\widehat{H}_y^{s(1,2)} - \widehat{H}_y^{f(1,2)})(\widehat{H}_y^{s(1,2)} + \widehat{H}_y^{f(1,2)} - 2)}, \quad (56)$$

$$\widehat{F}_2 = \frac{\pi \widehat{H}_y^{s(1,2)} (2 - \widehat{H}_y^{s(1,2)})}{(\widehat{H}_y^{s(1,2)} - \widehat{H}_y^{f(1,2)})(\widehat{H}_y^{s(1,2)} + \widehat{H}_y^{f(1,2)} - 2)}. \quad (57)$$

A typical magnetization response, after calibration is presented in Figure 27. In this study, motivated by Ni₂MnGa material data, we choose $\widehat{H}_y^{s(1,2)} = 0.480$ and $\widehat{H}_y^{f(1,2)} = 0.768$.

The nondimensional form of the magnetostatic problem requires three material parameters, \widehat{k} , $\widehat{H}_y^{s(1,2)}$ and $\widehat{H}_y^{f(1,2)}$.

2.2 2D Finite Element Analysis During Forward Re-orientation: Observation of Localization zones

As demonstrated in the Figure 3, we have two regions. We denote the MSMA sample by domain Ω_m and the surrounding free space by Ω_{fs} . In the whole domain, Equation (48) is defined in the following way

$$\widehat{\Delta} \widehat{\phi} = 0, \quad \widehat{\phi} \in \Omega_{fs}, \quad (58)$$

$$\frac{\partial^2 \widehat{\phi}}{\partial \widehat{x}^2} + \ell \widehat{k} \frac{d \widehat{M}_x}{d \widehat{H}_y} \frac{\partial^2 \widehat{\phi}}{\partial \widehat{x} \partial \widehat{y}} + \ell^2 \left(1 + \widehat{k} \frac{d \widehat{M}_y}{d \widehat{H}_y} \right) \frac{\partial^2 \widehat{\phi}}{\partial \widehat{y}^2} = 0, \quad \widehat{\phi} \in \Omega_m. \quad (59)$$

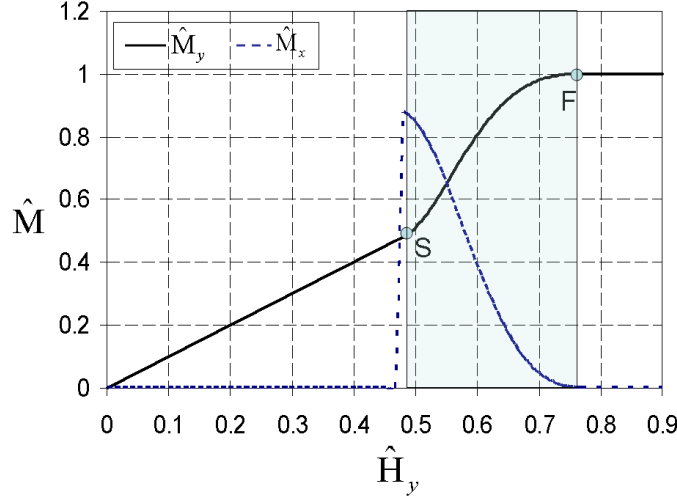


Figure 27: Non-dimensional magnetic constitutive response of \widehat{M}_x and \widehat{M}_y (Equations (52), (53) and (54)) with respect to non-dimensional magnetic field \widehat{H}_y . S and F represent the starting and the finishing points of the reorientation process.

For the boundary conditions, spatially constant magnetic flux is applied on all sides of the boundary $\partial\Omega_{fs}$, or, more precisely, the potential

$$\widehat{A}_x = \widehat{A}_y = 0; \quad \widehat{A}_z = -\frac{1}{\tilde{k}} \widehat{H}_y^a \widehat{x}, \quad (60)$$

is applied. The Laplace equations $\widehat{\Delta} \widehat{A}_x = 0$ and $\widehat{\Delta} \widehat{A}_y = 0$ with the above boundary conditions give $\widehat{A}_x(\widehat{x}, \widehat{y}) = \widehat{A}_y(\widehat{x}, \widehat{y}) = 0$.

Here we solve a specific example with a MSMA specimen with 2:1 ($\ell=2$) length to width ratio, $\widehat{k} = 0.745$, $\widehat{H}_y^{s(1,2)} = 0.480$ and $\widehat{H}_y^{f(1,2)} = 0.768$. The magnetization constitutive response for this specific geometry is considered to be the relation between material domain average of the magnetic field and magnetization vector. We will use the symbol ' $<>$ ' to denote the material domain average. In the following figures the length and width of the specimens are presented with their actual dimensions.

First we select a point P_1 in the average $\langle \widehat{M} \rangle - \langle \widehat{H}_y \rangle$ response at $\langle \widehat{H}_y \rangle = 0.248$ (Figure 28(a)), which lies in the linearly varying region 0-S. This point is well below the critical magnetic field to start the reorientation process and no reorientation occurs. The distribution of \widehat{H}_y for this boundary value problem at the particular point P_1 is presented in (Figure 28(b)). The

contour plot of magnetic field \hat{H}_y shows nonuniform distribution inside the specimen. It should be noted that the maximum value of \hat{H}_y is 0.288 (Figure 28(b)) where the critical value to onset the variant reorientation mechanism is 0.480. This means that new variant does not nucleate. Figure 29(a) shows the fact that the volume fraction of field induced martensitic variant, variant-2, is zero through out the specimen.

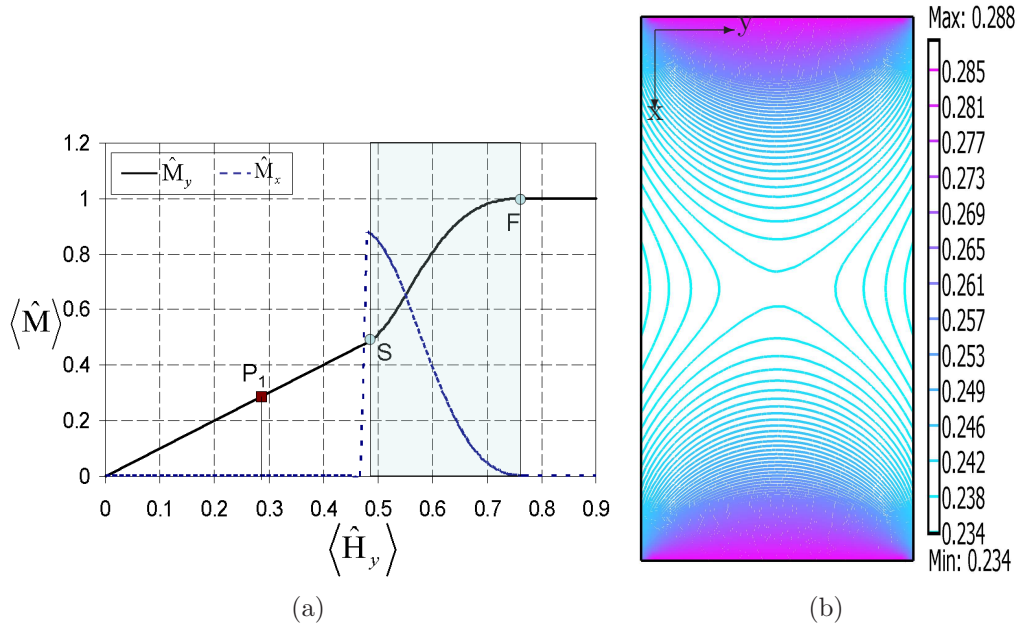


Figure 28: (a) A point P_1 which lies in the region before reorientation and (b) nondimensional magnetic field \hat{H}_y at $\langle \hat{H}_y \rangle = 0.248$.

In Figure 29(b) we present the normalized vector plot of the magnetization vector inside the specimen and we try to track the orientation of the magnetization. In the region of no reorientation, the macroscopic magnetization vectors have non-zero component only in the y -direction as indicated in Figure 29(b).

Next, we consider a point P_2 of the average constitutive response at $\langle \hat{H}_y \rangle = 0.506$ (Figure 30(a)), in which reorientation occurs almost everywhere inside the specimen. The contour plot of the magnetic field \hat{H}_y (Figure 30(b)) demonstrates the strong nonuniform distribution of \hat{H}_y inside the specimen. In this case the new martensitic variant, which has a nonlinear relation with the magnetic field \hat{H}_y (Equation (55)), starts to appear (Figure 31(a)). The range of magnitude of \hat{H}_y varies from 0.301 to 0.687 (Figure 30(b)) which

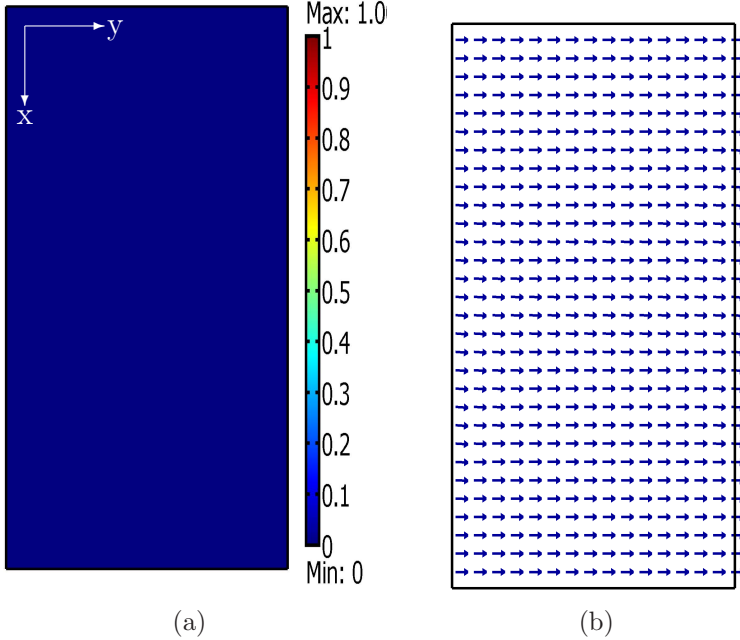


Figure 29: Distribution of (a) volume fraction of variant-2 and (b) orientation of magnetization vector at $\langle \hat{H}_y \rangle = 0.248$.

indicates that inside the specimen we have three cases. In the first case we have very small regions where \hat{H}_y is below the starting critical value (0.480) and no reorientation occurs. In the second case we have some regions where the new variant-2 is present, but with small value of ξ , and in the third case we observe regions where the magnetic field value is so high that it is close to the reorientation finish critical value (0.768). This observation is more clear in Figure 31(a) which represents the distribution of variant-2 volume fraction. We observe that at the regions of the top-left and bottom-right corners, the volume fraction almost reaches 1 while in the intermediate region, the volume fraction varies from 0-0.3.

In Figure 30(b) and Figure 31(a) an interesting observation is that two band like zones appear, which separate the specimen in three regions A, B, C (Figure 30(b)). The value of magnetic field or martensitic volume fraction changes abruptly across those narrow zones. For example, if we consider the region B between this narrow zones, the value of ξ is roughly 0.3. This value suddenly jumps to roughly 0.9 in regions A and C. The magnetization vector exhibits similar behavior. The direction of magnetization vectors (Figure 31(b)) also changes very sharply in the regions FG and GJ. The change in direction of magnetization vectors is almost uniform in the rest of the

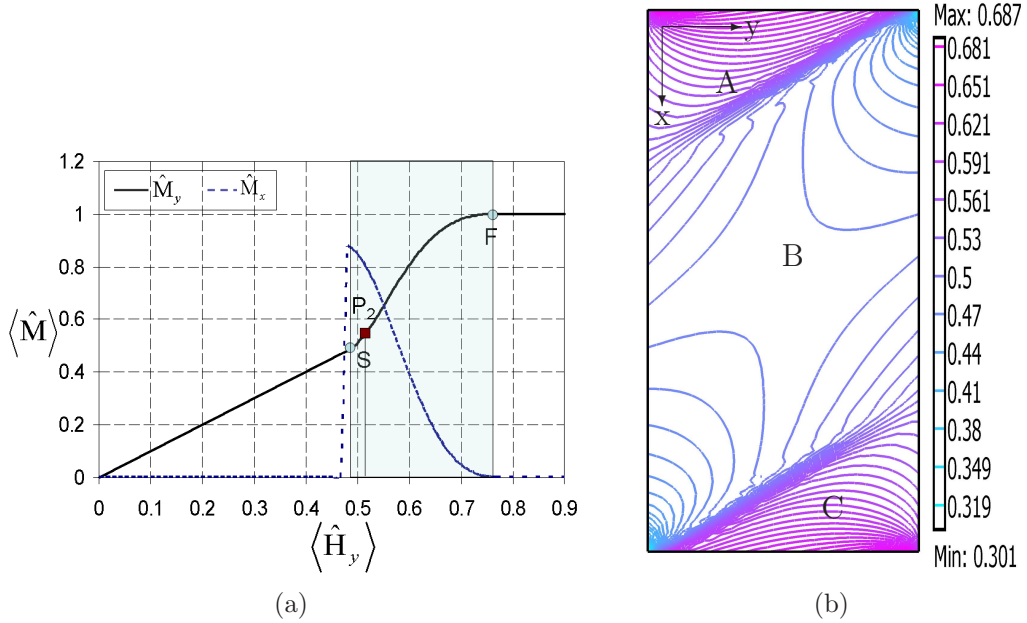


Figure 30: A point P_2 which lies in the region of reorientation and (b) nondimensional magnetic field \hat{H}_y at $\langle \hat{H}_y \rangle = 0.506$.

specimen.

The point P_3 in Figure 32(a) in the average magnetization-magnetic field response also lies in the reorientation region $S-F$ but with a higher magnetic field at $\langle \hat{H}_y \rangle = 0.551$. We still observe the band like zones in the \hat{H}_y distribution (Figure 33(a)) and a sharp change in direction (Figure 31(b)) of the magnetization vectors in the regions FG and GJ. In this case, the banded zones have moved closer to each other.

Finally, we consider the point P_4 at $\langle \hat{H}_y \rangle = 0.795$ (Figure 34(a)), in which reorientation process finishes. Figure 34(b) shows that the minimum and maximum value of the nonuniformly distributed magnetic field \hat{H}_y are 0.730 and 0.964 respectively. The minimum value is very close to the critical value to finish the reorientation process (0.768). Due to this reason, we observe that the specimen is almost fully reoriented and the value of martensitic volume fraction is close to 1 everywhere inside the specimen (Figure 35(a)). Moreover, the magnetization vectors (Figure 35(b)) are aligned in the y axis, the direction of the easy axis of the variant-2, due to high applied magnetic field. In this case, the band like zones disappear in the distribution of \hat{H}_y , martensitic volume fraction and magnetization vector.

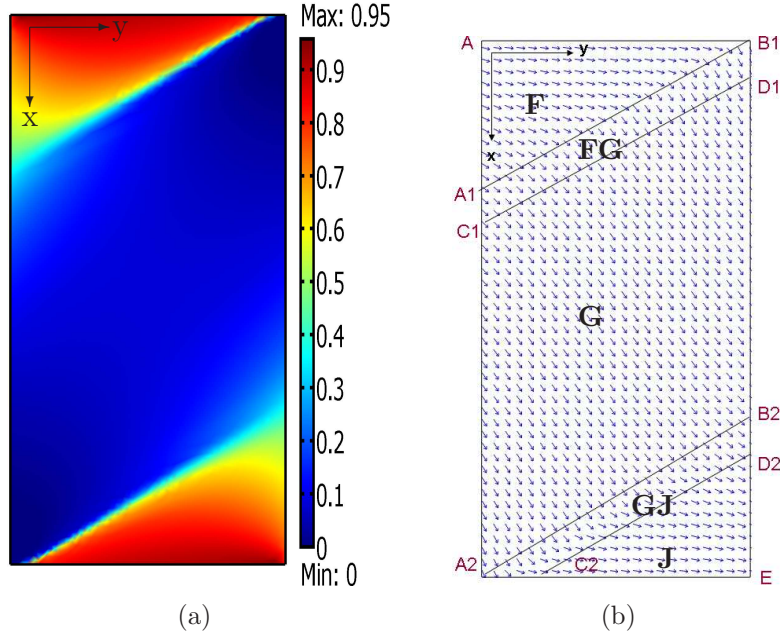


Figure 31: Distribution of (a) volume fraction of variant-2 and (b) orientation of magnetization vector at $\langle \hat{H}_y \rangle = 0.506$.

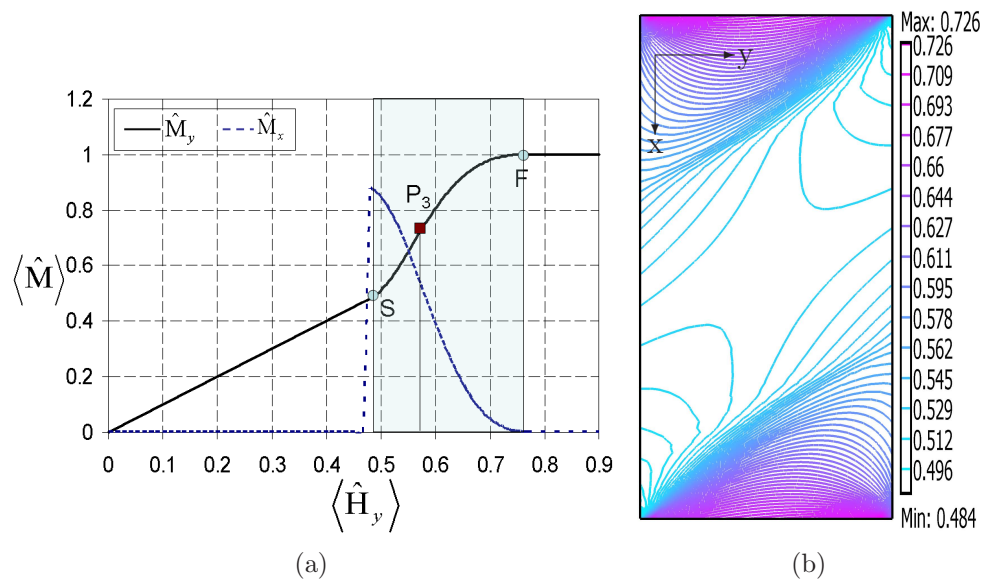


Figure 32: A point P_3 which lies in the region of reorientation and (b) nondimensional magnetic field \hat{H}_y at $\langle \hat{H}_y \rangle = 0.551$.

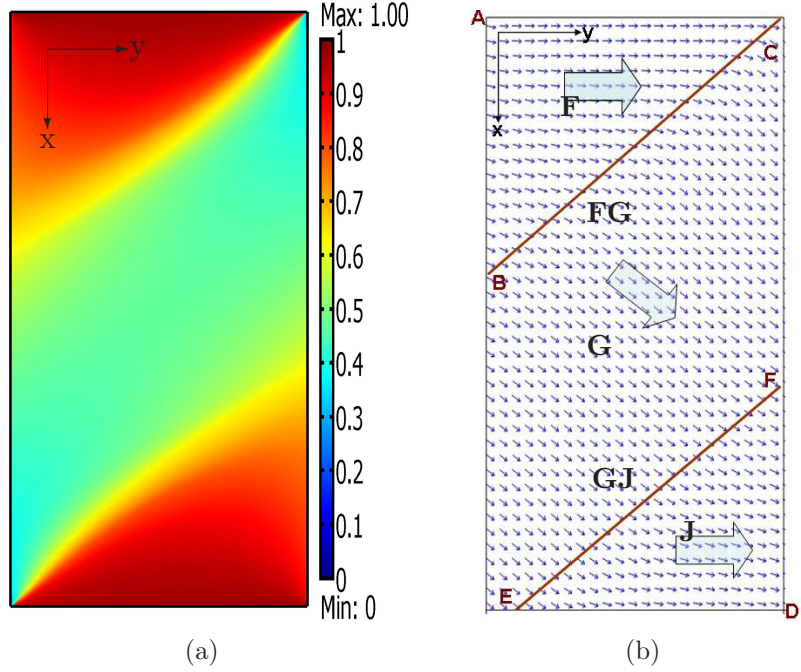


Figure 33: Distribution of (a) volume fraction of variant-2 and (b) orientation of magnetization vector at $\langle \hat{H}_y \rangle = 0.551$.

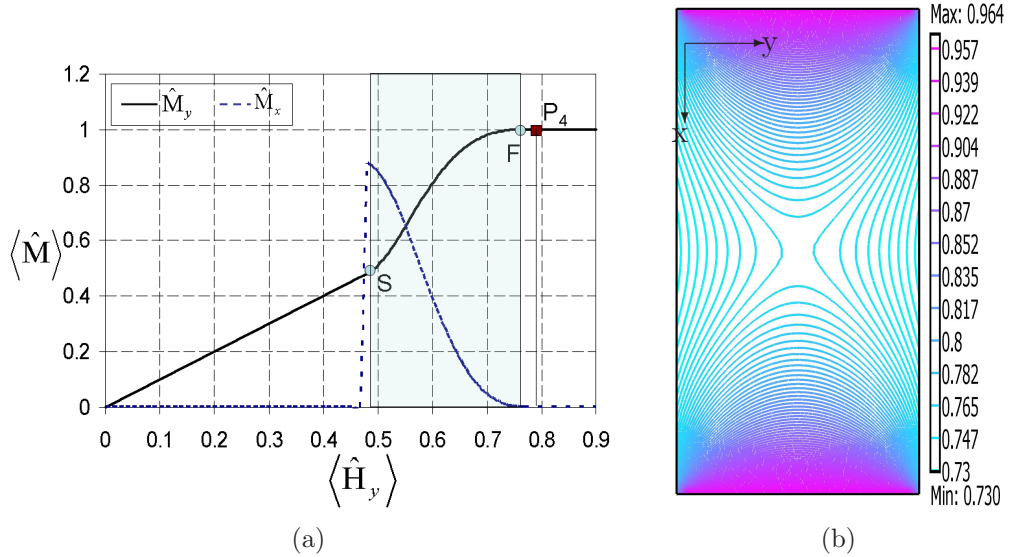


Figure 34: A point P_4 which lies in the region after reorientation and (b) nondimensional magnetic field \hat{H}_y at $\langle \hat{H}_y \rangle = 0.795$.

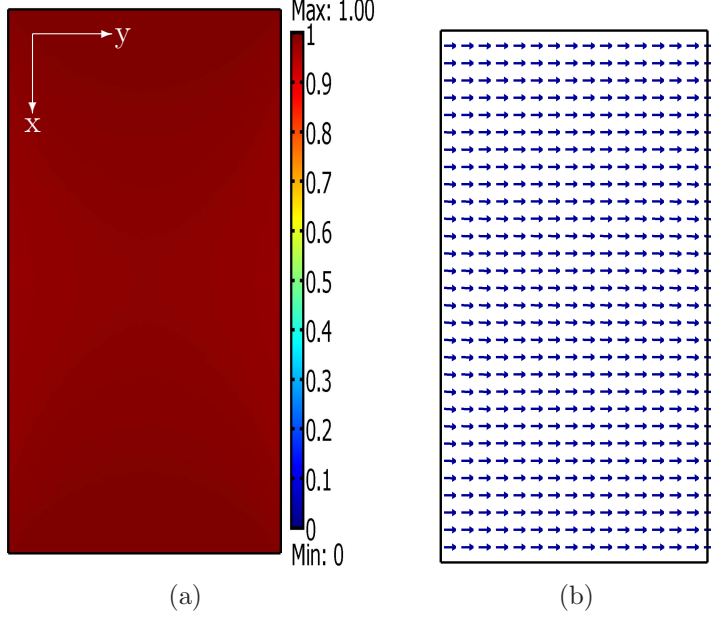


Figure 35: Distribution of (a) volume fraction of variant-2 and (b) orientation of magnetization vector at $\langle \hat{H}_y \rangle = 0.795$.

2.3 Stability Analysis and Parametric Study of Forward Reorientation

The numerical analysis reveals that a peculiar phenomenon occurs during the reorientation process. Two band like zones FG and GJ appear (Figure 31(b)). The appearance of band like zones can be explained by the loss of stability that occurs during reorientation. In this section we proceed to a stability analysis by investigating the magnetostatic system that we are solving. Combining equations (41) and (43), we can write,

$$\frac{\partial \hat{H}_x}{\partial \hat{x}} + \hat{k} \frac{d\hat{M}_x}{d\hat{H}_y} \frac{\partial \hat{H}_y}{\partial \hat{x}} + \ell \left(1 + \hat{k} \frac{d\hat{M}_y}{d\hat{H}_y} \right) \frac{\partial \hat{H}_y}{\partial \hat{y}} = 0. \quad (61)$$

Equations (42) and (61) form a system of quasi-linear partial differential equations of first order with respect to \hat{H}_x and \hat{H}_y . The slopes $\frac{d\hat{M}_x}{d\hat{H}_y}$ and $\frac{d\hat{M}_y}{d\hat{H}_y}$ are obtained from the constitutive response. The compact form of this system, after some simple computations, is written

$$\frac{\partial \hat{\mathbf{H}}}{\partial \hat{x}} + \hat{\mathbf{C}} \frac{\partial \hat{\mathbf{H}}}{\partial \hat{y}} = \mathbf{0}, \quad (62)$$

with

$$\widehat{\mathbf{H}} = \begin{bmatrix} \widehat{H}_x \\ \widehat{H}_y \end{bmatrix}, \quad \widehat{\mathbf{C}} = \ell \begin{bmatrix} \widehat{k} \frac{d\widehat{M}_x}{d\widehat{H}_y} & 1 + \widehat{k} \frac{d\widehat{M}_y}{d\widehat{H}_y} \\ -1 & 0 \end{bmatrix}. \quad (63)$$

Equation (62) is a system of two 1st order PDEs. It should be noted that for the stability analysis, we are focusing on the 1st order system, though we solved one second order PDE for the numerical analysis. The result of the stability analysis is the same for both cases. The second order PDE equation involves the magnetic potential ϕ , which does not have a direct interpretation of the physical quantities like magnetic field, magnetic induction etc. But, when we reduce the system in the system of 1st order PDEs, the variables become magnetic field components which are physical quantities.

The system can be elliptic, parabolic or hyperbolic (unstable) if $\widehat{\mathbf{C}}$ has two complex eigenvalues, one real eigenvalue, or two real and distinct eigenvalues respectively. If \mathbf{I} is the identity matrix, then the equation

$$\det(\widehat{\mathbf{C}} - \lambda \mathbf{I}) = 0, \quad (64)$$

leads to

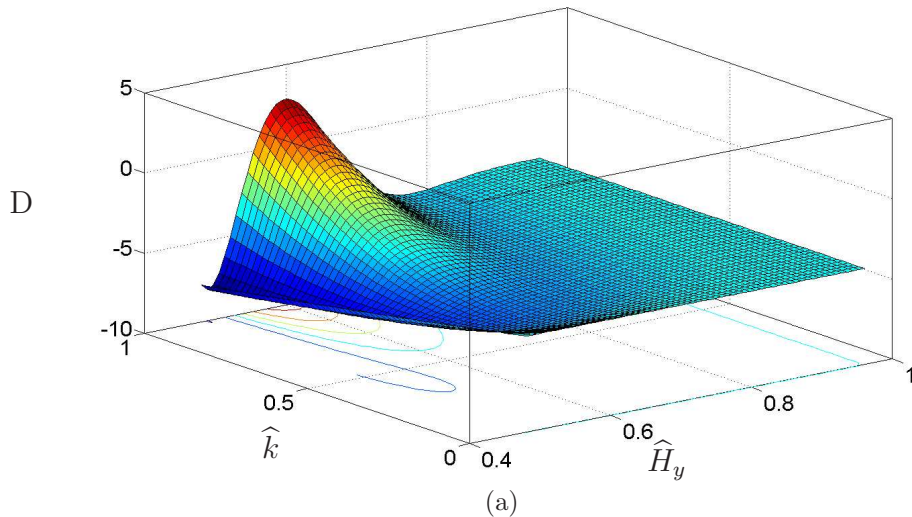
$$\lambda^2 - \ell \widehat{k} \frac{d\widehat{M}_x}{d\widehat{H}_y} \lambda + \ell^2 \left(1 + \widehat{k} \frac{d\widehat{M}_y}{d\widehat{H}_y} \right) = 0. \quad (65)$$

The roots λ_1, λ_2 of (65) are real, only if

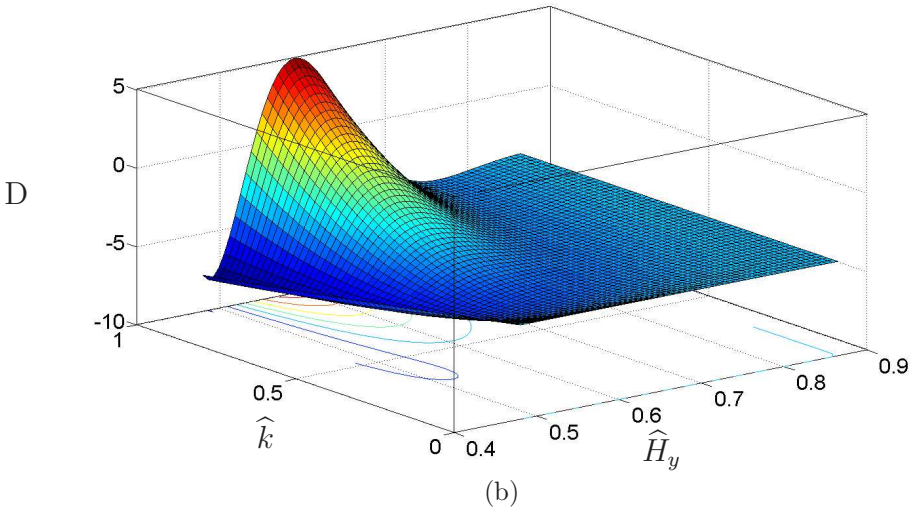
$$D(\widehat{k}, \widehat{H}_y) = \widehat{k}^2 \left(\frac{d\widehat{M}_x}{d\widehat{H}_y} \right)^2 - 4 \left(1 + \widehat{k} \frac{d\widehat{M}_y}{d\widehat{H}_y} \right) \geq 0, \quad (66)$$

From the previous equation it is evident that the type of the system (elliptic, parabolic or hyperbolic) depends exclusively on the value of the magnetic field component \widehat{H}_y . It should be noted that the value of D does not depend on the aspect ratio.

Normal ferromagnetic material like α -Fe with BCC crystalline structure, if we consider idealized single crystal structure with 180° domain wall, does not exhibit instability under the same magnetic loading condition as described for the MSMA sample. In this case, the mechanism of magnetization is mainly based on the rotation of the magnetization vectors when magnetic field is applied along the hard axis. It should be recalled that we fixed the direction of the hard axis along the y-axis. In general, the magnetization response becomes an increasing function of the applied magnetic field and we will always get a non-negative slope i.e. $\frac{d\widehat{M}_y}{d\widehat{H}_y} \geq 0$. At the same time,



(a)



(b)

Figure 36: Discriminant $D(\hat{k}, \hat{H}_y)$ at (a) $\hat{H}_y^{f(1,2)} = 0.960$ and (b) $\hat{H}_y^{f(1,2)} = 0.864$.

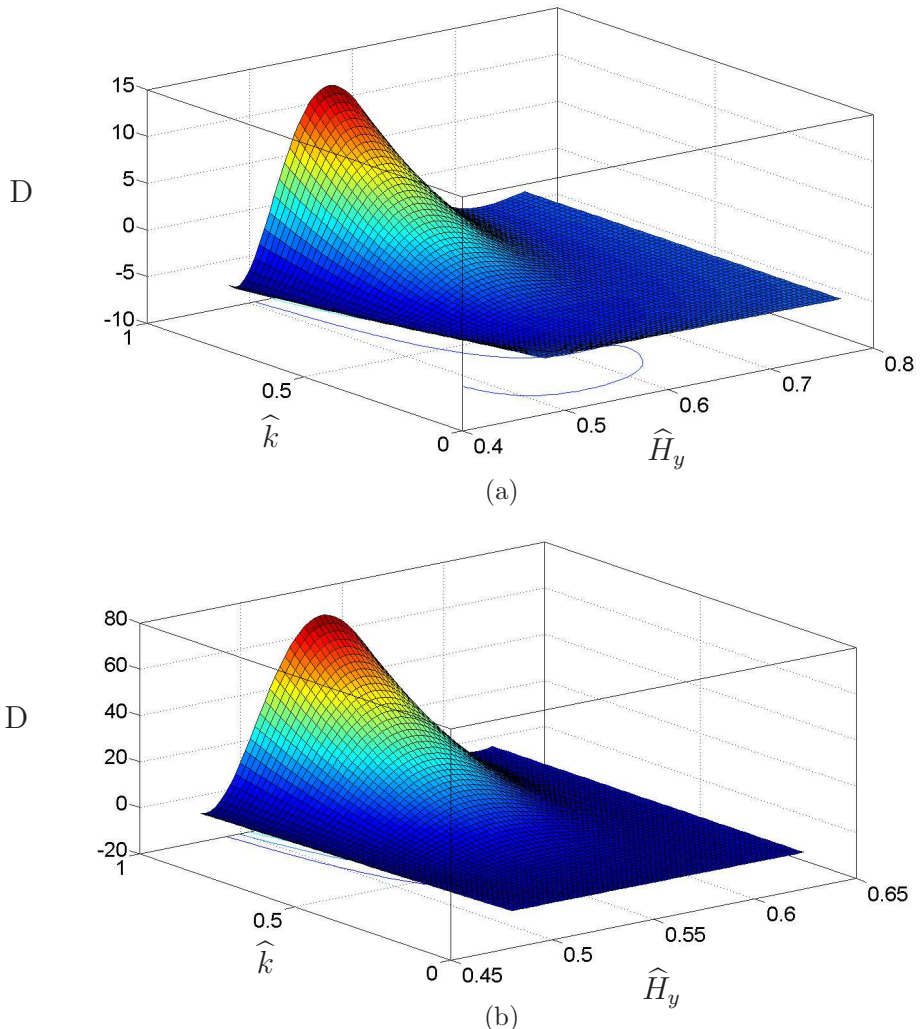


Figure 37: Discriminant $D(\hat{k}, \hat{H}_y)$ at (a) $\hat{H}_y^{f(1,2)} = 0.768$ and (b) $\hat{H}_y^{f(1,2)} = 0.624$.

since there is no driving force to move the domain walls, the magnetization response along the x direction is always zero. This means $\frac{d\widehat{M}_x}{d\widehat{H}_y} = 0$ and the ferromagnetic system remains always elliptic (66). For a ferromagnetic MSMA material, however, the case is different. The magnetic field is applied along the hard axis of the initial stress-favored variant of the MSMA specimen. Beyond a certain critical value of the applied field, a new variant nucleates due to the variant reorientation mechanism. The coexistence of two variants generates 90^0 domain walls. The new field-favored variant has its easy axis along the direction of the applied field. The critical magnetic field is high enough to eliminate the presence of 180^0 domain wall in each variant. Moreover, due to the 90^0 domain wall, stress-favored variant contributes a net magnetization along the direction perpendicular to the applied field i.e. in the x-direction. Under this condition loss of ellipticity can occur.

When the system becomes hyperbolic, there exist two families of characteristics. The differential equations which describe them are given by the solution of the quadratic equation (65),

$$\lambda = \frac{dy}{dx} = \frac{\ell}{2} \left(\widehat{k} \frac{d\widehat{M}_x}{d\widehat{H}_y} \pm \sqrt{\widehat{k}^2 \left(\frac{d\widehat{M}_x}{d\widehat{H}_y} \right)^2 - 4 \left(1 + \widehat{k} \frac{d\widehat{M}_y}{d\widehat{H}_y} \right)} \right), \quad (67)$$

where,

$$\frac{d\widehat{M}_x}{d\widehat{H}_y} = -\frac{\widehat{H}_y(1-\xi)}{\sqrt{1-\widehat{H}_y^2}} - \frac{d\xi}{d\widehat{H}_y} \sqrt{1-\widehat{H}_y^2}, \quad \frac{d\widehat{M}_y}{d\widehat{H}_y} = (1-\xi) + \frac{d\xi}{d\widehat{H}_y} (1-\widehat{H}_y). \quad (68)$$

The above analysis is illustrated clearly with the help of a parametric study. The four parameters $H_y^{s(1,2)}$, $H_y^{f(1,2)}$, M^{sat} , ρK_1 that describe the constitutive material response, are reduced in the non-dimensional model to three, $\widehat{H}_y^{s(1,2)}$, $\widehat{H}_y^{f(1,2)}$ and \widehat{k} . We will vary \widehat{H}_y from reorientation start $\widehat{H}_y^{s(1,2)}$ to reorientation finish $\widehat{H}_y^{f(1,2)}$ and \widehat{k} from 0 to 1 to examine the sign of $D(\widehat{k}, \widehat{H}_y)$. We fix $\widehat{H}_y^{s(1,2)}$ at 0.480 and consider the value of $\widehat{H}_y^{f(1,2)}$ at 0.960, 0.864, 0.768 and 0.480. The fixed value $\widehat{H}_y^{s(1,2)}=0.480$ and $\widehat{H}_y^{f(1,2)}=0.768$ correspond to the real material values as described in the earlier section. Figure 36(a) represents the distribution of D where we have reorientation finish magnetic field ($\widehat{H}_y^{f(1,2)}=0.960$) higher than the real experimental value (0.768). For a fixed value of \widehat{k} , the value of D gradually increases with the increasing magnetic field to a maximum value and then gradually decreases towards the end of reorientation process. This is due to the fact that the \widehat{M}_x - \widehat{H}_y constitutive response decreases monotonically due to formation of new field-favored

variant and the slope $\frac{d\hat{M}_x}{d\hat{H}_y}$ tends to zero. Similar trend is observed in Figure 36(b), where $\hat{H}_y^{f(1,2)}=0.864$. The key observation is the maximum value of D increases and $D \geq 0$ for larger range of \hat{k} and for magnetic field values that are closer to the reorientation start and finish. The next case with $\hat{H}_y^{f(1,2)}=0.768$ is presented in Figure 37(a), where higher value of D is observed and $D \geq 0$ expands in higher values of \hat{k} and in larger range between the magnetic field reorientation bounds. Finally, by decreasing the value of $\hat{H}_y^{f(1,2)}$ to 0.624, we observe a very high value of D nearly 70 and D becomes non-negative in most of the reorientation region (Figure 37(b)). This study shows that by keeping $\hat{H}_y^{s(1,2)}$ fixed, the instability ($D(\hat{k}, \hat{H}_y) \geq 0$) during reorientation becomes easier with the decrease of $\hat{H}_y^{f(1,2)}/\hat{H}_y^{s(1,2)}$ ratio. We can interpret the decreasing of the ratio as the faster energy release and steeper slopes of the nonlinear magnetization responses during the reorientation process. Faster dissipation means that the microstructure is changing rapidly and becomes unstable to accommodate the twin martensitic variants. The steeper nonlinear magnetization response also indicates that with a small change in magnetic field, the magnetization changes significantly and the twin structures need to be change quickly for the rapid change of the magnetization, causing unstable behavior to the material.

2.4 Discussion

The appearance of the band like zones (Figure 31(a)) in the FEM analysis during reorientation is due to loss of ellipticity. The discriminant D that dictates the loss of ellipticity is given by Equation (66). The plot of D at $\langle \hat{H}_y \rangle = 0.506$ is presented in Figure 38(a). The Figure shows that for $\langle \hat{H}_y \rangle = 0.506$ there are two distinct regions H where $D \geq 0$ and loss of ellipticity occurs. The stable elliptic regions (E in Figure 38(a)) with $D < 0$, which are separated by the unstable hyperbolic regions, have a completely different behavior in terms of the field variables, like the magnetic field \hat{H}_y (Figure 38(b)), the magnetization vector (Figure 31(b)) and the martensitic variant volume fraction (Figure 31(a)). This shows the drastic effect of the unstable zones appearance in the specimen response. In the absence of these hyperbolic regions, for instance before or after the reorientation process, the field variables have gradual transition in the specimen (Figures 28(b) or 34(b) respectively). In the hyperbolic zones the magnetization vector has a sudden change in direction (Figure 31(b)), especially at the areas closer to the corners.

The values of the characteristic angles in the unstable regions in the non-dimensional spatial description are given by the equation (67) and they

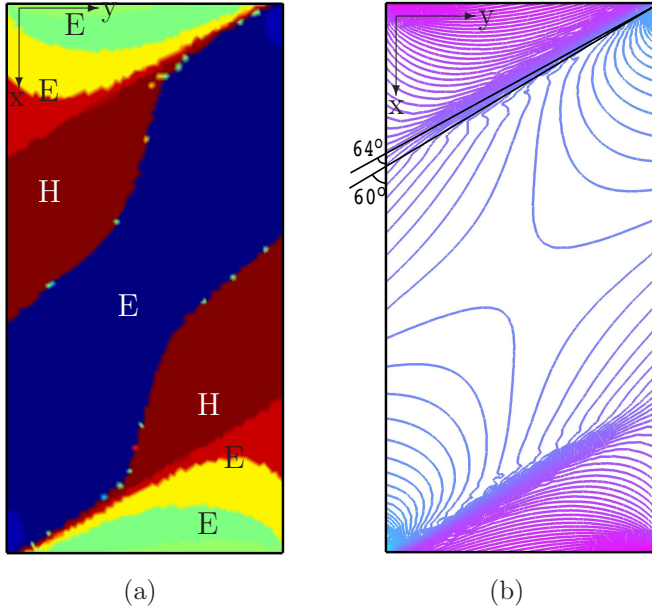


Figure 38: (a) Discriminant D at $\hat{H}_y \geq 0.506$ and (b) jump in the magnetic field across characteristics.

vary spatially. In the present study the two characteristic angles of all the critical points are almost the same (-60° and -64° in the actual specimen dimensions). The magnetic field shows a drastic change across characteristics that start from the top right and bottom left corners (Figure 38(b)). We need to mention that these angles refer to the actual dimensions, since in the non-dimensional spatial description, the angles that occur do not represent the real state of the specimen. It is also important to note that the characteristic angles that are computed are based on the microstructural description given in Figure 1. If the microstructural description changes, then the orientation of the characteristics will also change.

3 FIELD INDUCED PHASE TRANSFORMATION

The magnetic field associated with field induced phase transformation is nearly nine times higher than the magnetic field required for variant reorientation mechanism. This implies that the magnetic stress is very high compared to the variant reorientation mechanism. A non-linear continuum mechanics based

finite deformation formulation is developed to consider the strong coupling of high magnetic field with the mechanical media.

3.1 The Mechanism of Field Induced Phase Transformation

Experimental results [24] show that the transformation temperatures of Ni_2MnGa alloys increase when magnetic field is applied. Based on this experimental observation, the FIPT mechanism is represented schematically in Fig. 39(a). When magnetic field is not applied, the points 2, 3, 4, 1 in Fig. 39 represent martensite start, martensite finish, austenite start and austenite finish, respectively at a specific temperature. All the four critical points shift to higher values ($2'$, $3'$, $4'$, $1'$) in the presence of magnetic field while temperature remains constant. This indicates that magnetic field stabilizes austenite since austenite is more ferromagnetic than martensite. We shall now consider the case when a magnetic field and a constant compressive stress σ_c is applied to the specimen. The specimen is at P in Fig. 39 in the austenitic phase. If $\sigma_2 \leq \sigma_c \leq \sigma_{2'}$, the removal of applied magnetic field causes unstable austenitic phase. This leads to the forward phase transformation. At the same stress level, the specimen becomes stable in the martensitic phase (point Q in Fig. 39) and a significant amount of strain is generated. When magnetic field is applied again, martensitic to austenitic phase transformation takes place and the material returns to the initial state (point P in Fig. 39).

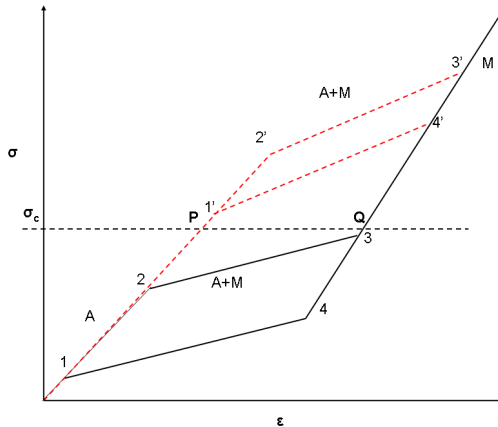


Figure 39: Pseudo elastic loops with and without magnetic field in Ni_2MnGa MSMAs.

In the present study, our material is $\text{Ni}_{45}\text{Mn}_{36.5}\text{Co}_5\text{In}_{13.5}$ which exhibits FIPT like Ni_2MnGa , however, in NiMnCoIn , martensite phase is antiferromagnetic while in Ni_2MnGa , it is ferromagnetic. This new material system can produce around 5% strain with 120 MPa blocking stress, which is almost four times higher than Ni_2MnGa material system [25]. The specimen was initially in the austenitic phase at constant temperature. A compressive stress is applied and the specimen is transformed to martensitic phase with subsequent cooling. The magnitude of spontaneous magnetization in the antiferromagnetic martensitic phase is much lower compared to the ferromagnetic austenitic phase. In the experiment, the traction is applied along the vertical axis and the direction of the applied magnetic field is along the horizontal axis [25]. We denote the volume fraction of martensitic phase due to the magnetic field and temperature by ξ_1 and ξ_2 respectively. This implies that the volume fraction of the austenitic phase is $(1 - \xi_1 - \xi_2)$.

3.2 Nonlinear Kinematics

The finite deformation analysis is an essential tool to know the decomposition of the total stress into a mechanical and a magnetic part. The contribution of the mechanical and the magnetic part to the total stress is very difficult to find out experimentally, because in most of the cases we measure the total stress. By following a systematic non-linear kinematic approach, we find out the relation between mechanical part and the magnetic part with the total stress. This decomposition is crucial due to the fact that the mechanical constitutive relation is associated only with the mechanical part of the total stress.

We denote the undeformed configuration by Ω_0 and the deformed configuration, at time t , by Ω_t . Let $\{\mathbf{b}, \mathbf{h}, \mathbf{m}\}$ are the magnetic induction, the magnetic field and the magnetization in the rest frame respectively. The magnetization vector \mathbf{m} is related through the constitutive relation $\mathbf{m} = \mathbf{b}/\mu_0 - \mathbf{h}$. Let a generic point $P \in \Omega_t$ moves with a velocity $\dot{\mathbf{x}}$. At this moving point, we denote the electro magnetic variables by $\{\tilde{\mathbf{e}}, \tilde{\mathbf{h}}, \tilde{\mathbf{b}}, \tilde{\mathbf{m}}\}$. According to Minkowsky formulation, at point P we have, $\tilde{\mathbf{e}} = \dot{\mathbf{x}} \times \mathbf{b}$, $\tilde{\mathbf{h}} = \mathbf{h}$, $\tilde{\mathbf{m}} = \mathbf{m}$, $\tilde{\mathbf{b}} = \mathbf{b}$. Since we are considering only magnetic medium, electric field and polarization vector are equal to zero. The advantage of the Minkowsky formulation is that all the electromagnetic field variables obey Euclidian transformation [2]. Moreover we denote the deformation gradient by \mathbf{F} , the temperature by T and total stress by $\sigma \in \Omega_t$.

Under this framework, we have the conservation of linear momentum

$$\nabla \cdot \boldsymbol{\sigma} + \rho \mathbf{f}_b = \rho \ddot{\mathbf{x}}, \quad (69)$$

the conservation of angular momentum,

$$\text{skw } \boldsymbol{\sigma} = \mathbf{0}, \quad (70)$$

the conservation of energy,

$$\rho \dot{u} = \boldsymbol{\sigma} : \mathbf{L} + \rho r^h - \nabla \cdot (\mathbf{q} + \tilde{\mathbf{e}} \times \tilde{\mathbf{h}}), \quad (71)$$

the entropy inequality,

$$\rho \dot{s} \geq \rho r^h / T - \nabla \cdot (\mathbf{q} / T), \quad (72)$$

and the moving frame Maxwell equations

$$\nabla \times \tilde{\mathbf{h}} = \mathbf{0}, \quad (73)$$

$$\nabla \cdot \tilde{\mathbf{b}} = 0, \quad (74)$$

$$\nabla \times \tilde{\mathbf{e}} = -\dot{\tilde{\mathbf{b}}}. \quad (75)$$

Here, \mathbf{f}_b is the nonmagnetic body force, $u = u(\mathbf{F}, \tilde{\mathbf{b}}, \mathbf{T}, \zeta_i)$ is the internal energy, \mathbf{L} is the velocity gradient, r^h and \mathbf{q} are the heat source per unit mass and heat flux vector respectively and ζ_i represent set of internal variables. Motivated by the application of Pointing's theorem, the energy flux vector $(\tilde{\mathbf{e}} \times \tilde{\mathbf{h}})$ is added to the energy equation to take into account the total electro magnetic energy in addition to the thermal and mechanical energy [26]. We denote the convective derivative of a vector \mathbf{v} by

$$\dot{\mathbf{v}} = \dot{\mathbf{v}} + \mathbf{v} \nabla \cdot \dot{\mathbf{x}} - (\mathbf{v} \cdot \nabla) \dot{\mathbf{x}}. \quad (76)$$

We will now very briefly discuss the steps to obtain the constitutive equations from the field equations listed above. First using the the set of Maxwell equations and the identity $\nabla \cdot (\tilde{\mathbf{e}} \times \tilde{\mathbf{h}}) = \tilde{\mathbf{h}} \cdot \nabla \times \tilde{\mathbf{e}} - \tilde{\mathbf{e}} \cdot \nabla \times \tilde{\mathbf{h}}$, we have

$$\begin{aligned} \nabla \cdot (\tilde{\mathbf{e}} \times \tilde{\mathbf{h}}) &= \mathbf{m} \cdot \dot{\mathbf{b}} + \left[\frac{1}{\mu_0} \mathbf{b} \otimes \mathbf{b} - \mathbf{m} \otimes \mathbf{b} + (\mathbf{m} \cdot \mathbf{b} - \frac{1}{\mu_0} \mathbf{b} \cdot \mathbf{b}) \mathbf{I} \right] : \mathbf{L} \\ &\quad - \left(\frac{1}{2\mu_0} \mathbf{b} \cdot \mathbf{b} \right). \end{aligned} \quad (77)$$

By defining the specific Helmholtz energy potential, we performing the Legendre transformation $\Psi(\mathbf{F}, \mathbf{h}, T, \zeta_i) = u - sT - \frac{1}{2\mu_0} \mathbf{b} \cdot \mathbf{b} + \frac{1}{2\mu_0} \mathbf{m} \cdot \mathbf{m}$ [26, 27] and using Eq. 71, Eq. 72 and Eq. 77 we get

$$-\dot{\Psi} - s\dot{T} + \frac{1}{\rho} \boldsymbol{\sigma}_c : \mathbf{L} - \frac{\mu_0}{\rho} \mathbf{m} \cdot \dot{\mathbf{h}} - \frac{1}{\rho} \mathbf{q} \cdot \nabla T / T \geq 0, \quad (78)$$

where

$$\boldsymbol{\sigma}_c = \boldsymbol{\sigma} - [\mu_0 \mathbf{h} \otimes \mathbf{h} + \mu_0 \mathbf{h} \otimes \mathbf{m} - \frac{1}{2} \mu_0 (\mathbf{h} \cdot \mathbf{h}) \mathbf{I}] , \quad (79)$$

or in short, $\boldsymbol{\sigma}_c = \boldsymbol{\sigma} - \boldsymbol{\sigma}_m(\mathbf{m}, \mathbf{h})$. The term $\boldsymbol{\sigma}_m$ can be recognized as the Maxwell stress. We will now change our working platform from deformed configuration to reference configuration due to two main reasons, 1) the experimental measurements of the mechanical constants are performed on the reference configuration and 2) all the magneto mechanical field variables become frame indifferent when they transform back from the deformed to undeformed configuration. Let \mathbf{H} , \mathbf{M} , $\nabla_0 T$ and \mathbf{Q} are the magnetic field, the magnetization vector, the temperature gradient and heat flux respectively in Ω_0 and $\Psi = \Psi(\mathbf{E}, \mathbf{H}, T, \zeta_i)$.

with the following pull back operations.

$$\mathbf{H} = \mathbf{F}^T \mathbf{h} , \quad (80)$$

$$\mathbf{M} = \mathbf{F}^T \mathbf{m} , \quad (81)$$

$$\nabla_0 T = \mathbf{F}^T \mathbf{q} , \quad (82)$$

$$\mathbf{Q} = \det(\mathbf{F}) \mathbf{F}^{-1} \mathbf{q} , \quad (83)$$

In addition

$$\mathbf{E} = \frac{1}{2}(\mathbf{C} - \mathbf{I}), \quad \mathbf{C} = \mathbf{F}^T \mathbf{F} , \quad (84)$$

where \mathbf{E} is the Green strain tensor and $\det(\mathbf{F}) = \rho_0 / \rho$.

We can rewrite Eq. 72 in Ω_0 in the following way,

$$-\dot{\Psi} - s\dot{T} + \frac{1}{\rho}(\boldsymbol{\sigma}_c + \mu_0(\mathbf{h} \otimes \mathbf{m})) : \mathbf{L} - \frac{\mu_0}{\rho_0} \mathbf{M} \cdot \dot{\mathbf{H}} - \frac{1}{\rho_0} \mathbf{Q} \cdot \nabla_0 \mathbf{T} / \mathbf{T} \geq \mathbf{0} . \quad (85)$$

We will define,

$$\begin{aligned} \boldsymbol{\sigma}_{cR} &= (\boldsymbol{\sigma}_c + \mu_0(\mathbf{h} \otimes \mathbf{m})) , \\ &= \boldsymbol{\sigma} - [\mu_0 \mathbf{h} \otimes \mathbf{h} - \frac{1}{2} \mu_0 (\mathbf{h} \cdot \mathbf{h}) \mathbf{I}] \quad (\text{using Eq. 79}) , \\ &= \boldsymbol{\sigma} - \boldsymbol{\sigma}_h(\mathbf{h}) , \end{aligned} \quad (86)$$

and the pull back operation on $\boldsymbol{\sigma}_{cR}$, denoted by

$$\mathbf{S}_{cR} = \det(\mathbf{F}) \mathbf{F}^{-1} \boldsymbol{\sigma}_{cR} \mathbf{F}^{-T} . \quad (87)$$

Moreover, considering the fact that $\frac{1}{\rho}(\boldsymbol{\sigma}_{cR} : \mathbf{L}) = \frac{1}{\rho_0}(\mathbf{S}_{cR} : \dot{\mathbf{E}})$ and $-\frac{1}{\rho_0} \mathbf{Q} \cdot \nabla_0 \mathbf{T} / \mathbf{T} \geq \mathbf{0}$, Eq. 85 reduces to

$$-\dot{\Psi} - s\dot{T} + \frac{1}{\rho_0}(\mathbf{S}_{cR} : \dot{\mathbf{E}}) - \frac{\mu_0}{\rho_0}\mathbf{M} \cdot \dot{\mathbf{H}} \geq 0 , \quad (88)$$

After performing the Legendre transformation $G(\mathbf{S}_{cR}, \mathbf{H}, T, \zeta_i) = \Phi(\mathbf{E}, \mathbf{H}, T, \zeta_i) - \frac{1}{\rho_0}\mathbf{S}_{cR} : \mathbf{E}$ and following Coleman-Noll procedure we get the following constitutive equations in terms of the Gibbs potential

$$\mathbf{E} = -\rho_0 G_{,\mathbf{S}_{cR}} , \quad (89)$$

$$\mathbf{M} = -\frac{\rho_0}{\mu_0} G_{,\mathbf{H}} , \quad (90)$$

$$s = -G_{,T} , \quad (91)$$

and the inequality

$$-\rho_0 G_{,\zeta_i} \dot{\zeta}_i \geq 0 , \quad (92)$$

Here

$$\mathbf{S}_{cR} = \det(\mathbf{F}) \mathbf{F}^{-1} \boldsymbol{\sigma}_{cR} \mathbf{F}^{-T} , \quad (93)$$

and

$$\boldsymbol{\sigma}_{cR} = \boldsymbol{\sigma} - [\mu_0 \mathbf{h} \otimes \mathbf{h} - \frac{1}{2}\mu_0(\mathbf{h} \cdot \mathbf{h})\mathbf{I}] . \quad (94)$$

3.3 Constitutive Modeling

Motivated by experiments, a constitutive model is proposed to account for temperature, magnetic field and stress induced phase transformation from martensitic to austenitic phase. The constitutive equations are derived in a consistent thermodynamic way. The model is calibrated from experimental data. The strain versus temperature constitutive response is simulated and the constitutive responses of magnetization versus magnetic field is then predicted and compared with experimental results. Magnetization versus temperature response is also presented. The proposed model has the ability to predict the nonlinear, hysteretic strain and magnetization response caused by martensitic phase transformation due to temperature and magnetic field effect. The model is able to capture the magneto-thermo-mechanical coupling effect and simulate quite accurately the experimental results.

Under the small strain assumption, the two laws of thermodynamics and the Coleman-Noll procedure lead to the following constitutive equations.

$$\boldsymbol{\varepsilon} = -\rho G_{,\boldsymbol{\sigma}_{cR}} , \quad (95)$$

$$\mathbf{M} = -\frac{\rho}{\mu_0} G_{,\mathbf{H}} , \quad (96)$$

$$s = -G_{,T} , \quad (97)$$

and the inequality

$$-\rho G_{,\zeta_i} \dot{\zeta}_i \geq 0 . \quad (98)$$

Here,

$$\boldsymbol{\sigma}_{cR} = \boldsymbol{\sigma} - [\mu_0 \mathbf{H} \otimes \mathbf{H} - \frac{1}{2} \mu_0 (\mathbf{H} \cdot \mathbf{H}) \mathbf{I}] , \quad (99)$$

is the mechanical stress and \mathbf{I} is the unit second order tensor. $\boldsymbol{\varepsilon}$, $\boldsymbol{\sigma}$, s , T and ρ are the total strain, total stress, entropy, temperature and density. \mathbf{M} and \mathbf{H} are the magnetization and magnetic field vectors respectively. It should be noted that for small strain assumption, $\mathbf{F} \simeq \mathbf{I}$ and so $\mathbf{H} \simeq \mathbf{h}$ and $\mathbf{M} \simeq \mathbf{m}$. Moreover, ζ_i are the set of internal variables. G represents the Gibbs free energy and for our specific problem, the Gibbs energy functional is given by

$$\begin{aligned} G(\boldsymbol{\sigma}_{cR}, \mathbf{H}, T, \boldsymbol{\varepsilon}^t, \xi_1, \xi_2) = & - \frac{1}{2\rho} \boldsymbol{\sigma}_{cR} : \mathcal{S} \boldsymbol{\sigma}_{cR} - \frac{1}{\rho} \boldsymbol{\sigma} : [\boldsymbol{\alpha}(T - T_0) + \boldsymbol{\varepsilon}^t] \\ & - \frac{\mu_0}{\rho} \mathbf{M} \cdot \mathbf{H} - s_0 T + u_0 + c[(T - T_0) - T \ln \frac{T}{T_0}] \\ & + \frac{1}{\rho} f_1(\xi_1) + \frac{1}{\rho} f_2(\xi_2) + G_0(T) . \end{aligned} \quad (100)$$

Here the transformation strain $\boldsymbol{\varepsilon}^t$ and the martensitic volume fractions ξ_1 , ξ_2 are the internal variables. Moreover, $\boldsymbol{\alpha}$, c , s_0 , u_0 are the effective thermal expansion tensor, effective specific heat, effective specific entropy at the reference state and effective specific internal energy at the reference state respectively. We assume additive decomposition of the strain such that $\boldsymbol{\varepsilon}^e = \boldsymbol{\varepsilon} - \boldsymbol{\varepsilon}^t$ holds, where $\boldsymbol{\varepsilon}^e$ is the elastic strain and we also neglect the effect of thermal expansion. The magnetic anisotropy energy is negligible in cubic austenite and has no contribution in the overall energetics. The available Zeeman energy is the main driving force to nucleate the new phase. To obtain the effective compliance tensor \mathcal{S} and the magnetization vector \mathbf{M} we use rule of mixtures.

The mechanical and magnetic constitutive equations are obtained by using Eq. 95, Eq. 96, Eq. 99 and Eq. 100.

$$\boldsymbol{\varepsilon} = \mathcal{S} : \boldsymbol{\sigma}_{cR} + \boldsymbol{\varepsilon}^t , \quad (101)$$

$$\mathbf{M} = (\mathbf{H} \otimes \mathbf{I}) : \boldsymbol{\varepsilon}^t + \mathbf{M}_A + (\xi_1 + \xi_2) \Delta \mathbf{M} . \quad (102)$$

For the internal variables $\boldsymbol{\varepsilon}^t$, ξ_1 and ξ_2 Eq. 98 becomes,

$$-\rho_0 G_{,\boldsymbol{\varepsilon}^t} : \dot{\boldsymbol{\varepsilon}}^t - \rho_0 G_{,\xi_1} \dot{\xi}_1 - \rho_0 G_{,\xi_2} \dot{\xi}_2 \geq 0 . \quad (103)$$

In the modeling of conventional shape memory behavior the transformation strain is usually related to the evolution of the new phase volume fraction [28–30]. Following this approach, the evolution of the transformation strain associated with both the thermal and the magnetic shape memory effect is proposed to be proportional to the rate of martensitic phase volume fraction

$$\dot{\boldsymbol{\varepsilon}}^t = \boldsymbol{\Lambda}_1 \dot{\xi}_1 + \boldsymbol{\Lambda}_2 \dot{\xi}_2 . \quad (104)$$

In the above equation $\boldsymbol{\Lambda}_1$ and $\boldsymbol{\Lambda}_2$ are the transformation tensors defining the direction in which the transformation strain develops. An explicit form of the tensors will be given in the next section for a specific example. We can further reduce Eq. 103 as following

$$\tilde{\pi}_{\xi_1} \dot{\xi}_1 + \tilde{\pi}_{\xi_2} \dot{\xi}_2 \geq 0 , \quad (105)$$

where $\tilde{\pi}_{\xi_1} = \boldsymbol{\pi}^t : \boldsymbol{\Lambda}_1 + \pi_{\xi_1}$ and $\tilde{\pi}_{\xi_2} = \boldsymbol{\pi}^t : \boldsymbol{\Lambda}_2 + \pi_{\xi_2}$. The entropy production of the individual terms of the equation (105) is non negative. So,

$$\tilde{\pi}_{\xi_1} \dot{\xi}_1 \geq 0 , \quad (106)$$

$$\tilde{\pi}_{\xi_2} \dot{\xi}_2 \geq 0 . \quad (107)$$

where the thermodynamic driving forces $\boldsymbol{\pi}^t$, $\boldsymbol{\pi}^{\xi_1}$ and $\boldsymbol{\pi}^{\xi_2}$ are given by

$$\boldsymbol{\pi}^t = -\rho_0 G_{,\boldsymbol{\varepsilon}^t} = \boldsymbol{\sigma} , \quad (108)$$

$$\boldsymbol{\pi}^{\xi_1} = -\rho_0 G_{,\xi_1} = \frac{1}{2} \boldsymbol{\sigma}_{cR} : \Delta \boldsymbol{\mathcal{S}} \boldsymbol{\sigma}_{cR} + \mu_0 \Delta \mathbf{M} \cdot \mathbf{H} + \rho \Delta s_0 - \rho \Delta u_0 - f(\xi_1)_{,\xi_1} . \quad (109)$$

$$\boldsymbol{\pi}^{\xi_2} = -\rho_0 G_{,\xi_2} = \frac{1}{2} \boldsymbol{\sigma}_{cR} : \Delta \boldsymbol{\mathcal{S}} \boldsymbol{\sigma}_{cR} + \mu_0 \Delta \mathbf{M} \cdot \mathbf{H} + \rho \Delta s_0 - \rho \Delta u_0 - f(\xi_2)_{,\xi_2} . \quad (110)$$

We assume that the specific heat difference between the martensitic and austenitic phase is zero ($\Delta c = 0$). The hardening function $f_1(\xi_1)$ and $f_2(\xi_2)$ are defined as below [30, 31].

$$f_{1,\xi_1} := \begin{cases} -A^H(\pi - \cos^{-1}(2\xi - 1) + B_1^H + B_2^H), & \dot{\xi} > 0 , \\ -C^H(\pi - \cos^{-1}(2\xi - 1) + B_1^H - B_2^H) & \dot{\xi} < 0 , \end{cases} \quad (111)$$

$$f_{2,\xi_2} := \begin{cases} -A^T(\pi - \cos^{-1}(2\xi - 1) + B_1^T + B_2^T), & \dot{\xi} > 0, \\ -C^T(\pi - \cos^{-1}(2\xi - 1) + B_1^T - B_2^T) & \dot{\xi} < 0, \end{cases} \quad (112)$$

and the Kuhn Tucker conditions [32] are given by

$$\Phi^{\xi_1} := \begin{cases} \tilde{\pi}^{\xi_1} - Y^{\xi_1}, & \dot{\xi}_1 > 0 \\ -\tilde{\pi}^{\xi_1} - Y^{\xi_1}, & \dot{\xi}_1 < 0 \end{cases}, \quad \Phi^{\xi_1} \leq 0 \quad (113)$$

$$\Phi^{\xi_1} \leq 0, \quad \Phi^{\xi_1} \dot{\xi}_1 = 0. \quad (114)$$

and

$$\Phi^{\xi_2} := \begin{cases} \tilde{\pi}^{\xi_2} - Y^{\xi_2}, & \dot{\xi}_2 > 0 \\ -\tilde{\pi}^{\xi_2} - Y^{\xi_2}, & \dot{\xi}_2 < 0 \end{cases}, \quad \Phi^{\xi_2} \leq 0 \quad (115)$$

$$\Phi^{\xi_2} \leq 0, \quad \Phi^{\xi_2} \dot{\xi}_2 = 0. \quad (116)$$

Here, Y^{ξ_1} and Y^{ξ_2} are related to the internal dissipation related to the corresponding phase transformations.

3.4 Model Simulation of Experiments on FIPT

A schematic representation of the experimental setup to measure magnetic field-induced strains is shown in Fig. 40. The setup consists of a 2 T electromagnet, which is adjustably mounted on a mechanical load frame such that the directions of the applied force and the magnetic field are perpendicular. The specimen is held in place by nonmagnetic grips. A polymer chamber, which encloses the grips and specimen, is filled with nitrogen gas for cooling. As depicted in Fig. 40, temperature, deformation, and magnetic field measurements are taken by a thermocouple, a capacitive displacement sensor and a Hall probe.

An ingot of $\text{Ni}_{45}\text{Mn}_{36.5}\text{Co}_5\text{In}_{13.5}$ was prepared by vacuum induction melting. The single crystals were cut into rectangular prisms with dimensions $4 \times 4 \times 8\text{mm}^3$ using wire electro-discharge machining. The magnetization response of the crystals as a function of temperature and magnetic field was measured using a Quantum Design Superconducting Quantum Interface Device (SQUID) magnetometer.

Following the experiments, we will consider a one dimensional mechanical and magnetic loading condition to calibrate the model from experiments. We

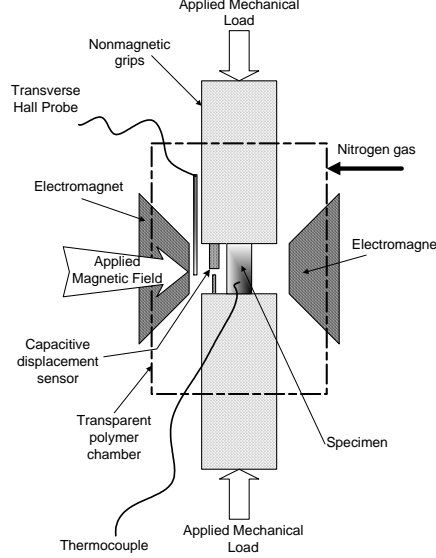


Figure 40: Experimental setup [25]

select the cartesian basis (e_x, e_y) along the x and y axis respectively. We take the x-axis as the axial direction of the rectangular bar specimen. The mechanical boundary conditions of the problem is $\sigma \mathbf{n}_x = \mathbf{t}^a$ and $\sigma \mathbf{n}_y = \mathbf{0}$. The traction $t_x^a = \sigma^a/A$ acts on the boundary surface along the direction of the normal \mathbf{n}_x , where A is the area of the boundary surface and σ^a is the total axial stress on the boundary.

The magnetic field is applied along y direction. For the comparison of model predictions with experimental results, the applied magnetic field \mathbf{H} can be interpreted as the average magnetic field in the specimen.

In the present uniaxial loading case and considering isochoric phase transformation, the transformation strain tensor has only the following components. $\varepsilon_{xx}^t = \varepsilon^t, \varepsilon_{yy}^t = \varepsilon_{zz}^t = -\frac{1}{2}\varepsilon^t$. For the proportional loading condition, the transformation tensor $\Lambda_i (i=1,2)$ in Eq. 104 is proposed in the following form.

$$\Lambda_i = \mu_i(\sigma^a)[\mathbf{e}_x \otimes \mathbf{e}_x - \frac{1}{2}\mathbf{e}_y \otimes \mathbf{e}_y - \frac{1}{2}\mathbf{e}_z \otimes \mathbf{e}_z]. \quad (117)$$

The parameter $\mu_1(\sigma^a)$ and $\mu_2(\sigma^a)$ are equal to the maximum transformation strain $\varepsilon_1^{t,max}$ and $\varepsilon_2^{t,max}$, generated at the end of forward phase transformation due to the magnetic field and the temperature respectively. These parameters can be obtained from experiments.

Experimental data for the model calibration have been obtained from Karaca et.al[25]. The stress-temperature phase diagram (Fig. 41(a)) is obtained from the isobaric strain temperature experiments at different stress levels and from pseudoelastic experiments at different temperature levels. In both cases, no magnetic field is applied. Similarly, the temperature-magnetic phase diagram (Fig. 41(b)) is obtained from magnetization-temperature experiments at different applied magnetic field and from magnetization-magnetic field experiments at different temperatures with no applied mechanical stress. We perform a linear fit with the experimental data points as shown by the solid straight line in the Fig. 41. In the model, we use the equation of the fitted line to find out the critical values to start and finish of the forward and reverse phase transformations. The obtained critical values are used for the model calibration.

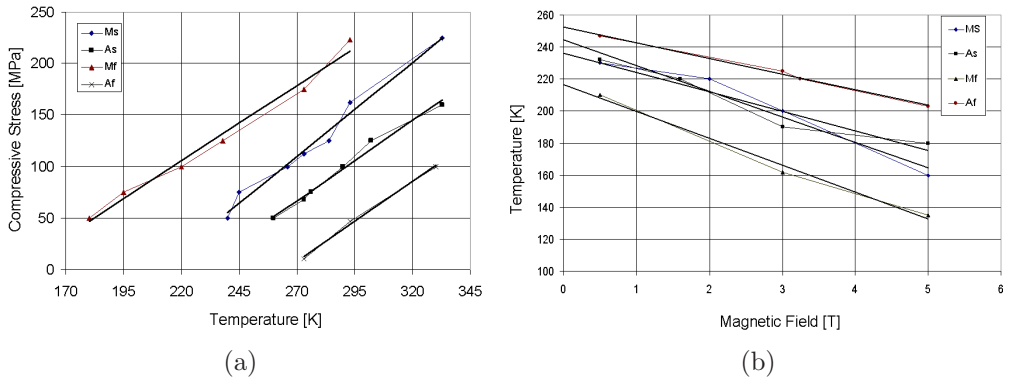


Figure 41: (a) Stress vs temperature phase diagram and (b) Temperature vs magnetic field phase diagram.

3.5 Results and Discussion:

In Fig. 42(a) we present the strain-temperature response with no applied magnetic field. The applied stress for this case is 100 MPa. This result is similar to the conventional phase transformation in SMAs due to the temperature effect. The pseudoelastic response at T=293K is presented in Fig. 42(b). We also use the maximum transformation strain data at different stress level for the model calibration. Next, we present the magneto-thermal coupling predicted by the model during phase transformation. The magnetization-temperature response is presented in Fig. 43(a). We assume in the model that saturation magnetization of the austenitic phase does not vary with

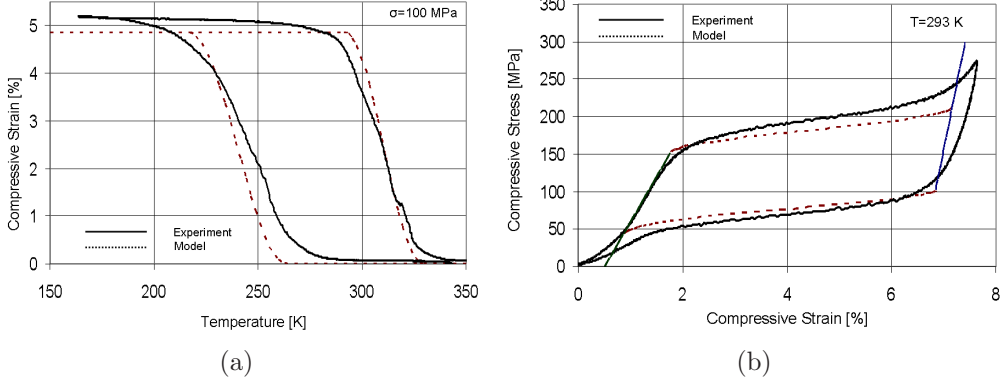


Figure 42: (a) Strain vs temperature response at a stress level 100 MPa and (b) Stress vs strain response at 293 K. In both cases, no magnetic field is applied.

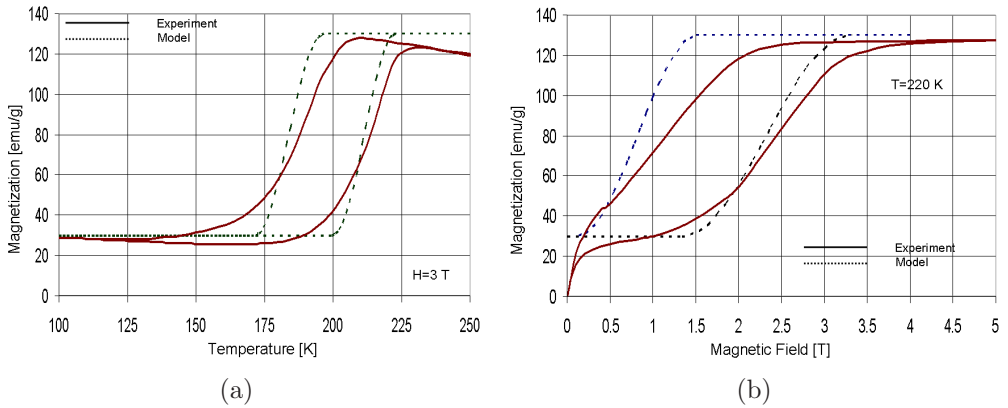


Figure 43: (a) Magnetization vs temperature response at a magnetic field level 3 T and (b) Magnetization vs magnetic field response at a temperature level 220 K.

temperature although, in reality the saturation magnetization varies slightly with the temperature, as it can be observed in the experimental results shown in Fig. 43(a). The magnetization-magnetic field response at constant temperature ($T=220\text{K}$) is given in Fig. 43(b). The temperature is kept below martensite start temperature, the sample is fully martensitic with all temperature induced martensite. This experiment is conducted under no applied stress and austenite to martensite phase transformation should occur due

to the applied magnetic field with twinned martensitic structure at the low magnetic field. In the model we assume that the material is fully magnetically saturated even at very low fields, for the sake of simplicity. Due to this assumption, the model simulation does not start from the origin. The initial portion of the magnetization-magnetic field diagram shown in the experiments is due to the magnetic saturation of martensite with increasing field and the model does not take this into account at the moment.

A Magneto Mechanical Boundary Conditions

We seek to prove that: if $\llbracket \boldsymbol{\sigma} + \boldsymbol{\sigma}^M \rrbracket \cdot \mathbf{n} = \mathbf{0}$, then $\boldsymbol{\sigma}^E \mathbf{n} = \mathbf{t}^a + \mu_0(\mathbf{H} \otimes \mathbf{M})\mathbf{n} + \frac{\mu_0}{2}(\mathbf{M} \cdot \mathbf{n})^2 \mathbf{n}$, where $\boldsymbol{\sigma}\mathbf{n} = \mathbf{t}^a$.

We define $\llbracket A \rrbracket = A^+ - A^-$, where $A \in \partial\Omega$ and \mathbf{n} is the outward normal to the boundary $\partial\Omega$. A^+ and A^- represent the values of A on either side of the discontinuity surface. From Amperes law, we can conclude that $\llbracket \mathbf{H} \rrbracket^t = 0$ (3(b)), where superscript t represents the tangential direction. It then follows $\mathbf{H} = \mathbf{H}^n + \mathbf{H}^t = (\mathbf{H} \cdot \mathbf{n})\mathbf{n} + \mathbf{H}^t$ and

$$\llbracket \mathbf{H} \rrbracket = \llbracket \mathbf{H}^n \rrbracket + \llbracket \mathbf{H}^t \rrbracket = \llbracket \mathbf{H}^n \rrbracket = (\llbracket \mathbf{H} \rrbracket \cdot \mathbf{n})\mathbf{n}. \quad (118)$$

Using the constitutive relation $\mathbf{H} = \frac{1}{\mu_0}\mathbf{B} - \mathbf{M}$ in (118) and (3(a)) we find,

$$\begin{aligned} \llbracket \mathbf{H} \rrbracket &= \left(\frac{1}{\mu_0} \llbracket \mathbf{B} \rrbracket \cdot \mathbf{n} - \llbracket \mathbf{M} \rrbracket \cdot \mathbf{n} \right) \mathbf{n} \\ &= -(\llbracket \mathbf{M} \rrbracket \cdot \mathbf{n})\mathbf{n} \\ &= -[(\mathbf{M}^+ - \mathbf{M}^-) \cdot \mathbf{n}]\mathbf{n} \\ &= (\mathbf{M} \cdot \mathbf{n})\mathbf{n} \end{aligned} \quad (119)$$

Here we use the fact that $\mathbf{M}^+ = 0$ and $\mathbf{M}^- = \mathbf{M}$. Note that Eq (26) can be rewritten as $\boldsymbol{\sigma}^m = \mathbf{H} \otimes \mathbf{B} - \frac{\mu_0}{2}(\mathbf{H} \cdot \mathbf{H})\mathbf{I}$. It follows that

$$\begin{aligned} \llbracket \boldsymbol{\sigma}^m \rrbracket \mathbf{n} &= \llbracket \mathbf{H} \otimes \mathbf{B} \rrbracket \mathbf{n} - \frac{\mu_0}{2} \llbracket (\mathbf{H} \cdot \mathbf{H})\mathbf{I} \rrbracket \mathbf{n} \\ &= (\mathbf{H}^+ \otimes \mathbf{B}^+ - \mathbf{H}^- \otimes \mathbf{B}^-)\mathbf{n} - \frac{\mu_0}{2}(\mathbf{H}^+ \cdot \mathbf{H}^+ - \mathbf{H}^- \cdot \mathbf{H}^-)\mathbf{n} \end{aligned} \quad (120)$$

The first term in Eq (120) may be written with $\llbracket \mathbf{B} \rrbracket \cdot \mathbf{n} = (\mathbf{B}^+ \cdot \mathbf{n}) - (\mathbf{B}^- \cdot \mathbf{n}) = 0$, as

$$\begin{aligned}
(\mathbf{H}^+ \otimes \mathbf{B}^+ - \mathbf{H}^- \otimes \mathbf{B}^-) \mathbf{n} &= (\mathbf{B}^+ \cdot \mathbf{n}) \mathbf{H}^+ - (\mathbf{B}^- \cdot \mathbf{n}) \mathbf{H}^- \\
&= (\mathbf{B}^+ \cdot \mathbf{n})(\mathbf{H}^+ - \mathbf{H}^-) \\
&= (\mathbf{B}^+ \cdot \mathbf{n}) [\mathbf{H}]
\end{aligned} \tag{121}$$

From equation (3(b)) it is clear that $[\mathbf{n} \times \mathbf{H}] = \mathbf{0}$ and consequently,

$$|\mathbf{n} \times \mathbf{H}^+|^2 = |\mathbf{n} \times \mathbf{H}^-|^2 \tag{122}$$

Using the identity $(\mathbf{A} \times \mathbf{B}) \cdot (\mathbf{C} \times \mathbf{D}) = (\mathbf{A} \cdot \mathbf{C})(\mathbf{B} \cdot \mathbf{D}) - (\mathbf{A} \cdot \mathbf{D})(\mathbf{B} \cdot \mathbf{C})$, we can write,

$$(\mathbf{n} \times \mathbf{H}^+) \cdot (\mathbf{n} \times \mathbf{H}^+) = (\mathbf{n} \cdot \mathbf{n})(\mathbf{H}^+ \cdot \mathbf{H}^+) - (\mathbf{H}^+ \cdot \mathbf{n})^2 \tag{123}$$

Similarly,

$$(\mathbf{n} \times \mathbf{H}^-) \cdot (\mathbf{n} \times \mathbf{H}^-) = (\mathbf{n} \cdot \mathbf{n})(\mathbf{H}^- \cdot \mathbf{H}^-) - (\mathbf{H}^- \cdot \mathbf{n})^2 \tag{124}$$

From Eq (122), Eq (123) and Eq (124), we conclude

$$|\mathbf{H}^+|^2 - (\mathbf{H}^+ \cdot \mathbf{n})^2 = |\mathbf{H}^-|^2 - (\mathbf{H}^- \cdot \mathbf{n})^2 \tag{125}$$

Now with Eq (125) we can write the second term on the right hand side of Eq (120) in the following form,

$$\begin{aligned}
\frac{\mu_0}{2} [\mathbf{H}^+ \cdot \mathbf{H}^+ - \mathbf{H}^- \cdot \mathbf{H}^-] \mathbf{n} &= \frac{\mu_0}{2} [(\mathbf{H}^+ \cdot \mathbf{n})^2 - (\mathbf{H}^- \cdot \mathbf{n})^2] \mathbf{n} \\
&= \frac{\mu_0}{2} [(\mathbf{H}^+ - \mathbf{H}^-) \cdot \mathbf{n}] [(\mathbf{H}^+ + \mathbf{H}^-) \cdot \mathbf{n}] \mathbf{n}
\end{aligned}$$

Considering that $(\mathbf{H}^+ - \mathbf{H}^-) = [\mathbf{H}] \cdot \mathbf{n}$ and $(\mathbf{H}^+ + \mathbf{H}^-) \cdot \mathbf{n} = [(\frac{1}{\mu_0} \mathbf{B}^+ - \mathbf{M}^+) + (\frac{1}{\mu_0} \mathbf{B}^- - \mathbf{M}^-)] \cdot \mathbf{n} = [\frac{1}{\mu_0} \mathbf{B}^+ + \frac{1}{\mu_0} \mathbf{B}^- - \mathbf{M}^-] \cdot \mathbf{n}$ and due to (3(a)) $\mathbf{B}^+ \cdot \mathbf{n} = \mathbf{B}^- \cdot \mathbf{n}$, it follows

$$\begin{aligned}
\frac{\mu_0}{2} [\mathbf{H}^+ \cdot \mathbf{H}^+ - \mathbf{H}^- \cdot \mathbf{H}^-] \mathbf{n} &= \frac{\mu_0}{2} [\mathbf{H}] \cdot \mathbf{n} \left[\frac{2}{\mu_0} (\mathbf{B}^+ - \mathbf{M}) \cdot \mathbf{n} \right] \mathbf{n} \\
&= (\mathbf{B}^+ \cdot \mathbf{n}) ([\mathbf{H}] \cdot \mathbf{n}) \mathbf{n} - \frac{\mu_0}{2} (\mathbf{M} \cdot \mathbf{n}) ([\mathbf{H}] \cdot \mathbf{n}) \mathbf{n} \\
&= (\mathbf{B}^+ \cdot \mathbf{n}) [\mathbf{H}] - \frac{\mu_0}{2} (\mathbf{M} \cdot \mathbf{n}) [\mathbf{H}] \\
&= (\mathbf{B}^+ \cdot \mathbf{n}) [\mathbf{H}] - \frac{\mu_0}{2} (\mathbf{M} \cdot \mathbf{n})^2 \mathbf{n}
\end{aligned} \tag{126}$$

Substitution of Eq (121) and Eq (126) into Eq (120) yields

$$[\![\boldsymbol{\sigma}^m]\!] \mathbf{n} = \frac{\mu_0}{2} (\mathbf{M} \cdot \mathbf{n})^2 \mathbf{n} \quad (127)$$

In consequence with Eq (32), we obtain

$$\begin{aligned} [\![\boldsymbol{\sigma} + \boldsymbol{\sigma}^m]\!] \mathbf{n} &= [\![\boldsymbol{\sigma}]\!] \mathbf{n} + [\![\boldsymbol{\sigma}^m]\!] \mathbf{n} \\ &= (\boldsymbol{\sigma}^+ - \boldsymbol{\sigma}^-) \mathbf{n} + [\![\boldsymbol{\sigma}^m]\!] \mathbf{n} \\ &= \mathbf{t}^a - \boldsymbol{\sigma} \mathbf{n} + \frac{\mu_0}{2} (\mathbf{M} \cdot \mathbf{n})^2 \mathbf{n} \\ &= \mathbf{t}^a - \boldsymbol{\sigma}^E \mathbf{n} + \mu_0 (\mathbf{H} \otimes \mathbf{M}) \mathbf{n} + \frac{\mu_0}{2} (\mathbf{M} \cdot \mathbf{n})^2 \mathbf{n} \end{aligned} \quad (128)$$

Finally, Eq (31) yields the boundary condition in the following form,

$$\boldsymbol{\sigma}^E \mathbf{n} = \mathbf{t}^a + \mu_0 (\mathbf{H} \otimes \mathbf{M}) \mathbf{n} + \frac{\mu_0}{2} (\mathbf{M} \cdot \mathbf{n})^2 \mathbf{n} \quad (129)$$

References

- [1] Eringen, A. C., and Maugin, G. A., 1990. *Electrodynamics of Continua I — Foundations and Solid Media*. Springer-Verlag, New York.
- [2] Hutter, K., and van de Ven, A. A. F., 1978. *Field Matter Interactions in Thermoelastic Solids*, Vol. 88 of *Lecture Notes in Physics*. Springer-Verlag, New York.
- [3] Sullivan, M. R., and Chopra, H. D., 2004. “Temperature- and field-dependent evolution of micromagnetic structure in ferromagnetic shape-memory-alloys”. *Physical Review B*, **70**, pp. 094427–(1–8).
- [4] Kiefer, B., and Lagoudas, D. C., 2005. “Magnetic field-induced martensitic variant reorientation in magnetic shape memory alloys”. *Philosophical Magazine Special Issue: Recent Advances in Theoretical Mechanics, in Honor of SES 2003 A.C. Eringen Medalist G.A. Maugin*, **85**(33–35), pp. 4289–4329.
- [5] Tickle, R., and James, R. D., 1999. “Magnetic and magnetomechanical properties of Ni₂MnGa”. *Journal of Magnetism and Magnetic Materials*, **195**(3), pp. 627–638.

- [6] Cullity, B. D., 1972. *Introduction to Magnetic Materials*. Addison-Wesley, Reading, MA.
- [7] O'Handley, R. C., 2000. *Modern Magnetic Materials*. John Wiley & Sons, New York.
- [8] O'Handley, R. C., Murray, S. J., Marioni, M., Nembach, H., and Allen, S. M., 2000. “Phenomenology of giant magnetic-field-induced strain in ferromagnetic shape-memory materials (invited)”. *Journal of Applied Physics*, **87**(9), pp. 4712–4717.
- [9] O'Handley, R. C., Allen, S. M., Paul, D. I., Henry, C. P., Marioni, M., Bono, D., Jenkins, C., Banful, A., and Wager, R., 2003. “Keynote address: Magnetic field-induced strain in single crystal Ni-Mn-Ga”. in: *Proceedings of SPIE, Symposium on Smart Structures and Materials*, **5053**, pp. 200–206.
- [10] Tickle, R., 2000. “Ferromagnetic shape memory materials”. PhD thesis, University of Minnesota, Minneapolis, MN, May.
- [11] Heczko, O., Straka, L., and Ullakko, K., 2003. “Relation between structure, magnetization process and magnetic shape memory effect of various martensites occurring in Ni-Mn-Ga alloys”. *Journal de Physique IV France*, **112**, pp. 959–962.
- [12] Kiefer, B., Karaca, H. E., Lagoudas, D. C., and Karaman, I., 2006. “Characterization and modeling of the magnetic field-induced strain and work output in Ni₂MnGa shape memory alloys”. *Journal of Magnetism and Magnetic Materials*, **312**, November, pp. 164–175.
- [13] Jackson, J. D., 1975. *Classical Electrodynamics*, 2nd ed. John Wiley & Sons, New York.
- [14] Bertram, H. N., 1994. *Theory of Magnetic Recording*. Cambridge University Press, Cambridge, UK.
- [15] Schlömann, E., 1962. “A sum rule concerning the inhomogeneous demagnetizing field in nonellipsoidal samples”. *Journal of Applied Physics*, **33**(9), pp. 2825–2826.
- [16] Bozorth, R. M., 1993. *Ferromagnetism*, reissue of 1951 ed. IEEE Press.
- [17] Eshelby, J. D., 1957. “The determination of the elastic field of an ellipsoidal inclusion, and related problems”. *Proceedings of the Royal Society*

of London. Series A, Mathematical and Physical Sciences, **241**(1226), pp. 376–396.

- [18] Mura, T., 1987. *Micromechanics of Defects in Solids*, 2nd revised ed. Mechanics of Elastic and Inelastic Solids. Kluwer Academic Publisher, Dordrecht, The Netherlands.
- [19] Moskowitz, R., and Della Torre, E., 1966. “Theoretical aspects of demagnetization tensors”. *IEEE Transactions on Magnetics*, **2**(4), pp. 739–744.
- [20] Fukushima, H., Nakatani, Y., and Hayashi, N., 1998. “Volume average demagnetizing tensor of rectangular prisms”. *IEEE Transactions on Magnetics*, **34**(1), pp. 193–198.
- [21] Shield, T. W., 2003. “Magnetomechanical testing machine for ferromagnetic shape-memory alloys”. *Review of Scientific Instruments*, **74**(9), pp. 4077–4088.
- [22] Murray, S. J., Marioni, M., Allen, S. M., and O’Handley, R. C., 2000. “6% magnetic-field-induced strain by twin-boundary motion in ferromagnetic Ni-Mn-Ga”. *Applied Physics Letters*, **77**(6), pp. 886–888.
- [23] Karaca, H. E., Karaman, I., Basaran, B., Chumlyakov, Y. I., and Maier, H. J., 2006. “Magnetic field and stress induced martensite reorientation in NiMnGa ferromagnetic shape memory alloy single crystals”. *Acta Materialia*, **54**(1), pp. 233–245.
- [24] Karaman, I., Karaca, H. E., Basaran, B., Lagoudas, D. C., Chumlyakov, Y. I., and Maier, H. J., 2006. “Stress-assisted reversible magnetic field-induced phase transformation in Ni₂MnGa magnetic shape memory alloys”. *Scripta Materialia*, **55**(4), pp. 403–406.
- [25] Karaca, H. E., Karaman, I., Basaran, B., Yang, R., Chumlyakov, Y. I., and Maier, H. J., 2009. “Magnetic field-induced phase transformation in NiMnCoIn magnetic shape memory alloys-a new actuation mechanism with large work output”. *Advanced Functional Materials*, **19**, pp. 1–16.
- [26] Kovetz., A., 2000. *Electromagnetic Theory*. Oxford.
- [27] Steigmann., D. J., 2004. “Equilibrium theory for magnetic elastomers and magnetoelastic membranes”. *Non-Linear Mechanics*, **39**, pp. 1193–1216.

- [28] Boyd, J. G., and Lagoudas, D. C., 1996. “A thermodynamical constitutive model for shape memory materials. Part I. The monolithic shape memory alloy”. *International Journal of Plasticity*, **12**(6), pp. 805–842.
- [29] Lagoudas, D. C., Bo, Z., and Qidwai, M. A., 1996. “A unified thermodynamic constitutive model for SMA and finite element analysis of active metal matrix composites”. *Mechanics of Composite Materials and Structures*, **3**, pp. 153–179.
- [30] Bo, Z., and Lagoudas, D. C., 1999. “Thermomechanical modeling of polycrystalline SMAs under cyclic loading, Part I: Theoretical derivations”. *International Journal of Engineering Science*, **37**, pp. 1089–1140.
- [31] Liang, C., and Rogers, C. A., 1990. “One-dimensional thermomechanical constitutive relations for shape memory materials”. *Journal of Intelligent Material Systems and Structures*, **1**, pp. 207–234.
- [32] Simo, J. C., and Hughes, T. J. R., 1998. *Computational Inelasticity*, Vol. 7 of *Interdisciplinary Applied Mathematics*. Springer-Verlag, New York.